SURFACE MODIFICATION OF NANOPARTICLES FOR POLYMER/CERAMIC NANOCOMPOSITES AND THEIR APPLICATIONS

A Dissertation
Presented to
The Academic Faculty

by

Philseok Kim

In Partial Fulfillment
of the Requirements for the Degree
Doctor of Philosophy in the
School of Chemistry and Biochemistry

Georgia Institute of Technology
December, 2008

SURFACE MODIFICATION OF NANOPARTICLES FOR POLYMER/CERAMIC NANOCOMPOSITES AND THEIR APPLICATIONS

Approved by:

Dr. Joseph W. Perry, Advisor
School of Chemistry and Biochemistry
Georgia Institute of Technology

Dr. Robert L. Whetten
School of Chemistry and Biochemistry
Georgia Institute of Technology

Dr. Seth R. Marder
School of Chemistry and Biochemistry
Georgia Institute of Technology

Dr. L. Andrew Lyon
School of Chemistry and Biochemistry
Georgia Institute of Technology

Dr. Bernard Kippelen
School of Electrical and Computer Engineering
Georgia Institute of Technology

Date Approved: [Oct. 17, 2008]

[This dissertation is dedicated to my wife, Hyejung, and my family in Korea for their love and endless support during my Ph. D. study.]

ACKNOWLEDGEMENTS

I would like to express my sincere gratitude to my advisor, Professor Joseph W. Perry, for his guidance, encouragement, and endless support and interest provided during the course of this research. He has been and will always be my best source of inspiration and support. I am also deeply indebted to Professors Seth R. Marder and Bernard Kippelen for the invaluable advice and support they have provided to make this research possible. I would like to thank Professors Robert L. Whetten and L. Andrew Lyon for serving on my Ph. D. committee and for their discussions and insights.

I would like to thank all other fellow co-workers in Dr. Perry's group, Dr. Marder's group, and Dr. Kippelen's group who contributed to this research: Dr. Simon C. Jones, Mr. Peter J. Hotchkiss, Dr. Joshua N. Haddock, Ms. Xiao-Hong Zhang, Dr. Benoit Domercq, Ms. Natalie M. Doss, and Mr. Wojtek Haske.

I would also like to thank other fellow folks who provided valuable discussions, ideas, helps with a stimulating work environment, and friendship: Dr. Mariacristina Rumi, Dr. Stephen Barlow, Dr. Joel M. Hales, Dr. Wenting Dong, Dr. Seunghyup Yoo, Mr. Jungbae Kim, Dr. Christina M. Bauer, Mr. Michal Malicki, Mr. Nisan Siegel, Ms. Arianna Biesso, Dr. Andreas Haldi, Mr. William Potscavage, Dr. Canek F. Hernandez, Dr. Sungjae Chung, Dr. Matthew M. Sartin, Mr. Matteo Cozzuol, Dr. Ali Hayek, Dr. Yunnan Fang, Dr. Johannes Leisen, Dr. Yiqing Wang, and all other members of the Perry group.

My co-workers outside Georgia Tech who partially contributed to this research are also acknowledged: Professor Jiangyu Li at University of Washington, Professor

Qing Wang at University of Pennsylvania, Drs. Ming-Jen Pan and Jeffrey P. Calame at the Naval Research Laboratory, Washington, DC.

I wish to thank other professors and fellows at Georgia Tech, who kindly offered the use of their equipments and provided valuable advice: Professor Kenneth H. Sandhage, Professor Satish Kumar and Dr. Han Gi Chae, Professor Nils Kröger, Dr. Nicole Poulsen, Professor Angus P. Wilkinson, Professor Christopher Jones, Professor Uwe H. F. Bunz, Professor C. P. Wong, and Dr. Pulugurtha M. Raj.

My special thanks go to the faculty and staff members in the School of Chemistry and Biochemistry, Microelectronics Research Center, and the Center for Nanostructure Characterization: Ms. Beverly Scheerer, Ms. Veatrice Aggison, Professor Brent Carter, Mr. Gary Spinner, Mr. Joel Pikarsky, Mr. Brandon Harrington, Mr. Charlie Suh, and Ms. Yolande Berta.

I would like to acknowledge the undergraduate research assistants who worked with me for this research: Ms. Ariel S. Marshall, Ms. Krystle L. Dzienis, Mr. John P. Tillotson, and Mr. Nathan Hankins.

This research was financially supported by the Office of Naval Research (N00014-05-1-0760), National Science Foundation through the Science and Technology Centers Program (MDITR, DMR 0120967). The support from the Center for Organic Photonics and Electronics and the staff members are also acknowledged. I also would like to acknowledge the financial support from LG Chem, Ltd.

Finally, I would like to thank my family in Korea and my wife, Hyejung, for their continuous support and encouragement. Without them, this dissertation would not be possible.

TABLE OF CONTENTS

LIST OF TABLES

LIST OF FIGURES

LIST OF SYMBOLS

ε_0	permittivity of vacuum
ε_r	relative permittivity
κ	relative permittivity
C	Capacitance
$\mathbf{P}$	electric polarization
$\mathbf{E}$	electric field
$\mathbf{E}_{loc}$	local field
α	polarizability
α (Weibull Analysis)	scale parameter
β (Weibull Analysis)	shape parameter
f	volume fraction
V_B	breakdown voltage
$\mathbf{E}_B$	breakdown field
U_{max}	maximum energy density
$\tan\delta$	dielectric loss tangent
μ	carrier mobility
V_T	threshold voltage
V_{DS}	drain-source voltage
V_{GS}	gate-source voltage
$I_{on/off}$	on/off current ratio
S	sub-threshold slope
V_B	breakdown voltage
δ	chemical shift (ppm)

a	electric field concentration factor
f_T	threshold volume fraction
J_L	leakage current density
n	refractive index
α_{SC}	scattering coefficient

LIST OF ABBREVIATIONS

AC	Alternating current
ACPA	Acryloylundecylphosphonic acid
AFM	Atomic force microscopy
BDDAC	Benzyl dodecyl dimethyl ammonium chloride
BOPP	Bi-axially oriented polypropylene
BST	Barium strontium titanate
BT	Barium Titanate, $BaTiO_3$, (30 – 50 nm)
BT-8	Barium Titanate, $BaTiO_3$, (120 – 150 nm)
CA	Carboxylic acid
CDF	Cumulative distribution function
CEP	Cyanoethylpullulan
CP	Cold plasma
CP	Cross polarization
DC	Direct current
DF	Dissipation factor
DMF	*N*,*N*-Dimethylformamide
DP	Direct polarization
EDS	Energy dispersive spectroscopy
EMA	Effective medium approximation
FT-IR	Fourier transform infrared
GPC	Gel permeation chromatography
HMMM	Hexamethylmethoxymelamine

IEP	Isoelectric point
ITC	Isothermal titration calorimetry
ITO	Indium tin oxide
MAEAA	2-(Methacryloyloxy)ethyl acetoacetate
MIBK	Methylisobutyl ketone
NMP	*N*-methyl-2-pyrrolidone
ODPA	Octadecylphosphonic acid
OFET	Organic field-effect transistor
OLA	Oleylamine
OPA	Octylphosphonic acid
P(VDF-HFP)	Poly(vinylidene fluoride-*co*-hexafluoropropylene)
P(VDF-TrFE)	Poly(vinylidene fluoride-*co*-trifluoroethylene)
P(VDF-TrFE-CTFE)	Poly(vinylidene fluoride-*co*-trifluoroethylene-*co*-chlorotrifluoroethylene)
P25	TiO_2 nanoparticle, Degussa
P3HT	Poly(3-hexylthiophene)
P3OT	Poly(3-octylthiophene)
PA	Phosphonic acid
PBBZPA	Pentabromobenzylphosphonic acid
PBG	Photonic band gap
PBPM	Pentabromophenyl methacrylate
PC	Polycarbonate
PDI	Polydispersity index
PE	Place exchange
PEGPA	{2-[2-(2-Methoxyethoxy)ethoxy]ethyl}phosphonic acid
PFBPA	Pentafluorobenzylphosphonic acid

PF	Power factor
PGME	Propyleneglycol methyl ether
PGMEA	Propyleneglycol methyl ether acetate
PSAN	Poly(styrene-*co*-acrylonitrile)
PVP	Poly(4-vinylphenol)
QF	Quality factor
RMS	Root-mean-square
rpm	Revolution per minute
SA	Sulfonic acid
SAM	Self-assembled monolayer
SC-EMT	Self-consistent effective medium theory
SCLC	Space-charge limited current
SEM	Scanning electron microscopy
SI	Silane
SS-NMR	Solid-state nuclear magnetic resonance
TEM	Transmission electron microscopy
TGA	Thermogravimetric Analysis
TL-SCLC	Trap limited space-charge limited current
ToF	Time-of-flight
TPM	Two-photon microfabrication
XPS	X-ray photoelectron spectroscopy
XRD	X-ray diffraction
YSZ	Yttria-stabilized zirconia

SUMMARY

This thesis describes the surface modification of barium titanate nanoparticles and their application to high quality, solution-processable polymer/ceramic dielectric nanocomposites with improved dielectric properties. Phosphonic acid-based ligands were found to yield a high surface coverage and robust surface modification on the surface of barium titanate nanoparticles. The study on the dielectric properties of the nanocomposites utilizing surface-modified barium titanate nanoparticles is presented by systematically changing the materials parameters, such as the nanoparticle volume fraction, the host permittivity, and the size of the nanoparticles. The dielectric properties of the nanocomposites were examined by fabricating parallel-plate capacitors and organic field-effect transistors and characterizing their electrical performances. A new model combining effective medium theory and finite difference simulation is proposed to explain the experimentally observed behaviors of the nanocomposites especially at high volume fractions where the porosity in the nanocomposites becomes significant. The new nanocomposite materials presented in this study are potentially useful as dielectrics for high-energy-density capacitors and gate insulators in organic field-effect transistors.

CHAPTER 1

INTRODUCTION

Ever since the observation of Moore's law in 1965, the evolution of downsizing electronic circuits has been calling for the development of new materials with low-cost, better processability, and with improved properties from the reduced size of the materials. (Moore 1965) High performance dielectric materials are of primary importance, as they are needed in capacitors which comprise the majority of passive elements (capacitors, resistors, and inductors) in an electronic circuit. (Tummala, Rymaszewski et al. 1999) Capacitors are typically used in timing, A/D conversion, termination, decoupling, filtering, dynamic random access memory, and energy storage. With the evolution of electronic packaging, the passive elements are buried (or embedded) in the substrate instead of surface mounted. High permittivity materials are imperative for embedded capacitors to attain small form factors with the advantages of reduced parasitic inductance. In high power applications, capacitors play an important role in storing and extracting electrical energy in a very short time, which is generally difficult to achieve with batteries and electric double-layer cells (supercapacitors). Among the approaches to obtain high performance dielectric materials, the polymer/ceramic dielectric nanocomposite approach is the primary focus of this thesis. Homogeneity and improved processability of polymer/ceramic nanocomposites are key features to achieve high permittivity and high dielectric strength nanocomposites. This requires good knowledge and good control of the interfaces present in the system. Organically modifying the surface of high permittivity dielectric nanoparticles is a desirable approach to control such interfaces. This chapter introduces basic concepts of dielectric materials, polymer/ceramic nanocomposites, and the basic idea of surface modification of dielectric nanoparticles. With the identification of scientific and technical challenges in this field, the overall scope of this thesis is presented.

1.1 Physics of Dielectric Materials

1.1.1 Capacitors

A capacitor is composed of two conducting surfaces and a dielectric media between the electrodes which prevents the charges from flowing between the electrodes. Parallel plate capacitors have the geometry of the conducting surfaces parallel to each other. Under a given voltage (V), a capacitor can store electric charge (Q) shown as in Equation 1.1:

$$Q = CV \qquad \text{Equation 1.1}$$

The proportionality coefficient (C) is defined as the capacitance, a measure of charge per electric potential, which has units of 1 Coulomb/1 Volt = 1 Farad (F). The simplest geometry of a capacitor is a parallel-plate capacitor, in which two electrodes (area = A) are separated by a distance t. In an ideal parallel-plate capacitor filled with a dielectric material, the capacitance is given by the following expression:

$$C = \varepsilon_0 \varepsilon_r \frac{A}{t} \qquad \text{Equation 1.2}$$

where $\varepsilon_0 = 8.854 \times 10^{-12}$ F/m and is a constant representing the permittivity (or dielectric constant) of free space and ε_r is the relative permittivity of the dielectric material between the electrodes. Hence the capacitance of a capacitor can be increased by changing the geometry (increasing area and decreasing thickness) or by increasing the permittivity of the dielectric medium.

The separated charges in a capacitor in an electric field store energy (E) that can be released when a load is connected, as expressed in Equation 1.3.

$$E = \frac{1}{2} CV^2 \qquad \text{Equation 1.3}$$

The maximum stored energy (E_{max}) in a capacitor thus depends upon the maximum applicable voltage that can be applied without dielectric breaking the capacitor, as shown in Equation 1.4. This is known as the dielectric breakdown voltage (V_B).

$$E_{\max} = \frac{1}{2} C V_B^2 \qquad \text{Equation 1.4}$$

The maximum energy density, U_{max}, (stored energy per volume) can be also derived from Equation 1.4:

$$U_{\max} = \frac{E_{\max}}{volume} = \frac{\frac{1}{2} C V_B^2}{A \times t} = \frac{1}{2} \frac{\varepsilon_0 \varepsilon_r (A/t) V_B^2}{A \times t} = \frac{1}{2} \varepsilon_0 \varepsilon_r \left(\frac{V_B}{t} \right)^2 = \frac{1}{2} \varepsilon_0 \varepsilon_r E_B^2 \qquad \text{Equation 1.5}$$

where E_B is the dielectric breakdown field strength. Therefore, the maximum energy density is proportional to the permittivity of dielectric material and the square of the breakdown field strength of the dielectric material.

1.1.2 Origins of Microscopic Polarizations

The origins of dielectric polarizations are typically described by four major microscopic mechanisms that occur in specific frequency ranges: electronic polarization, vibrational polarization (displacement of atoms), rotational polarization (orientational polarization), and translational polarization (interfacial or space charge polarization).(Zaky and Hawley 1970) These mechanisms are depicted in Figure 1.1.(Hess and Jensen 1989)

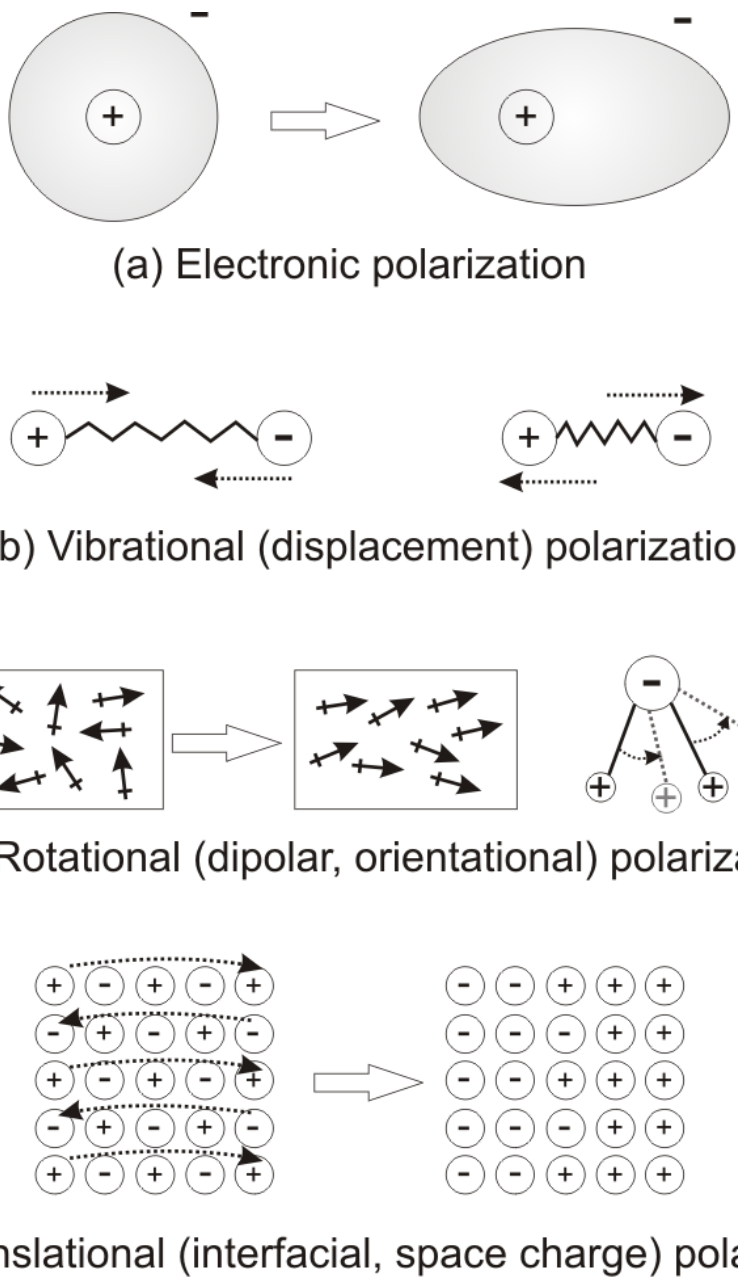

Figure 1.1 The microscopic origins of polarization.

The electron cloud of an isolated neutral atom can be displaced by an electric field and giving rise to a dipole moment. The atom is then said to be polarized. This electronic polarization is not permanent and is dissipated once the applied electric field is removed. The electronic polarization is common in all dielectric materials.

As the name implies, the vibrational polarization is related to the displacement of atoms giving rise to the separation of charges. This is typically found in ionic substances (*e.g.* NaCl) in which the atoms have excess charges of opposite polarities. The applied electric field shifts the relative position of positive and negative ions of a molecule. Similarly, the relative positions of the atoms in non-ionic molecules can be displaced by an applied electric field which also can induce polarization.

Rotational or orientational polarization is found in certain dipolar ceramic and polymeric substances and is associated with permanent dipoles. The microscopic units such as molecular segments, unit cells, and domains, possess a dipole moment even in the absence of applied field due to particular association of molecules or ions. In the presence of an applied electric field, these dipoles tend to orient along the direction of the applied field so that the net dipole moment is non-zero. However, such dipole moments are typically not observed macroscopically as their orientation is randomly distributed due to thermal agitation and averages to zero in a macroscopic volume.

Translational polarization (or interfacial or space charge polarization) is usually associated with the presence of migrating charges (electrons or ions) over macroscopic distances in the applied field. They tend to be trapped and accumulated at physical barriers such as defects, voids, impurities, grain or phase boundaries, and at the electrode interfaces where the materials have different charge transportation properties (*e.g.* conductivity). The accumulated charges distort the local electric field and giving rise to changes in permittivity. Interfacial polarization is particularly important in heterogeneous or multiphase systems such as polymer-ceramic nanocomposites.

The total polarizability of a dielectric material is made up of the above four polarizations. Therefore, the average dipole moment per molecule is expressed as

$$\mathbf{p} = \alpha \mathbf{E}_{loc} \qquad \text{Equation 1.6}$$

and the electric polarization is given by

$$\mathbf{P} = N\alpha \mathbf{E}_{loc} \qquad \text{Equation 1.7}$$

where $\alpha = \alpha_{electronic} + \alpha_{ionic} + \alpha_{orientational} + \alpha_{interfacial}$, N is the number density, and $\mathbf{E}_{loc}$ is the local electric field intensity on each molecule which is usually referred to as the local or the internal field. The local field is different from the applied external field and is discussed in the next section.

1.1.3 The Local Field

The calculation of the exact local field ($\mathbf{E}_{loc}$) in a condensed media is a problem of great mathematical difficulty as there are many interaction forces between molecules present in the system. Simplification of the system can be made by ignoring short-ranged interaction forces and taking only the long-ranged interaction forces between dipoles into account, as they are dominant at long distances. Further simplification can be made by assuming that the medium is macroscopically continuous beyond the interaction distance of a molecule. Lorentz used a fictitious cavity in a dielectric continuum to calculate the local field intensity acting on a molecule under an external field ($\mathbf{E}$) as given by

$$\mathbf{E}_{loc} = \mathbf{E} + \frac{1}{3}\mathbf{E}(\varepsilon_r - 1) = \mathbf{E}\frac{\varepsilon_r + 2}{3} \quad \text{(Lorentz local field relation)} \qquad \text{Equation 1.8}$$

Combining with Equation 1.7 gives a relation

$$\mathbf{P} = \varepsilon_0(\varepsilon_r - 1)\mathbf{E}_{loc} = \frac{1}{3}\mathbf{E}(\varepsilon_r + 2)N\alpha$$

$$\text{or} \quad \frac{N\alpha}{3\varepsilon_0} = \frac{\varepsilon_r - 1}{\varepsilon_r + 2} \qquad \text{Equation 1.9}$$

which is known as the Clausius-Mossotti relation which relates the relative permittivity to the electronic polarizability when Lorentz local field relation is valid.(Kittel 1996)

1.1.4 Dielectric Materials in Alternating Field

The permittivity of a material is constant in DC field when there is no significant dielectric saturation. The dielectric saturation will be discussed later in Section 2.7.5. Under AC field, the permittivity of a material strongly depends on the frequency of the

applied field and can be expressed as a complex number with a real part (ε') and an imaginary part (ε'').

$$\varepsilon^* = \varepsilon' - j\varepsilon'' = \varepsilon_0\varepsilon_r - j\varepsilon'' \qquad \text{Equation 1.10}$$

Figure 1.2 illustrates the frequency dependence of ε' and ε'' of a dielectric material which is directly related to the microscopic polarization mechanisms described in Section 1.1.2.

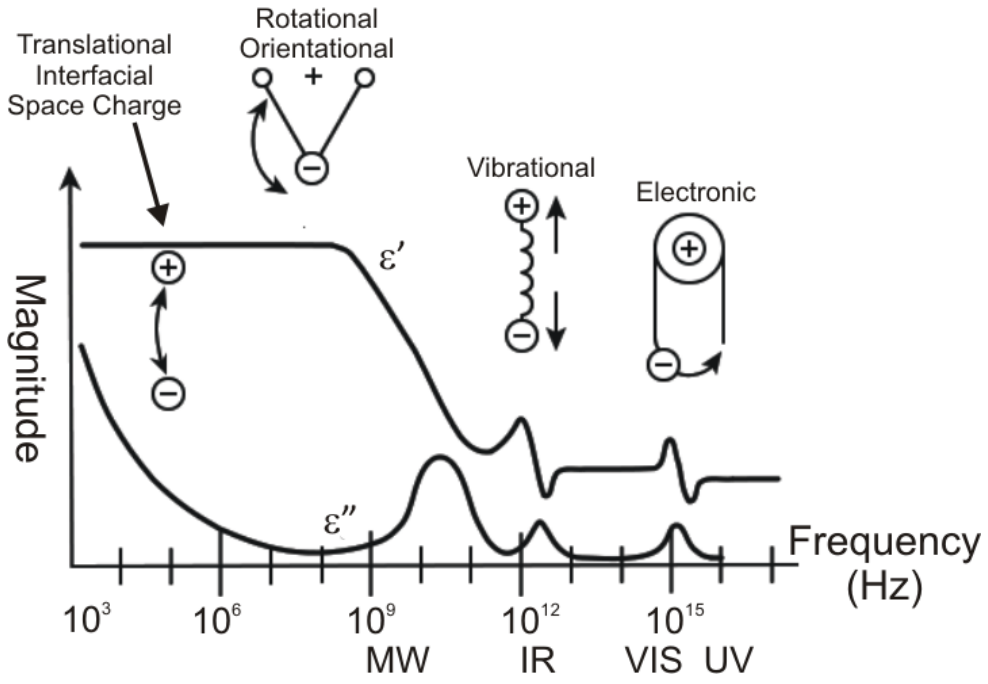

Figure 1.2 Representation of the variation of the real (ε') and imaginary (ε'') part of permittivity as a function of frequency. (copyright Prof. Kenneth A. Mauritz, Univ. Southern Mississippi)

The ratio of the imaginary part to the real part of permittivity, $\varepsilon''/\varepsilon'$, is defined as dissipation factor (DF) which is also known as the loss tangent because it is related to the dielectric loss.(Johnson 2001)

$$\text{Dissipation Factor (DF)} = \tan\delta \equiv \frac{\varepsilon''}{\varepsilon'} \qquad \text{Equation 1.11}$$

Dissipation factor can also be defined as the ratio of the equivalent series resistance to the reactance:

$$\mathrm{DF} = \frac{R}{X_C} \qquad \text{Equation 1.12}$$

This quantity is a materials parameter and varies with frequency, capacitance, and series resistance. It also depends on the environmental changes such as temperature, moisture, pressure, etc. that can cause changes in *C* and *R*. The quality factor (QF) is also a measure of the inefficiency (or loss of power) of a device which is defined as the ratio of the reactance to the series resistance:

$$\mathrm{QF} = \frac{X_C}{R} = \frac{1}{\mathrm{DF}} \qquad \text{Equation 1.13}$$

A good knowledge of dielectric loss is very important in high frequency-operating applications, since at high frequencies, the applicable voltage limit to a capacitor is determined by the ability of the capacitor to dissipate heat. Therefore, dielectrics with a high loss reduce the performance of capacitor devices.(Johnson 2001)

When a capacitor is in use, a certain amount of total power (energy) is applied. Some of the energy can be stored and released but some portion of the energy is lost and dissipated usually as a form of heat. The power factor (PF) is the ratio of the power loss to the input power and is a direct measure of the inefficiency of a capacitor, which is defined as the cosine of the angle between the current flowing through the capacitor and the voltage across it. For a non-ideal capacitor, there is always some loss and the current as a component in phase with the voltage. Therefore, the PF can be expressed as:

$$\mathrm{PF} = \cos\theta = \frac{\varepsilon''}{\sqrt{\varepsilon''^2 + \varepsilon'^2}} \qquad \text{Equation 1.14}$$

For a good dielectric material, $\varepsilon' >> \varepsilon''$, so

$$\cos\theta \approx \frac{\varepsilon''}{\varepsilon'} = \tan\delta \qquad \text{Equation 1.15}$$

The capacitive reactance for alternating current is defined as

$$X_C = \frac{1}{\omega C} \qquad \text{Equation 1.16}$$

where $\omega = 2\pi f$ rad./sec., and f is in Hz.

The apparent power flow into a capacitor can be defined as(Johnson 2001)

$$S = VI = \frac{V^2}{-iX_C} = iV^2\varpi C^* = jV^2\frac{\omega A}{d}(\varepsilon' - i\varepsilon'') = V^2\frac{\varpi A}{d}\varepsilon_0\varepsilon_r\left(i + \tan\delta\right) \qquad \text{Equation 1.17}$$

Therefore, the power lost for a capacitor can be expressed as(Johnson 2001)

$$P_{lost} = V^2\omega C'' = V^2\omega C\tan\delta \qquad \text{Equation 1.18}$$

Typically, the power factor is used for capacitors when the PF is 10 % of greater and the dissipation factor is used when the PF is less than 10 %. QF is usually used for inductors and total circuits and is rarely used for capacitors.(Electrocube 2008)

1.2 Polymer-Ceramic Composite Dielectric Materials

Conventional dielectric materials based on ceramics have been extensively used since the discovery of barium titanate ($BaTiO_3$, $\kappa \sim 3{,}000$), due to their large dielectric constant (or permittivity, ε_r or κ).(Arit, Hennings et al. 1985; Fujishima 2000; Ihlefeld, Laughlin et al. 2005) These ABO_3 type metal oxides have a perovskite structure and can exhibit spontaneous polarization under zero-field due to the displacement of the center atom, B, along the crystalline axis *c*, as shown in Figure 1.3. However, these materials have many restrictions such as a high temperature requirement in processing, large leakage current under relatively small applied bias, and low dielectric strength (~2 V/μm) that limits operating voltages.

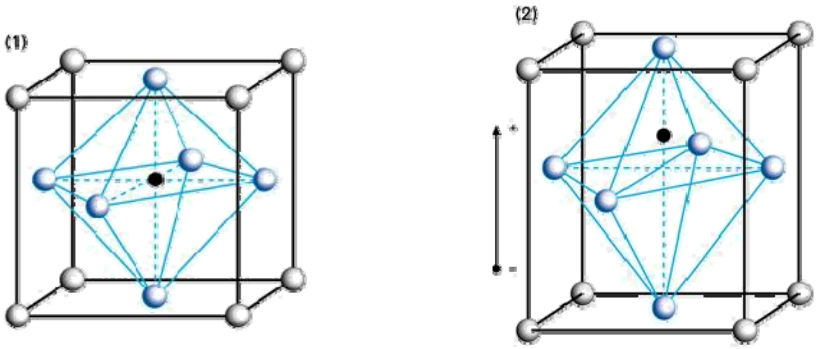

Figure 1.3 The crystalline structure of ABO_3 perovskite. (1) Non-ferroelectric phase (cubic phase), A: octahedral sites on each face, B: center atom, and oxygen atoms in each corner. (2) Perovskite structure under an applied electric field where the center atom is displaced along the crystalline axis c (tetragonal phase). A ferroelectric material tends to maintain this displacement exhibiting a spontaneous polarization even after turning off the external field. The orientation of this polarization can be switched by applying moderate magnitude of external field. It can be also removed when the thermal energy ($k_B T_c$, k_B = Boltzman constant, T_c = Curie temperature) is sufficiently high or when a coercive field is applied.

On the other hand, polymeric materials such as bi-axially oriented polypropylene (BOPP) exhibit very high dielectric strengths (~640 V/μm) with facile low temperature processability (<250 °C) to form uniform thin films. However, polymers generally show small dielectric constants (ε_r = 2~12) and thus are not very attractive as dielectric materials for energy storage. For example, the energy storage density of BOPP is limited to only about 1~1.2 J/cm^3 due to its low permittivity (ε_r ~ 2.2).

The development of easily processable materials with desired properties often not only comes from synthesizing novel materials, but also from combining existing materials. A composite material is a mixture of two or more component materials behaving like one material system with combined properties of multiple constituents. Thus the concept of mixing high permittivity ceramic particles with polymers has been

introduced to make easily processable, high permittivity, low leakage, and high breakdown strength materials. Recently, some results based on this concept have been demonstrated, but the properties obtained are suitable only for some limited applications. Thus, breakthroughs in processing these composite materials are required to fulfill the increasing demand for high performance materials, *e.g.* higher capacitance densities and breakdown strengths, in modern electronics.

The concept of the connectivity of each constituent in a composite system has been well established by Newnham, as shown in Figure 1.4.(Newnham, Skinner et al. 1978) The notation A-B for a biphasic composite refers to the number of directions in which phase A and B are self-connected. For example, 0-3 refers to a biphasic composite where one phase (A, active phase, filler) is not self-connected in any of the three (x, y, and z) directions (0), while the other phase (B, passive phase, matrix) is surrounding the active phase in such a way that the phase B is continuously self-connected in all three directions (3).

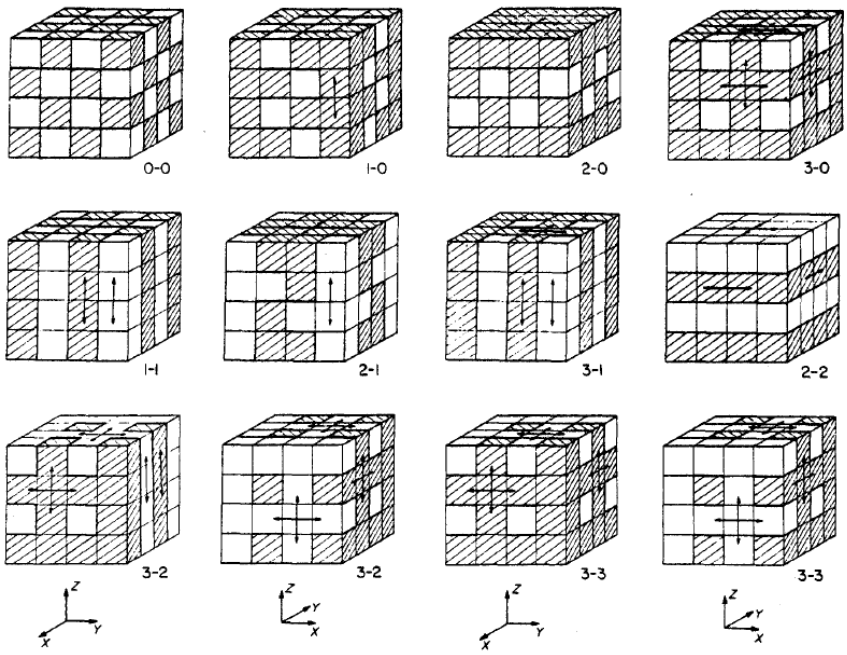

Figure 1.4 The connectivity patterns of a biphasic solid showing each phase having zero-, one-, two-, or three-dimensional self-connectivity. Arrows indicate the direction of connectivity.

Analytical theories describing the effective permittivity of a composite system having a 0-3 connectivity predict that the effective permittivity increases either with increasing volume fraction of the active phase (high permittivity fillers) or with increasing permittivity of the passive phase (host polymer). One commonly used model to describe dielectric composite systems was developed by Jayasundere and Smith, as shown in Equation 1.19.(Jayasundere and Smith 1993) The details about different models will be described in Section 5.1.2. Two example calculation results using this equation for effective permittivity of nanocomposites are shown in Figure 1.5. Therefore, high volume fractions of high permittivity fillers in high permittivity polymer hosts are the key features to achieve high permittivity polymer/ceramic composites.

$$\varepsilon_{eff} = \frac{\varepsilon_h v_h + \varepsilon_f v_f \left[3\varepsilon_h \Big/ \left(\varepsilon_f + 2\varepsilon_h \right) \right] \left[1 + 3v_f \left(\varepsilon_f - \varepsilon_h \right) \Big/ \left(\varepsilon_f + 2\varepsilon_h \right) \right]}{v_h + v_f \left[3\varepsilon_h \Big/ \left(\varepsilon_f + 2\varepsilon_h \right) \right] \left[1 + 3v_f \left(\varepsilon_f - \varepsilon_h \right) \Big/ \left(\varepsilon_f + 2\varepsilon_h \right) \right]} \qquad \text{Equation 1.19}$$

ε_{eff}: effective permittivity of the composite, ε_f: permittivity of the filler, ε_h: permittivity of the host, v_f: volume fraction of the filler, v_h: volume fraction of the host.

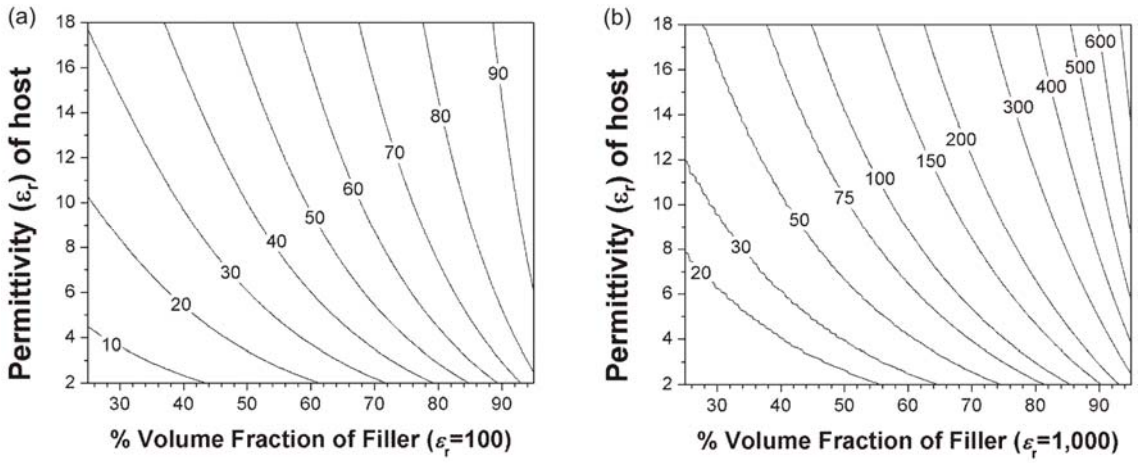

Figure 1.5 Contours of the effective permittivity of model composite systems calculated using Equation 1.13 with a filler permittivity of 100 (a) and 1000 (b).

Polymer/ceramic composite materials have found many applications so far as a dielectric components, but current research is directed to the use of much smaller particles (nanoparticles) as the miniaturization and integration of electronic components require similar or better performance from much smaller area and/or volume of materials.

1.3 Surface Modification of Nanoparticles

Nanocomposites are different from conventional composites where the active phase has relatively large surface area to bulk volume.(Balazs, Emrick et al. 2006) In dielectric composites, the capacitance density increases with decreasing dielectric layer thickness. Therefore, dielectric nanoparticles of a few hundred nanometers in diameter or smaller have been used to fabricate much thinner (~micron) composite films.(Ramesh,

Shutzberg et al. 2003; Rao and Wong 2004) The properties of nanocomposites are often influenced by the interfacial properties of the nano-sized filler materials and thus the control of the nanoparticle interface becomes very important. If one fails to control the interfacial energy, such nanocomposites become inhomogeneous mixtures, with agglomeration and phase separation, that are difficult to process into uniform, high-quality, nanocomposite thin films. The homogeneity of dielectric nanocomposite films is an important feature as it is closely related to the effective permittivity and leakage current density of the nanocomposites.

Simple mixing of nanoparticles in a polymer host generally results in poor quality and inhomogeneous films, mainly due to the agglomeration of the nanoparticles.(Gilbert, Schuman et al. 2005) As explained in the previous section, large volume fractions of the high permittivity nanoparticles are desirable to increase the effective permittivity of nanocomposites. Increasing the volume fraction of the nanoparticles increases the interfacial area of nanoparticles in the system. The processing and achieving high quality nanocomposite thin films with high nanoparticle volume fractions becomes even more challenging without control of the nanoparticle interfaces. Therefore, approaches to chemical modification of the nanoparticle surfaces are highly desirable. Chemically modifying the surface of nanoparticles has many potential advantages: i) capping of the nanoparticle surface with a chemical modifier, or ligand, can effectively suppress nanoparticle aggregation, which is the first problem to be solved in order to accomplish homogeneous nanocomposites, ii) the compatibility of guest materials (nanoparticle filler) in host materials (polymer) can be improved by changing the structure of a chemical modifier according to that of surrounding media, iii) other desired chemical functionality can be tailored for further processing, studies, and other applications, and iv) once the surface modification chemistry is established, it can be easily applied to other similar systems.

1.4 Thesis Objective and Synopsis

One objective of the thesis is to answer some important questions in surface modification of barium titanate and related metal oxide nanoparticles such as: What are the important structural features of ligands for binding to the surface of nanoparticles? How are the thermodynamics and kinetics of binding? What is the molecular structure of ligands bound to the surface of barium titanate nanoparticles? The next objective is to investigate the effect of surface modification of the nanoparticles on the properties of nanocomposites, such as the stability of dispersions and their processability to thin films. Another objective following these initial studies is to investigate the dielectric performance of nanocomposites based on surface-modified barium titanate nanoparticles dispersed in polymer hosts. In order to develop materials suitable for potential applications such as high-energy-density capacitors and gate insulators in organic field-effect transistors, materials parameters, such as the volume fraction of nanoparticles and the permittivity of host materials, need to be optimized. The investigation of the effects of such materials parameters on their properties is also a significant part of the thesis objective.

This thesis begins with an introduction (this chapter) followed by chapter II that describes the details of materials and experiments for the entire thesis. This will be used as a cross-reference in later chapters. In chapter III, a comparative study aimed to find a good binding group for the surface modification of barium titanate nanoparticles is described along with the details of the binding modes and stabilities of those ligands. In chapter IV, several studies of the effects of surface modification and the permittivity of nanoparticle fillers and host polymers on the processability, homogeneity, effective permittivity, leakage current density, and dielectric breakdown strength of the nanocomposites are described. The dielectric properties of poly(vinylidene fluoride-*co*-hexafluoropropylene) (P(VDF-HFP), Viton^{TM}) makes it a very interesting host material for high energy density capacitors, yet this material is still at the initial stage of

investigation as a polymer host in this field. In chapter V, experimental and theoretical studies of surface-modified barium titanate:P(VDF-HFP) nanocomposites are described for the optimization the parameters to maximize the extractable energy. Nanocomposites in other high permittivity host materials and their properties are described in chapter VI. Chapter VII describes the application of solution-processable high permittivity nanocomposite thin films as a gate insulator in organic field-effect transistors (OFETs). General conclusions of the thesis and suggested future work are described in chapter VIII. Appendices A and B contain some work performed by the author from which significant progresses have been obtained, but are not directly related to the main thesis work. However, in some sense, these appendices are related to the main thesis from the processing point of view, as they both involve the surface modification of nanoparticles and the processing of nanocomposite films.

CHAPTER 2

EXPERIMENTAL DETAILS

This chapter describes the details of the materials used, synthetic details, experimental principles and methods, and data analysis. Most of the experimental details for the entire thesis can be found in this chapter. Experimental details only specific to particular chapters will be described separately in each chapter. Therefore, other chapters will mainly have introduction, results and discussion, and conclusions.

2.1 Materials

2.1.1 Nanoparticles

All the barium titanate ($BaTiO_3$) nanoparticles used in this study, unless specifically mentioned, was purchased from Aldrich Inc. (St. Louis, MO), which has a spherical and/or truncated cubic shape with *ca.* 30 – 50 nm in diameter and has a cubic phase. This $BaTiO_3$ nanoparticles from Aldrich is referred as BT in the entire thesis. Figure 2.1 shows the SEM, TEM images of BT nanoparticles and Figure 2.2 shows the powder X-ray diffraction of BT nanoparticles.

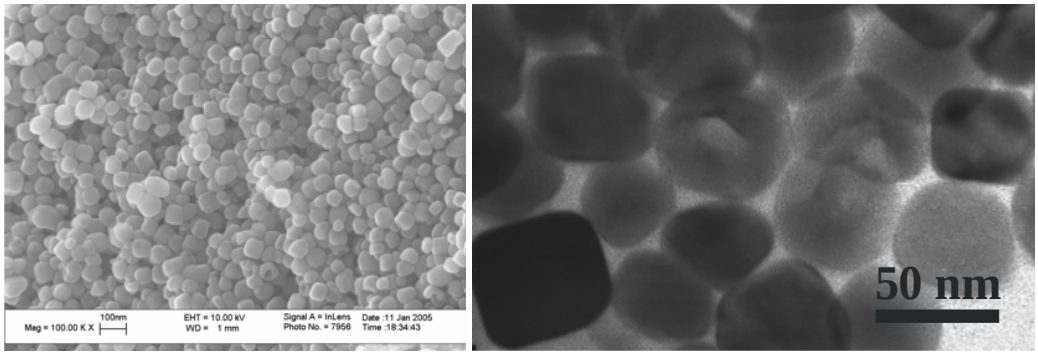

Figure 2.1 SEM image (left) and TEM image (right, 100 kV) of BT nanoparticles.

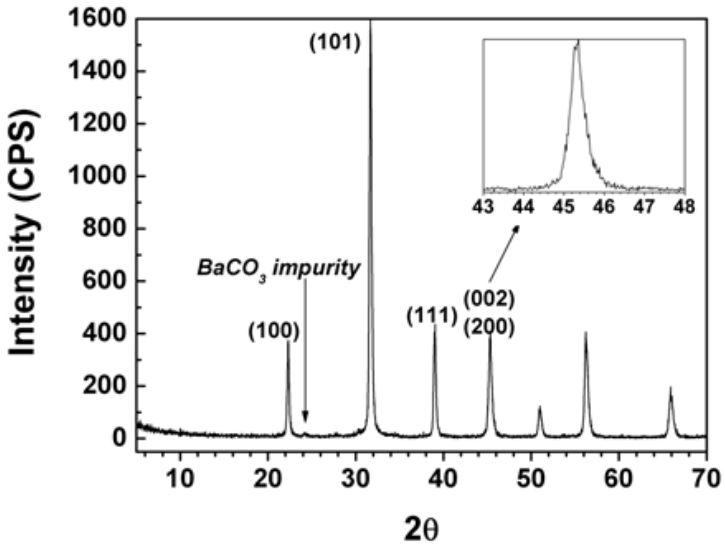

Figure 2.2 Powder X-ray diffraction of BT nanoparticles.

The permittivity of BT is estimated to be about 80 at 1 kHz at room temperature. BT nanoparticles were prepared using a proprietary low temperature hydrothermal synthesis method developed at TPL Inc. (Albuquerque, NM). The particles have abundant surface hydroxyl groups as observed in the FT-IR spectrum in Figure 2.3 recorded using a KBr pellet containing 5 wt. % of BT. The BET specific surface area of dried and unmodified BT nanoparticles was measured by a nitrogen adsorption/desorption experiment and was found to be 25.8 m^2/g.

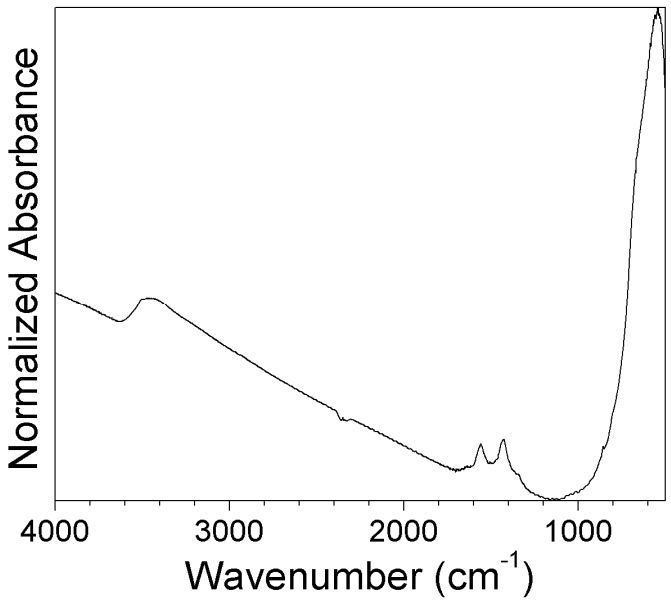

Figure 2.3 FT-IR spectrum of BT nanoparticles showing surface hydroxyl groups ($\nu \approx$ 3500 cm^{-1} and $BaCO_3$ (ν = 1400 – 1600 cm^{-1}) impurities. The spectrum was normalized using the lattice Ti-O absorption peak centered at ~540 cm^{-1}.

Commercially available $BaTiO_3$ nanoparticles slightly larger than BT nanoparticles were also used in this study. BT-8 (120-150 nm) and BT-16 (65 nm) were purchased from Cabot corporation (Boston, MA). BT-8 has mixed cubic and tetragonal phases and BT-16 is mainly in the cubic phase. BT-150 (HPB-1250) was purchased from TPL, Inc. (Albuquerque, NM) which is ~150 nm spherical powder (BET sp. surface area = 7.22 m^2/g) with mixed cubic and tetragonal phases. BT-120 was purchased from Inframat Advanced Materials, LLC (Farmington, CT) which is a ~120 nm spherical powder with mixed cubic and tetragonal phases. SEM images of these nanoparticles are shown in Figure 2.4. As the size of the nanoparticle increases, the relative strength of hydroxyl group decreased as shown in Figure 2.5.

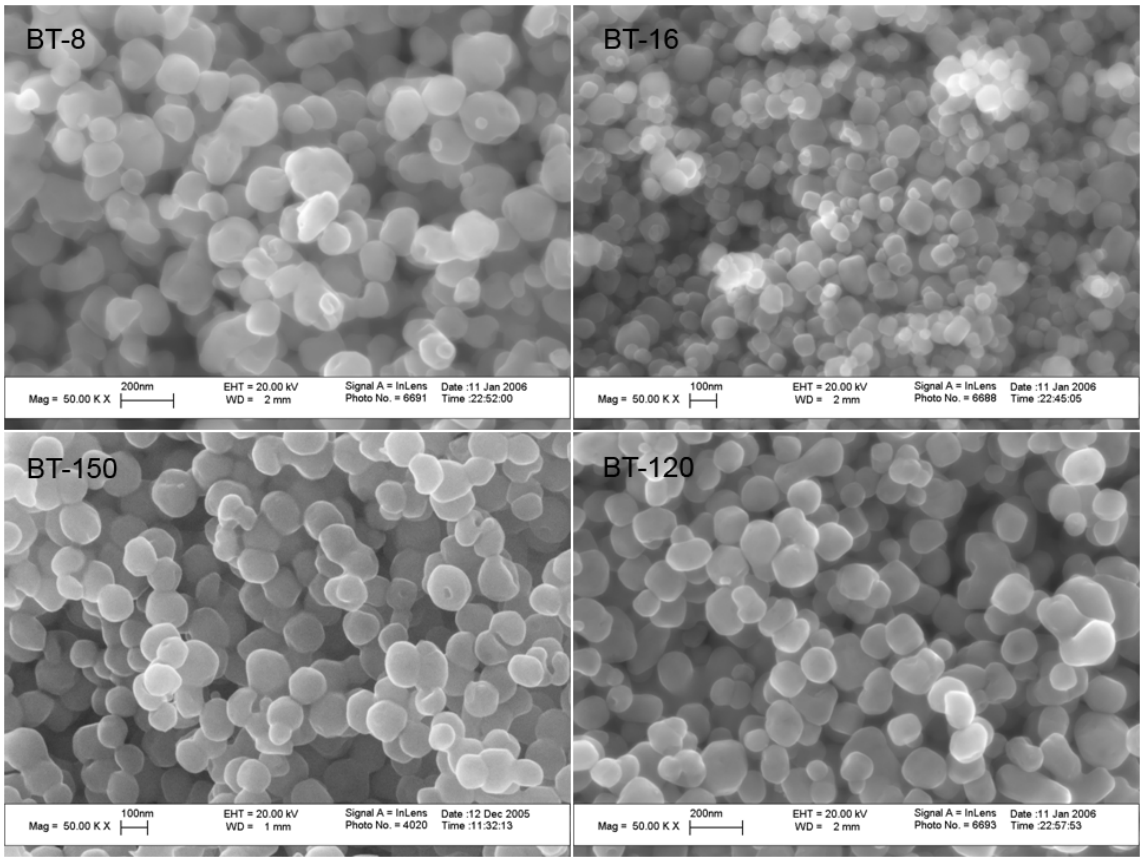

Figure 2.4 SEM images of commercially available $BaTiO_3$ nanoparticles.

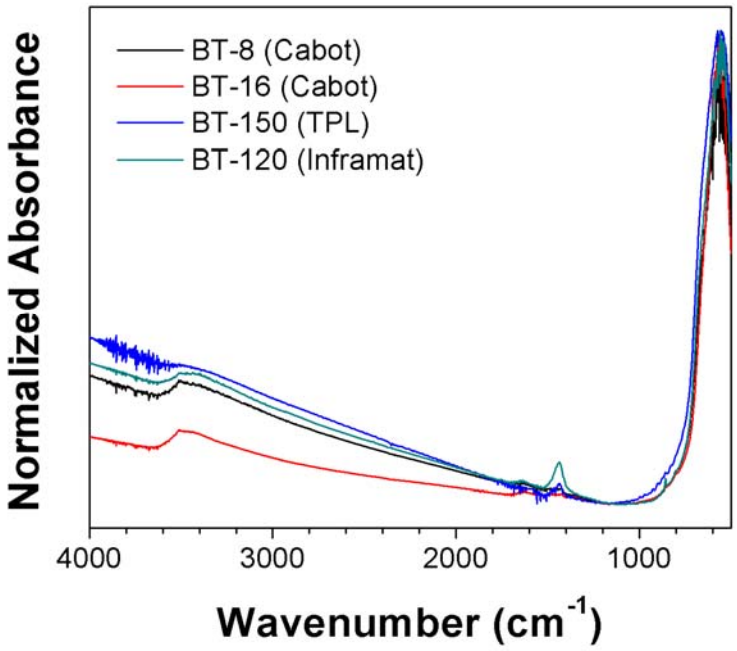

Figure 2.5 FT-IR absorption spectra of commercially available $BaTiO_3$ nanoparticles. The spectra were normalized using the lattice Ti-O absorption peak centered at ~540 cm^{-1}.

Barium zirconium titanate ($BaZr_{0.2}Ti_{0.8}O_3$, ~200 nm), and strontium titanate ($SrTiO_3$, ~100 nm) nanoparticles were purchased from Inframat Advanced Materials (Farmington, CT).

2.1.2 Polymers

2.1.2.1 Commercially Available Polymers

Poly(vinylidene fluoride-*co*-hexafluoropropylene), (P(VDF-HFP) with <25% HFP), was purchased from Aldrich (cat. no. 427187, melt index = 4.00 – 10.00 g/10min, d= 1.78, ε_r = 11.38 at 100 Hz).

Poly(bisphenol-A carbonate), PC, was purchased from PolySciences, Inc. (Warrington, PA). Gel permeation chromatography (GPC) was performed using polystyrene standards and M_w was found to be 47 kDa and the PDI was found to be 2.00.

Poly(4-vinylphenol), PVP, was purchased from Aldrich (cat. no. = 436224, average M_w = ~20,000, d= 1.16).

Poly(styrene-co-acrylonitrile), PSAN, was purchased from PolySciences.

Poly(vinylidene fluoride-*co*-trifluoroethylene), P(VDF-TrFE) with VDF:TrFE of 65:35 was purchased from Ktech Corporation (Albuquerque, NM).

Cyanoethylated O-(2,3-dihydroxypropyl)-cellulose (Cyanoethylpullulan, CEP, cat. no. CR-S), was purchased from ShinEtzu chemicals Co. (Tokyo, Japan).

2.1.2.2 Custom Synthesized Ferroelectric Polymers

Poly(vinylidene fluoride-*co*-trifluoroethylene-*co*-chlrorotrifluoroethylene), P(VDF-TrFE-CTFE), was obtained from Professor Qing Wang's group at Materials Science and Engineering, University of Pennsylvania. The polymer was prepared as shown in Figure 2.6.(Lu, Claude et al. 2006)

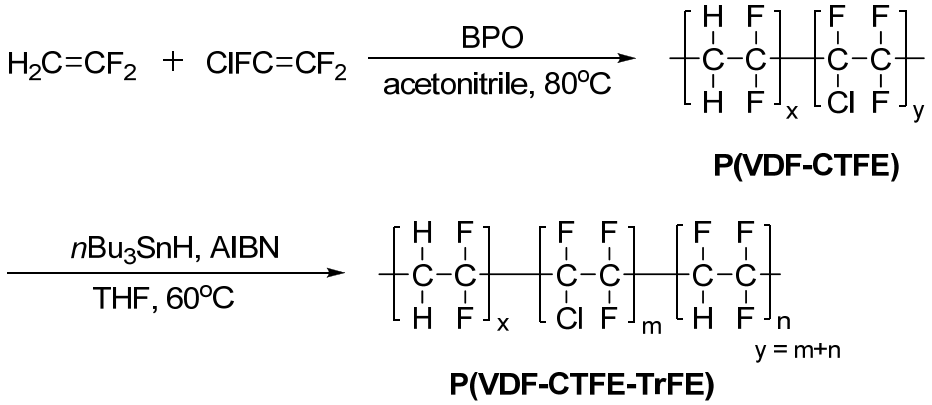

Figure 2.6 A Synthetic scheme for P(VDF-CTFE-TrFE).

The reactivity of TrFE monomer is quite different from those of VDF and CTFE. As a result, a simple radical polymerization of a quantitative mixture of the three monomers does not result in terpolymers with desired ratio of the three monomers. Therefore, VDF and CTFE are initially co-polymerized by free radical polymerization

initiated by benzoyl peroxide (BPO) then subsequently hydrogenated using tributyl tin and azobisisobutylonitrile (AIBN). The second step is quantitative and thus makes it possible to control the monomer ratio in the terpolymer. This modular approach allows the fine tuning of the ratio of each block which in turn changes the Curie temperature. With fine control of the ratio (VDF:CTFE:TrFE = 78.8 : 7.2 : 14 mol %), the permittivity reached ~50 (at 1 kHz) with a low dielectric loss ($\tan\delta < 0.05$, at 1 kHz) at room temperature.

2.1.3 Ligands and Other Chemicals

2.1.3.1 Commercially Available Chemicals

The chemicals were obtained from the following sources and used without further purification: *n*-octylphosphonic acid (OPA, Alfa-Aesar, 98 %), *n*-octyltrimethoxysilane (OTMOS, Aldrich, 96 %), nonanoic acid (OCA, Aldrich, 96 %), 1-octane sulfonic acid sodium salt (OSA, Aldrich, 98 %),

The surfactant BYK-w-9010 (a proprietary copolymer mixture with acidic groups) was provided by BYK Chimie USA (Wallingford, CT) and was used as received.

Methyl phosphonic acid (98 %) and *n*-octadecyl phosphonic acid (98 %) were purchased from Aldrich and used without further purification. Phenyl phosphonic acid (98 %) was purchased from Aldrich and was used after purification (*vide infra*).

2.1.3.2 Custom Synthesized Phosphonic Acid Ligands

Phosphonic acids are prepared from alkyl halides that undergo Arbuzov reaction with triethylphosphite giving alkylphosphonic acid diethyl esters.(Bhattacharya and Thyagarajan 1981)

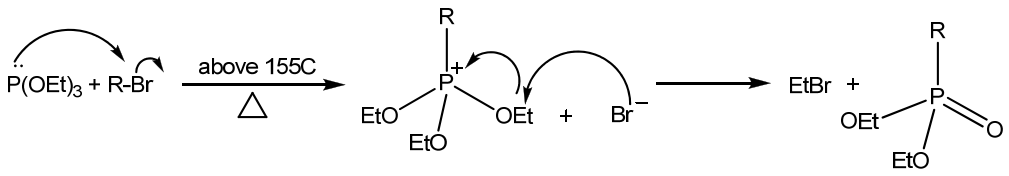

Figure 2.7 Schematics of Arbuzov reaction.

Typically the reaction is performed in a fractional distillation setup, in which the product is isolated by distillation. The second step is the hydrolysis of phosphonate to phosphonic acid by converting phosphonic acid ester to trimethylsilyl phosphonate and then detaching the trimethylsilyl group by hydrolysis. The first attempt was made using the following hydrolysis condition.

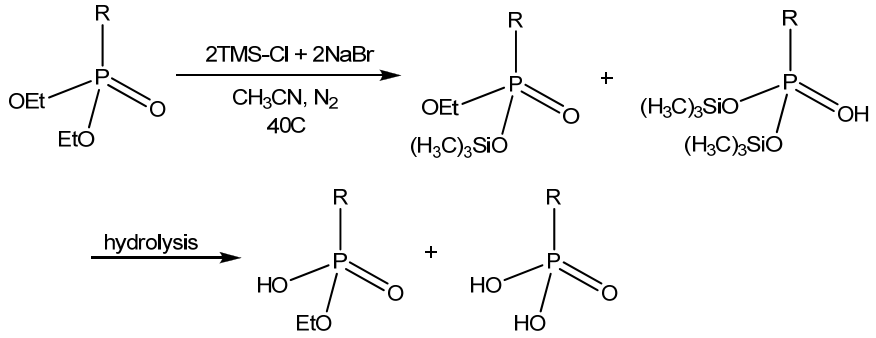

Figure 2.8 Hydrolysis reaction of phosphonate ester to phosphonic acid.

The *n*-octadecylphosphonic acid was synthesized by using the schemes described above. First, 5 g (0.015 mol) of 1-bromooctadecane (96%, Aldrich) was mixed with 10 mL of triethylphosphite (98%, Aldrich) as a solvent and the mixture was refluxed overnight at 180°C. Fractional distillation of the reaction product at 177°C and 177±10 mmHg yielded a thick, yellow oil which was identified as *n*-octadecylphosphonic acid diethyl ester by NMR. The ester was dissolved in 20 mL of acetonitrile under nitrogen purging, then trimethylsilylchloride (3.81 mL, 0.03 mol) and sodium bromide (3.087 g, 0.03 mol) were injected and stirred at 40°C. The product mixture was filtered and

washed with cold acetonitrile. The product was collected with methanol and ultrasonicated to dissolve remaining sodium bromide. Then, it was cooled in an ice bath, filtered and washed with methanol. NMR analysis revealed that the product was still mainly the diethyl phosphonate with very little portion of phosphonic acid.

The second attempted hydrolysis reaction scheme is shown in Figure 2.9, where bromotrimethylsilane was used.

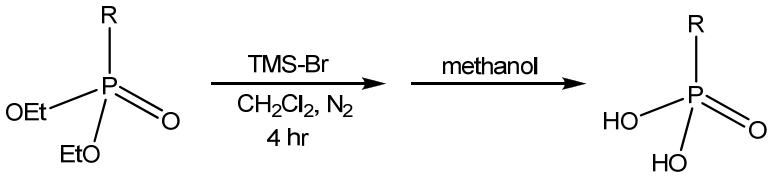

Figure 2.9 Hydrolysis of phosphonate.

This method allowed a successful preparation of *n*-octadecylphosphonic acid as white powders, which was performed in collaboration with Dr. Simon C. Jones (SCJ) in Marder group. 5.5 g of *n*-octadecylphosphonic acid diethyl ester (15 mol) was dissolved in CH_2Cl_2 (25 ml) under nitrogen. Bromotrimethylsilane (4.3 ml, 33 mol) was added, and the mixture was stirred for 2 hours. Volatiles were removed to give a thick, orange oil, which was dissolved in methanol (20 ml) with fuming to give a white precipitate. The mixture was stirred for 2 hours and the product was collected by filtration. Subsequently, purified fractions were obtained by recrystallization of the crude product in methanol at –35 °C. The combined material was washed with acetonitrile to yield a white solid (4.3 g, yield 92%, confirmed by NMR).

Benzyl phosphonic acid was prepared using similar method.

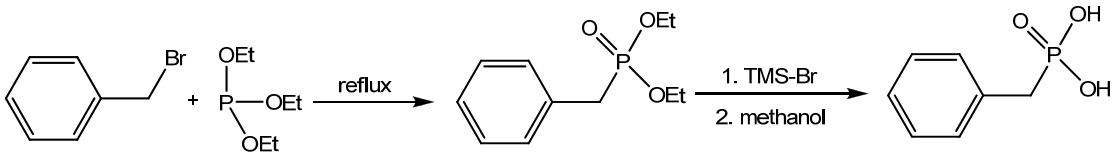

Figure 2.10 Synthesis of benzylphosphonic acid.

10.18 g of Benzylbromide (98%, Aldrich) was mixed with 11.93 g of triethylphosphite. Both reactants are clear liquids and refluxing the mixture for 2 hours showed no significant trace of starting material in TLC. The reaction product was distillated *in vacuo* at 100°C to give *ca.* 9 mL of liquid. The phosphonate ester was dissolved in 20 mL of dry CH_2Cl_2 under nitrogen, then 27 mL of bromotrimethylsilane was added and stirred under nitrogen at room temperature for 4 hours. Volatiles were removed *in vacuo* to give a yellow, viscous liquid. The product was dissolved in 300 mL of methanol and stirred for a few days for recrystallization. Finally, the recrystallized product was cooled to 4°C. Filtering and drying the solid in 60°C vacuum oven gave white powders. This crude product contained incompletely hydrolyzed by-products, *i.e.* the mixture of unreacted phosphonates and partially hydrolyzed phosphonic acids as confirmed by FT-IR and NMR analysis. The crude product can be purified by further recrystallizing the reaction products in methanol. However, even after the recrystallization, the product still contained impurities of phosphonate esters. In general, phosphonic acids are insoluble in acetonitrile, while ethyl phosphonates are very soluble in acetonitrile. Washing of the recrystallized products several times with acetonitrile yields >99 % pure phosphonic acids. This simple purification method was also used for some commercial phosphonic acids such as phenyl phosphonic acid.

The Arbuzov reaction often requires high temperatures (> 150°C) and long reaction time (> 24 hrs) to achieve an acceptable yield. Microwave irradiation can offer an improvement in this regard, as the typical reaction takes only a few hours.(Kaboudin and Nazari 2001) The following synthesis was performed using a microwave reactor.

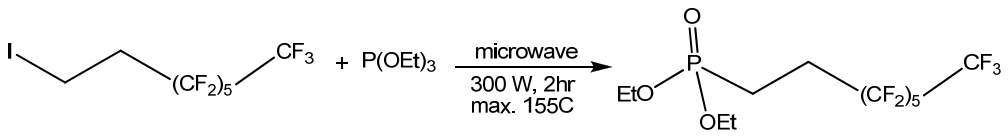

Figure 2.11 Synthesis of (3,3,4,4,5,5,6,6,7,7,8,8,8-tridecafluorooctyl)phosphonic acid.

In 2 hours of microwave application (100 W, with a 2455 MHz magnetron, Focused Microwave Synthesis System, Model Discover, CEM Corp.), the starting iodide was no longer observed by TLC. The synthesized ester was further hydrolyzed by SCJ with bromotrimethylsilane and methanol to yield (3,3,4,4,5,5,6,6,7,7,8,8,8-Tridecafluorooctyl)phosphonic acid which was further purified by recrystallization with acetonitrile (yield 82 %).

Besides the initially synthesized phosphonic acids in collaboration with SCJ, various custom made phosphonic acids were prepared by SCJ and/or by Mr. Peter J. Hotchkiss (PJH) in Marder group. These are presented in Table 2.1 and Figure 2.12.

Phosphonic acids with useful terminal functional groups can allow coupling of other molecules at the terminal *via* esterification, etherification, and click chemistry.(Werne and Patten 2001; White, Johnson et al. 2006) The terminal functional groups can also allow the initiation of controlled radical polymerization. Several phosphonic acids were also prepared for this purpose in collaboration with SCJ and/or by PJH and are also listed in Table 2.1 and Figures 2.12 and 2.13.

Table 2.1 List of custom synthesized phosphonic acid ligands.

Name of phosphonic acid ligand	Abbreviation
n-Octylphosphonic acid	OPA
Octadecylphosphonic acid	ODPA
Benzylphosphonic acid	BPA
(3,3,4,4,5,5,6,6,7,7,8,8,8-tridecafluorooctyl)phosphonic acid	FOPA
11-hydroxyundecylphosphonic acid	HUPA
(11-phosphonoundecyl)phosphonic acid	DPPA
{2-[2-(2-Methoxyethoxy)ethoxy]ethyl}phosphonic acid	PEGPA
[3-(4-{[4'-(Phenyl-*m*-tolylamino)biphenyl-4-yl]-*m*-tolylamino}phenoxy)propyl]-phosphonic acid (11-Prop-2-ynyloxyundecyl)phosphonic acid	TPDPA
pentafluorobenzyl phosphonic acid	PFBPA
(11-Prop-2-ynyloxyundecyl)phosphonic acid	TKYNPA

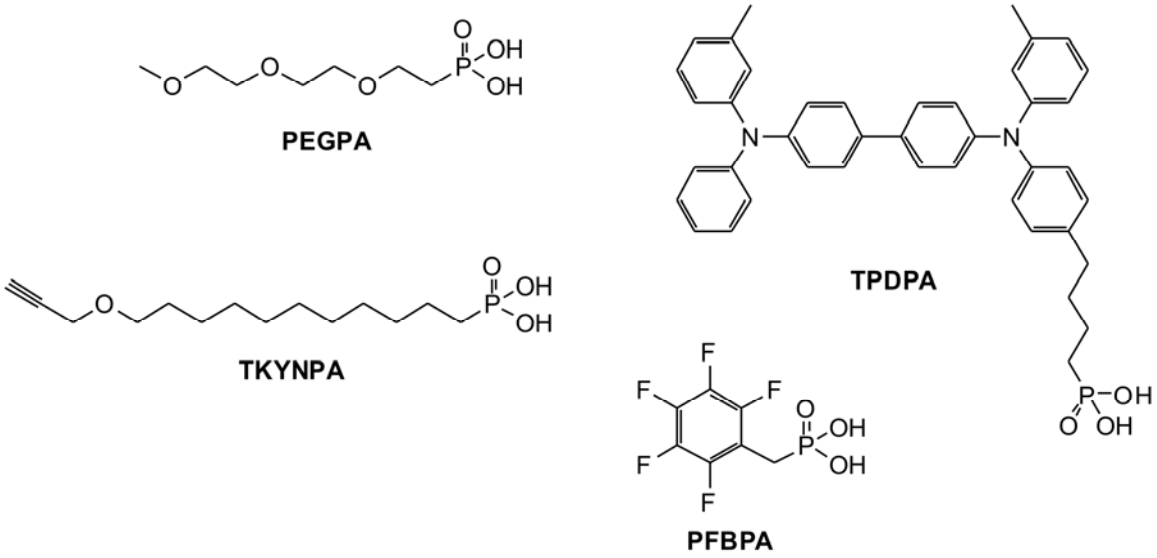

Figure 2.12 Structures of custom synthesized phosphonic acid ligands.

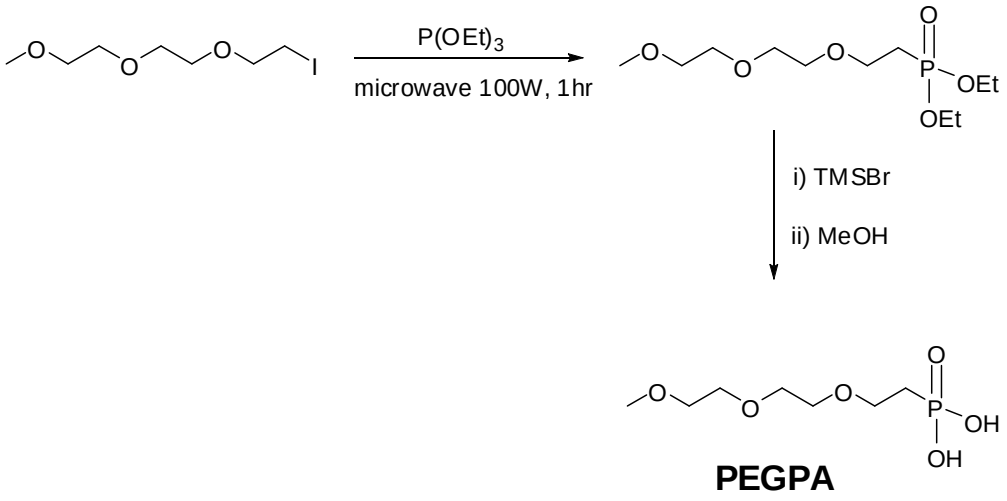

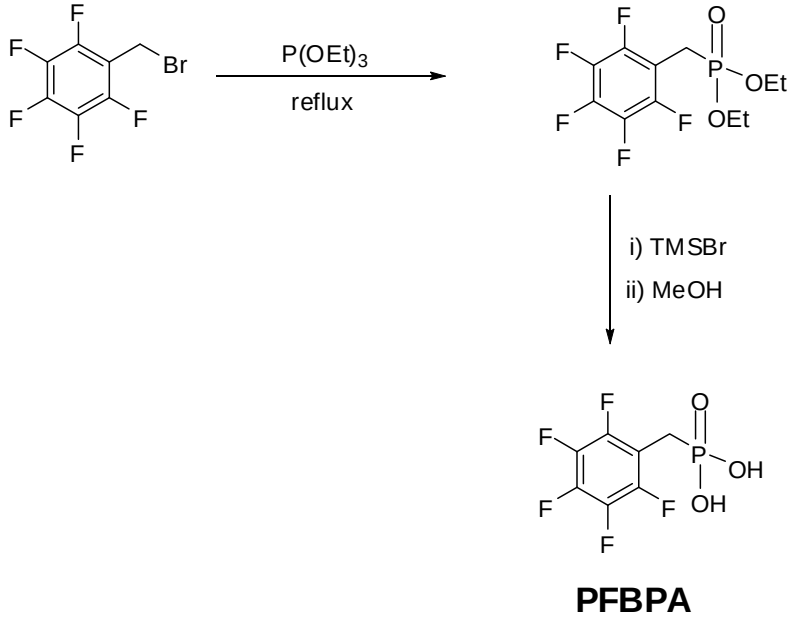

Figure 2.13 Synthesis of PEGPA and PFBPA. Synthetic details and characterizing data are given below. Alternative syntheses have been reported previously: S. Yamanaka, K. Yamasaka, and M. Hattori, *J. Inclusion Phenomena* **1984**, 2, 297 (PEGPA); B.L. Rice, C.Y. Guo, and R.L. Kirchmeier, *Inorg. Chem.* **1991**, 30, 4635 (PFBPA).

{2-[2-(2-Methoxyethoxy)ethoxy]ethyl}phosphonic acid diethyl ester: {2-[2-(2-Methoxyethoxy)ethoxy]ethyl}iodide (6.64 g, 24.3 mmol) and $P(OEt)_3$ (4.22 ml, 24.3 mmol) were dissolved in 1,4-dioxane (30 ml) and stirred under reflux for 24 hours. Volatiles were distilled *in vacuo* (150 °C, 0.01 Torr) to give the crude material as a thick, yellow oil. Column chromatography (silica gel, EtOAc:MeOH 95:5 elution) afforded the desired product as a pale yellow oil. Yield 1.0 g, 15 %. Alternative synthesis using {2-[2-(2-Methoxyethoxy)ethoxy]ethyl}iodide (5.00 g, 18.2 mmol) and $P(OEt)_3$ (10 ml, excess) under microwave irradiation (100 W, 1hr) gave higher yield after column chromatography (3.06 g, 10.7 mmol, 59 %). ^{1}H NMR ($CDCl_3$, 400 MHz, 298 K): δ 4.08 (m, 4H), 3.67 (d of t, J_{H-P} = 10 Hz, J_{H-H} = 7 Hz, 2H), 3.60 (m, 6H), 3.50 (m, 2H), 3.36 (s, 3H), 2.09 (d of t, J_{H-P} = 20 Hz, J_{H-H} = 7 Hz, 2H), 1.28 (t, J = 7 Hz). $^{13}C\{^{1}H\}$ NMR ($CDCl_3$, 100 MHz, 298 K): δ 71.72, 70.35, 70.30, 69.97, 64.92, 61.44 (d, J_{C-P} = 6 Hz), 58.82, 26.77 (d, J_{C-P} = 138 Hz), 16.22 (d, J_{C-P} = 6 Hz). $^{31}P\{^{1}H\}$ NMR ($CDCl_3$, 162 MHz, 298 K): δ 29.23. MS (FAB, m/z): 285 ($[M+H]^+$, 100 %). Exact mass found (calculated for $[M+H]^+$, m/z): 285.15395 (285.14670).

{2-[2-(2-Methoxyethoxy)ethoxy]ethyl}phosphonic acid: {2-[2-(2-Methoxyethoxy)ethoxy]ethyl}phosphonic acid diethyl ester (1.00 g, 3.5 mmol) was dissolved in CH_2Cl_2 (20 ml) under N_2. Bromotrimethylsilane (2.3 ml, 17.5 mmol) was added *via* syringe and the mixture was stirred for 2 hours. Volatiles were removed *in vacuo* to give a thick, orange oil; this was dissolved in MeOH (100 ml) with fuming to give a give a yellow solution. The mixture was stirred for 2 hours and evaporated to dryness to give a thick, yellow oil which was dissolved in CH_2Cl_2 and extracted with NaOH (3 x 50 ml, aq., 1M). HCl (conc.) was added to the yellow aqueous layer until the solution was acidic to pH paper. Removal of water *in vacuo* gave a yellow crystalline solid that was extracted with EtOH and filtered. Cooling the filtrate to -35°C resulted in precipitation of further white solid which was removed by filtration. Removal of volatiles

from the yellow supernatant under vacuum (0.01 torr) afforded the desired product as a thick, yellow oil. Yield 0.60 g, 2.6 mmol, 74 %. ^{1}H NMR (d_6-DMSO, 400 MHz, 298 K): δ 3.55 (ap. q. J = 7 Hz, 2H), 3.48 (m, 6H), 3.41 (m, 2H), 3.23 (s, 3H), 1.83 (d of t, J_{H-P} = 19 Hz, J_{H-H} = 7 Hz, 2H). ^{13}C{^{1}H} NMR (d_6-DMSO, 100 MHz, 298 K): δ 71.25, 69.69, 69.58, 69.27, 65.41, 58.05, 28.99 (d, J_{C-P} = 132 Hz). ^{31}P{^{1}H} NMR (d_6-DMSO, 162 MHz, 298 K): δ 23.15. MS (ESI, m/z): 227 ([M-H]$^{+}$, 100 %), 229 ([M+H]$^{+}$, 10 %). Exact mass found (calculated for [M+H]$^{+}$, m/z): 229.08490 (229.08410).

Pentafluorobenzyl Phosphonic Acid Diethyl Ester:

Pentafluorobenzyl bromide (2.00 g, 7.66 mmol) and $P(OEt)_3$ (1.66 g, 9.96 mmol) were dissolved in 1,4-dioxane (10 ml) and refluxed for 14 hours. Fractional distillation (66-78 °C, 60 mm Hg) afforded the product as a colorless oil (2.43 g, 96 %). ^{1}H NMR (500 MHz, $CDCl_3$) δ 4.15 – 4.10 (m, 4H), 3.22 (d, J = 21.0 Hz, 2H), 1.31 (t, J = 7.00 Hz, 6H).

Pentafluorobenzyl Phosphonic Acid:

Diethyl pentafluorobenzylphosphonate (1.90 g, 5.97 mmol) was dissolved in dry CH_2Cl_2 (4 ml), stirred and TMSBr (3.66 g, 23.88 mmol) was added. The mixture was stirred for 2 hours at room temperature after which volatiles were removed to give a thick, yellow oil. MeOH (5 ml) was added and the suspension stirred for 90 minutes, after which the product was collected by filtration yielding white crystals (1.20 g, 77 %). ^{1}H NMR (400 MHz, d_6-DMSO) δ 3.05 (d, J = 20.4 Hz, 2H). ^{31}P{^{1}H} NMR (161.98 MHz, d_6-DMSO): δ 17.44.

2.1.3.3 Other Chemicals

Cymel 300 (hexamethoxymethylmelamine, HMMM) was purchased from Cytec Industries, Inc. (West Paterson, NJ) and was used without purification.

2.2 Surface Modification of Nanoparticles

The surface modification of nanoparticles was performed in a 95:5 (vol./vol.) ethanol:H_2O (or 50:50 ethanol:H_2O, pH adjusted to 1 for sulfonic acid salt) mixed solvent. In a typical reaction, BT nanoparticle dispersion (0.4 g/10 mL) was prepared by a total of 4 – 6 hours of ultrasonic processing (30 second pulse on and 5 second pulse off at 35 % of max. power (750 W), A. Daigger Co.) by using a 1/8" stepped tip to deagglomerate the largely clumped nanoparticles.(Markovic, Mitric et al. 2008) A solution containing 0.2 mmol of each ligand dissolved in 1 mL solvent was added to the pre-dispersed nanoparticle solution. The mixture was ultrasonicated for 10 minutes and stirred at 80°C for 1 hour. After the surface modification reaction, the mixture was cooled to room temperature then the stirring was turned off to allow sedimentation of nanoparticles. At this step, most large agglomerates and nanoparticles modified with ligands that are not compatible with the reaction solvent are precipitated. The nanoparticles were separated by centrifugation and redispersed in ethanol (50:50 ethanol:H_2O for sulfonic acid-modified BT) by ultrasonic processing. At this step, surface-modified nanoparticles are re-dispersed and do not readily precipitate while large agglomerates precipitate quickly. The large agglomerates were separated by differential centrifugation. This step was repeated until no rapid sedimentation was observed. The surface modified nanoparticles were then washed multiple times by centrifugation and redispersion (30 ~ 40 °C for 1 hour in ultrasonic bath) using appropriate solvent to remove weakly bound and physisorbed ligands. After washing, the nanoparticles were dried *in vacuo* at 80°C overnight. A control experiment was performed in the absence of ligand under the same condition.

2.3 Spectroscopic Characterizations

2.3.1 Fourier Transform Infrared Spectroscopy (FT-IR)

The FT-IR spectra were taken by using KBr pellets containing 5 wt. % of unmodified or surface-modified nanoparticles in a transmission geometry with 2 cm^{-1} resolution using a Perkin-Elmer Spectrum 1000. FT-IR spectra of neat ligands were also obtained using KBr pellets with reduced amount of ligands.

2.3.2 Solid-State Nuclear Magnetic Resonance (SS-NMR)

The ^{31}P magic angle spinning (MAS) solid state NMR spectra were recorded on a Bruker DSX 400 (161.98 KHz ^{31}P frequency, 10 kHz MAS frequency, 256 scans, 10 seconds delay time) for both direct polarization (DP, 5 μs 90º pulse length, high power ^{1}H decoupling) and cross polarization (CP, 1 ms contact time) experiments. The chemical shift was referenced using ammonium dihydrogen phosphate (ADP) which was set to δ = 1 ppm. All the SS-NMR spectra presented in this thesis were recorded by Dr. Johannes Leisen.

2.3.3 Powder X-ray Diffraction (XRD)

The X-ray diffractogram of nanoparticles were obtained to determine the crystal structure using a Scintag X-ray Diffractometer. The diffracted Cu-K_α X-ray radiation (λ = 1.54178 Å) on the sample surface was collected using a continuous scanning at ~0.8°/min from 5° to 90°.

2.3.4 X-Ray Photoelectron Spectroscopy (XPS)

Model SSX-100 (Service Physics, Inc.) X-ray Photoelectron Spectroscopy system was used to obtain surface-specific elemental and chemical information. A low energy electron flood gun was used to neutralize charges build up for non-conducting samples.

2.4 Microscopic Characterizations

2.4.1 Field-Emission Scanning Electron Microscopy (FE-SEM)

The scanning electron microscopy images were recorded using either a LEO 1530 SEM with a thermally assisted field emission gun (TFE) equipped with a Noran energy dispersive spectroscopy (EDS) system or a Zeiss Ultra60 scanning electron microscopy. Both SEMs have a secondary electron (SE) detector and an in-lens detector. High magnification SEM images were taken using in-lens detectors at working distance of 1 mm at 20 kV (LEO 1530) or 4 mm at 5 kV (Zeiss Ultra60). For nanoparticle imaging, no surface conductive coating was needed but for nanocomposite films, gold sputter coating was necessary to minimize charging. Freeze-fractured nanocomposite films in liquid nitrogen were sputter coated with gold before imaging. The samples were mounted vertically and observed at working distance of 6 – 8 mm at 15 – 20 kV.

2.4.2 Transmission Electron Microscopy (TEM)

The transmission electron microscopy images were recorded using a JEOL 100CX II 100 kV TEM. The nanoparticle samples were typically dispersed in ethyl alcohol by ultrasonic agitation. A drop of nanoparticle dispersion was added to a copper/Lacey carbon grid (#300 mesh, Ted-Pella, Inc.) on a filter paper. The specimen was directly used after the evaporation of the solvent. For high resolution TEM (HR-TEM), a Hitachi HF2000 (200 kV) was used.

2.4.3 Atomic Force Microscopy (AFM)

TappingMode AFM images were recorded using silicon probes on a Dimension 3100 Scanning Probe Microscopy system (Veeco Instruments). All images were recorded under ambient condition.

2.5 Nanocomposite Processing and Thin Film Fabrication

2.5.1 Nanocomposite Processing

The polymer host and the surface modified nanoparticles were weighed according to the intended volume fractions. The nanoparticles were placed in a 60 mL HDPE jar with an appropriate amount of solvent for the desired viscosity. Grinding media (Yttria-stabilized Zirconia, Inframat Advanced Materials, LLC., Farmington, CT) of three different sizes (0.5 mm diameter, spherical; 5 mm diameter and 10 mm diameter, cylindrical) were added then ball-milled (200 rpm) for 2 days. The pre-weighed polymer pellets were then added to the nanoparticle dispersion and the mixture was further ball-milled for 5 to 12 days. The nanoparticle/polymer/solvent mixture formed a stable dispersion after ball-milling suitable for thin film fabrication using solution processes such as spin coating, drop casting, doctor-blade casting, and ink-jet printing.

2.5.2 Substrate Preparation

The substrate for parallel-plate capacitor was either prepared by deposition of 200 nm aluminum with a 20 nm Ti or Cr adhesion layer on a glass slide using a DC sputterer or purchased from Newport Thin Film Laboratory, Chino, CA. The wetting of the electrode surface required a high hydrophilicity for spin-coating. To make the surface clean and hydrophilic, cold air plasma treatment was performed (3 SCFH, 750 W, 1 – 10 min., PlasmaPreen). The hydrophilicity was confirmed by observing the static sessile water contact angle change from 101.7±0.03 degree (as prepared) to near zero degree (after cold plasma treatment).

2.5.3 Thin Film Fabrication

Nanocomposite dispersions were spin coated on aluminum-coated glass slides after the cold air plasma treatment. The typical spinning condition was 1000 – 3000 rpm for 40 to 60 seconds. The wet films were then soft baked on a hot plate at 70 – 100°C for

1 minute, then cooled to room temperature slowly to prevent unwanted micro-cracks in the composite films due to the differences in the thermal expansion coefficients of the nanoparticle and the polymer. The films were then annealed in a vacuum oven at 120°C for an overnight period to remove residual solvent and moisture and to allow densification of the nanocomposite.

2.5.4 Thin Film Characterization

The thicknesses of the films were recorded using a stylus contact profilometer (Tencor Model P-15 or Veeco Dektac 6M Profilometer). Steps were created by scraping out nanocomposite films after cooling the film in liquid nitrogen. The thickness measurement was made by scanning the stylus across the step from the exposed bottom electrode to an area near each device. The nanocomposite film quality and uniformity were checked by an optical microscope and a non-contact surface profilometer (Wyko Profilometer in vertical-step interference (VSI) mode, Veeco Instruments).

2.6 Device Fabrication

All the electrical characterizations were performed using a probe station (Signatone, model H100) with a blunt tungsten tip (Signatone, SE-T, 5.0 μm tip diameter, 25 mil. shank diameter) to minimize the mechanical damage to the soft organic-containing films. The characterizations of the capacitor and OFET devices were performed in a humidity and oxygen controlled (<0.1 ppm) glove box filled with nitrogen.

2.6.1 Mask Design and Fabrication

The capacitor array shadow mask containing circular electrodes of two different areas (small: 0.25 mm^2, large: 1.00 mm^2, tolerance: within ±1 mil.) was designed using a CAD program (AutoCAD, Autodesk) (Figure 2.14) and the 0.005” thick (tolerance: ±0.002”) nickel alloy mask was prepared at Thin Metal Parts (Colorado Springs, Co).

After each aluminum deposition, the deposited aluminum and oxidized aluminum were cleaned by immersing the mask in 50 wt. % sodium hydroxide aqueous solution for about 1 minute.

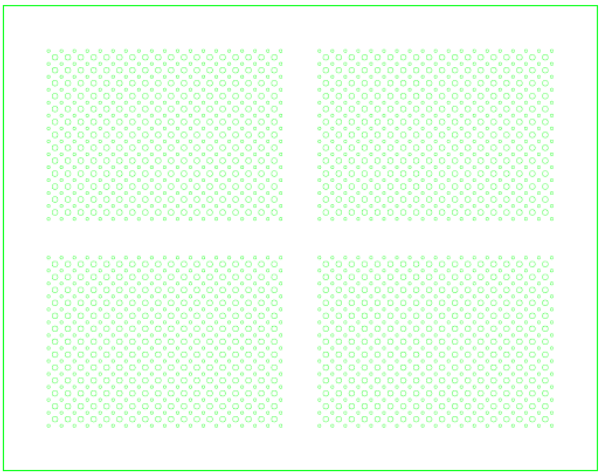

Figure 2.14 The layout of a shadow mask used for fabrication of capacitor array.

2.6.2 Metallization

The top surface of nanocomposite films were metallized by evaporating aluminum through a shadow mask, using a thermal evaporator (Kert J. Lesker, PVD75 Filament Evaporator) at 0.3 nm/sec. deposition rate. Two aluminum pellets were subsequently evaporated from a heated tungsten boat to the samples mounted about 3 feet above the evaporation source. No adhesion layer was required and the deposited aluminum electrodes on the nanocomposite surface stayed on the film throughout the electrical test.

2.6.3 OFET Fabrication

This section describes the fabrication process of OFET based on pentacene (p-type organic semiconductor) and nanocomposite thin films as gate insulator.

2.6.3.1 Substrate Preparation

A heavily n-doped, one-side polished 500 μm thick silicon wafer (n^{++}-Si, 5×10^{-3} Ω-cm) was etched using buffered HF to remove native oxide layer. Immediately after the removal of the oxide, a thin photoresist film was applied to the polished side to prevent growth of oxide layer. To the etched backside, Ti/Au (10 nm / 100 nm) layer was deposited by an electron-beam evaporator to form a gate electrode. The substrate was then stored in a glove box filled with nitrogen until further device fabrication.

The backside etched Si wafer with Ti/Au electrode was cleaned successively with a stripper, acetone, and ethanol. The polished surface was further cleaned by cold air plasma to remove residual photoresist and to make the surface suitably hydrophilic for the spin coating of a nanocomposite gate layer.

2.6.3.2 Nanocomposite Preparation

BT nanoparticles (30~50 nm, Aldrich) were modified with {2-[2-(2-Methoxyethoxy)ethoxy]ethyl}phosphonic acid (PEGPA) then dispersed in 1-butanol with poly(4-vinylphenol) (PVP, MW ~20,000, Aldrich), hexamethoxymethylmelamine (HMMM, Cyamel 300, Mitsui Cyanamide) as a cross-linker, and a catalytic amount of *p*-toluenesulfonic acid (TsOH, Aldrich) (PVP:HMMM:TsOH = 15:5:1 by weight). The cross-linking of PVP matrix takes place by transetherification with HMMM, which gives off methanol as a side product. There was a 10.26 % weight reduction after crosslinking of this mixture. This value was taken into account when calculating the final volume fraction of PEGPA-BT in the nanocomposite. The ratio of PEGPA-modified BT

(PEGPA-BT) to PVP was varied from 16 to 37% by volume. The nanocomposite dispersion was homogenized by ball-milling the dispersion.

2.6.3.3 Thin Film Fabrication

The nanocomposites were spin coated on the substrate and the films were soft baked at 100°C for 1 minute before thermally curing them under vacuum at 160°C for 72 hours to ensure full crosslinking of the PVP matrix. The film thickness was controlled in the 200 - 500 nm range by changing the viscosity and spin speed. Control samples were prepared in the same way without surface modification of the BT nanoparticles.

2.6.3.4 OFET Fabrication

Bottom gate and top contact p-type OFETs of various channel widths and lengths were fabricated on top of these nanocomposite thin films. 50 nm thick pentacene (Aldrich, purified by gradient zone sublimation) films were deposited using a standard physical vapor deposition (PVD, 5×10^{-8} Torr) at 0.3 – 0.6 Å/sec deposition rate onto the substrate held at room temperature. Subsequent deposition of Au electrodes (40 nm) capped with Al (100 nm) were deposited through a shadow mask by electron-beam evaporation. A series of capacitor devices were also fabricated using the nanocomposite thin films for dielectric characterization. OFET fabrication on the nanocomposite films was performed by Ms. Xiao-Hong Zhang and Dr. Benoit Domercq (Prof. Kippelen group).

2.7 Electrical Characterizations

All the electrical characterizations were performed using a probe station (Signatone, model H100) with a blunt tungsten tip (Signatone, SE-T, 5.0 μm tip diameter, 25 mil. shank diameter) to minimize the mechanical damage to the soft organic-

containing films. The characterizations of the capacitor and OFET devices were performed in a humidity and oxygen controlled (<0.1 ppm) glove box filled with nitrogen.

2.7.1 Dielectric Spectroscopy

The frequency-dependent capacitance and loss tangent of a capacitor were measured using an Agilent 4284A LCR meter operating in an equivalent parallel circuit where a known resistor is in place in the circuit with the device under test, and the measured impedance is analyzed to calculate the real and imaginary parts of permittivity. The calibration was performed using an open circuit and a closed circuit. No load calibration was performed. The dielectric spectra were recorded from 20 Hz to 1 MHz with a probing voltage of 1 V_{RMS} under no DC bias unless specified. The instrumental control and data collection were automated using LabView™ software. The temperature-dependent dielectric response was performed under ambient condition (i.e. outside the glove box) in order to use a temperature-controlled hot stage.

2.7.2 I-V Characterization

The leakage current density was characterized by applying DC field while monitoring current output using an Agilent E5272A source monitor unit connected to a probe station in a glove box. OFET characteristics were also measured using this setup.

2.7.3 Dielectric Breakdown Measurement

The breakdown strength is sensitive to the presence of moisture and oxygen near the test device and must be kept minimized to truly test the materials property. Therefore, all the breakdown measurements were performed in a glove box. 50 V_{DC} was initially applied across the device under test (DUT) using a Keithley Model 248 high voltage supplier, then the voltage was ramped at 10 V/sec. until catastrophic failure of the device was achieved. The voltage when the failure took place was recorded as the breakdown voltage. The breakdown voltage can be measured from either a device or a film itself. In

the former case, the electric field is applied over a large area electrode (0.25 mm^2) and measures the device property, while the latter case uses only a point contact (tip radius = 5 μm, contact area = 79 μm^2) and measures the materials property. In this thesis, all the reported breakdown strengths were measured using a large area (0.25 mm^2) contact.

2.7.4 Weibull Analysis of Breakdown Data

The breakdown data were analyzed using Weibull failure analysis method which has been frequently adopted for the investigation of dielectric breakdown of different material systems in this field.(Ul-Haq and Raju 2002; Raju, Katebian et al. 2003; Prendergast, O'Driscoll et al. 2005; Tuncer, James et al. 2006; Tuncer, Sauers et al. 2007; Tuncer, Sauers et al. 2007). Weibull analysis is based on an empirical failure probability which is typically described using three parameters:

$$P_F(E) = 1 - \exp[-\{(E-\gamma)/\alpha\}^{\beta}] \qquad \text{Equation 7.1}$$

where, α is a scale parameter, β is a shape parameter that shows dispersion of E, and γ is a threshold parameter below which value of E no failure occurs. For the analysis of breakdown results of nanocomposites in this study, γ was set to zero. The failure probability can now be expressed as:

$$\log\left[-\ln\{1-P_F(E)\}\right] = \beta \log E - \beta \log \alpha \qquad \text{Equation 7.2}$$

This probability is equated with a median ranked positioning (Bernard-Levenbach positioning) which is expressed as:

$$P_F(i,n) = \left[(i-0.3)/(n+0.4)\right] \times 100\% \qquad \text{Equation 7.3}$$

where, i is the index (1, 2, 3, … n) and n is the sample size. The measured n breakdown field values (E) are reordered in ascending order and then the failure probability, $P_F(E)$, for each E is given from the positioning equation. A linear fitting of $\log\{-\ln(1-P)\}$ *vs.* $\log E$ gives the parameters α and β. The breakdown field for the data set is found to be $E_B = \alpha$ when the failure probability is 63.2 % (*i.e.* 1 – 1/e). These parameters can be plugged

back to Equation 7.1 to find the cumulative distribution function (CDF) which represents the probability of failure as a function of applied field.

2.7.5 P-E Measurement

Dielectric saturation is one important phenomenon that should be considered when choosing materials system for high-energy storage applications.(Chu, Zhou et al. 2006) Though the theoretical maximum energy storage density is calculated as $U_{max} = ½\varepsilon_0\varepsilon_r\mathbf{E}_B^2$ where ε_r is the permittivity of the dielectrics and $\mathbf{E}_B$ is the dielectric breakdown field, the actual maximum energy stored depends on the dielectric saturation behavior of the material. Therefore, the actual stored energy must be separately measured. One method of characterizing the stored energy is measuring the polarization (**P**) of the material as a function of the applied electric field (**E**). The stored energy can be calculated from the area of a **P**-**E** curve expressed as $U_{measured} = \int EdP$, as shown in Figure 2.15.(Chu, Zhou et al. 2006)

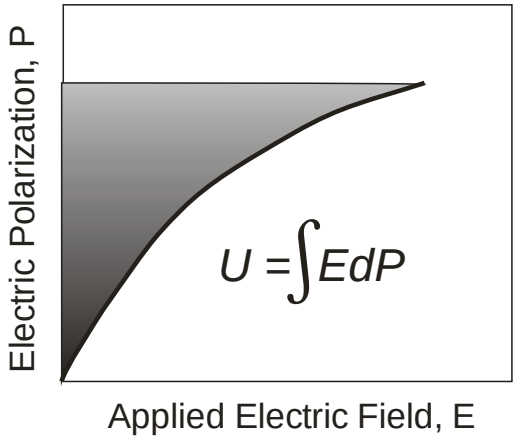

Figure 2.15 A typical **P**-**E** curve of a ferroelectric material. The stored energy is equal to the area under a **P**-**E** curve.

The **P**-**E** measurement was performed at Naval Research Lab by Dr. Ming-Jen Pan using a charge-discharge circuit shown in Figure 2.16. The device under test (DUT)

is initially charged by applying a known DC field through a charging circuit. A high voltage relay switches the DUT to a discharge circuit connected to a known load resistor. The current output from DUT is measured by a voltage drop across this known resistor, which is amplified by an operational amplifier. An oscilloscope integrates the output voltage over time to calculate released energy.

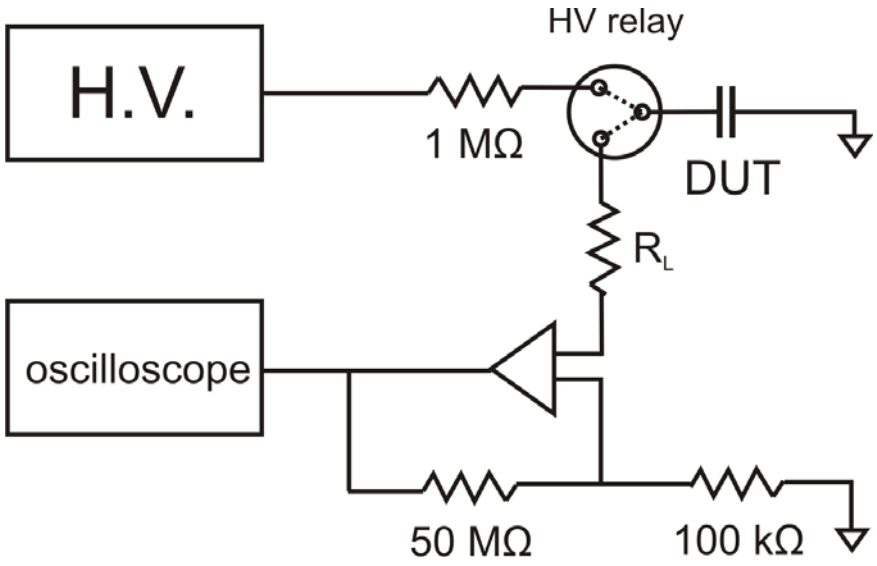

Figure 2.16 Schematics of a charge-discharge circuit.

2.7.6 OFET Characterization

The OFETs were characterized in a dark, nitrogen-filled glove box at ambient pressure and at room temperature using an Agilent 4284A LCR meter for capacitance-voltage (C-V) measurement and an Agilent E5272A two-channel source/monitor unit (SMU) for current-voltage (I-V) characterization.

Carrier mobilities (μ) and threshold voltages (V_T) were calculated in the saturation regime by fitting the square root of drain-source current (I_{DS}) *vs.* the gate-source bias (V_{GS}) to the metal-oxide-semiconductor field-effect transistor (MOSFET) square law:

$$I_{DS} = \mu C_{OX} \frac{W}{2L}(V_{GS} - V_T)^2 \qquad \text{Equation 7.4}$$

where μ is the carrier mobility, C_{OX} is the capacitance density of the gate insulator, V_T is the threshold voltage, and W and L are the width and the length of the semiconductor channel defined by the source and drain electrodes. Sub-threshold slopes (S) and on/off current ratios ($I_{on/off}$) were also extracted from the transfer characteristics. For each type of transistor, 2 – 4 devices with identical geometry were measured to obtain a mean value and a standard deviation. OFET characterizations were performed by Ms. Xiao-Hong Zhang (Prof. Kippelen group).

2.8 Other Characterizations

2.8.1 Thermal Analysis

Thermogravimetric analysis (TGA) results were obtained using a TA Instruments Model TA 2950 TGA under nitrogen. The temperature ramping rate was kept at 20°C/min. and samples were placed on a platinum pan which was pre-cleaned with dilute acid to remove ash then subsequently washed with acetone and ethanol.

2.8.2 Contact Angle Analysis

The water contact angles on pre-treated substrates were measured with a digital goniometer (Model 250-00-115, Ramé-hart, Inc., Netcong, NJ) using static sessile drop method.

2.8.3 Dynamic Light Scattering

A zeta sizer (Malvern Zeta Sizer Nano ZS) was used to measure the average hydrodynamic volume of dispersed nanoparticles in a solvent at 20°C with known refractive index to estimate the particle size and distribution. Polydispersity Index (PDI) obtained from this instrument and software represents the width parameter defined below. The log of the correlation function ($G1$) is fitted by a polynomial:

$$\ln[G1] = a + bt + ct^2 + dt^3 + et^4 + \cdots \qquad \text{Equation 7.5}$$

where the value of b and c were used to calculate PDI as:

$$\text{PDI} = \frac{2c}{b^2} \qquad \text{Equation 7.6}$$

Typically three independent measurements were taken and their average mean sizes (Z) and the average PDI values were reported as the final results.

CHAPTER 3

THE SURFACE MODIFICATION OF BARIUM TITANATE

3.1 Introduction

Chemical surface modification of inorganic nanomaterials using organic surface modifiers provides tailoring of various surface functionalities.(Love, Estroff et al. 2005) Thiols and silane coupling agents are the most widely used surface modifiers for noble metal nanoparticles and silica surfaces.(Hanson, Schwartz et al. 2003; Love, Estroff et al. 2005) Surface functionalization has been used in broad applications such as prevention of nanoparticle aggregation(Ramesh, Shutzberg et al. 2003), changing solubility and dispersability(Neouze and Schubert 2008), control of wetting(Whitesides and Laibinis 1990; Wenzl, Yam et al. 2003) and adhesion(Houston and Kim 2002), chemical and bio-sensing(Love, Estroff et al. 2005; Mingalyov and Lisichkin 2006), tuning interfacial force for self-organization(Aizenberg 2000), modifying electrodes(Paniagua, Hotchkiss et al. 2008), separation sciences(Randon and Paterson 1997), implants(Viornery, Chevolot et al. 2002), anticorrosion coatings and surface passivation(Jennings, Yong et al. 2003), etc. Current material science and technology seek for the use of new types of inorganic materials other than silica or noble metals, for which organosilicon compounds may not be appropriate surface modifiers.

The structure of a surface modifier (also refered to as 'ligand' in this thesis) can be viewed as depicted in Figure 3.1. They have three major functional fragments: i) the binding group (or anchoring group, or coupling group) that provides strong binding to the substrate, ii) the terminal functional group that carries intended specific chemical functions and interacts directly with the surroundings, and iii) the linker that connects the binding group and the terminal group, and controls the length, the solubility, structural

rigidity and flexibility, and the packing density of the ligand. Tailoring of the structure of a surface modifier is thus very important in improving the properties of a polymer/ceramic nanocomposite system.

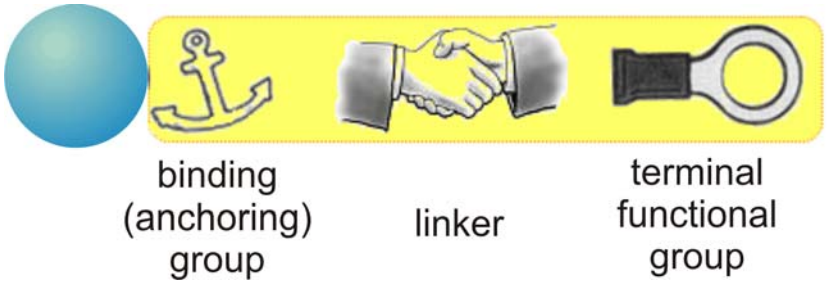

Figure 3.1 The structure of a surface modifier attached to the surface of a nanoparticle represented as a blue sphere.

The surface of metal oxides usually has many defective sites which are typically terminated with a hydroxyl group in the form of M-OH (M: metal). There are also many reactive sites on the surface of metal oxides, such as surface metal atoms with vacant orbitals and oxo bridges, which can be hydrolytically cleaved to yield surface hydroxyl groups. The surface hydroxyl groups are generally considered to be responsible for the organic coupling reactions with surface modifiers, in which an electrophilic substitution takes place replacing the proton in the surface hydroxyl group with the binding group of the surface modifier. Thus, the surface modifier has to have at least one good leaving group which can receive the hydroxyl proton and form a stable product. The binding group also should have valence of two or greater to provide a bridge between the surface and the linker/terminal functional group. Other desired aspects of surface modifiers are strong binding with large grafting density, fast binding kinetics, stability of the binding after surface modification under storage and usage conditions, straightforward binding reaction, easy synthetic route to structural variety of surface modifiers, and non-toxicity of the surface modifiers. In this sense, the elements that can be considered as surface

anchoring elements in binding groups are B, C, N, Al, Si, P, S, Ge, As, Sn, Sb, and Hg, Pb.(Mingalyov and Lisichkin 2006)

3.2 Comparative Study of Different Binding Groups on $BaTiO_3$

A large surface coverage and the stability of ligands on the surface are vital to effective surface modification. With the objective of identifying ligands that can form stable bonds to the barium titanate ($BaTiO_3$, BT) surfaces through coordination or condensation, various binding groups were considered. Trialkoxysilanes are widely used surface modifiers for silicate, indium tin oxide and other metal oxide surfaces. Phosphonic acids have been reported to modify TiO_2, ZrO_2, and indium tin oxide surfaces(Gao, Dickinson et al. 1996; Mutin, Guerrero et al. 2005; McDonald, Holt et al. 2006) and are thought to couple to the surface of metal oxides either by heterocondensation with surface hydroxyl groups (M-OH) or coordination to metal ions on the surface.(Mutin, Guerrero et al. 2005) Carboxylic acid has been used in the preparation of organo-capped barium titanate (Wu, Zou et al. 2001) and sulfonic acid groups may also bind to the surface in a similar manner. The following set of ligands, each bearing an aliphatic octyl chain with a different binding group, were chosen for the study of the surface modification of barium titanate nanoparticles (Figure 3.2): C_8H_{17}-A, where A = $PO(OH)_2$ (PA), SO_2ONa (SA), $Si(OCH_3)_3$ (SI), and CO_2H (CA).

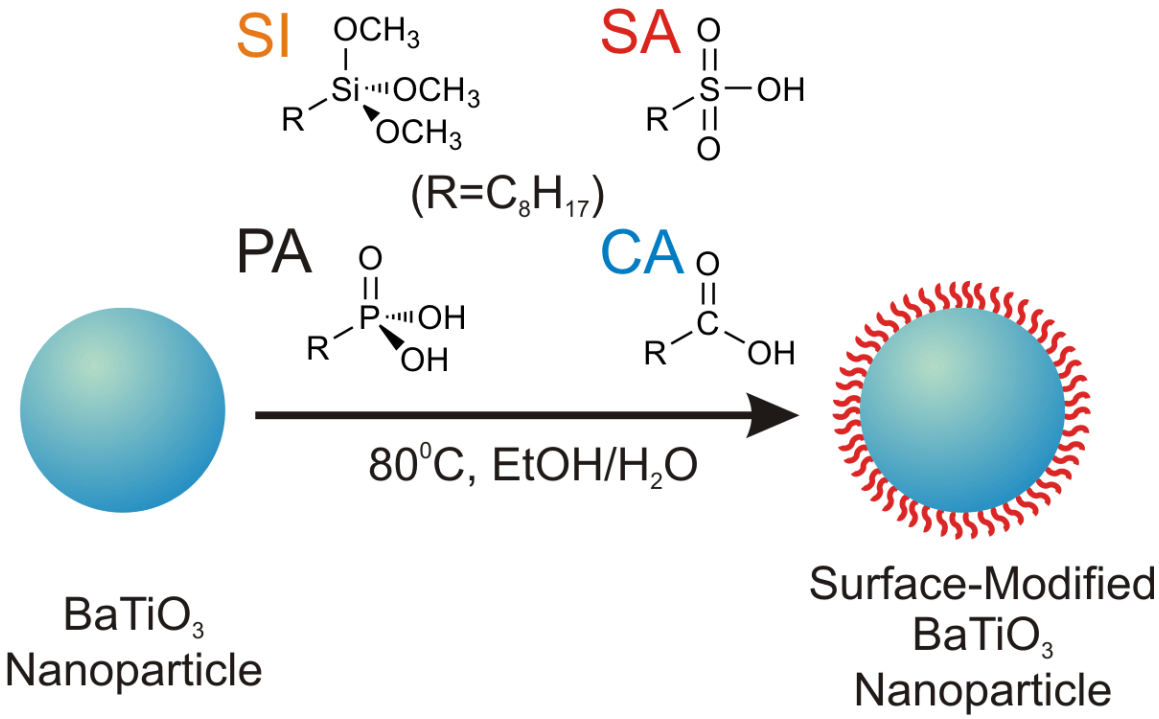

Figure 3.2. Schematic of a comparative experiment to find a good binding group to the surface of barium titanate nanoparticles.

The barium titanate (BT) nanoparticles chosen in this study are spherical nanoparticles with 30~50 nm diameter and the surface is rich in hydroxyl groups, as confirmed by FT-IR. A sample of each ligand was mixed with BT nanoparticles (30~50 nm, 0.5 mmol ligand/g BT) in an ethanol/water (95:5 v/v) solution (0.4 g BT/10 mL solution) and stirred at 80 ºC for 1 hour, followed by extensive washing with ethanol or water and centrifugation to remove excess and/or physisorbed ligand. The treated BT nanoparticles were dried at 80°C *in vacuo* and characterized by FT-IR spectroscopy, thermogravimetric analysis (TGA), elemental analysis, energy dispersive spectroscopy (EDS), and X-ray photoelectron spectroscopy (XPS). Upon successive washing of modified BT nanoparticles with ethanol (1:1 vol. ethanol and water mixture for SA), physisorbed and loosely bound ligands were washed away. The final propensity of

binding of each ligand on the BT surface is compared in Figure 3.3 for successive washing cycles.

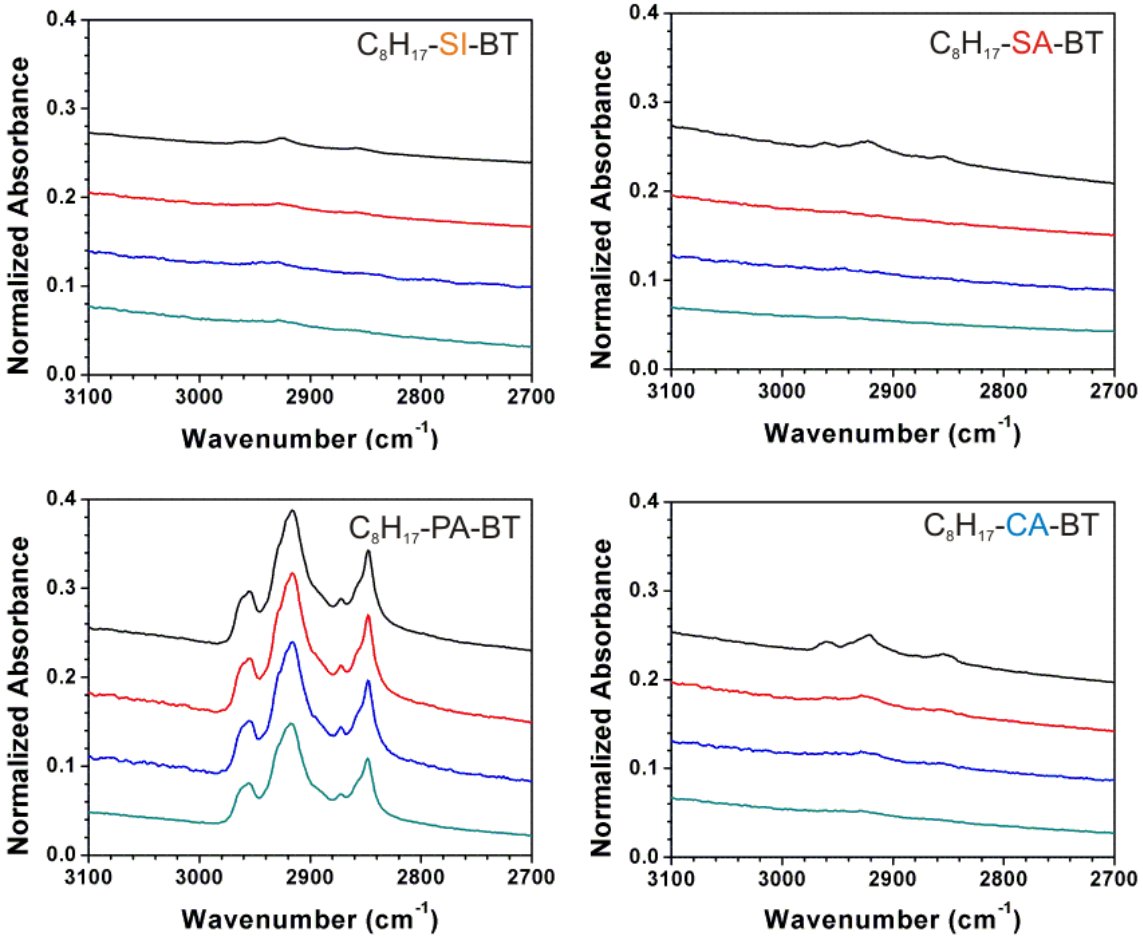

Figure 3.3 FT-IR absorption spectra of BT nanoparticles treated with each ligand at 80°C for 1 hour. Each set of spectra show the relative intensities of C-H stretching modes of the n-octyl chain upon successive washing (top to bottom). The spectra were normalized using the absorption peak of the Ti-O lattice vibration mode (~540 cm^{-1}).

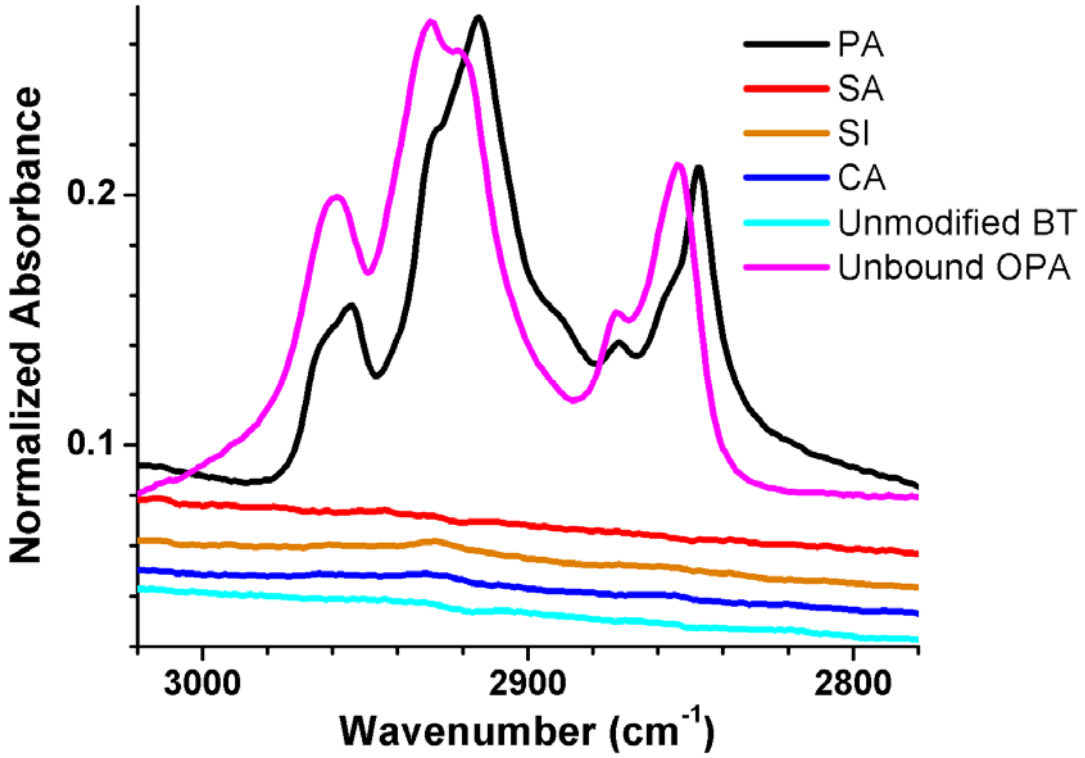

Figure 3.4. FT-IR spectra of treated BT nanoparticles in KBr pellets showing the relative strengths of C-H stretching vibration bands. BT nanoparticles were reacted with different ligands and washed repeatedly by ultrasonication and centrifugation. The spectra were normalized using the lattice Ti-O absorption peak centered at ~540 cm^{-1}. The spectra have been offset vertically for clarity. Solid lines: surface-modified BT with PA, SA, SI, and CA (from top to bottom), BT from a control experiment where no ligand was added. The spectrum of the C_8H_{17}-PA ligand is also included for comparison.

The FT-IR results indicate that only the C_8H_{17}-PA (OPA) ligand yielded a large coverage on the particles, whereas other ligands gave low or negligible coverage. In addition, the bound OPA formed a densely packed layer on the surface of BT as evidenced by the red shift of the methylene C-H stretching peaks with respect to those of free OPA. The C-H stretching energy decreases when there is a strong inter-chain interaction which is only possible when the molecules are densely packed. (Folkers, Gorman et al. 1995; Gao, Dickinson et al. 1996) Elemental analysis (Desert Analytics,

Tucson, AZ) on C_8H_{17}-PA-modified $BaTiO_3$ (OPA-BT) showed about 0.82 % of phosphorus by weight (~5 % when converted to OPA), which corresponds to 11.3 ligands / nm^2 or 1.74×10^5 ligands/particle assuming that the BT nanoparticle is a sphere with 50 nm diameter and there is no change in shape after modification. Energy dispersive spectroscopy (EDS) showed about 0.54 wt. % P corresponding to a surface coverage of only ~7 ligands / nm^2. For more accurate surface coverage comparisons, the surface area of dried and unmodified BT was determined to be 25.8 m^2/g by using a gas adsorption/desorption experiment and analyzing the data using BET isotherm. TGA measurements on the BT nanoparticles modified with different ligands were performed and a significant weight loss only for OPA-BT (4.4 % when heated above 250 °C, Figure 3.5) was observed. This total weight loss corresponds to the loss of 0.71 wt. % phosphorous. Unmodified BT and BT nanoparticles treated with other ligands showed little weight loss mainly due to adsorbed water molecules and other volatile contaminants. The footprint of a phosphonic acid binding to the surface of TiO_2 has been reported to be about 24 $Å^2$ per molecule.(Gao, Dickinson et al. 1996) Using this value and the BET surface area of BT, the surface coverage of OPA on BT surface was found to be about 1.3 times larger than a theoretical monolayer. If a full monolayer formation is assumed, as supported by FT-IR and SS-NMR results (*vide infra*), the footprint of OPA on BT nanoparticle should be 18.7 $Å^2$ based on the weight loss in TGA experiment and the BET surface area. This value is consistent with the values for close-packed aliphatic chains reported by Schwartz (18.5 $Å^2$)(Hanson, Schwartz et al. 2003) and Kitaigorodskii (18.6 $Å^2$)(Kitaigorodskii 1961). This suggests that the footprint of phosphonic acid may vary depending on the structure of the linker and the end functional group. The binding modes of phosphonic acid on BT surface will be discussed in the next section.

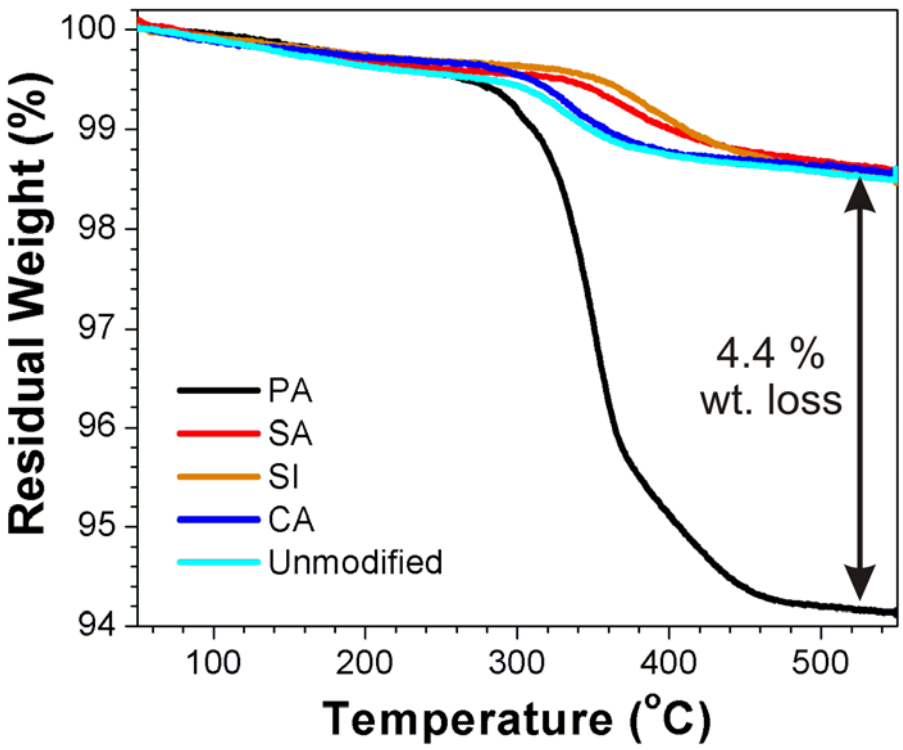

Figure 3.5 Thermogravimetric analysis (TGA) of surface modified BT nanoparticles with different binding groups. Significant weight loss only in the case of the PA binding group is observed at high temperature.

The results show that a comparatively high surface coverage on BT particles is achieved only by the ligand bearing the phosphonic acid functional group. The relative ordering of the coverage obtained by the different ligands examined is as follows: PA >> SI >~ CA > SA. This trend could be explained in terms of both the number of hydroxyl groups attached to the center atom of the binding group as well as the electronegativity of the center atom. Phosphonic acid has two hydroxyl groups that can take part in the hetero-condensation reaction with the surface hydroxyl groups (M-OH), while carboxylic acid and sulfonic acid have only one hydroxyl group. Sulfur is more electronegative (2.58 in the Pauling scale) than carbon (2.55), phosphorous (2.19), and silicon (1.90) which makes the neighboring oxygen(s) less nucleophilic. Consequently, the tendency of oxygen atoms (Lewis base) coordinating to electron-deficient barium or titanium atoms

(Lewis acid) on the surface of $BaTiO_3$ is expected to decrease. Silanes have three alkoxy groups that can be hydrolyzed to hydroxyl groups. However, the hydrolysis condition of Si-O-R bond can also re-hydrolyze the product ester (Si-O-M) in the same manner making the silanes a weak binding group. In addition, silanes have a tendency to form self-condensate gels with extensive Si-O-Si network rather than a surface layer, which is insoluble in the solution and precipitates with the nanoparticles. (Mingalyov and Lisichkin 2006) Unlike Si-O-C bond in trialkoxysilanes, the P-O-C bond in dialkyl phosphonate is not easily hydrolyzed. Similarly, the cleavage of P-O-M bond on the surface is not expected.(Mutin, Guerrero et al. 2005)

In conclusion, phosphonic acid ligands were found to form a densely packed surface layer on barium titanate nanoparticles with a high surface coverage than analogous trimethoxysilane, carboxylic acid, and sulfonic acid ligands.

3.3 Binding of n-Octyl Phosphonic Acid on $BaTiO_3$

The binding kinetics of n-octyl phosphonic acid on the surface of the BT nanoparticles was examined by treating a BT dispersion in ethanol/water mixture with same amount of phosphonic acid ligand for different times at 80°C. The relative strength of C-H stretching modes in FT-IR spectra (Figure 3.6) and the ^{31}P Solid State NMR (SS-NMR) spectra (Figure 3.7) from the reaction product after 1 hour and 24 hours exhibited no significant difference, except for a slight difference of the peak intensity at 1139 cm^{-1} (ν_{as}P-O-M), indicating that the reaction had reached equilibrium at 80°C within an hour under the conditions used. The peak intensity at 1139 cm^{-1} was always slightly changing from sample to sample and the reason is unclear. However, it should be closely related to the surface conditions of the BT nanoparticles as this mode is directly related to the binding modes of OPA. In subsequent experiments, the OPA was found to bind to BT nanoparticle surface by ultrasonication of the mixture in a warm (30 40°C) bath and even by stirring at room temperature. Other ligands with different binding groups were also

compared using the same condition but increasing the surface modification reaction time did not improve the degree of surface modification.

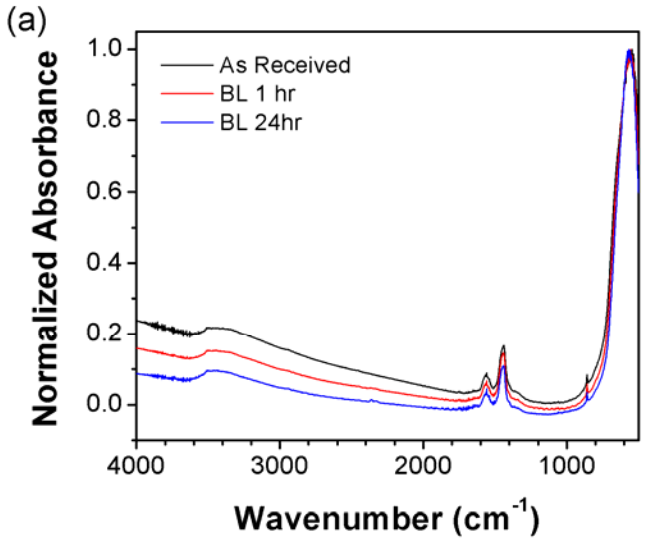
(a)
Normalized Absorbance
1.0
0.8
0.6
0.4
0.2
0.0
As Received
BL 1 hr
BL 24hr
4000
3000
2000
1000
Wavenumber (cm-1)

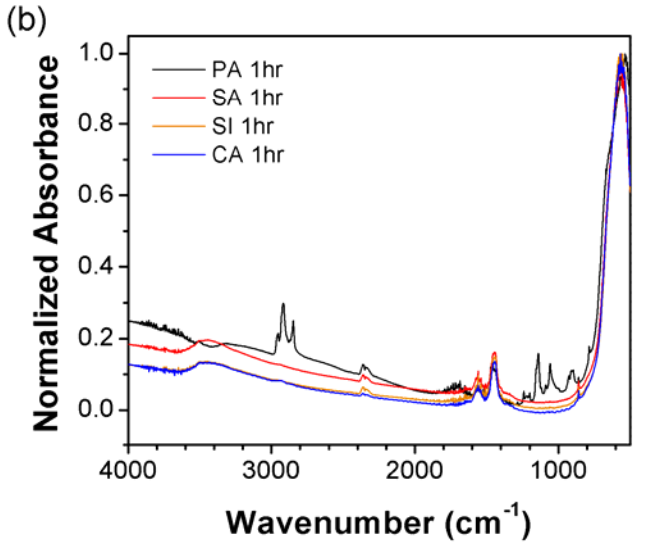
(b)
Normalized Absorbance
1.0
0.8
0.6
0.4
0.2
0.0
PA 1hr
SA 1hr
SI 1hr
CA 1hr
4000
3000
2000
1000
Wavenumber (cm-1)

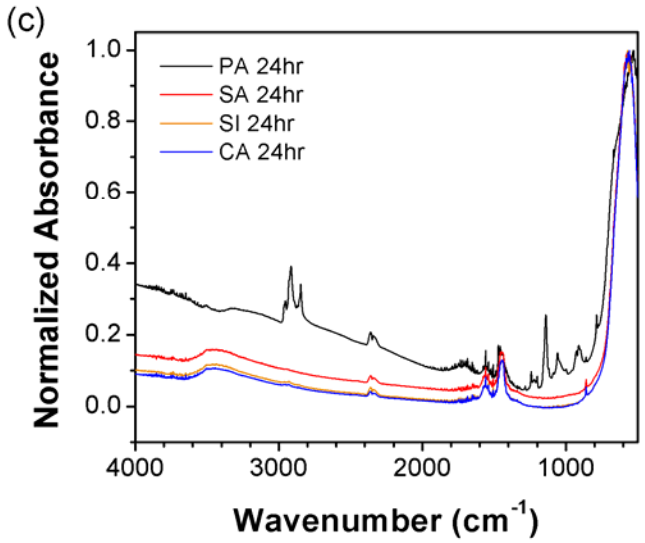
(c)
Normalized Absorbance
1.0
0.8
0.6
0.4
0.2
0.0
PA 24hr
SA 24hr
SI 24hr
CA 24hr
4000
3000
2000
1000
Wavenumber (cm-1)

Figure 3.6 FT-IR absorption spectra of BT nanoparticles treated with different ligands for different periods of time at 80°C. (a) As received unmodified BT and control experiments (BL) where no ligand was added, (b) after 1 hour treatment, and (c) after 24 hour treatment. The spectra were normalized using the lattice Ti-O absorption peak centered at ~540 cm^{-1}. Note that there is no significant difference between 1 hour and 24 hour-treated BT nanoparticles for all the ligands tested.

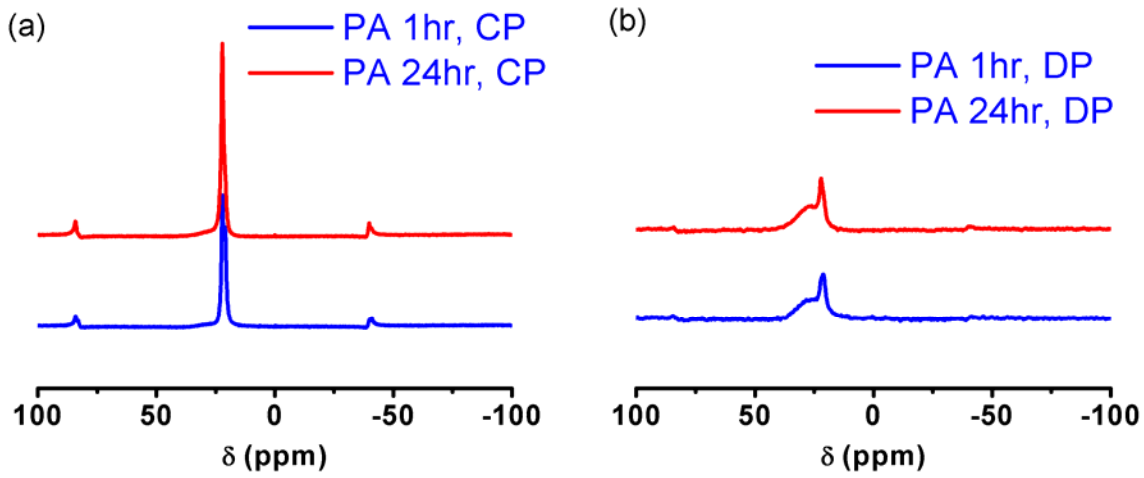

Figure 3.7 Cross polarization (CP), (a) and direct polarization (DP), (b) ^{31}P MAS SS-NMR spectra of BT nanoparticles treated with OPA for 1 hour (blue) and 24 hours (red). Y-axis scales are the signal intensities (arbitrary unit).

The surface bound OPA showed high stability to solvolysis, either under ultrasonic (40°C, 6 hours) (Figure 3.8), or microwave irradiation (100 W, 10 min with a 2455 MHz magnetron, Focused Microwave Synthesis System, Model Discover, CEM Corp.) conditions (Figure 3.9), remaining bound after extensive washing with a wide range of common organic solvents, (polar protic, non-polar, polar-aprotic), water, and 1 N HCl (OPA is thus a good corrosion inhibition layer against strong acids) but being washed away by a strong base (1 N KOH).

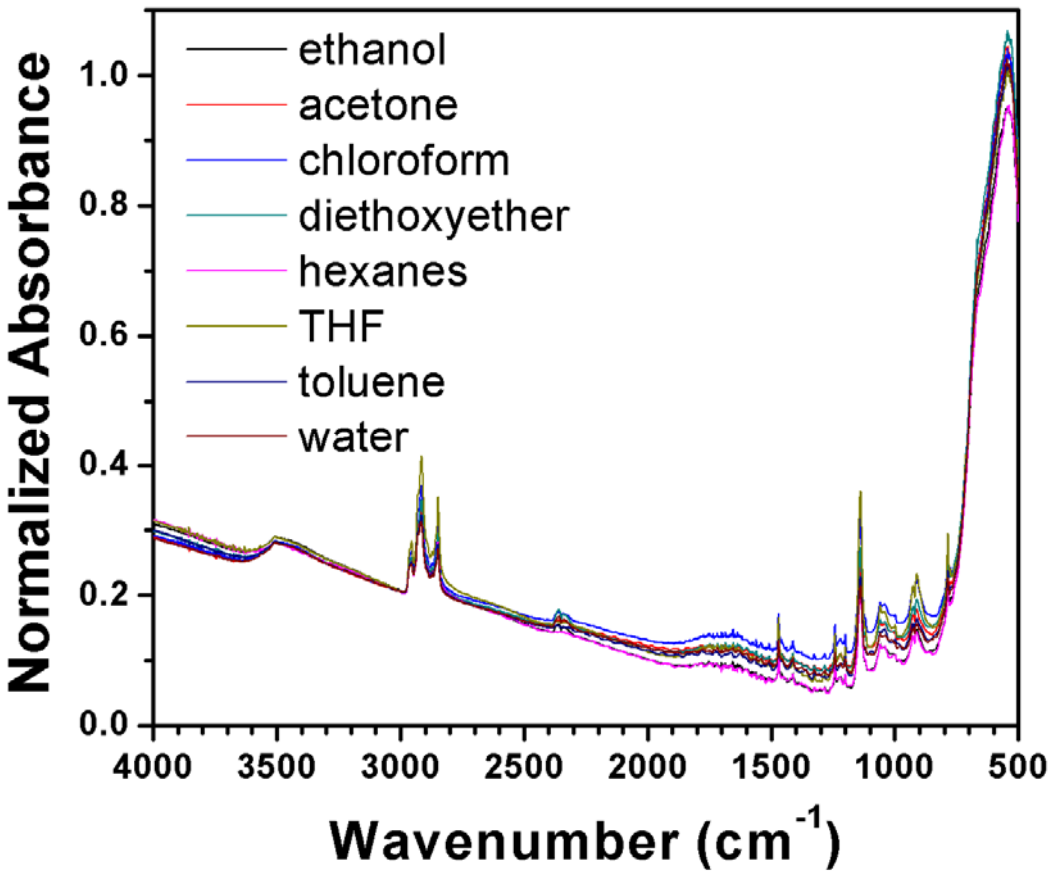

Figure 3.8 FT-IR absorption spectra of OPA-BT after washing with various solvent in an ultrasonic bath (40°C, 6 hours) showing the stability of bound phosphonic acid against solvolysis. The spectra were normalized using the lattice Ti-O absorption peak centered at ~540 cm^{-1} and offset to have same value at 3000cm^{-1} for comparison.

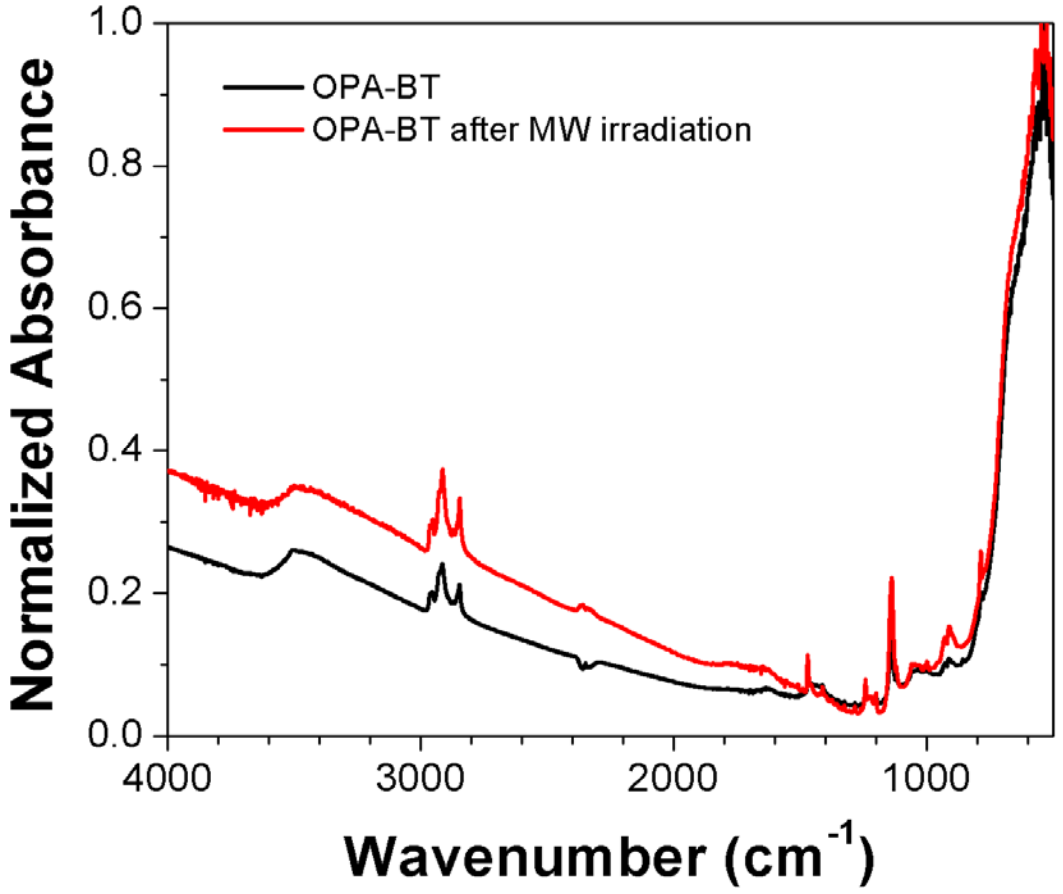

Figure 3.9 FT-IR absorption spectra of OPA-BT after microwave irradiation (100 W, 10 min) showing the stability of bound phosphonic acid on BT nanoparticle surface. The spectra were normalized using the lattice Ti-O absorption peak centered at ~540 cm^{-1}.

Powder X-ray diffraction data and SEM observation indicated that neither the crystal structure of the nanoparticles nor the morphology of the nanoparticles was affected by the surface modification with n-octyl phosphonic acid ligand.

Surface modifications of other perovskite nanoparticles with n-octylphosphonic acid showed the presence of similar ligand peaks observed from OPA-BT implying that the phosphonic acid ligand coating method could be applied to general metal oxide nanoparticles. (Figure 3.10) Because the surface properties of the particles of different composition and from different manufacturers are different, direct quantitative

comparisons cannot be made. However, it was generally observed that high density of surface hydroxyl group is needed for phosphonic acid coupling on the surface. OPA was examined on wide range of metal oxide nanoparticle surfaces and found to afford surface modification as evidenced by FT-IR. The morphology of the nanoparticles remains unchanged during this surface modification reaction. The nanoparticles tested are $CoFe_2O_4$ (Figure 3.11), $NiFe_2O_4$, indium tin oxide (ITO)(Paniagua, Hotchkiss et al. 2008), CuO, HfO_2, Dy_2O_3, and ZnO.(Figure 3.12)

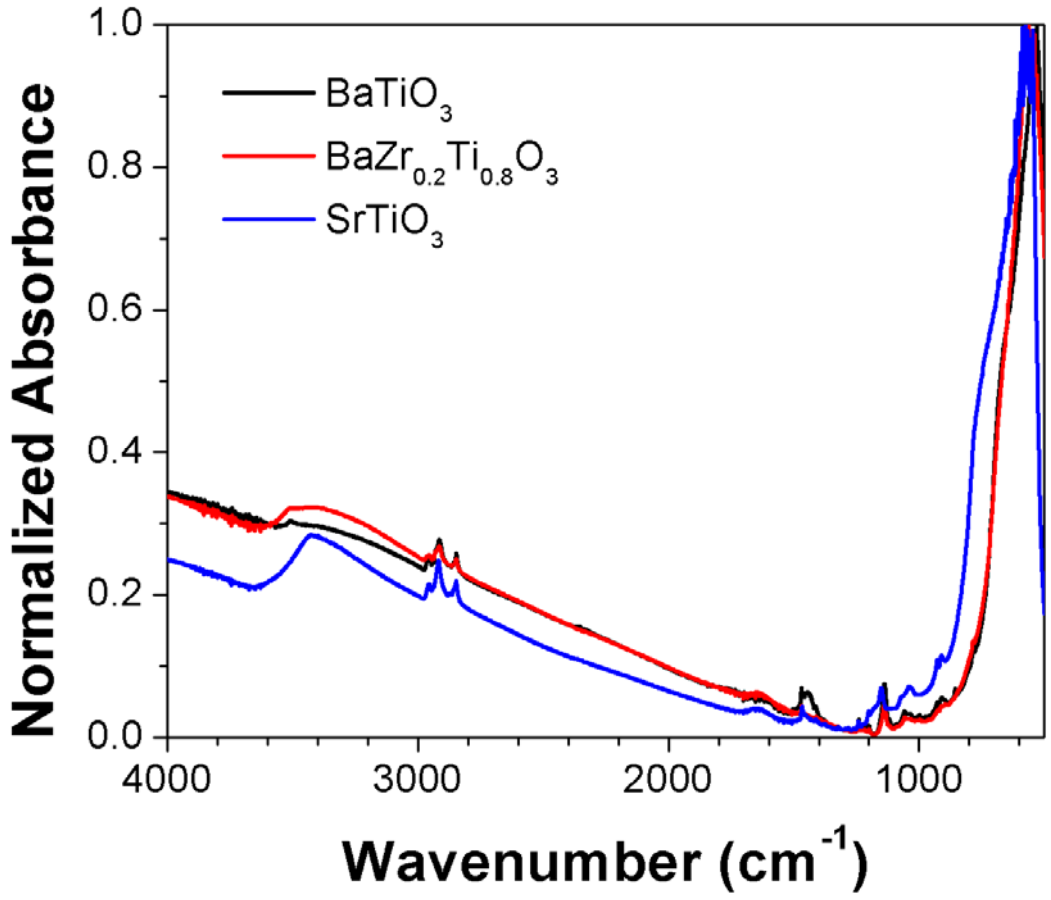

Figure 3.10 FT-IR absorption spectra of a large $BaTiO_3$ (120 nm) and similar perovskite nanoparticles modified with OPA. The spectra were normalized using the lattice Ti-O absorption peak centered at ~540 cm^{-1}.

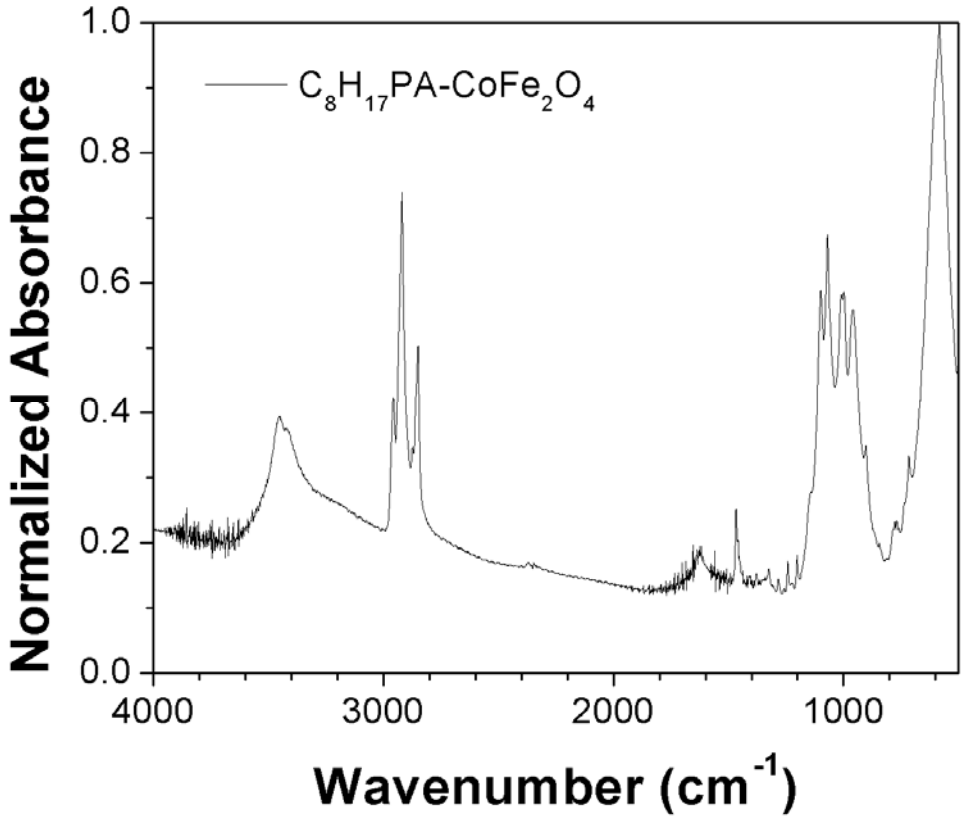

Figure 3.11 FT-IR spectra of 10 nm Cobalt ferrite ($CoFe_2O_4$) nanoparticles modified with OPA. The spectrum was normalized at the largest absorption peak.

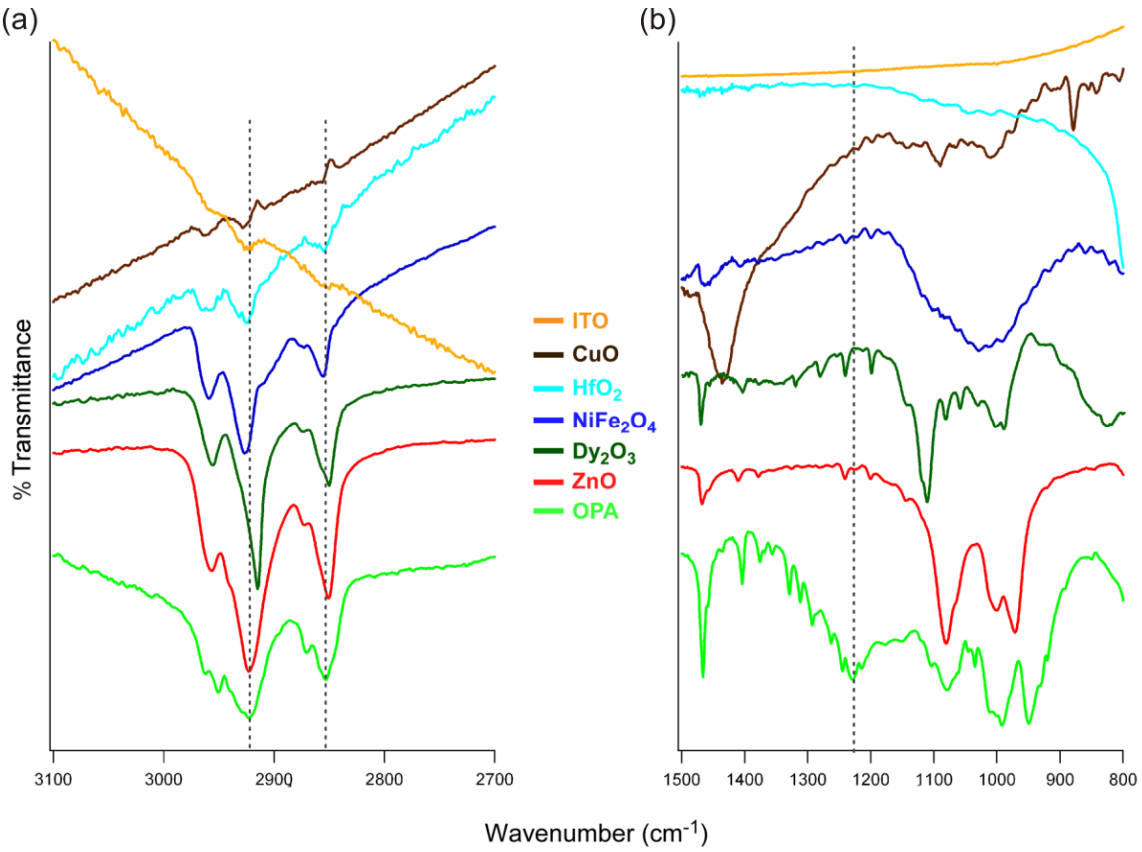

Figure 3.12 FT-IR spectra of OPA and OPA-modified metal oxide nanoparticles. C-H stretching region (a), and P-O and P=O stretching region (b). The dotted lines indicate the locations of asymmetric and symmetric C-H stretching peaks (a) and the P=O stretching peak (b), respectively.

Recently, the binding of organophosphonic acid on titanium dioxide surfaces has been studied by FT-IR and solid-state NMR.(Gao, Dickinson et al. 1996; Guerrero, Mutin et al. 2001; Mutin, Guerrero et al. 2005; Mingalyov and Lisichkin 2006; Brodard-Severac, Guerrero et al. 2008) It is generally accepted that phosphonic acid binds to the titanium oxide surface by the condensation reaction between the P-OH and the surface hydroxyl group (Ti-OH) as well as the coordination of phosphoryl oxygen (P=O) to a surface Ti atom by either a chelating or bridging configuration. In addition, the remaining P-OH and P=O groups not directly taking part in the binding with the titanium dioxide surface

can be involved in hydrogen bonding with an adjacent phosphonic acid molecule and/or with uncoupled surface hydroxyl (Ti-OH) or oxo (Ti-O-Ti) groups. This leads to a variety of possible binding modes of organophosphonic acid ($R\text{-}O_3H_2$) on the titanium dioxide surface, as described by Mutin et al., who used ^{17}O MAS NMR to study these binding modes (Figure 3.13).(Brodard-Severac, Guerrero et al. 2008)

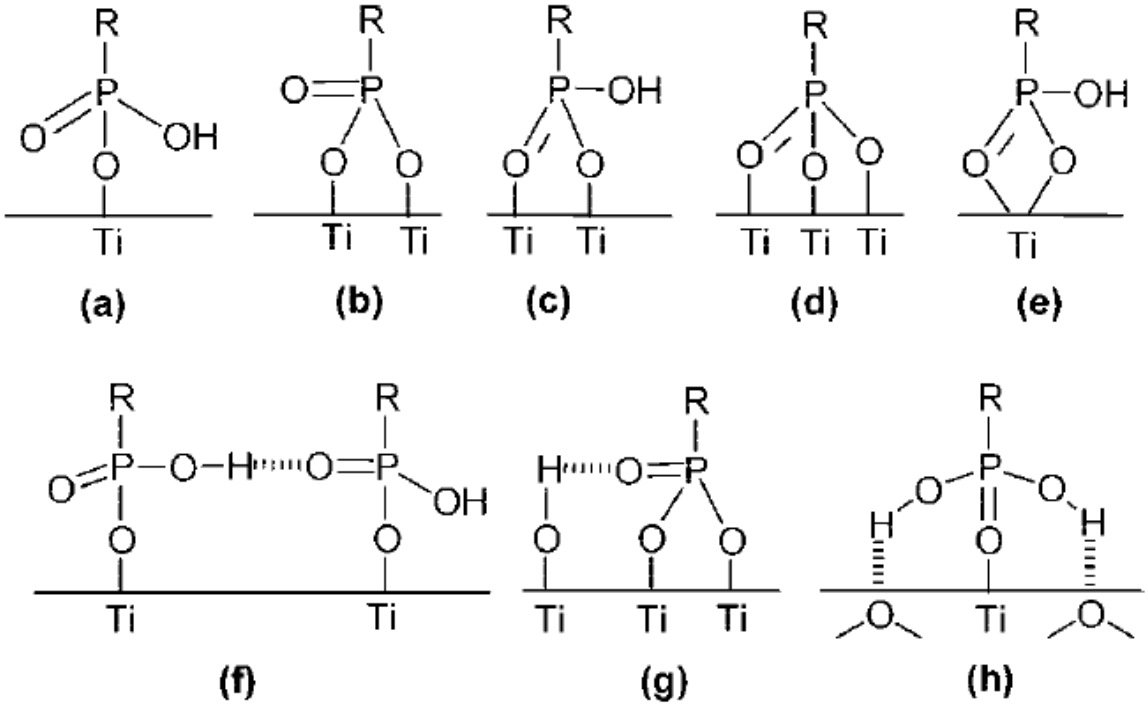

Figure 3.13 Schematic representation of binding modes of phosphonic acid on titanium dioxide surface (from *Chem. Mater.* 20(16) **2008**, p. 5192).

In the case of binding of phosphonic acid to the barium titanate surface, the binding mechanism initiated by the coordination of phosphoryl oxygen is unlikely because the surface of barium titanate is slightly basic (*vide infra*) and does not favor the chelation of phosphoryl oxygen. Therefore, the binding mode (h) in Figure 3.13 is unlikely for phosphonic acid binding to barium titanate surface, though it was found as the most

probable binding configuration on TiO_2 based on the adsorption strength calculated using density functional theory.(Nilsing, Lunell et al. 2005)

FT-IR spectra of OPA and OPA-BT nanoparticles provide insight into the binding modes of organophosphonic acid to the surface of barium titanate. Binding is evidenced by strong C-H stretching absorptions (2915 and 2848 cm^{-1}), major changes in the number and frequencies of the P=O and P-O stretching bands (1260~1300 cm^{-1}, 1106 and 990~1010 cm^{-1} for OPA; 1140 and 1057 cm^{-1} for OPA-BT), and the disappearance of PO-H stretching (2321 cm^{-1}) bands (Figure 3.14).(Thomas 1974; Socrates 1994) The changes in P=O and the P-O stretching peaks suggest that the majority of the ligand is bound to the surface in a tridentate form ((d), (g), and (h) in Figure 3.13), involving all three oxygen atoms. These changes are consistent with previous IR studies of phosphonic acids bound to TiO_2 and ZrO_2 surfaces, which were interpreted as evidence of tridentate binding.(Gao, Dickinson et al. 1996; Mutin, Guerrero et al. 2005) These results indicate that the phosphonic acid reacts with the surface hydroxyl group (M-OH, M = metal) *via* a hetero-condensation reaction, in which the M-O-H bond is replaced with M-O-P bond. Therefore, phosphonic acid can effectively passivate the surface of barium titanate by removing easily ionizable surface hydroxyl groups. This is very important for thin films used in electronic components, where the films are usually exposed to a strong electric field that can induce field ionization and create mobile charge carriers. These ionic species, once created, can migrate along the charge percolation pathways and contribute to leakage current and eventually lead to premature device failure.

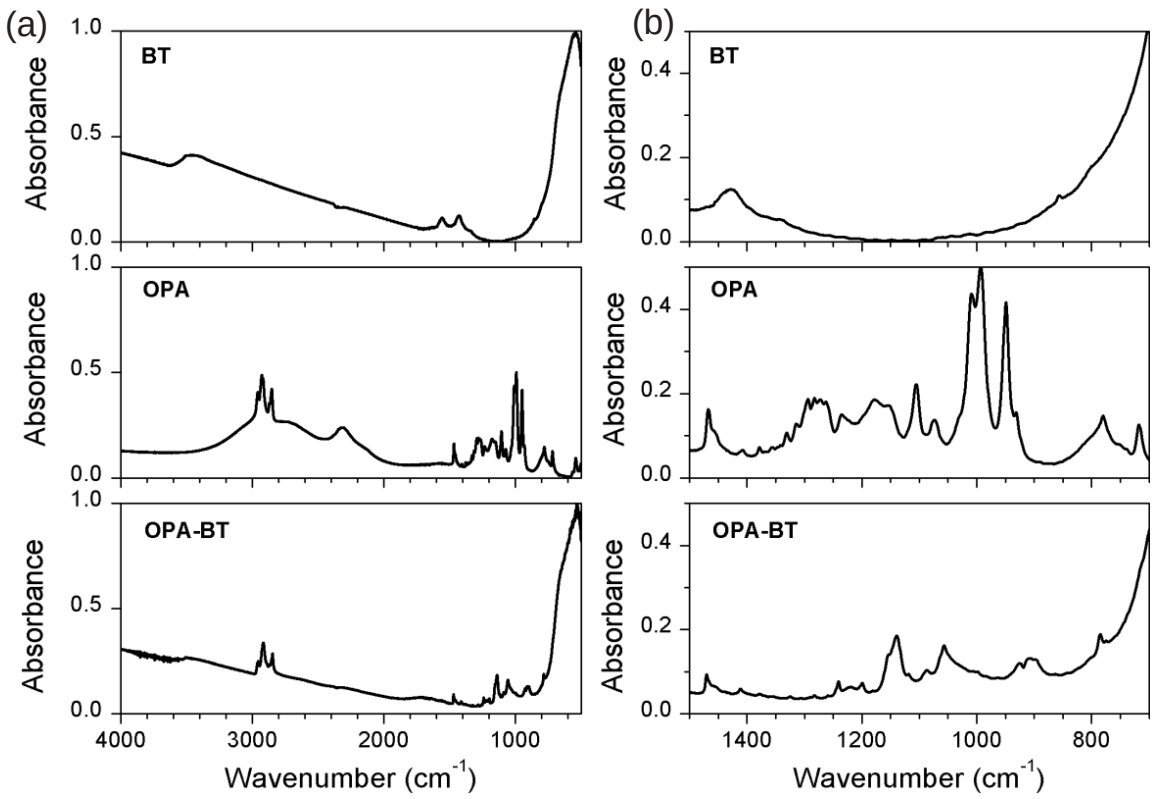

Figure 3.14 (a) FT-IR spectra of BT, n-octylphosphonic acid (OPA), and n-octyl phosphonic acid-modified BT (OPA-BT) in a wide range, (b) details of the P-O stretching region. The spectra for BT and OPA-BT were normalized using the lattice Ti-O absorption peak centered at ~540 cm^{-1}.

^{31}P Solid-state NMR (SS-NMR) can distinguish the surface-bound phosphonic acids from physisorbed and bulk metal phosphonate gels, as they show different chemical shifts. To further assess the binding mode of phosphonic acid on barium titanate surface, both cross polarization (CP) and direct polarization (DP) magic angle spinning (MAS) ^{31}P SS-NMR spectra were obtained (Figure 3.15). In the CP experiment the hydrogen atoms are first magnetically excited and the polarization is transferred from the hydrogen atoms to nearby phosphorous atoms. Therefore, only phosphorous atoms in relatively rigid configurations are selectively excited. As a result, the signals from the phosphorous atoms in relatively rigid configurations (*e.g.* tridentate and bidentate form) are enhanced

in the cross polarization mode. In the DP experiment, all the phosphorous atoms in the sample are directly excited and thus all phosphorous atoms are detected. CP-MAS spectra showed sharp singlets at $\delta = 36.5$ ppm for free OPA and $\delta = 23$ ppm for OPA-BT; the sharp resonance for OPA-BT suggests the presence of a tightly-packed, approximately homogeneous ('monolayer-like') phosphonate layer on the BT surface. The ^{31}P MAS SS-NMR spectrum of OPA-BT measured by direct polarization reveals an additional broad peak at intermediate chemical shift ($\delta \sim 27$ ppm). This suggests the presence of some loosely-bound phosphonate groups, possibly monodentate ((a) in Figure 3.13) and/or unbound phosphonic acid molecules linked to a surface-bound phosphonic acid *via* P-O-P bond. The observations from FT-IR and ^{31}P SS-NMR strongly suggest, but not definitively, that the majority of the phosphonic acids bind in tridentate and bidentate form.

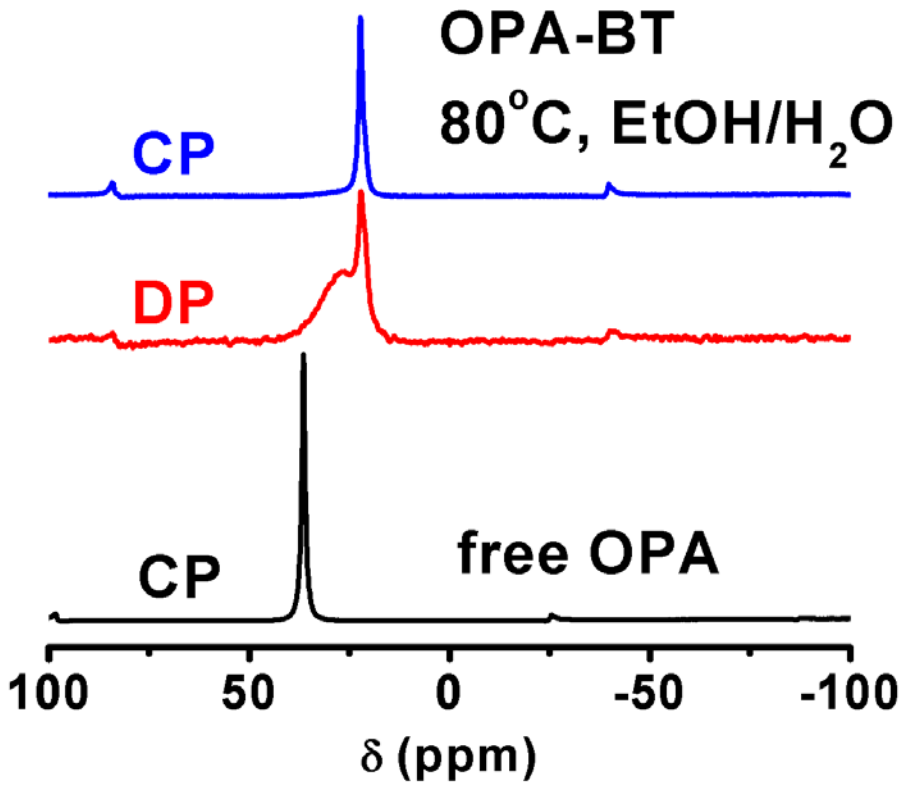

Figure 3.15 Cross-polarization (CP) and direct-polarization (DP) magic angle spinning (MAS) ^{31}P solid state NMR spectra of OPA-modified $BaTiO_3$. The chemical shift change from free OPA (δ = 36.5 ppm) to surface-attached OPA (δ = 23 ppm) suggests binding of the ligand in the phosphate (RPO_3^{2-}) form (reference chemical shift: Ammonium dihydrogen phosphate, δ = 1 ppm). The differences between CP and DP spectra show that there are at least two different types of phosphorous environments present on the $BaTiO_3$ surface. The sharp peak is attributed to densely-packed, strongly-bound tridentate and bidentate ligands, and the broad peak to other, more weakly-associated ligands with a range of possible binding modes. The Y-axis scale is the signal intensity (arbitrary unit).

The surface modification condition used throughout this thesis (*i.e.* ethanol and water mixture, stirring at 80°C for 1 hour) did not result in bulk metal phosphonate gel (e.g. α-$Ti(RPO_3)_2$) by dissolution-precipitation process, which would appear as a sharp

peak around -4.0 – -7.0 ppm.(Bars, Tinet et al. 1991) Thus the surface modification condition used here selectively yielded a surface layer on the barium titanate surface.(Mutin, Guerrero et al. 2005)

Isothermal titration calorimetry (ITC) of solution-phase self-assembly of alkylphosphonic acids on the surfaces of TiO_2 and ZrO_2 has been recently used to estimate the enthalpy/energy balance for the formation of SAMs at solid-liquid interfaces.(Ferreira, Marcinko et al. 2005). The binding energy of OPA on TiO_2 and ZrO_2 surfaces were determined as 58 kJ/mol and 55 kJ/mol, respectively. The binding energy of OPA on $BaTiO_3$ surface was determined to be 82 kJ/mol, which was measured using a MircoCal VP-ITC with Hastelloy© alloy C276 cells. This strongly supports that the dominant binding mode of OPA on the BT nanoparticle surface is tridentate and the stability of the binding is stronger than on TiO_2 or ZrO_2 surfaces.

3.4 Binding of Phosphonate and Phosphate Ligands on $BaTiO_3$

The synthesis of phosphonic acids typically involves two steps: the Arbuzov reaction and the hydrolysis of the phosphonate ester. The former step is relatively simple reaction with easy purification and can be easily scaled up at minimal cost, but the hydrolysis step requires expensive, moisture-sensitive chemicals, and the purification step typically generates a large volume of solvent waste. Alkyl phosphonates are the intermediate of the synthesis of phosphonic acids and are readily soluble in most organic solvents. In addition, the synthesis of functional phosphonic acids with acid-labile groups such as glycidyl is often not possible due to the high acidity (pK_a ~2.0) of the phosphonic acid group. Dialkyl phosphonate can also bind to the surface of titanium oxide or aluminum oxide through a stepwise reaction mechanism as shown in Figure 3.16: i) the coordination of phosphoryl oxygen to the surface, which favors Bronstead or Lewis acidic site on the substrate surface, ii) the attack of the oxygen in M-O-H (Lewis base) to the partially positively charged (thus more electrophilic) phosphorous atom, iii)

the leaving of the alkoxy group, iv) attack of alkoxide on the proton, forming an alcohol and the final product.(Guerrero, Mutin et al. 2001; Mutin, Guerrero et al. 2005)

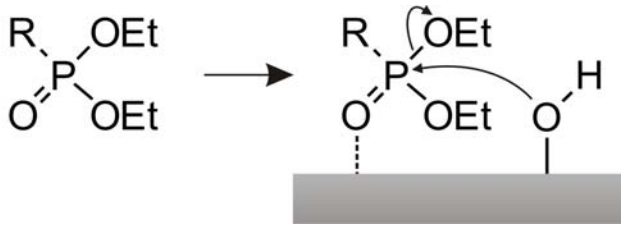

Figure 3.16 The proposed binding mechanism of dialkyl phosphonate via coordination of phosphoryl oxygen.

In this regard, the binding of dialkyl phosphonates and dichloro phosphonates to the surface of barium titanate was examined. The surface modification reactions of BT nanoparticles with n-octylphosphonic acid diethyl ester were performed under the same condition described in the previous section. The treated BT nanoparticles were extensively washed and dried then characterized by FT-IR. Unlike on titanium oxide, n-octylphosphonic acid diethyl ester did not yield surface modification on the BT surface.

The addition of a base in the surface modification reaction was also attempted as the base can facilitate the formation of phosphonate anions ($RPO(OEt)^-$). However, it seems that the added base (triethylamine, TEA) was deactivating the surface hydroxyl groups by hydrogen bonding, and surface modification was not observed. This can be attributed to the basic nature of the surface of BT nanoparticles (pH = 7.92 for as received BT, pH = 8.12 for NH_4Cl washed BT), since the donor-acceptor type coordination of phosphoryl oxygen to the surface metal favors acidic surface (i.e. Lewis acid), such as titanium oxide and aluminum oxide. It should be noted that the binding of phosphonic acids on surfaces with few surface hydroxyl groups did not yield a high coverage of phosphonic acid. This supports the interpretation that the major binding

mechanism of phosphonic acid is by condensation reactions and the mechanism involving phosphoryl oxygen chelating to the surface metal is unlikely.

Treatment of BT nanoparticles with 1-octylphosphonic dichloride in dry toluene also did not result in significant surface modification, as evidenced by the peaks of the characteristic ligand found in the IR spectrum of the nanoparticles. This is primarily due to the evolved hydrochloric acid during the reaction which can destroy the BT surface and lead to uncontrollable changes of the surface properties of BT. Addition of acid scavengers such as triethylamine and proton sponge did not improve the surface modification as they rather deactivated the acidic sites on the surface by adsorption.

Figure 3.17 shows the surface modification reaction of mono-, bis-, and tris-(2-ethylhexyl) phosphate on BT nanoparticle surface. Similarly to the case of alkyl and chloro phosphonate, the tris(2-ethylhexyl) phosphate did not show any evidence of surface modification and the number of hydroxyl groups in the binding group was roughly proportional to the extent of surface modification. OPA yielded a higher surface coverage than the equivalent phosphate.

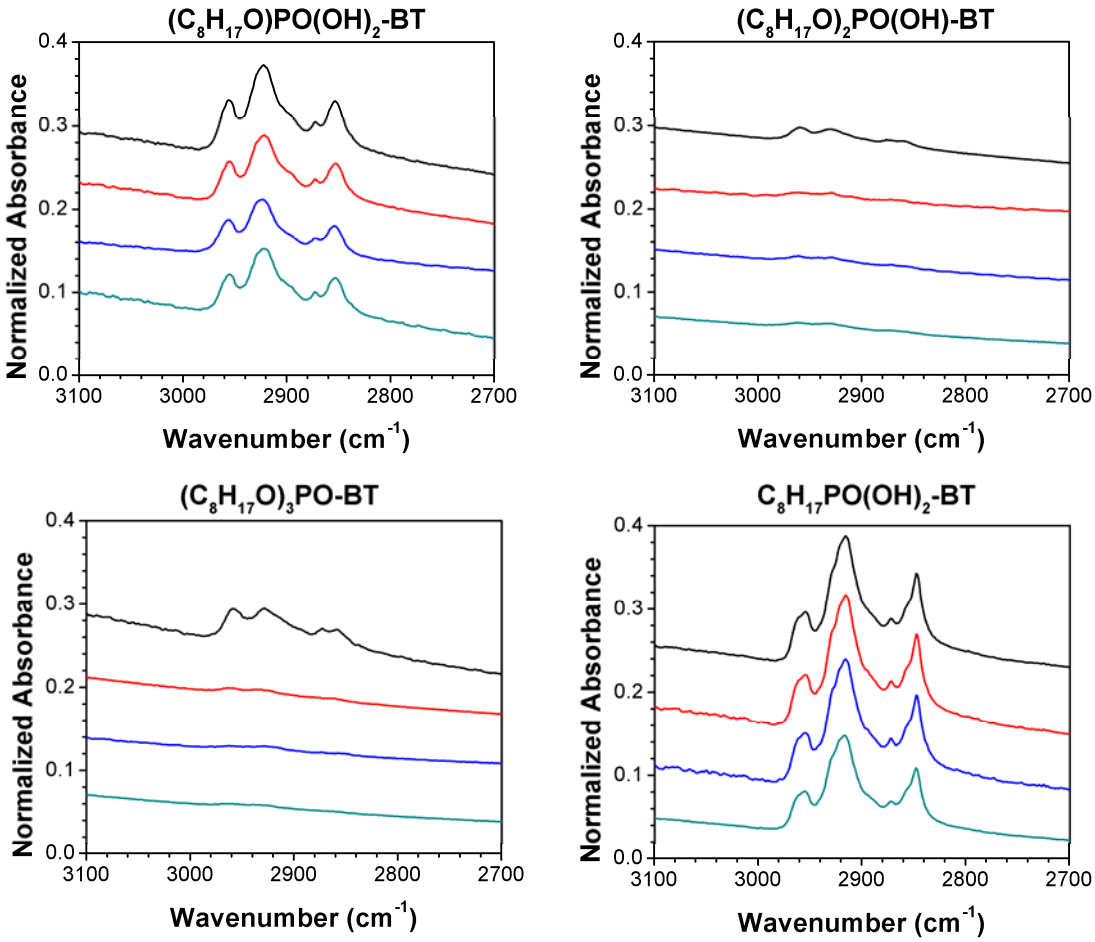

Figure 3.17 FT-IR spectra of BT nanoparticles modified with mono-, bis-, and tris-(2-ethylhexyl) phosphate. The results are compared with those from OPA. The solid lines (from top to bottom) in each group correspond to an increasing number of washing after surface modification reaction. All the spectra were normalized using the lattice Ti-O absorption peak centered at ~540 cm^{-1}.

OPA modification on high temperature-sintered barium titanate nanoparticles with a low amount of surface hydroxyl concentration (qualitative comparison of the O-H stretching peak intensity of FT-IR spectra) yielded significantly less surface modification as shown in Figure 3.18. Since the size and shape of the high temperature-sintered nanoparticle was similar to that of BT nanoparticles, the surface area should not be

greatly different. These results confirm that the phosphonic acid binding mechanism on BT surface is through a condensation reaction and the mechanism involving the coordination of phosphoryl oxygen is unlikely. This clearly rules out the binding configuration (h) in Figure 3.13 from major binding modes of OPA on BT.

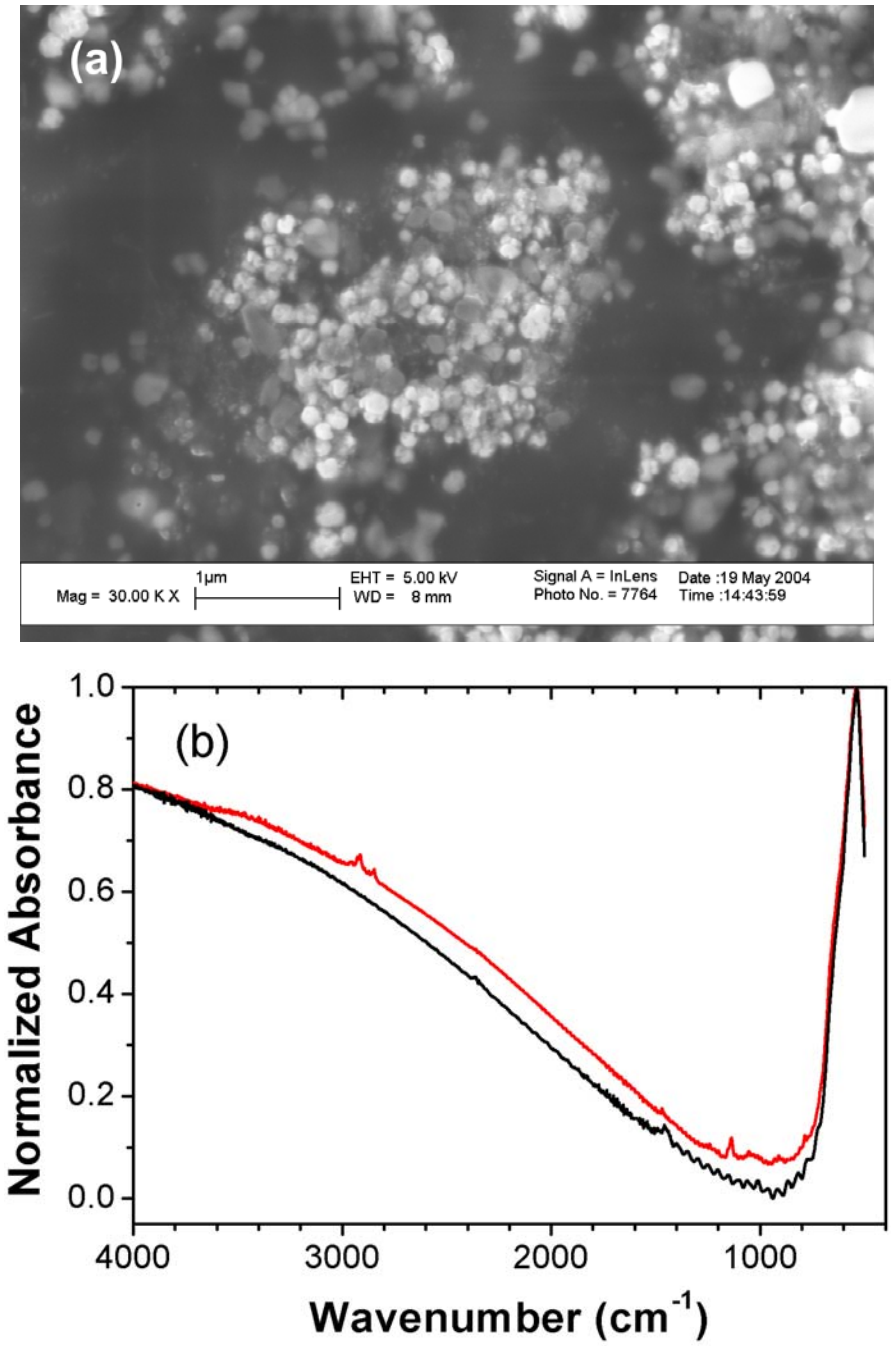

Figure 3.18 (a) The SEM images of high temperature-sintered $BaTiO_3$ nanoparticles. (b) FT-IR spectrum of high temperature-sintered $BaTiO_3$ powder (black) and the spectrum after surface modification with OPA. The spectra were normalized using the lattice Ti-O absorption peak centered at ~540 cm^{-1}.

In conclusion, functional phosphonic acid should be used to effectively modify the surface of metal oxide nanoparticles regardless of the acidity and/or basicity of the surface. In some cases, the intermediate product, dialkyl phosphonate, could be used on metal oxide surfaces of high acidity (*e.g.* TiO_2), yet the effectiveness of surface modification was usually inferior to that of phosphonic acid. (see Appendix B)

3.5 Pre-Treatment of $BaTiO_3$ Surface

Barium carbonate ($BaCO_3$) is one of the major known impurities found in barium titanate and other types of barium-containing oxides in addition to common foreign ions such as Si, Al, Ca, or Na. (Lopez, Fourlaris et al. 1999) It is known to exist as separate domains in barium titanate rather than as surface coating layers. Barium carbonate is significantly soluble in water at room temperature releasing carbonate, hydrogen carbonate, and barium ions. Therefore, barium carbonate impurities are particularly important in aqueous processing of barium titanate. Barium ions (Ba^{2+}) are known to leach into aqueous system and are specifically adsorbed on a barium titanate particle surface.(Chiang and Jean 2003; Yoon, Lee et al. 2003) The increased amount of Ba^{2+} on the surface of barium titanate changes the surface properties. The increased concentration of Ba^{2+} also affects the iso-electric point (IEP) of barium titanate suspensions in aqueous systems. Since the surface modification reaction of barium titanate is typically performed in an alcohol/water mixture, it is important to minimize the amount of barium carbonate impurities to keep consistent surface conditions, such as the number density of surface hydroxyl groups.

The effect of a typical surface modification condition, *i.e.* ultrasonication and stirring in 95:5 vol./vol. mixtures of ethanol and distilled water, on the relative amount of barium carbonate was examined without any ligands added. Barium carbonate remained almost unaffected in this solvent mixture as determined from the FT-IR spectra of the nanoparticles. (Figure 3.19) (Lopez, Fourlaris et al. 1999) Treating the surface of barium

titanate nanoparticles with water and aqueous solution of ammonium chloride (0.4 and 0.8 g NH_4Cl / g BT) can remove barium carbonate impurities (Figure 3.20). The washing of barium carbonate with ammonium chloride was examined in a quantitative manner but increasing the ratio of ammonium chloride to barium titanate more than 0.4 wt./wt. did not significantly improve the removal of barium carbonate.

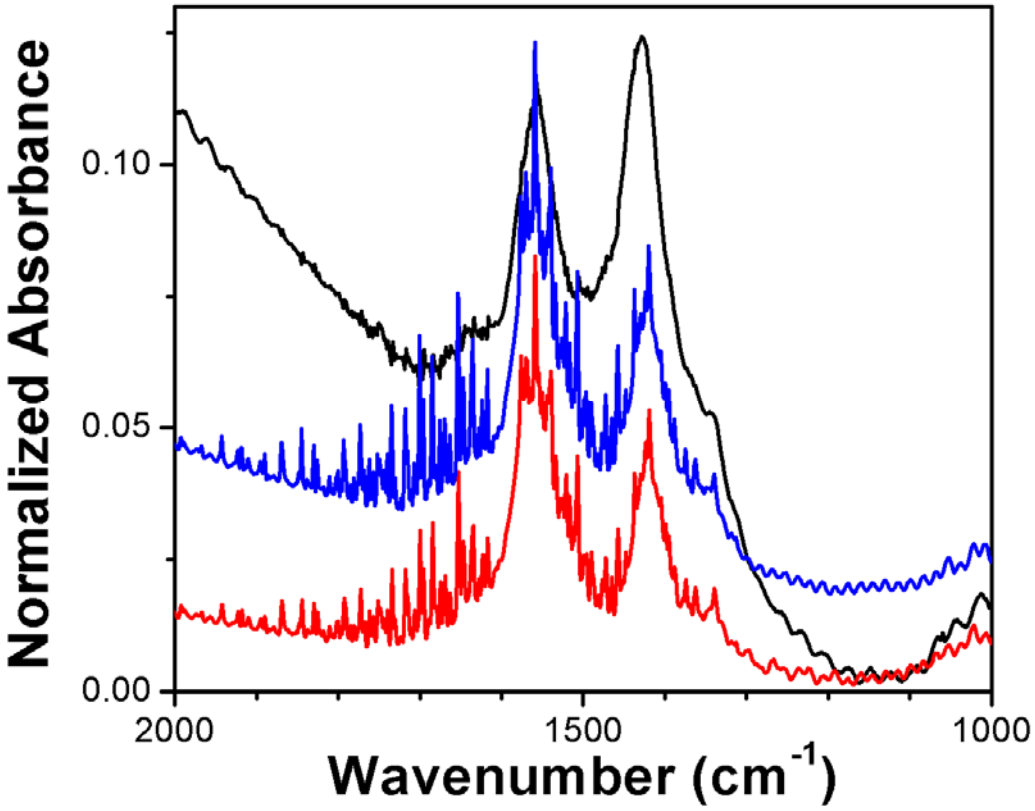

Figure 3.19 FT-IR spectra of BT nanoparticles. The bands at ~1400 cm^{-1} and 1550 cm^{-1} are due to $BaCO_3$ impurities. As received (black), after ultrasonic treatment in 95:5 (vol./vol.) ethanol/water mixture (red), and after ultrasonic treatment and stirring at 80°C for 1 hour in 95:5 (vol./vol.) ethanol/water mixture (blue). The spectra were normalized using the lattice Ti-O absorption peak centered at ~540 cm^{-1}.

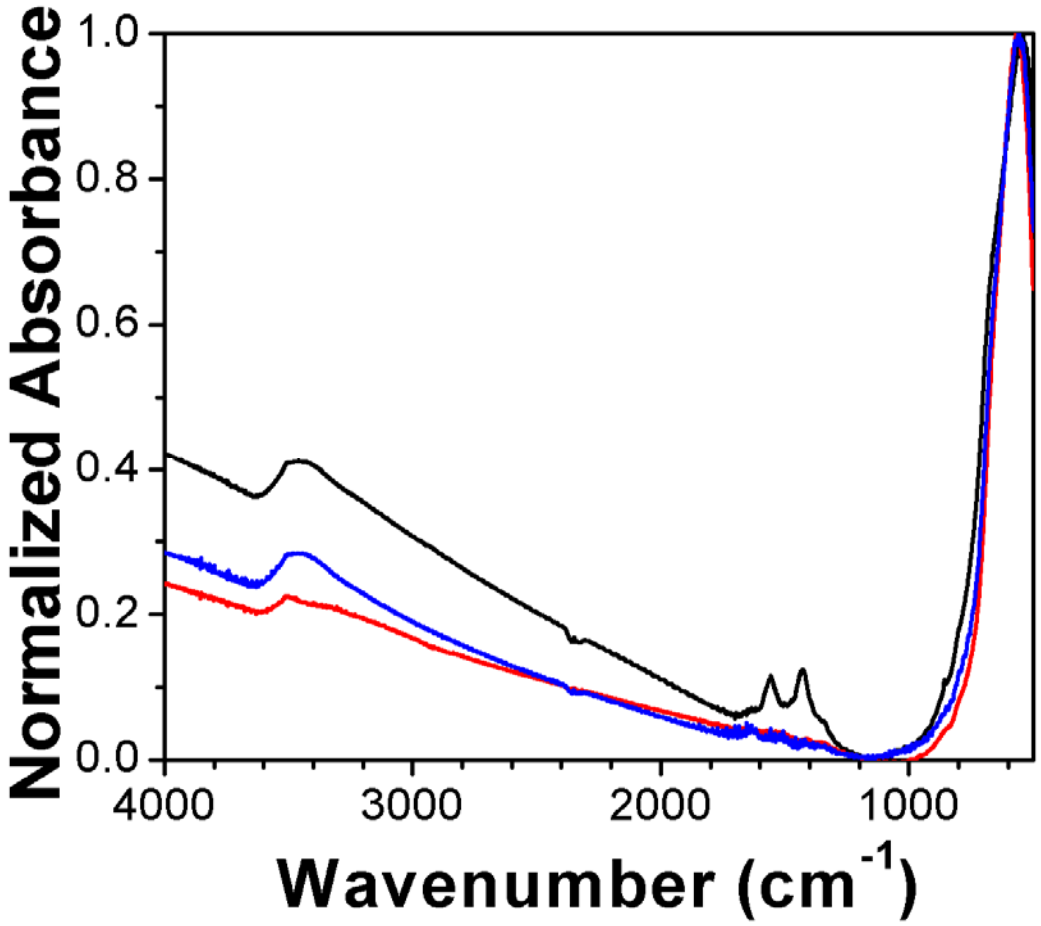

Figure 3.20 FT-IR spectra of BT nanoparticles before and after washing with aqueous solution of ammonium chloride (NH_4Cl). As received BT (black), after washing with 0.4 g NH_4Cl / g BT (red), and after washing with 0.8 g NH_4Cl / g BT (blue). The spectra were normalized using the lattice Ti-O absorption peak centered at ~540 cm^{-1}.

To determine if $BaCO_3$ impurities would reform after removal using ammonium chloride treatment, the washed BT nanoparticles were stored in a desiccator and monitored over time. No significant growth of barium carbonate was observed for up to one month storage, as shown in Figure 3.21. When the treated particles were stored under ambient air in a capped vial, barium carbonate also did not significantly increased when checked after 19 days of storage.

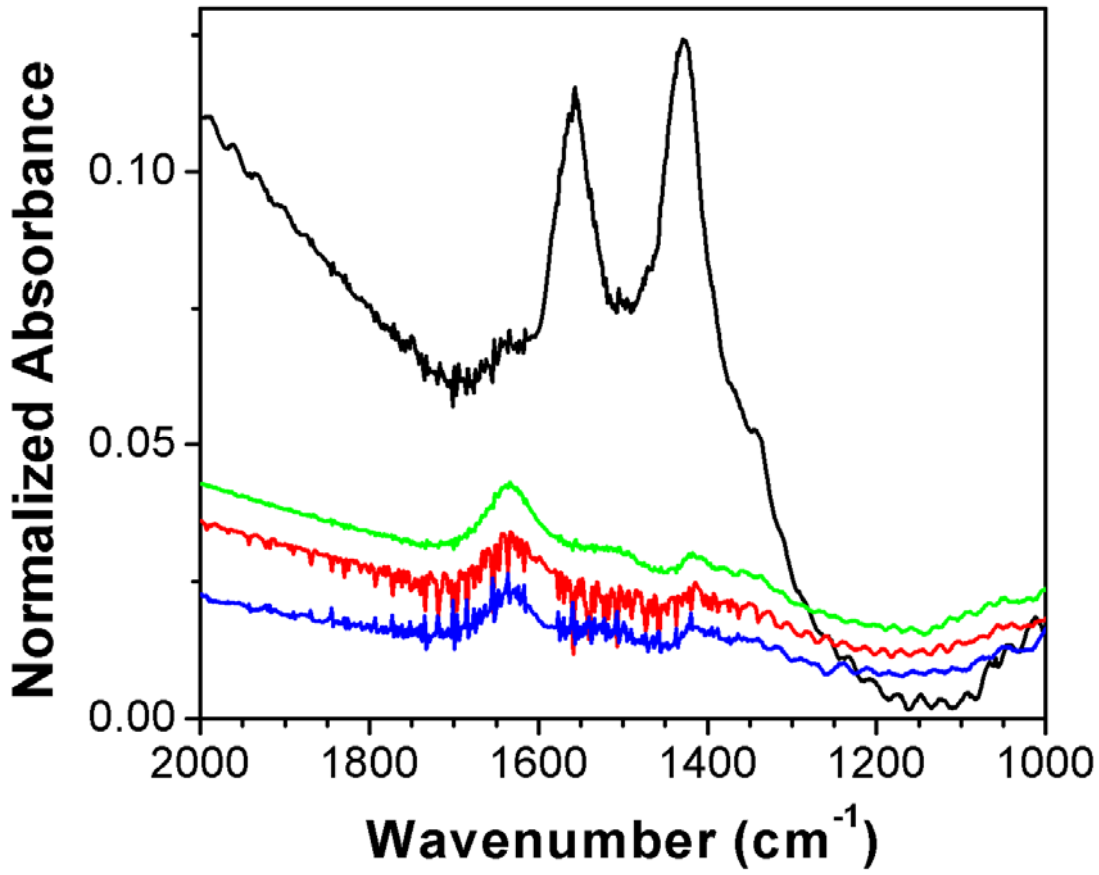

Figure 3.21 FT-IR spectra of BT nanoparticles after NH_4Cl treatment as a function of storage time. As received, unwashed BT (black), after washing with NH_4Cl (red), after storage of washed BT in a desiccator for 12 days (green) and for 1 month (blue). The spectra were normalized using the lattice Ti-O absorption peak centered at ~540 cm^{-1}.

The ammonium chloride washing did not significantly change the morphology of the BT nanoparticles when observed under SEM. Other surface properties also seem to be unchanged because the modification of barium titanate powders with n-octyl phosphonic acid is not affected by the presence of ammonium chloride, as suggested by the similarity of the FT-IR spectra in Figure 3.22. Therefore, it can be concluded that aqueous ammonium chloride-treated barium titanate nanoparticles have at least about one month shelf-life with no significant change in the amount of barium carbonate impurity

when stored in a desiccator. This is practically useful because the particles can be treated in large quantities and then stored for further experiments.

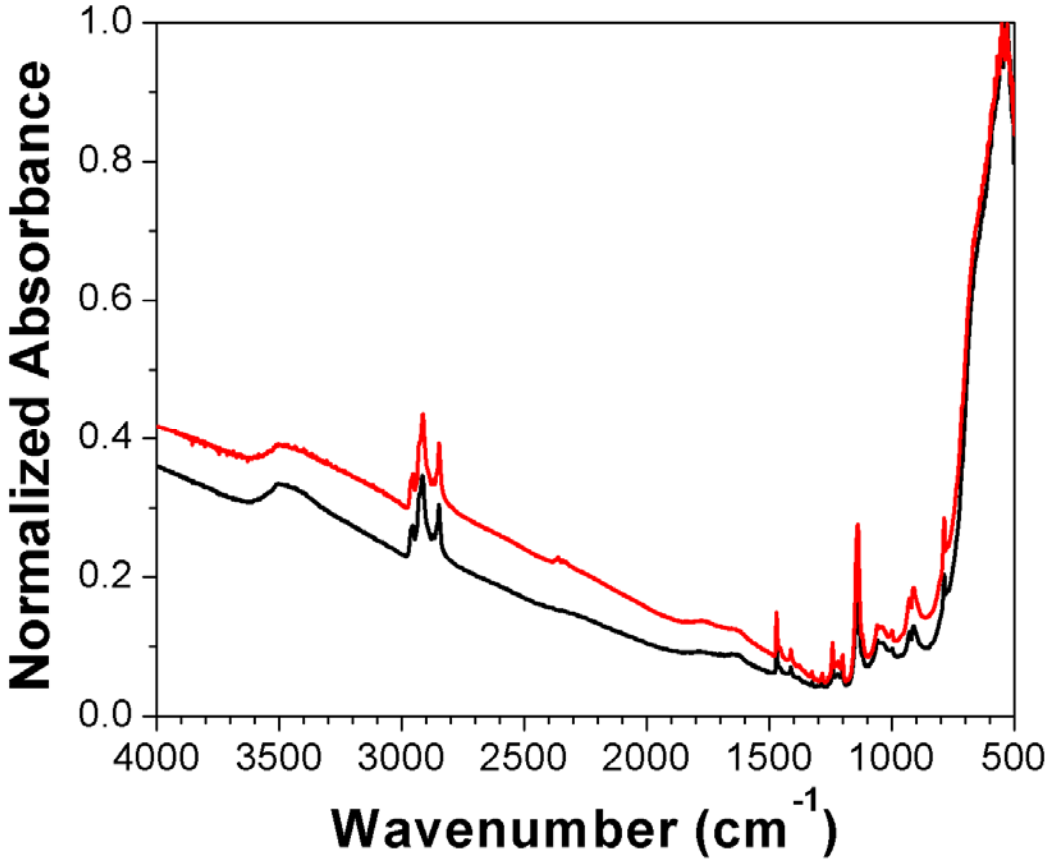

Figure 3.22 FT-IR spectra of OPA surface modified BT nanoparticles with (red) and without (black) added ammonium chloride (0.4 g/g BT). The spectra were normalized using the lattice Ti-O absorption peak centered at ~540 cm^{-1}.

The surface modification of barium carbonate-free BT nanoparticles showed slightly increased coupling of n-octyltrimethoxy silane than in the case of untreated BT nanoparticles, as shown in Figure 3.23. However, it is not clear whether the increased intensity of C-H stretching mode is from surface bound silanes or from self-condensed siloxane gels. In general, the surface modifications of trimethylsilane-based ligands on NH_4Cl-washed BT nanoparticles were not very reproducible. For example, the surface

modification of 3-glycydoxypropyltrimethoxy silane on NH_4Cl-treated BT nanoparticles did not show noticeable surface coupling. Therefore, the binding affinity of trimethoxysilane-based ligands to the surface of NH_4Cl-washed BT varied from one ligand to another. The binding affinity of other ligands to the NH_4Cl-wahsed BT nanoparticles was similar to that of untreated BT nanoparticles.

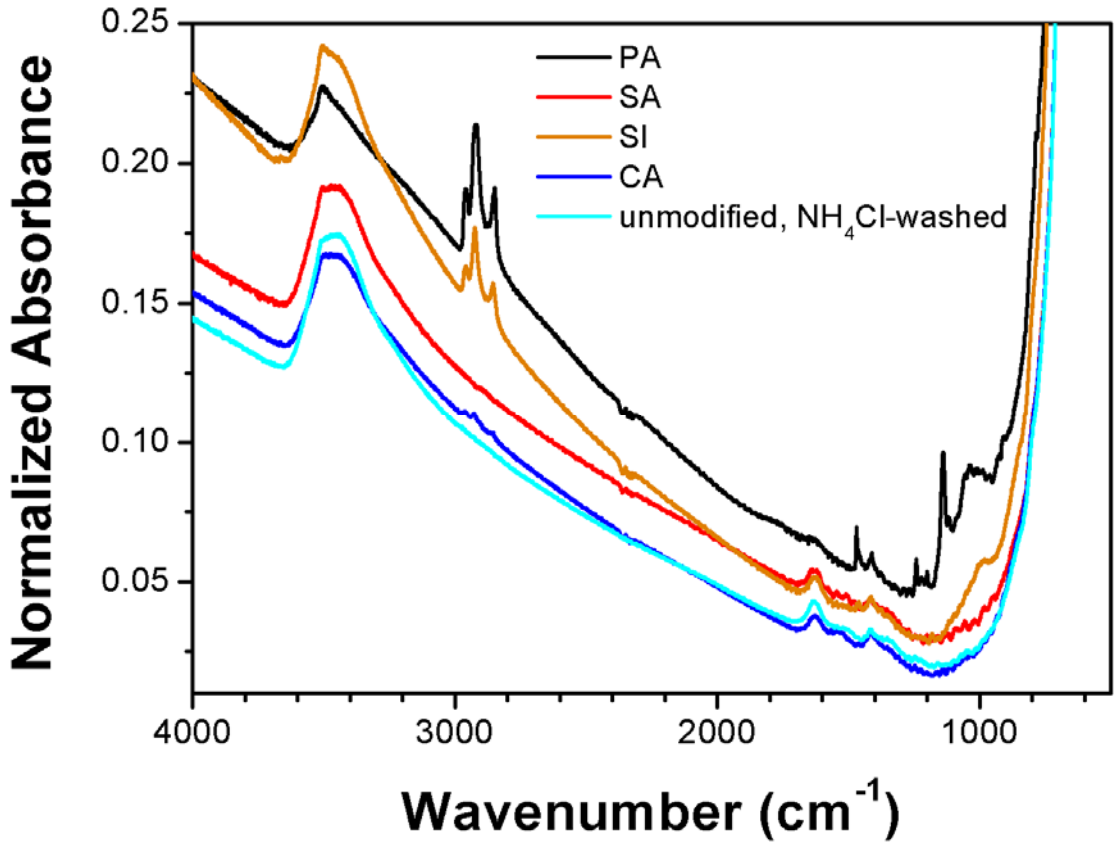

Figure 3.23 FT-IR spectra of barium carbonate-free (i.e. NH_4Cl-washed) BT nanoparticles modified with four different binding groups with n-octyl side chain. The spectra were normalized using the lattice Ti-O absorption peak centered at ~540 cm^{-1}. (see Figure 3.2 for structures and abbreviations)

Besides ammonium chloride, washing with weak acids such as formic acid and acetic acid can also remove barium carbonate. It should be noted that, in most cases,

phosphonic acid surface modifiers were acidic enough to remove the carbonaceous impurities from the barium titanate and did not require pre-treatment of barium titanate nanoparticles. Additionally, barium carbonate removal did not improve the binding of phosphonate esters.

In conclusion, phosphonic acid-based ligands can serve as good surface modifiers to barium titanate and similar perovskite type metal oxides. Phosphonic acids form robust surface layers with high coverage and excellent thermal and hydrolytic stability which can be easily formed under relatively mild conditions. Multi-dentate binding of phosphonic acid on barium titanate provides effective surface passivation of the surfaces. This straightforward surface modification chemistry can be easily adapted to a wide range of materials systems by a suitable choice of ligand functionality.

CHAPTER 4

PROCESSING, FABRICATION, AND CHARACTERIZATION OF NANOCOMPOSITE THIN FILM CAPACITORS USING SURFACE-MODIFIED BARIUM TITANATE NANOPARTICLES

4.1 Introduction

Materials with high dielectric permittivity are important in electronic components such as capacitors, gate dielectrics, memories, and power storage devices.(Rao and Wong 2004; Lee, Hur et al. 2005; Schroeder, Majewski et al. 2005; Slenes and Bragg 2005) Conventional high permittivity materials such as barium titanate ($BaTiO_3$, BT) can be processed into thin films by chemical solution deposition yielding a relative permittivity (ε_r) of about 2500 and relatively low dielectric loss but require high temperature sintering, which is not compatible with many substrate materials.(Ihlefeld, Laughlin et al. 2005) Polymer-based dielectrics, such as bi-axially oriented polypropylene, have good processability with high dielectric strengths (~640 V/μm) suitable for high-energy-density capacitors, but the storage capacity (~1 to 1.2 J/cm^3) is limited by the low permittivity (~2.2) of these materials.(Rabuffi and Picci 2002) Various approaches to high ε_r materials based on nanocomposites containing metal particles or other conductive materials have been pursued. Such nanocomposites have afforded huge ε_r values but the resulting materials are limited by the high temperature processing required, high dielectric loss, or low dielectric strength.(Pecharroman, Esteban-Betegon et al. 2001; Dang, Lin et al. 2003; Li, Huang et al. 2004; Qi, Lee et al. 2005)

Polymer/ceramic nanocomposites in which high permittivity metal oxide nanoparticles such as BT(Ramesh, Shutzberg et al. 2003; Gilbert, Schuman et al. 2005) and lead magnesium niobate–lead titanate (PMN-PT)(Bai, Cheng et al. 2000; Ogitani,

Bidstrup-Allen et al. 2000; Rao and Wong 2004) are incorporated into a polymer host have also been investigated as an approach to provide easily processable high performance dielectric materials. Typically, the processing methods used in these recent reports stem from the conventional simple solution processing of large (typically a few μm or larger) ceramic powders where the ceramic particles are mixed with a host material (or binder) with a dispersing agent. However, this conventional method, when applied to nanocomposites where the interfacial area of the filler is of significant importance, generally results in poor film quality and inhomogeneities which are mainly due to the agglomeration of the nanoparticles.(Gilbert, Schuman et al. 2005) Addition of surfactants or dispersants, such as phosphate esters and oligomers thereof, can improve the dispersion of BT nanoparticles in host polymers and consequently the overall nanocomposite film quality.(Mikeska and Cannon 1988; Ogitani, Bidstrup-Allen et al. 2000; Rao and Wong 2004) However, in such systems, there are still many direct particle-particle contacts in the nanocomposite system and the residual free surfactant can lead to high leakage current and dielectric loss.(Cho and Paik 2001) This is mainly due to the changes in local concentration of P^{5+} at the grain boundaries which is responsible for the increase in the grain boundary conductivity.(Caballero, Fernandez et al. 1997) Thus, approaches to bind surface modifiers to BT nanoparticles via robust chemical bonds are highly desirable since the organic surface capping layer can effectively prevent the nanoparticle agglomeration, improve the dispersion of nanoparticles in polymer host, and eliminate direct nanoparticle-nanoparticle contact. The concept of surface modification of BT nanoparticles for polymer/ceramic dielectric nanocomposites has been first reported by Ramesh et al.(Ramesh, Shutzberg et al. 2003) They used trialkoxysilane surface modifiers with different terminal groups for the dispersion of BT nanoparticles in epoxy polymer hosts resulting in nanocomposites with reasonably high permittivity, up to 45. Following this result, there have been many similar studies reported using silane coupling agents on Al/Al_2O_3 particles(Xu and Wong 2005) and

silver/silver oxide nanoparticles(Lu and Wong 2007), for dielectric ceramic/polymer nanocomposites. However, the efficiency of surface modification using silane modifiers on these metal oxide surfaces is dubious as discussed earlier in this thesis. In addition, the dielectric breakdown strength of the nanocomposite capacitors has been rarely reported which is an important property for the nanocomposites to be used in energy storage applications. In this chapter, the processing, fabrication, and characterization of nanocomposite-based capacitors using functional phosphonic acid-modified BT nanoparticles are described.

4.2 Initial Studies and Materials Consideration

Having demonstrated the effective binding of n-octyl phosphonic acid on BT, phosphonic acids bearing specific functionalities in order to control interfacial interactions between BT particles and dielectric host materials were investigated. (Figure 4.1) Properly designed surface modifiers are expected to facilitate the formation of homogenously dispersed, high ε_r nanocomposites.

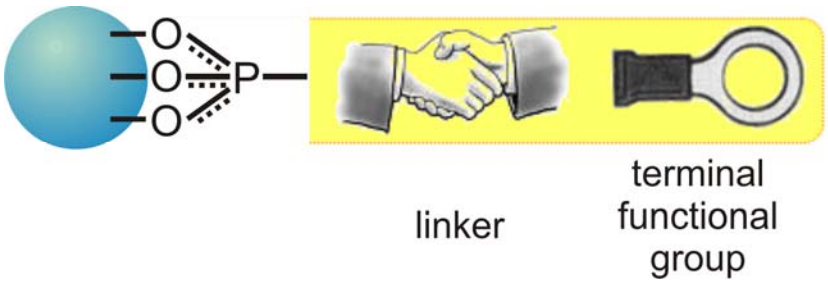

Figure 4.1 The structure of a phosphonic acid ligand.

Initially, n-OPA-modified BT (OPA-BT) was dispersed in poly(styrene-*co*-acrylonitrile) (PSAN) dissolved in chloroform by ultrasonic treatment. The spin coated nanocomposite thin films on aluminum-coated glass slide were soft baked at 50°C in an oven overnight followed by drying at 100°C in a vacuum oven for another overnight

period. The films exhibited good quality only for the composites with volume fractions of OPA-BT up to 15 %. Some visible macroscopic pinholes were observed due to incomplete wetting but no micro-sized pinholes were observed under optical microscope. Scanning electron microscopy (SEM) (Figure 4.2) of the films showed well dispersed nanoparticles over large area under low magnification, but the some aggregates were observed at high magnification.

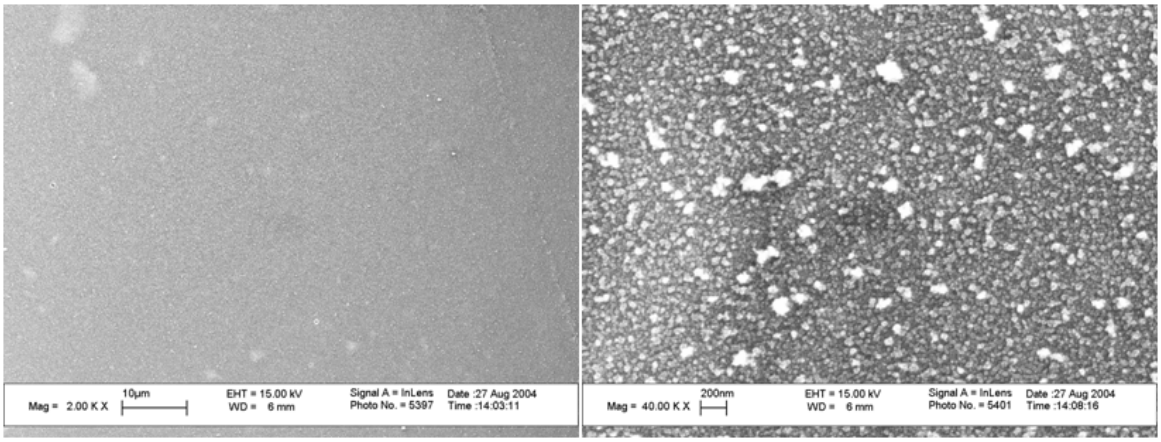

Figure 4.2 SEM images of 15 % volume OPA-BT in PSAN nanocomposite thin film prepared by spin coating the dispersion on aluminum-coated glass slide.

In contrast, the 52 % volume nanocomposite dispersion showed obvious sedimentation within 5 minutes due to poor dispersability, and the quality of nanocomposite thin films from this dispersion was not as good as those from low volume fraction nanocomposite dispersions. A series of circular top electrodes (area = 2.4×10^{-1} cm^2 to 3.1×10^{-3} cm^2) was deposited on the nanocomposite films. The dielectric characterization results of the capacitors are summarized in Table 4.1.

Table 4.1 Properties of n-octylphosphonic acid-$BaTiO_3$/PSAN capacitors.

Sample Name	$BaTiO_3$ loading (% vol.)	Film thickness (μm)	ε_r (1.0 kHz)	tanδ	Leakage Current (at 100 VDC)	Breakdown field (V/μm)
PK-117-06	0.36	0.74	3.21	< 0.1	< 0.1 nA	240
PK-117-10	15	2.20	4.78	< 0.1	< 0.1 nA	> 275
PK-119-A	52	0.69	10.48	< 0.1	N/A	N/A

In an attempt to optimize the structure of phosphonic acid ligand, some commercially available and custom synthesized phosphonic acid ligands were used to modify the surface of BT nanoparticles. Figure 4.3 shows the FT-IR spectra of the modified BT nanoparticles. (See chapter 2 for the details of the synthesis of ligands and surface modification reaction) The results indicate that the attachment of the phosphonic acids to the BT nanoparticles was successful in all ligands. This shows the possibility of modifying BT nanoparticles with phosphonic acid ligands with various functionalities.

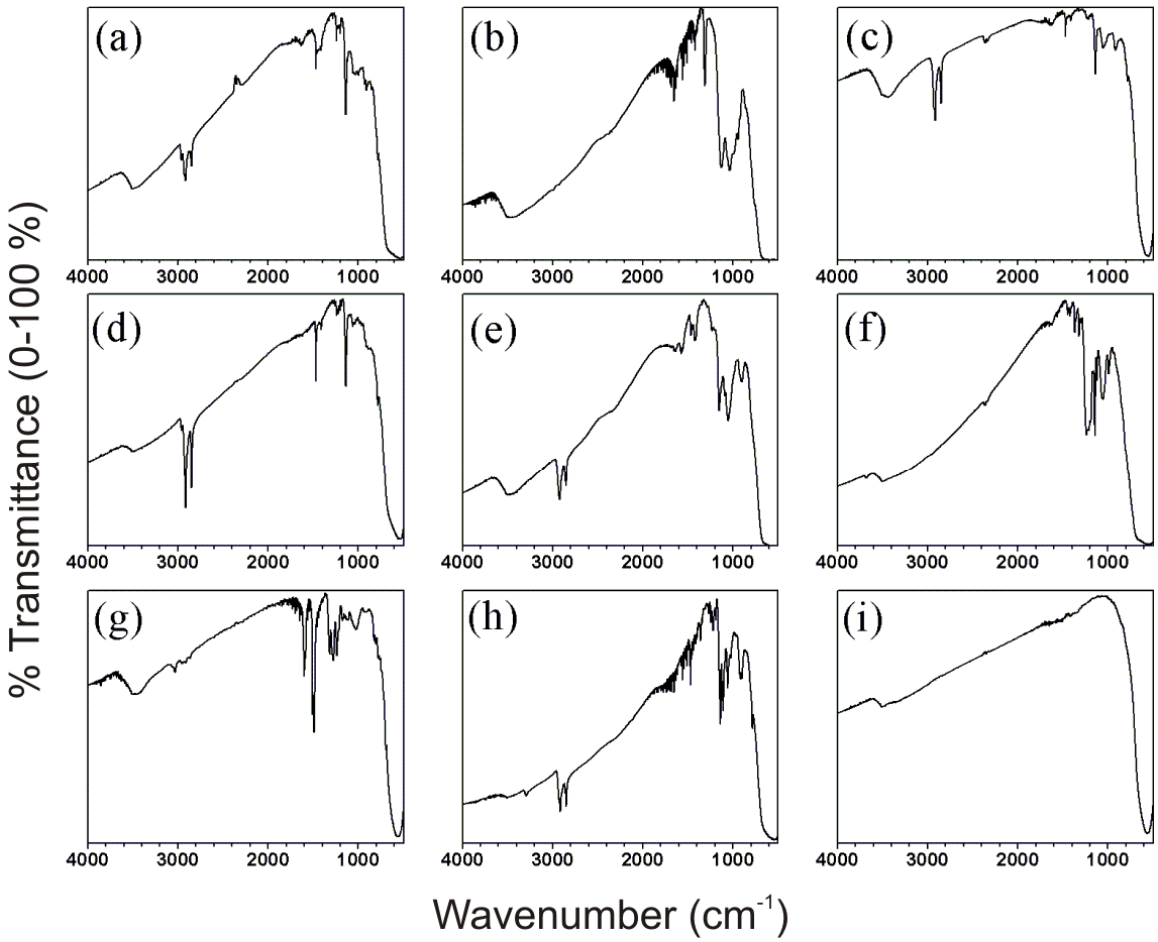

Figure 4.3 FT-IR spectra of BT nanoparticles modified with functional phosphonic acid ligands. OPA, (b) MPA, (c) HUPA, (d) ODPA, (e) DPPA, (f) FOPA, (g) TPDPA, (h) TKYNPA, and (i) unmodified $BaCO_3$ free-$BaTiO_3$. See table 2.1 for abbreviations of each phosphonic acid.

1 mg/mL dispersions of unmodified BT, n-octadecyl phosphonic acid-modified BT (ODPA-BT), and 11-phosphonoundecyl phosphonic acid-modified BT (DPPA-BT) nanoparticles in methanol were prepared and the stability of the dispersions was compared. The BT nanoparticles modified with a non-polar ligand (ODPA-BT) completely sedimented after one day. In contrast, the dispersion of DPPA-BT was still stable with no sign of sedimentation, while the dispersion of unmodified BT showed some sedimentation within a 1 day period. These results confirm that the coating of BT

nanoparticles by phosphonic acid ligands can greatly alter the surface properties of nanoparticles such that the solubility and compatibility can be easily manipulated depending on the nature of the host materials.

4.3 Choice of Host Polymer and Design and Synthesis of Phosphonic Acid Ligands

As described in section 1.2, the effective permittivity of nanocomposites can be increased by using a large volume fraction of a high permittivity filler and using a high permittivity host material. (see section 1.2). For this reason, two host polymers, with distinct chemical and physical properties, poly(bisphenol-A carbonate) (PC, a low permittivity host) and poly(vinylidene fluoride-*co*-hexafluoropropylene) (P(VDF-HFP), a high permittivity host) were selected to investigate the effects of the surface modification of the filler and the host permittivity on the nanocomposite permittivity and dielectric properties (Figure 4.4).

poly(bisphenol-A carbonate)
PC

poly(vinylidene fluoride-*co*-hexafluoro propylene)
P(VDF-HFP)

Figure 4.4 The structure of a low permittivity host (PC, $\varepsilon_r \approx 2.8$) and a high permittivity host (P(VDF-HFP), $\varepsilon_r \approx 11.9$). The permittivity values were measured from spin-coated films of pure polymer at 1 kHz.

PC is a hydrophilic resin and has been extensively used for high-energy density capacitors due to its high dielectric strength and low dissipation factor (<0.15 % at 1 kHz), while P(VDF-HFP) is a chemically inert and highly processable co-polymer with high permittivity due to the ferroelectric domains and is expected to have high dielectric strength comparable to that of poly(vinylidene fluoride) (~590 V/μm).(Rabuffi and Picci

2002) The details of ferroelectricity of polymers and co-polymers containing vinylidene fluoride units will be further described in chapter 6.

The structures of the phosphonic acids used for modification of BT nanoparticles and their compatibilization with the PC and P(VDF-HFP) host materials are shown in Figure 4.5. {2-[2-(2-methoxyethoxy)ethoxy]ethyl}phosphonic acid (PEGPA) has a tri(ethylene glycol) chain designed to compatibilize BT nanoparticles with polar, hydrophilic resins and solvents. Pentafluorobenzyl phosphonic acid (PFBPA) features a fluorinated aryl group to afford good compatibility with fluoro-elastomers and host polymers with aromatic groups. (Coates, Dunn et al. 1997) PEGPA and PFBPA were synthesized by Arbuzov reactions of their respective bromides followed by hydrolysis (these ligands were synthesized and characterized by Dr. Simon C. Jones and Mr. Peter J. Hotchkiss in Marder group. See chapter 2 for the synthetic schemes and characterization results).

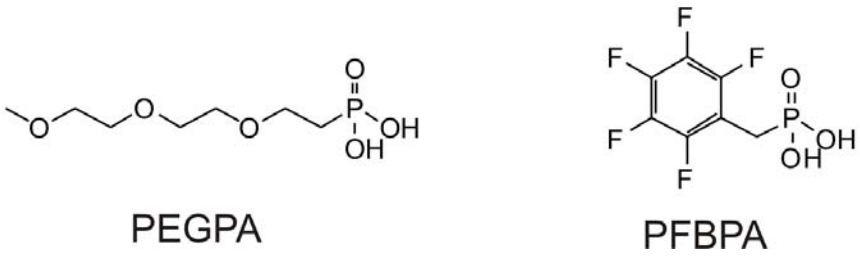

Figure 4.5 Molecular structures of phosphonic acid ligands used to modify BT for dispersion in PC (PEGPA) and P(VDF-HFP) (PFBPA) host materials.

The dispersing solvents were selected among known solvents for each host polymer and by testing the stability of the dispersions of surface modified BT nanoparticles with each ligand. The surface modification of BT nanoparticles with each ligand was performed using the schemes described in section 2.2. The particle size of the BT nanoparticles used in this study is 30 – 50 nm in diameter. Without surface modification, the BT nanoparticles formed large aggregates when dispersed in organic

solvents. The chemical functionalization of BT effectively decreased the degree of nanoparticle aggregation in suitable organic solvents, as evidenced by a 3 to 4 fold decrease in the average aggregate size measured by dynamic light scattering summarized in Table 4.2.

Table 4.2 Average particle size from dynamic light scattering measurements for unmodified BT and surface-modified BT nanoparticles dispersed in organic solvents.

Dispersion (0.01 mg/mL)	Average diameter (nm)*	Average PDI
unmodified BT in pyridine	580 ± 10	0.32 ± 0.07
PEGPA-BT in pyridine	143 ± 1	0.11 ± 0.02
unmodified BT in DMF	403 ± 4	0.28 ± 0.02
PFBPA-BT in DMF	125 ± 1	0.15 ± 0.05

*The errors reported in the table correspond to twice the standard deviation of the measurement. Refractive index of BT = 2.3, measurement temperature = 20°C. All measurement showed a mono-disperse distribution of particle sizes.

The use of PEGPA and PFBPA modified BT particles (PEGPA-BT and PFBPA-BT, respectively) also led to considerable improvement of the stability of their suspensions in PC/pyridine and P(VDF-HFP)/*N*,*N*-dimethylformamide solutions, whereas unmodified BT showed relatively rapid sedimentation, as shown in the digital photograph images of the dispersions (Figure 4.6).

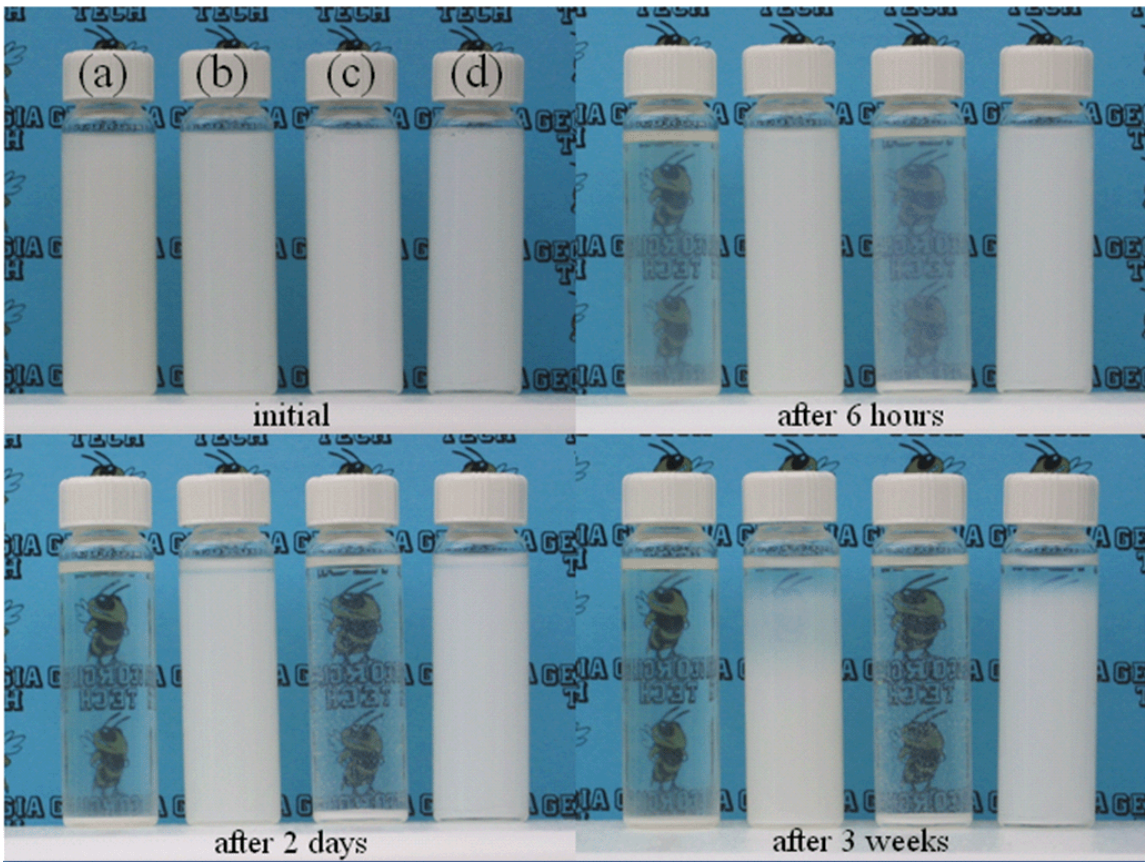

Figure 4.6 Digital photographs of suspensions of surface modified and unmodified BT nanoparticles (20 mg BT in 200 mg/10 mL polymer solutions) taken at various times following preparation. (a) BT/PC/pyridine, (b) PEGPA-BT/PC/pyridine, (c) BT/P(VDF-HFP)/DMF, and (d) PFBPA-BT/P(VDF-HFP)/DMF. The dispersions were prepared by The stability of the dispersions of surface-modified BT nanoparticles in each host polymer solution is evidenced by slow sedimentation.

4.4 Substrate Pre-treatment

Spin coating of nanocomposite dispersions on Al/glass substrates does not always yield good quality films even from very stable and well-dispersed nanocomposite dispersions. It was empirically found that this is mainly due to the poor wetting of the aluminum electrode surface by the dispersions. Therefore, achieving a good wettability of the electrode by the dispersions, which typically are prepared in polar solvents such as

NMP, DMF, pyridine, and chloroform, is critical to ensure high quality nanocomposite films. To obtain a clean and hydrophilic electrode surface, the aluminum electrodes were initially washed and primed in ethanol and water mixture. However, the results obtained using this method were not very reproducible and the wetting of hydrophilic dispersions was still not satisfactory. This was attributed to the fact that the aluminum substrate as prepared (or as received) exhibited very hydrophobic surface due to the presence of adsorbed organic residues. These organic residues could be efficiently removed by treating the substrate by a cold air plasma treatment (room air through a filter at 3 SCFH (standard cubic feet per hour), 750 W power). The cold air plasma treatment dramatically changed the water contact angle of the aluminum substrate from 101.7° to ~0°, as shown in Figure 4.7. The substrates immediately after the cold air plasma-treatment were found to be extremely hydrophilic but the water contact angle gradually increased with time.

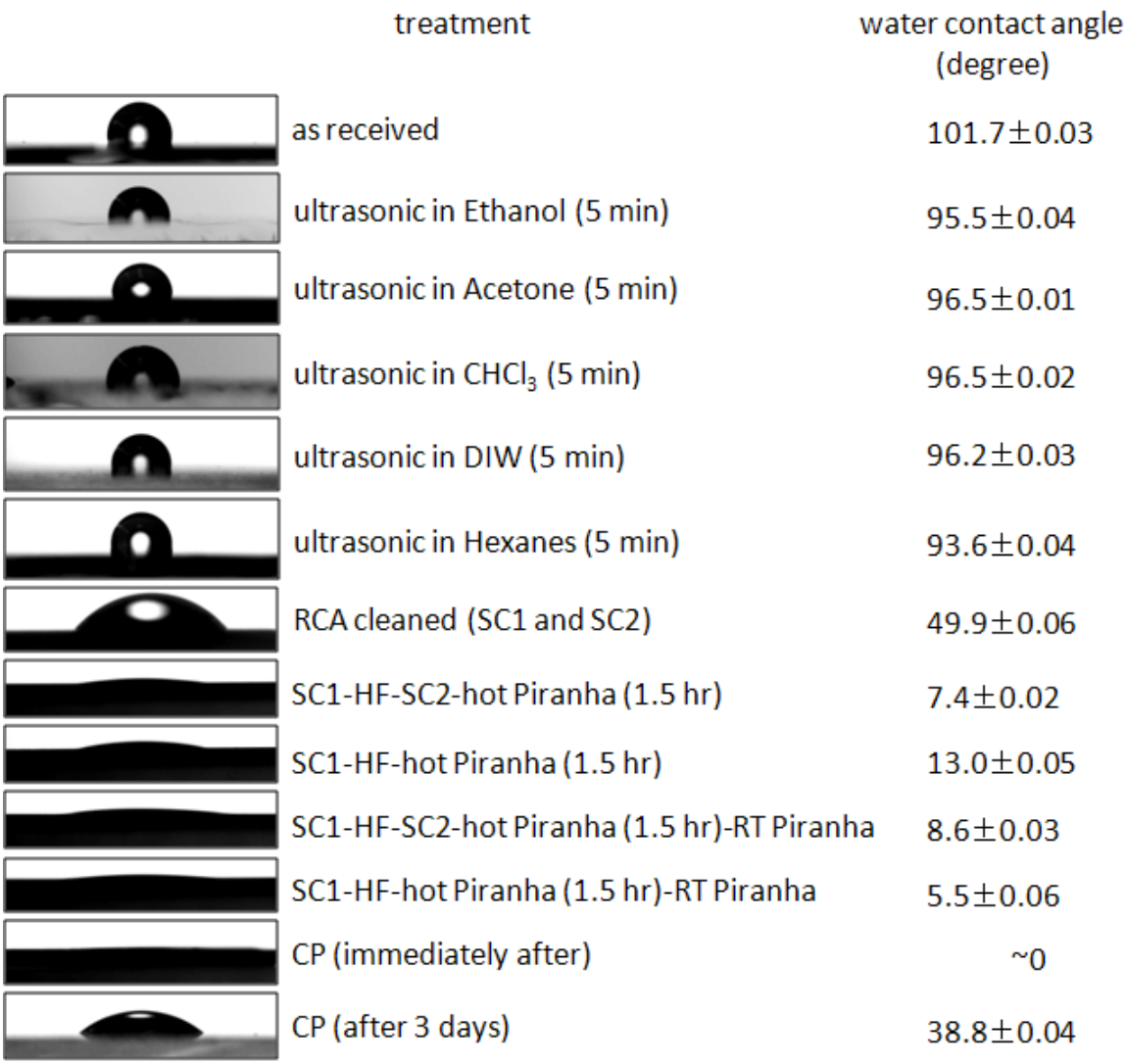

Figure 4.7 Static sessile water drop contact angle measurements of aluminum electrode surfaces treated with different ways. CP: cold plasma treatment (750 W, 3 SCCF air), SC1: 1st standard cleaning (SC) of RCA cleaning protocol (1:1:5 NH_4Cl:H_2O_2:H_2O, 75-80°C), SC2: 2nd standard cleaning of RCA cleaning protocol (1:1:6 HCl:H_2O_2:H_2O, 75-80°C), HF: immersion in 1:50 hydrogen fluoride:H_2O mixture at room temperature, Piranha: 3:1 H_2SO_4 and 30 % H_2O_2 mixture, hot Piranha: Piranha mixture heated to bubbling.

To probe the actual surface conditions of aluminum electrodes, after different treatments, three representative samples were prepared and analyzed by X-ray photoelectron spectroscopy (XPS). The carbon content on the aluminum electrode surface was slightly reduced by solvent immersion and was significantly reduced by treating with cold air plasma for just 1 minute, as shown in Figure 4.8 and Table 4.3.

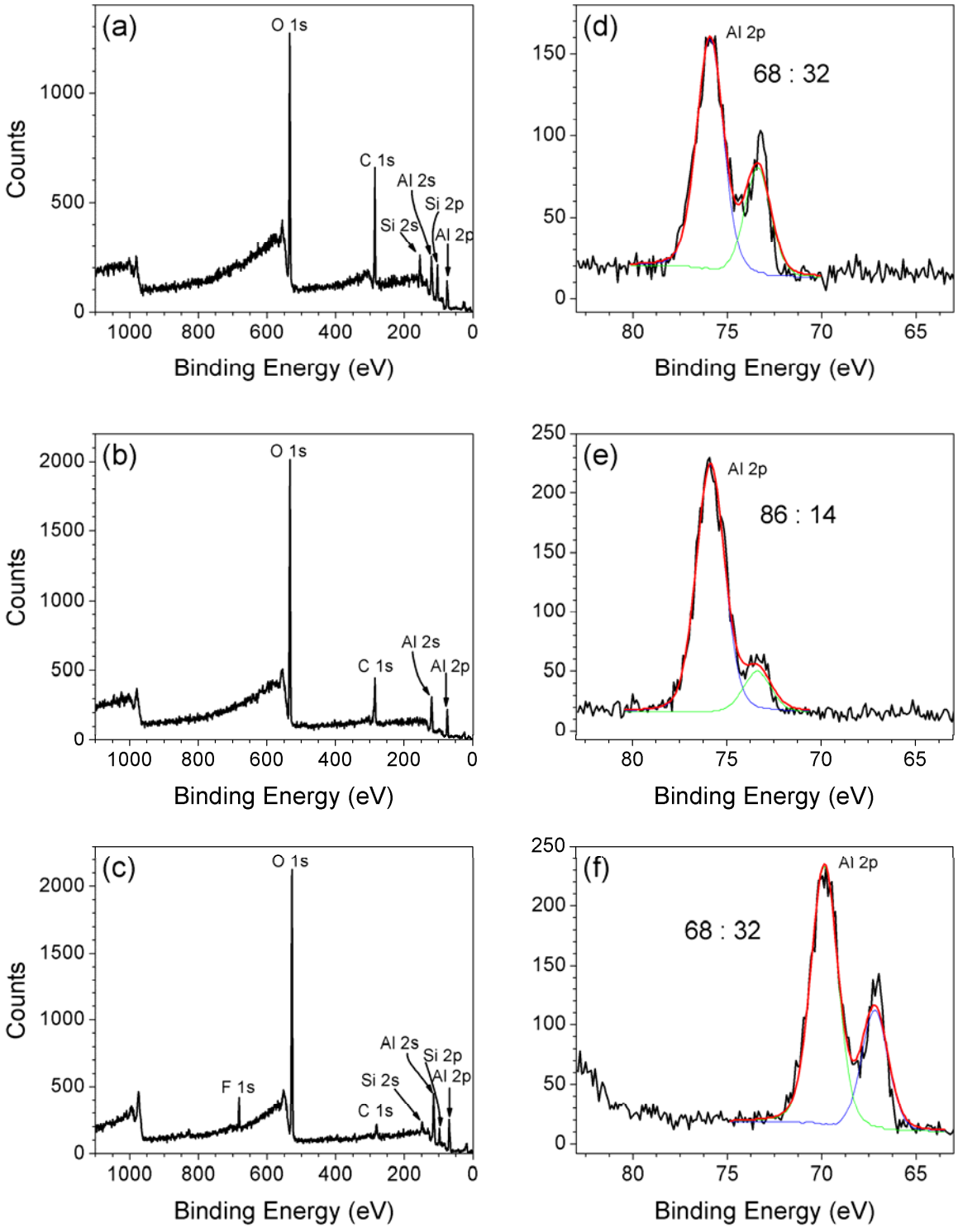
(a)
O 1s
C 1s
Al 2s
Si 2p
Si 2s
Al 2p
Counts
Binding Energy (eV)
(b)
O 1s
Al 2s
C 1s
Al 2p
Counts
Binding Energy (eV)
(c)
O 1s
F 1s
Al 2s
Si 2p
Si 2s
Al 2p
C 1s
Counts
Binding Energy (eV)
(d)
Al 2p
68 : 32
Binding Energy (eV)
(e)
Al 2p
86 : 14
Binding Energy (eV)
(f)
Al 2p
68 : 32
Binding Energy (eV)

Figure 4.8 XPS survey scans (a - c) and Al 2p narrow scans (d - f) of aluminum electrode surfaces: As received (a, d), after solvent immersion in 3:1 ethanol:water mixture for 48 hours (b, e), and after cold plasma treatment (750 W, 3 SCFH room air for 60 seconds) (c, f). The numbers in Al 2p narrow scan represent the relative ratio of oxidized aluminum to metallic aluminum on the surface. The F 1s peak from cold plasma treated sample is a contamination from the Viton O-ring used to seal the plasma treatment chamber. The large shift of the peaks to low binding energy in data (f) is due to the over-compensation of the charge using a low energy electron flood gun.

Table 4.3 The relative elemental compositions of the aluminum electrode surfaces. The compositions were calculated using the data (a), (b), and (c) in Figure 4.8.

Sample	As Received	Solvent Immersed	Cold Plasma Treated
Element Lines	Atomic %	Atomic %	Atomic %
O 1s	35.4	51.8	57.7
C 1s	33.9	25.2	9.4
Al 2p	17.9	23.0	18.3
Si 2p	12.8	not detected	10.6
F 1s	not detected	not detected	4.0

The aluminum electrode has a native oxide layer on the surface. The Al 2p peak of as received aluminum surface can be deconvoluted into two peaks, one centered at ~73 eV (metallic aluminum) and the other at ~75.5 eV (aluminum oxide or aluminum hydroxide) with a ratio of 68:32 oxidized/metallic aluminum. The solvent immersion in ethanol:water mixture induced slight oxidation of aluminum surface resulting in the increase of oxidized form of aluminum from 68 % to 86 %. In contrast, the cold air plasma treatment only selectively cleaned the surface adsorbed carbon species and did

not significantly induce the oxidation of aluminum electrode, as the ratio of oxidized/metallic aluminum remained almost unchanged from that of as received aluminum. Note that the overall binding energy of the cold plasma treated aluminum sample was shifted to low binding energy due to an over-compensation of the charging of the surface by the low energy electron flood gun.

In summary, the pre-treatment of the aluminum electrode surface using cold air plasma is a quick way to clean the surface and to make the surface hydrophilic, which is desirable for spin-coating.(Polini and Sorrentino 2003) In addition, cold air plasma treatment does not induce significant surface oxidation of aluminum electrode. This method was used for the preparation of all the spin-coated nanocomposite thin films discussed below.

4.5 Nanocomposite Processing, Thin Film Fabrication, and Characterization

The processing of nanocomposites require a good way of breaking up clumps of dried nanoparticles, of mixing nanoparticles with the polymer solution, and of homogenizing the mixture. Ultrasonic treatment of nanoparticle dispersion was initially used for this purpose, but it was empirically found that wet ball-milling was a more efficient method to achieve homogenized nanocomposite dispersions. Yttria-stabilized zirconia (YSZ) grinding media was chosen, due to the hardness of barium titanate. The Moh hardness of barium titanate is about 5 but less than 6, and the value for YSZ is greater than 9. For maximum efficiency of ball-milling, the size of the grinding media should be as small as possible and the size of the ball should be approximately 10 times larger than the grain size of the samples to be milled, such that the gaps between the balls are about the size of the nanoparticles. In addition, in wet ball-milling, the grinding rate increases with solid contents up to 35 volume % due to pulp rheology.(Perry 1997) This includes the amount of ball charged and the amount of BT nanoparticles filled in the grinding cylindrical jar. The optimum grinding rate is achieved when the volume of the

nanoparticles is equal to the ball-void volume. The nanocomposite dispersions were processed according to these general guidelines(Perry 1997). Unfortunately, the smallest size of the commercially available YSZ grinding media was 0.5 mm and this made the ball-milling time required to crack clumped nanoparticles extremely long (2 weeks). It was also empirically found that the polymer should be added after about 2 days of ball-milling of BT nanoparticles in the dispersing solvent, to minimize the required ball-milling time. If the polymer and the BT nanoparticles are added at the same time, the viscosity of the nanocomposite mixture becomes too high to effectively mill the nanoparticles. This is contrary to the common use of additives in ball-milling to reduce the viscosity of the media.(Perry 1997) Therefore, the BT nanoparticles should be milled first and the polymer should be added later, when the BT/dispersion solvent mixture becomes sufficiently thin.

The processing sequence of nanocomposites is summarized in the flow chart shown in Figure 4.9.

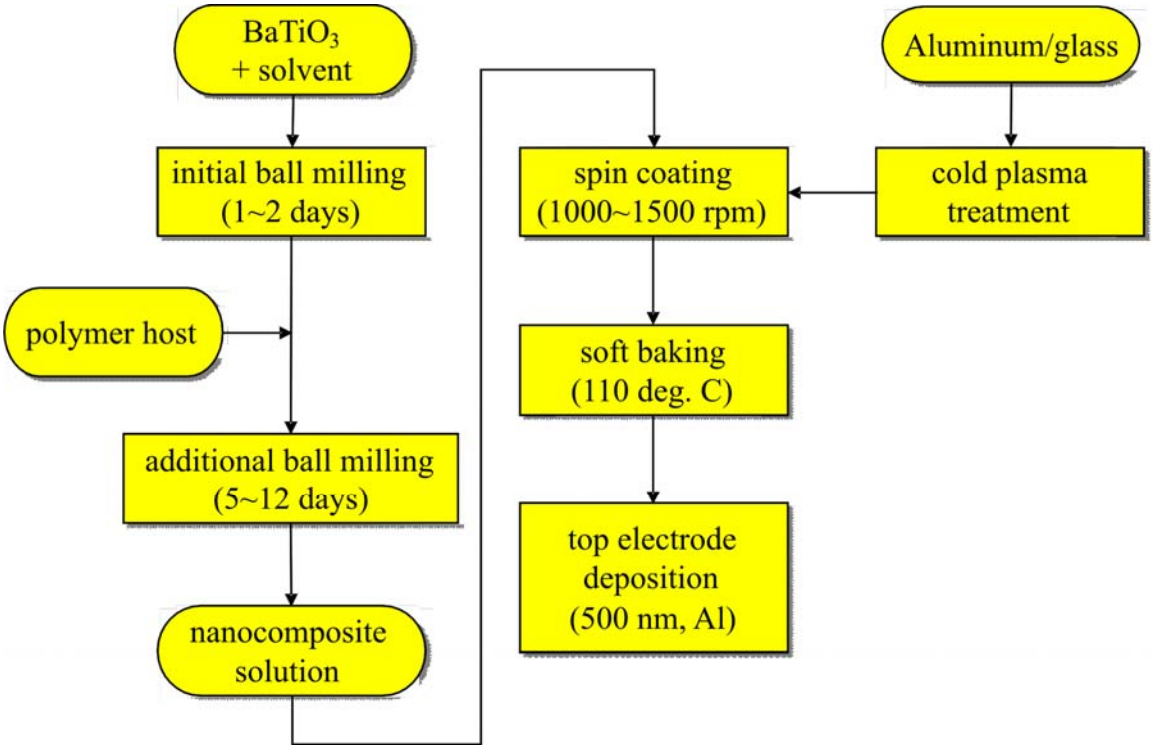

Figure 4.9 Typical processing flow chart of nanocomposites.

Thin films of nanocomposites were prepared by spin-coating the dispersion at 1,000 rpm – 1,500 rpm and had thicknesses ranging from 700 nm to 4000 nm. The films were soft baked at 110°C to evaporate the solvent, then slowly cooled to room temperature to avoid micro cracks. Then the films were hard baked at 120°C in a vacuum oven overnight to evaporate residual solvent and moisture. Figure 4.10 shows the effect of surface modification on the quality of the nanocomposite thin films. The cross-sections were prepared by freeze fracturing the films in liquid nitrogen.

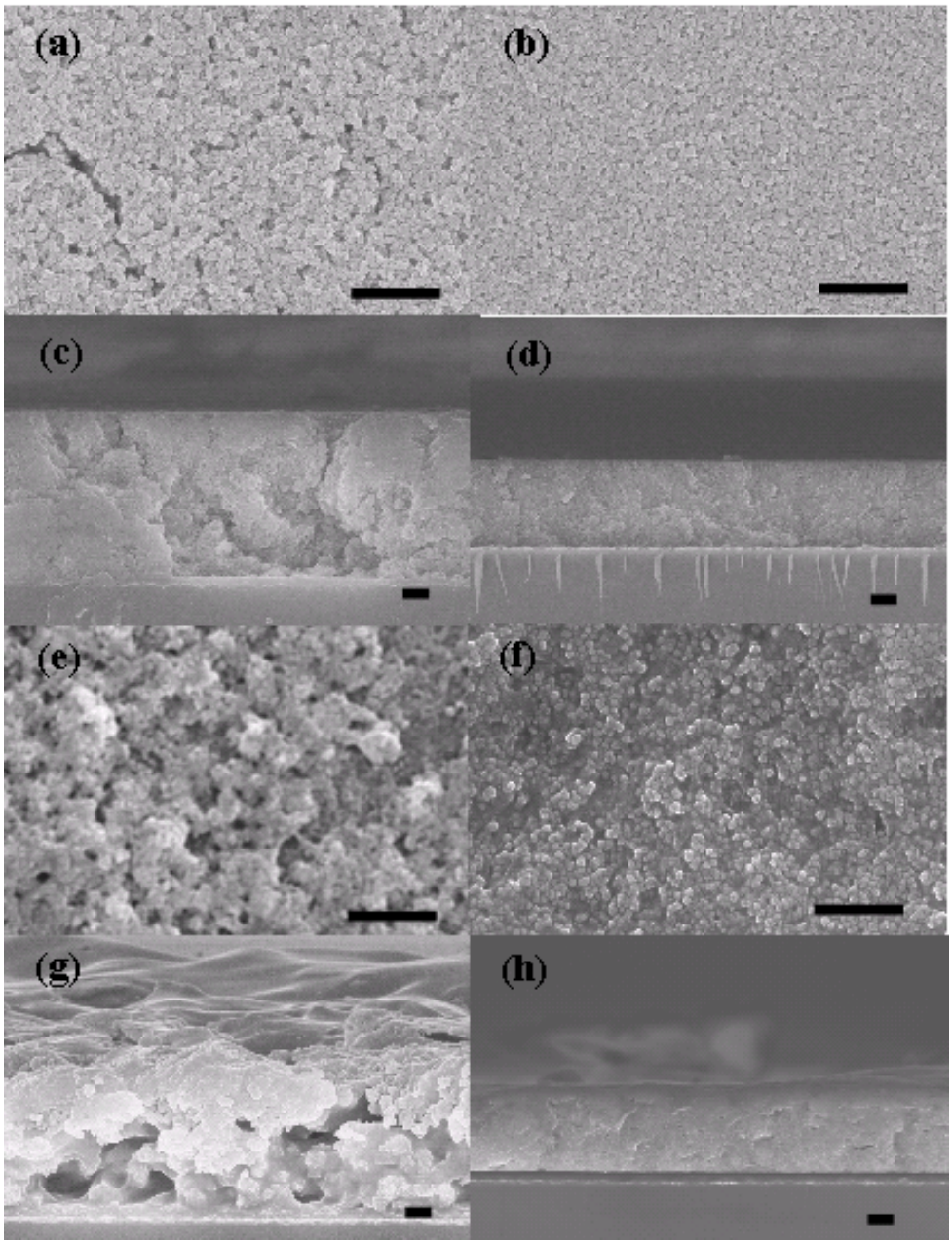

Figure 4.10 Surface (a, b, e, f) and cross-sectional (c, d, g, h) SEM images of spin-coated nanocomposite thin films. (a) and (c): BT/PC, (b) and (d): PEGPA-BT/PC, (e) and (g): BT/P(VDF-HFP), (f) and (h): PFBPA-BT/P(VDF-HFP). The volume fraction of BT nanoparticles are 50 % in all films. For unmodified BT, the nanocomposite contained 2 wt. % of BYK-w-9010 surfactant. All scale bars are 1 μm.

The nanocomposite films fabricated from unmodified BT nanoparticles with 2 wt. % of a surfactant, BYK-w-9010, prepared under similar conditions as described above exhibited large-scale aggregates, cracks and pinhole defects. In contrast, the nanocomposites with modified BT nanoparticles yielded comparatively uniform films with homogeneous nanoparticle dispersions.

4.6 Device Fabrication and Characterization

Arrays of parallel-plate capacitors were prepared by evaporative deposition of circular Al electrodes on top of the phosphonic acid-modified BT/PC and P(VDF-HFP) nanocomposites films as shown in Figure 4.11.

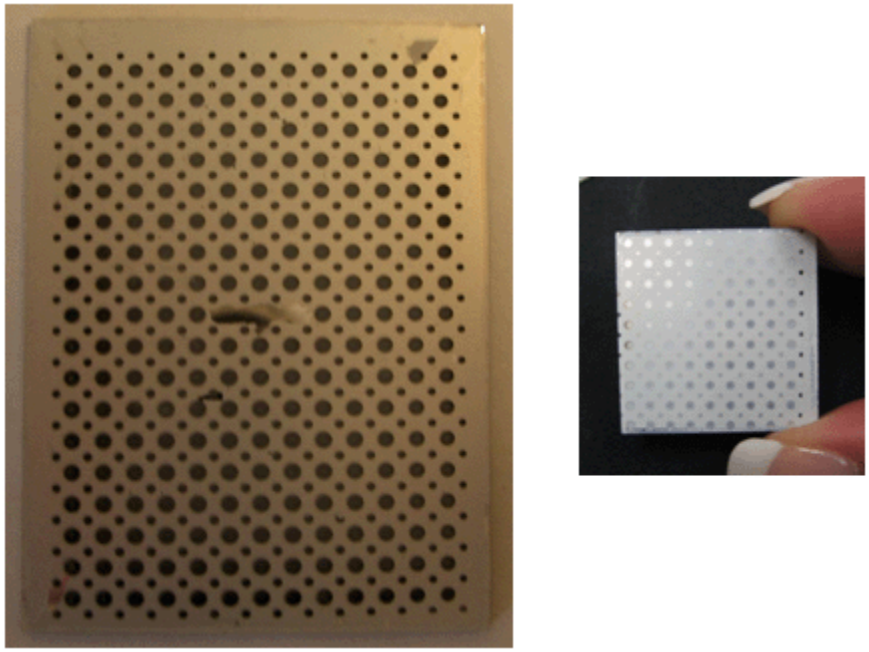

Figure 4.11 Digital photographs of capacitor arrays on 1.5 in. × 2 in. substrate (left) and on 1 in. × 1 in. (right) substrate. The diameters of large and small circular electrodes are 22 mil and 11 mil, respectively.

The dielectric characterization and spectroscopic results for the nanocomposite films are presented in Table 4.4 and Figure 4.12. Large permittivity and reasonably low loss up to frequencies of 1 MHz are observed for both types of nanocomposites. The role of the host permittivity is evident in the nearly two-fold increase of the effective permittivity observed for the nanocomposite based on P(VDF-HFP) relative to the PC host. Of particular significance is that for both composites the dielectric strength is quite large (over 200 V/μm, ca. ½ ~ ⅓ of that for the pure host polymer) as compared to results reported for other polymer-ceramic nanocomposites based on uncoated BT (76~124 V/μm), PMN-PT (80~120 V/μm), and PMN-PT/BT mixtures (17 V/μm) in epoxy hosts.(Bai, Cheng et al. 2000; Rao and Wong 2004; Gilbert, Schuman et al. 2005) These dielectric breakdown values were reproduced in an independent experiment performed by Dr. Ming-Jen Pan (MJP) at the Naval Research Lab (Washington, DC) using a separate batch of samples.

Table 4.4. Dielectric characteristics of $BaTiO_3$ nanocomposite thin films.

	50% vol. PEGPA-BT in PC[a]	50% vol. PFBPA-BT in P(VDF-HFP)[a]
Film thickness (μm)	3.89	3.84
Capacitance density (nF/cm^2)	4.6 ± 0.6	8.6 ± 0.4
Relative permittivity, ε_r (at 1 kHz)	20 ± 2	35 ± 2
Dielectric loss (at 1 MHz)	<0.01	<0.07
Leakage current density (nA/cm^2)[b]	<30	<60
Dielectric strength (V/μm)	210 ± 20	215 ± 50
Maximum energy density (J/cm^3)[c]	3.9	6.1

[a]$BaTiO_3$ nanoparticles were 30-50 nm in diameter, [b]measured at 100 V_{DC} for 0.25 mm^2 circular area, [c]Calculated energy density; average relative permittivity and dissipation factors measured at 1 MHz were used.

An important characteristic of a capacitor is the maximum energy density (U_{max}), which is given by $U_{\max} = 1/2\,\varepsilon_0 \varepsilon_r E_B^{\,2}$, where ε_0 is the permittivity of vacuum, ε_r is the permittivity of the dielectric material, and E_B is the breakdown strength. Because of their large dielectric strength and high permittivity, the modified BT nanocomposites afford large calculated energy densities of up to 6.2 J/cm^3 (for PFBPA-BT in P(VDF-HFP)), which is greater than the current state-of-the-art high-energy-density capacitors based on wound metallized BOPP films (3.5 ~ 4 J/cm^3).(Slenes and Bragg 2005) The actual stored energy in one of the 50 vol. % PFBPA-BT:P(VDF-HFP) device was measured using a charge-discharge circuit described in section 2.7.5 at the Naval Research Laboratory. The energy storage under an applied field of 100 V/μm was measured to be 1.62 J/cm^3 as shown in Figure 4.13. If a linear response is assumed, the projected energy storage density at the breakdown field (210 V/μm) is close to 7 J/cm^3. These modified BT nanocomposites also exhibit relatively low dielectric loss and leakage current, both of which are important for energy storage or peak load leveling applications.(Calame 2006) The nanocomposites showed dielectric loss at most ~7 % at 1 MHz, which is much smaller than those observed in the nanocomposites with conductive fillers (18~50 %).(Dang, Shen et al. 2002; Dang, Lin et al. 2003)

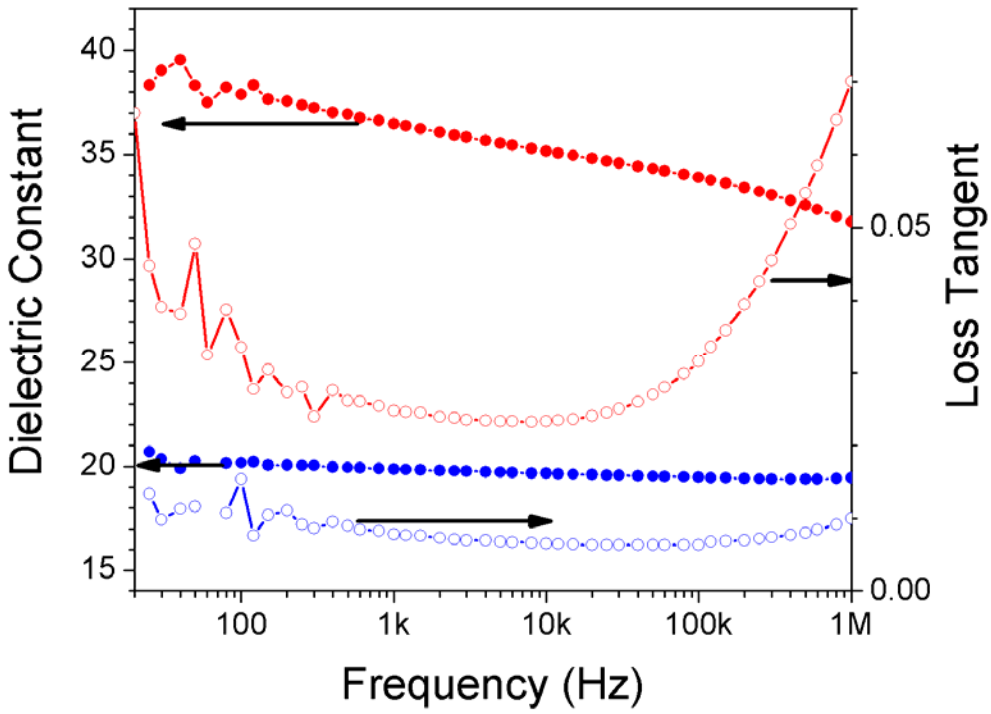

Figure 4.12 Frequency-dependent dielectric response of capacitor devices fabricated from PEGPA-BT/PC (blue circles) and PFBPA-BT/P(VDF-HFP) (red circles).

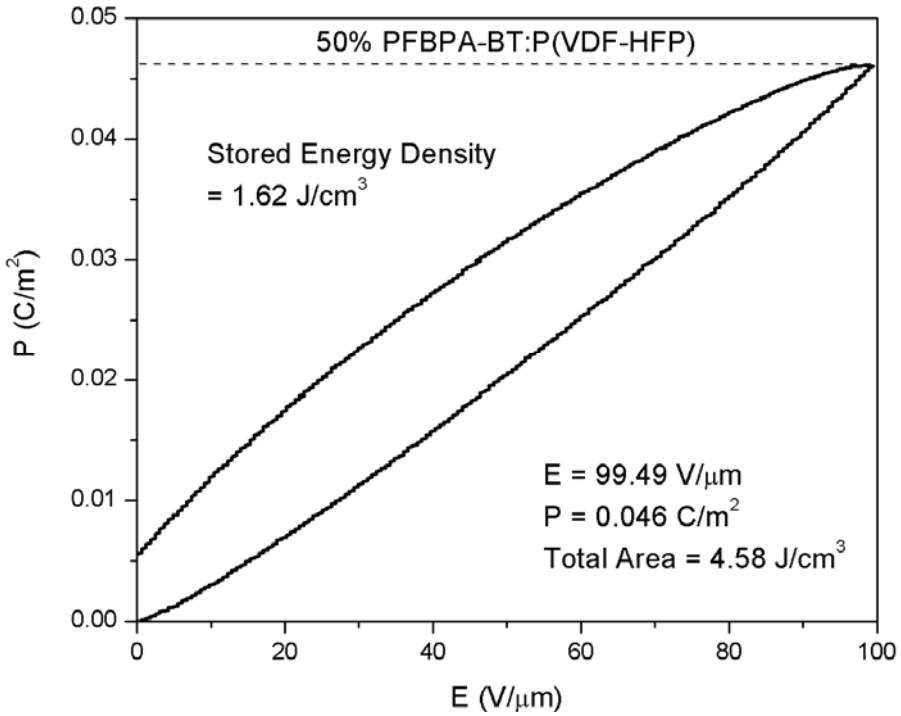

Figure 4.13 **P-E** measurement result from a 50 vol. % PFBPA-BT:P(VDF-HFP) device.

Larger effective permittivity values are expected for nanocomposites containing higher permittivity nanoparticles. The BT nanoparticles used in the experiments described above were relatively small (30~50 nm) with the relative permittivity estimated(Jayasundere and Smith 1993) to be only ~100 (at 1 kHz). The size effect on the Curie temperature and relative permittivity of BT nanoparticles indicates an increase in relative permittivity with particle size.(Yashima, Hoshina et al. 2005) (Arit, Hennings et al. 1985) Accordingly, larger $BaTiO_3$ nanoparticles (BT-150, #HPB-1250 TPL Inc.) with diameter of 150 nm were also used to make nanocomposites in P(VDF-HFP). These resulted in further increase in the measured nanocomposite permittivity to 44.6 (at 1kHz), which is comparable to the previously reported value for BT nanocomposites (ε_r = 45).(Ramesh, Shutzberg et al. 2003)

The high breakdown strengths and low leakage currents of these nanocomposite materials can be attributed directly to the use of phosphonic acid surface modifiers, which

both provide effective surface passivation of BT nanoparticles and significantly improve their dispersability. These factors have two major influences: firstly, the phosphonic acids serve to reduce nanoparticle aggregate formation and, thus, percolative pathways available to the metal oxide particles, both of which offer conduits for leakage current and weak links for dielectric breakdown.(Calame 2006) This is particularly important for nanocomposites that feature a high volume fraction of metal oxide nanoparticles. Secondly, the phosphonic acids act as effective passivation layers, reducing the concentration of ionizable hydroxyl groups on the nanoparticle surface, thereby minimizing the concentration and mobility of charge carriers normally associated with the surface. This also reduces leakage currents and sources of runaway conduction that can lead to dielectric breakdown. Devices based on unmodified BT nanoparticles with a surfactant in P(VDF-HFP) showed decreased breakdown strength (130 ± 40 V/μm) reflecting the effect of ionizable species present.

Figure 4.14 shows the temperature-dependent dielectric response of P(VDF-HFP), 50 % vol. PFBPA-BT filled P(VDF-HFP), and 50 % vol. PFBPA-BT150 filled P(VDF-HFP) nanocomposites. The P(VDF-HFP) host showed strong temperature-dependent dielectric responses at low frequency range (< 1 kHz) but showed relatively stable responses from 10 kHz to 1 MHz. The huge anomaly at near DC frequencies is closely related to the microscopic polarization mechanisms in P(VDF-HFP) at these frequencies. The low frequency anomaly was observed for both nanocomposites filled with small BT nanoparticles and large BT nanoparticles. However, only the nanocomposites filled with large BT nanoparticles showed additional temperature-dependent anomaly at high frequencies. This means that the dielectric response of small BT nanoparticles has little or no dependence on the temperature within the measurement range (25 – 150°C). This is because the small BT nanoparticles were determined to have only cubic crystalline phase by XRD and thus have no phase transition over the temperature range tested, while the large BT nanoparticles were determined to have some portion of tetragonal phase that

undergo phase transition across the Curie temperature of BT nanoparticles (~120°C).(Yashima, Hoshina et al. 2005)

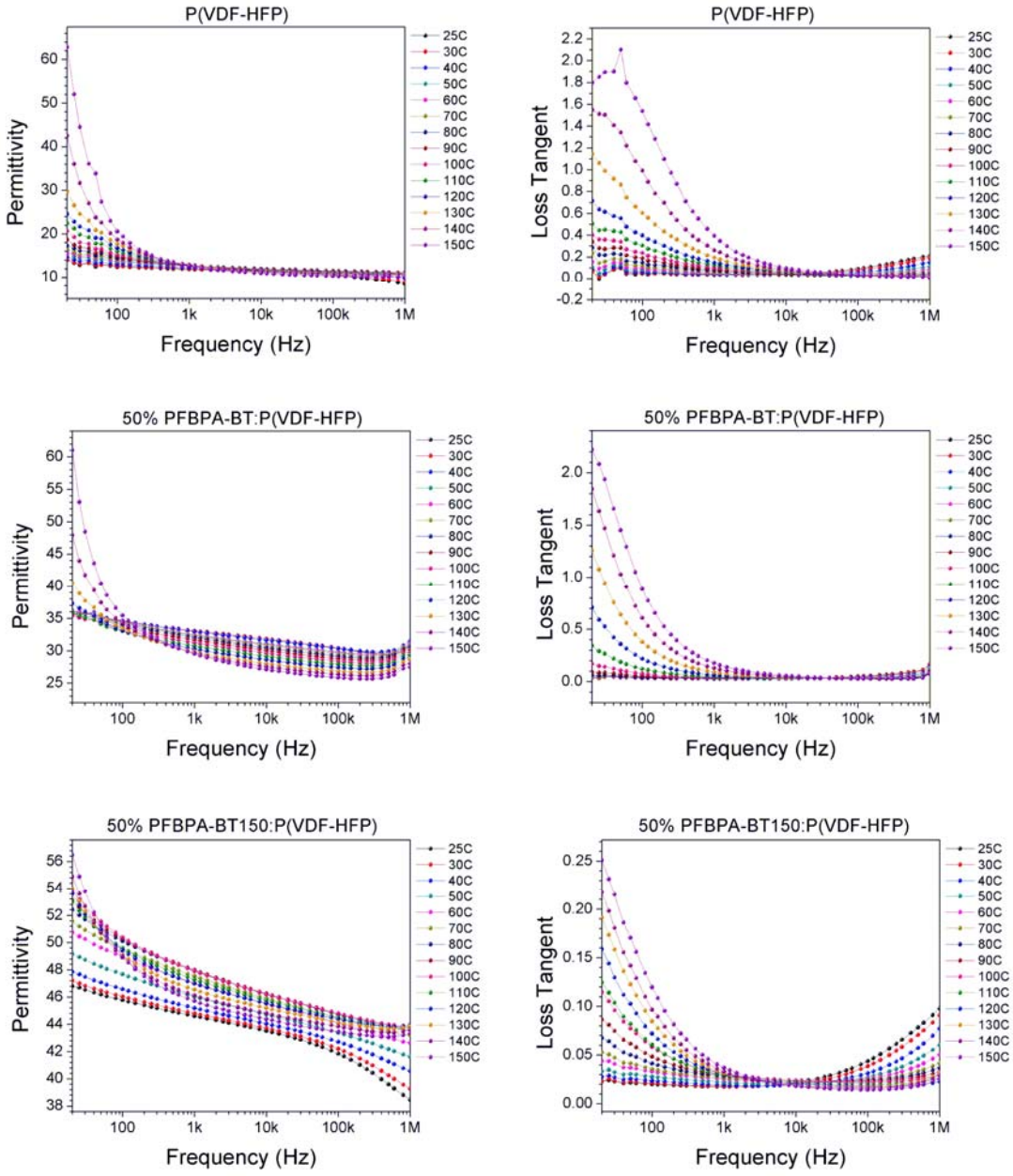

Figure 4.14 Temperature-dependent dielectric responses of P(VDF-HFP) host and its 50% vol. nanocomposites filled with small BT (PFBPA-BT) and large BT (PFBPA-BT150) nanoparticles modified with PFBPA.

In conclusion, high quality and high volume fraction dielectric nanocomposites can be formed from phosphonic acid-modified BT dispersed in polymers by simple solution processing techniques. These nanocomposites exhibit a remarkable combination of high permittivity and large dielectric strength, yielding a high energy storage capacity. The composite energy density (or other dielectric property, as required) can be further improved by optimization of the dielectric nanoparticles and the host material system, using the same straightforward surface modification methodology.

CHAPTER 5

THE ROLE OF NANOPARTICLE VOLUME FRACTION IN NANOCOMPOSITES

This chapter describes the dependence of dielectric properties on nanoparticle volume fraction in nanocomposites of surface-modified $BaTiO_3$ and a ferroelectric polymer. The experimental results are compared with an analytical model based on the effective medium theory (EMT) and a simulation result from a finite difference method to determine the optimum volume fraction nanoparticles for maximum energy density.

5.1 Introduction

The study on the effect of the volume fraction of nanoparticles in polymer/ceramic dielectric nanocomposites on the dielectric properties (permittivity and breakdown strength of nanocomposites), comprising surface-modified $BaTiO_3$ nanoparticles in a ferroelectric polymer host, poly(vinylidene fluoride-*co*-hexafluoropropylene), (P(VDF-HFP)) is presented in this chapter. For low volume fractions of particles, the effective permittivity of the nanocomposite was in good agreement with effective medium theory. Above a threshold volume fraction (50~60 %), porosity was observed by electron microscopic examination of the nanocomposite films concomitant with a slower increase and then a turnover of the effective permittivity with increasing nanoparticle volume fraction. The dielectric breakdown strength was found to decrease with increasing volume fraction of the high permittivity particles, with an abrupt decrease around 10 % and a gradual decrease for volume fractions over 20 %. Comparison of these results with combined effective medium theory and finite difference simulations indicate important roles of the porosity of the nanocomposites on the

dielectric properties. These results suggest that the volume fraction of nanoparticles should be rationally chosen for maximum energy density at certain operation frequency.

5.1.1 Optimization of Dielectric Nanocomposites

Polymer-ceramic nanocomposites are currently of considerable interest as solution processable high-permittivity materials for electronic applications such as embedded capacitors, multi-layer capacitors, high-energy-density capacitors, and gate insulators in organic field effect transistors.(Rao, Qu et al. 2000; Ramesh, Shutzberg et al. 2003; Schroeder, Majewski et al. 2005; Kim, Jones et al. 2007; Kim, Zhang et al. 2008) These materials can have both high permittivity and high dielectric strength and can be solution processed on large and flexible substrates at low temperatures and ambient pressures. However, the high surface energy of dielectric nanoparticles usually leads to agglomeration of nanoparticles and phase separation from the host matrix, resulting in poor processability of the films and a high defect density.

As discussed in previous chapters, surface modification of $BaTiO_3$ and other perovskite nanoparticles with functional phosphonic acids can allow the formation of high quality nanocomposite films that exhibit good solution processability, low leakage current, high permittivity, and high dielectric strength. Previous studies show that as the volume fraction of the high permittivity component (nanoparticle fillers) is increased, the effective permittivity of the nanocomposites also increases.(Jayasundere and Smith 1993; Rao, Qu et al. 2000; Calame 2006) However, increasing the volume fraction of nanoparticles typically decreases the apparent dielectric strength of the nanocomposite due to the enhancement of the local electric field in the host material.(Huang and Zhang 2004; Gilbert, Schuman et al. 2005) Therefore, the volume fraction of a nanocomposite should be rationally optimized in order to maximize the stored energy density.

Ferroelectric polymers based on poly(vinylidene fluoride) and its co-polymers are considered to be useful materials for energy storage due to their large permittivities and

dielectric strengths. (Zhang, Bharti et al. 1998; Bai, Cheng et al. 2000; Chu, Zhou et al. 2006; Faria, Welter et al. 2006; Ranjan, Yu et al. 2007) However, their large dielectric loss (>10% above 100 kHz) limits their use in high frequency applications (>100 kHz) that require fast charge/discharge cycles. High loss materials dissipate energy as heat, which in turn effectively reduces the breakdown strength.(Johnson 2001) Therefore, the combination of high permittivity but low loss nanoparticles and a ferroelectric polymer host can potentially provide high permittivity, high dielectric strength, and low loss nanocomposite materials that retain comparable processability to polymeric materials. However, nanocomposites with a large volume fraction of nanoparticles typically exhibit porosity that is detrimental to their dielectric performance. This brings about a question of what is the optimum volume fraction of a nanocomposite, which gives the maximum extractable energy at certain frequency. In this regard, the role of the volume fraction of high permittivity nanoparticles on the dielectric properties (permittivity, dielectric loss, and breakdown strength) of nanocomposites was investigated to determine the optimum volume fraction.

This chapter describes a systematic study of the effect of nanoparticle volume fractions on the dielectric properties of nanocomposites based on phosphonic acid-modified $BaTiO_3$ (BT) and poly(vinylidene fluoride-*co*-hexafluoropropylene) (P(VDF-HFP)). Self-consistent effective medium theory (SC-EMT) and finite difference simulations were employed to model the dielectric properties then the experimental trends have been compared with these models. In order to assess the role of the porosity, the effects of void volume fractions were also investigated. The porosity in composite materials has been observed to occur in other systems at high filling ratio of fillers, which have also been experimentally observed and predicted with simulations in this study.(Schulze, Zaman et al. 2003; Calame 2006) The results obtained in this study can provide a guideline for the optimization of dielectric nanocomposites for energy storage applications.

5.1.2 A Minireview of Theories in Dielectric Composites

The Clausius-Mossotti relation is a very simple description relating the dielectric constant to the electronic polarization for simple crystal structures for which the Lorentz local field relation can be used(Zaky and Hawley 1970; Kittel 1996)

$$\frac{1}{3\varepsilon_0}\sum_j N_j\alpha_j = \frac{\varepsilon - 1}{\varepsilon + 2} \qquad \text{(Clausius-Mossotti, SI)} \qquad \text{Equation 5.1}$$

where N, α, and ε are the number of model lattice points per unit volume, the polarizability, and the dielectric constant of the macroscopic system, respectively. However, this model relates microscopic quantities to the macroscopic dielectric function of the equivalent homogeneous system, which tends to obscure important physical origins of local-field effects such as neighboring dipoles.(Aspnes 1982) Moreover, this model is not suitable for describing heterogeneous systems such as composites, amorphous materials, molecules adsorbed on a surface, and other low-symmetry systems where the fictitious spherical cavity model proposed by Lorentz is no longer appropriate.(Bottcher, Belle et al. 1973) These microscopic aspects can be taken into account by using an approach of exactly solving the microscopic problem, then taking suitable averages of the microscopic solution to calculate the macroscopic observables. When a heterogeneous material is a mixture of constituents of different polarizabilities, ε_a and ε_b with volume fractions of f_a and f_b, the dielectric behavior can be described by Lorentz-Lorentz effective medium expression.(Lorentz 1916)

$$\frac{\varepsilon_{eff} - 1}{\varepsilon_{eff} + 2} = f_a\frac{\varepsilon_a - 1}{\varepsilon_a + 2} + f_b\frac{\varepsilon_b - 1}{\varepsilon_b + 2} \qquad \text{(Lorentz-Lorentz)} \qquad \text{Equation 5.2}$$

To picture a heterogeneous system where a dielectric sphere (ε_f) is embedded in a medium (ε_h), the microscopic derivation is slightly modified, then the volume average is taken again to calculate dielectric constant in terms of the macroscopic parameters **E** (electric field) and **P** (electric polarization) to yield so-called Maxwell Garnett effective-medium expression(Garnett 1904)

$$\frac{\varepsilon_{eff}-\varepsilon_h}{\varepsilon_{eff}+2\varepsilon_h}=f_f\frac{\varepsilon_f-\varepsilon_h}{\varepsilon_f+2\varepsilon_h}$$ Maxwell Garnett (isolated spheres) Equation 5.3

where ε_f, ε_h, and f_f, are the dielectric constant of filler, host, and the volume fraction of the filler, respectively. This equation can be rewritten as

$$\varepsilon_{eff}=\varepsilon_h\left[1+\frac{sf_f(\varepsilon_f-\varepsilon_h)}{s\varepsilon_h+(\varepsilon_f-\varepsilon_h)(1-f_f)}\right]$$ Maxwell Garnett (non-spherical particles)

Equation 5.4

where the new parameter s is a shape factor to describe non-spherical particles. However, when the filler volume fraction is greater than that of the host, the resulting effective dielectric constants are different, depending on which constituent is considered to be the 'host' material. This problem was resolved by Bruggeman, who proposed that the concept of inclusion of one material in another should be considered as being embedded in the effective medium itself. Therefore, ε_h in the Maxwell Garnett expression simply becomes that of the effective medium, ε_{eff}. This leads to the Bruggeman effective-medium expression written for a generalized two-component system, which is more generally known as the effective-medium approximation (EMA).(Jayannavar and Kumar 1991)

$$0=f_f\frac{\varepsilon_f-\varepsilon_{eff}}{\varepsilon_f+2\varepsilon_{eff}}+f_h\frac{\varepsilon_h-\varepsilon_{eff}}{\varepsilon_h+2\varepsilon_{eff}}$$ Bruggeman's Effective-Medium Approximation

Equation 5.5

The Lorentz-Lorentz, Maxwell Garnett, and Bruggeman expressions are closely related to each other and differ only in the choice of ε_h. The Maxwell Garnett result better describes isolated and coated-spheres, where the inclusion always occurs by complete isolation of a filler by the host material. On the other hand, the Bruggeman result better describes aggregated spheres, where the particles are randomly mixed with the host material. The effective-medium approximation very accurately describes a homogeneous macroscopic system but generally fails to describe a multiphasic system

close to the percolation threshold, where the system is governed by large fractal clusters and long-range correlations.(Kirkpatrick 1973) Though the percolation threshold for a 2-dimensional system is accurately predicted as 50 % by this theory, the predicted percolation threshold for a 3-dimensional system from this theory is 33 %, which is much greater than the value predicted by percolation theory (16 %) and observed values in many experiments.(Kirkpatrick 1973; Zallen 2004)

Many other models have been developed to describe small volume fractions (< 50 %) of spherical fillers in continuous dielectric media (*e.g.* polymer host). These models are based on the assumption that the filler materials are isolated spheres, and do not consider long-range interactions. Among these models, the Landauer and Kerner equations are claimed to be valid for large volume fractions.(Jayasundere and Smith 1993; Rao, Qu et al. 2000) The dielectric spheres are polarized under an applied field, so they can be represented as dipoles filling in the medium. The dipoles, in turn, can modify the local electric field of the surroundings. At relatively low volume fractions of those spheres, this effect can be neglected and thus predictions using 'isolated spheres' are suitable in this regime. However, at relatively high volume fractions, the influence of these dipoles on neighboring medium has to be taken into account. Lichtenecker model employed a fitting parameter to compensate for this effect

$$\log \varepsilon_{eff} = \log \varepsilon_f + f_f (1-k) \log\left(\frac{\varepsilon_h}{\varepsilon_f}\right) \quad \text{Lichtenecker model (The log-law)} \qquad \text{Equation 5.6}$$

where the fitting parameter k is usually 0.3 for well-dispersed composites.(Lichtenecker 1926; Rao, Qu et al. 2000)

Randomly dispersed nanoparticle fillers in a polymeric host can be viewed as a 0-3 type connectivity where nanoparticles are dispersed in a continuous polymeric medium. Kerner developed a model based on isolated spheres which is claimed to reasonably predict the dielectric constant at relatively high volume fractions.(Kerner 1956)

$$\varepsilon_{eff} = \frac{\varepsilon_h f_h + \varepsilon_f f_f \left(\mathbf{E}_{fz} / \mathbf{E}_{hz}\right)}{f_h + f_f \left(\mathbf{E}_{fz} / \mathbf{E}_{hz}\right)} \qquad \text{Kerner equation} \qquad \text{Equation 5.7}$$

where the average electric fields in filler and host are given as

$$\mathbf{E}_{hz} = \mathbf{E}_0 \text{ and } \mathbf{E}_{fz} = \frac{3\varepsilon_h}{2\varepsilon_h + \varepsilon_f}\mathbf{E}_0 \qquad \text{Equation 5.8}$$

by Bötcher when isolated dielectric spheres are surrounded by a medium.(Bottcher, Belle et al. 1973) For high volume fractions, the Kerner equation gives much better agreement with experimental results than the Landauer equation does.(Landauer 1952) Jayasundere and Smith modified this Kerner equation to include the interactive influence of neighboring dipoles that alters the internal field of spheres. They first employed a finite element model to calculate the local fields of two spheres lying parallel and perpendicular to the applied electric field as a function of the separation between the two spheres. From this calculation, the hypothesis of increased interactions between neighboring spheres at large volume fractions was confirmed. The interactive term was calculated analytically by finding an average field $\mathbf{E}_{av}$ in the continuum. An external field was applied first, giving rise to randomly distributed, induced dipole moments (μ), then $\mathbf{E}_{av}$ was calculated after removing the external field, which in turn modified the dipole moment of the spheres. This modified dipole moment is represented by an apparent surface charge density. An individual sphere with this apparent surface charge density in the presence of $\mathbf{E}_{av}$ was used to construct a boundary value problem, and this problem was solved to calculate the interactive component inside the sphere. Substituting the recalculated average field of the spheres involving the interactive terms into the Kerner equation yielded a modified Kerner equation.(Jayasundere and Smith 1993)

$$\varepsilon_{eff} = \frac{\varepsilon_h f_h + \varepsilon_f f_f \left[3\varepsilon_h / \left(\varepsilon_f + 2\varepsilon_h\right)\right]\left[1 + 3 f_f \left(\varepsilon_f - \varepsilon_h\right) / \left(\varepsilon_f + 2\varepsilon_h\right)\right]}{f_h + f_f \left[3\varepsilon_h / \left(\varepsilon_f + 2\varepsilon_h\right)\right]\left[1 + 3 f_f \left(\varepsilon_f - \varepsilon_h\right) / \left(\varepsilon_f + 2\varepsilon_h\right)\right]} \quad \text{Modified Kerner}$$

Equation 5.9

The modified Kerner equation has been widely adopted to describe 3-0 type composite systems at both low and high volume fractions.(Ogitani, Bidstrup-Allen et al. 2000; Xu and Wong 2005; Dang, Xie et al. 2007; Lu and Wong 2007)

5.1.3 Dielectric Breakdown Mechanisms

Dielectric breakdown of solid material is roughly classified in three different mechanisms based on experimental observations: 'Intrinsic', 'Thermal', and 'Avalanche' mechanisms. In breakdown measurements, the breakdown occurs distinctively in either of the following three mechanisms.(O'Dwyer 1964)

Intrinsic breakdown occurs at low temperatures (room temperature or lower) and is independent of the size and the shape of the sample, the electrode material, and the geometry of the electrode. It is intrinsic materials property of the dielectric below certain temperature. It is also independent of the functional form of applied voltage from DC to single shot impulses of microsecond rise times and thus assumed to occur in a timescale of microsecond of less.

Thermal breakdown is strongly dependent on the functional form of applied voltage. In the case of slow ramping rate, the breakdown is called steady-state or DC thermal breakdown, while it is called impulse thermal breakdown in the case of rapid voltage ramping, both of which occur at high temperatures. The former breakdown depends on the size and shape of the sample, the electrode material and geometry, and the thermal properties of electrode and testing medium. If the electrode geometry supports better heat dissipation, the breakdown strength increases. This breakdown requires at least milliseconds or often very much longer time to develop and shows lower breakdown strength for AC field, since the dielectric materials at high frequency alternating field typically show large dielectric losses which contribute to thermal effect. The latter breakdown is independent of the size and shape of the sample and the electrode

arrangement such that the heat is not dissipated rapidly. It also varies with the time scale of the applied field and is decreased for pulsed fields with longer duration.

Avalanche breakdown is related to the intrinsic breakdown occurring at low temperatures. It is observed in thin dielectric films with low conductivity and the breakdown fields are generally very high. The avalanche breakdown strength usually decreases with increasing the thickness of the dielectric sample due to increased number of defects in the sample. When a relatively low field is applied, the pre-breakdown currents (or leakage current) tend to be very noisy and the time required for developing breakdowns generally shows large statistical variations.

5.2 Materials and Methods

5.2.1 Experimental Study

The preparation of PFBPA-modified BT nanoparticles, processing of nanocomposites in P(VDF-HFP) host, fabrication and characterizations of nanocomposite thin film capacitors are described in Chapter 2. The breakdown strengths were analyzed using Weibull statistics as described in section 2.7.4.

5.2.2 Self-Consistent Effective Medium Approximation

The effective permittivities and the breakdown strengths of PFBPA-BT:P(VDF-HFP) nanocomposites at each volume fraction was calculated using a self-consistent effective medium approximation with the consideration of possible voids in the nanocomposites. This model was originally described by Professor Jinagyu Li at University of Washington(Li, Zhang et al. 2007). The effective permittivity (ε_{eff}) according to this model can be expressed as

$$\varepsilon_{eff} = \varepsilon_1 + f_2(\varepsilon_2 - \varepsilon_1)a_2 + f_3(\varepsilon_3 - \varepsilon_1)a_3 \qquad \text{Equation 5.10}$$

where a_r (r = 1 for the host matrix, 2 for the filler, and 3 for the possible void) represents the electric-field concentration factor that relates the average electric field in phase r as

$\langle \mathbf{E}_r \rangle = a_r \mathbf{E}_0$, when the applied field is equal to $\mathbf{E}_0$. From the effective medium approximation, the field concentration factor can be rewritten using permittivities as

$$a_r = 1 - s\left[\left(\varepsilon_r - \varepsilon_{eff}\right)^{-1} \varepsilon_{eff} + s\right]^{-1}, \quad r = 2,\ 3 \qquad \text{Equation 5.11}$$

where s is a component of dielectric tensor related to the depolarization factor. This parameter is also related to the shape and the orientation of the filler particles in the field and is 1/3 for a spherical particle. After the calculation of a_2 and a_3, the normalization condition given below is used to calculate a_1.

$$\sum_{r=1}^{3} f_r a_r = 1 \qquad \text{Equation 5.12}$$

Equation 5.10, whose right hand side depends on ε_{eff} through Equation 5.11, has to be numerically solved.

The inclusion of high permittivity filler particles in a host matrix induces the enhancement of the average field in polymer host, $\langle \mathbf{E}_1 \rangle$, which in turn reduces the dielectric breakdown strength. The breakdown criterion is given based on the average field in the host polymer

$$\langle \mathbf{E}_1 \rangle = a_1 \mathbf{E}_0 \geq \mathbf{E}_b \qquad \text{Equation 5.13}$$

where $\mathbf{E}_b$ is the breakdown field of unfilled pure polymer. Since the breakdown is a failure process, the above criterion using simply an average field is not accurate to predict reasonable breakdown field and seriously overestimates it. Therefore, a statistical fluctuation of the average field should be taken into account to predict a more accurate breakdown field.(Li, Huang et al. 2004)

$$\langle E_1 \rangle + \sqrt{\langle E_1^2 \rangle - \langle E_1 \rangle^2} \geq \mathbf{E}_b \text{ where } \langle E_1^2 \rangle = \frac{1}{f_1} \frac{\partial \varepsilon_{eff}}{\partial \varepsilon_1} E_0^2 \qquad \text{Equation 5.14}$$

Now, the new breakdown criterion becomes the following:

$$E_0 \left(a_1 + \sqrt{\frac{1}{f_1} \frac{\partial \varepsilon_{eff}}{\partial \varepsilon_1} - a_1^2} \right) \geq \mathbf{E}_b \qquad \text{Equation 5.15}$$

5.2.3 Finite Difference Simulation

The onset of the air void formation in the nanocomposite studied in this thesis was separately computed by Dr. Jeffrey P. Calame (JPC) at Naval Research Laboratory (Washington, DC) using a finite difference simulation. The simulation used a model space with 200 cubical cells per each x, y, and z axis. These cells were filled with dielectric spheres which have radius of 15 cells. When filling the space with spheres, partial spheres were also allowed near the edges, as long as the center of the sphere lied within the model space. Once a particle was placed, the center position was not allowed to move (*i.e.* 'frozen' and no relaxation processes were considered). Therefore, the models do not represent a maximally dense composite.

5.3 Results and Discussion

5.3.1 Surface Modification of BT for Incorporation in Fluoropolymer Host

$BaTiO_3$ (BT) nanoparticles tend to form large aggregates due to their high surface energy and large surface area, which leads to a highly inhomogeneous film when blended in a polymer matrix. In order to mitigate this problem for incorporation in a fluoropolymer matrix, poly(vinylidene fluoride-*co*-hexafluoropropylene) (P(VDF-HFP)), BT nanoparticles were surface modified using an organophosphonic acid ligand, pentafluorobenzyl phosphonic acid (PFBPA), in an ethanol/water mixture. (Figure 5.1) The surface-modified BT nanoparticles (PFBPA-BT) were washed thoroughly to remove excess ligand, then mixed with P(VDF-HFP) in *N,N*-dimethylformamide (DMF) at known volume ratio. The host matrix has >25% hexafluoropropylene and is known to show ferroelectric behavior.

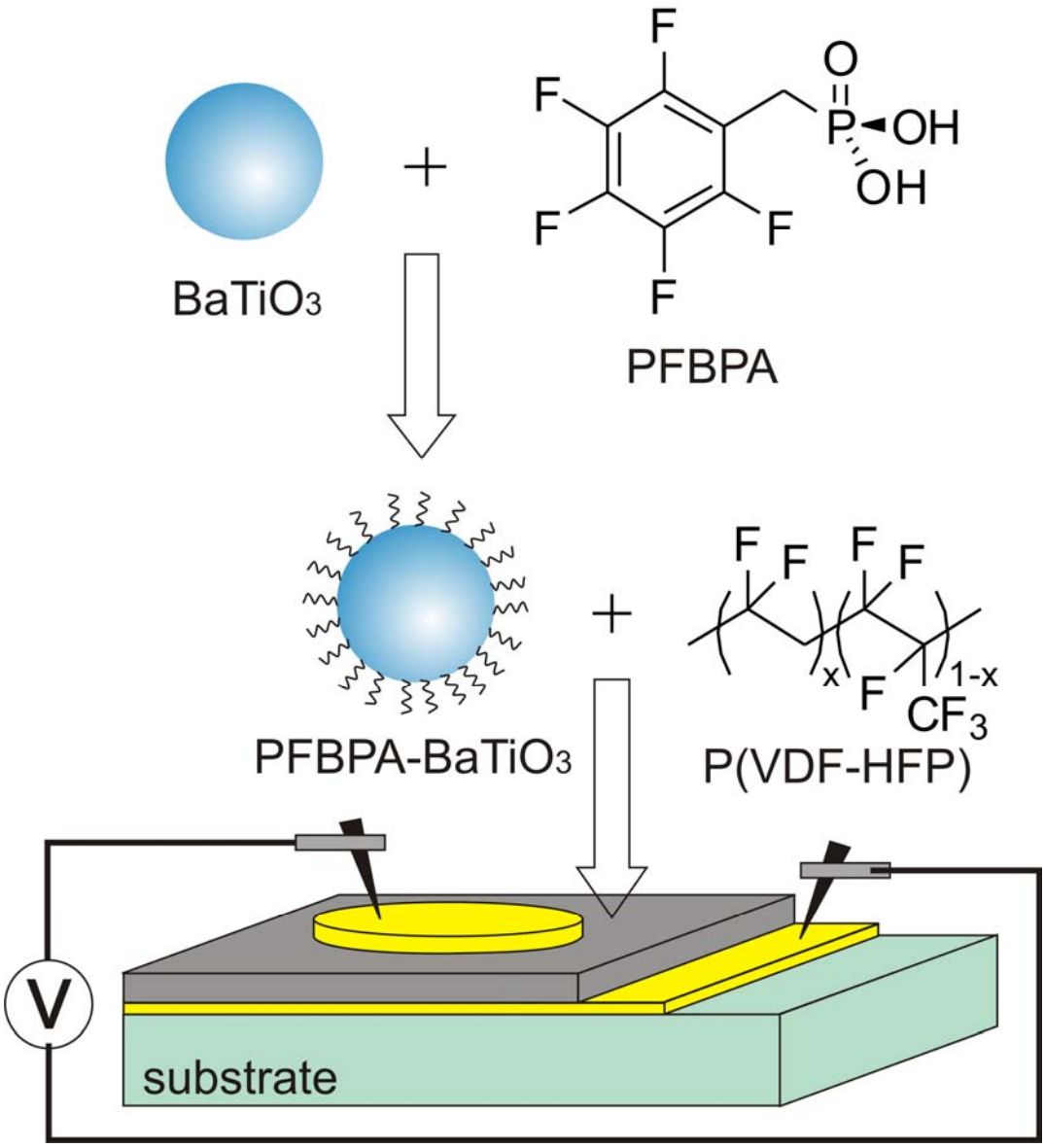

Figure 5.1 Schematic illustration of surface modification of BT, nanocomposite formation, and the geometry of fabricated nanocomposite thin film capacitors.

In order to assess the surface modification of PFBPA ligand on the BT nanoparticle surface, FT-IR and ^{31}P solid state NMR (SS-NMR) spectra were recorded. The binding of phosphonic acids to the BT surface is reflected in the changes in the FT-IR spectra before and after the surface modification. (Figure 5.2) The aromatic skeletal vibration modes at 1502 and 1528 cm^{-1} and the C-F stretching mode at 1126 cm^{-1} of

PFBPA were also detected in PFBPA-modified BT nanoparticles. There was a reduction in the intensity of surface hydroxyl stretching (3400 – 3500 cm^{-1}) of BT and the broad free hydrogen bonded (P)O-H stretching mode (2240 – 2380 cm^{-1}) implying the condensation of surface hydroxyl groups of BT and the hydroxyl groups of PFBPA in the surface modification reaction. In the fingerprint region, the initially complex pattern of P=O (1200 cm^{-1}) and P-O (1090 – 990 cm^{-1}) stretching modes collapses to two major peaks at 1095 and 1045 cm^{-1} that are assigned as the asymmetric and symmetric P-O-M (M = surface metal) stretching modes.(Kim, Jones et al. 2007; Paniagua, Hotchkiss et al. 2008)

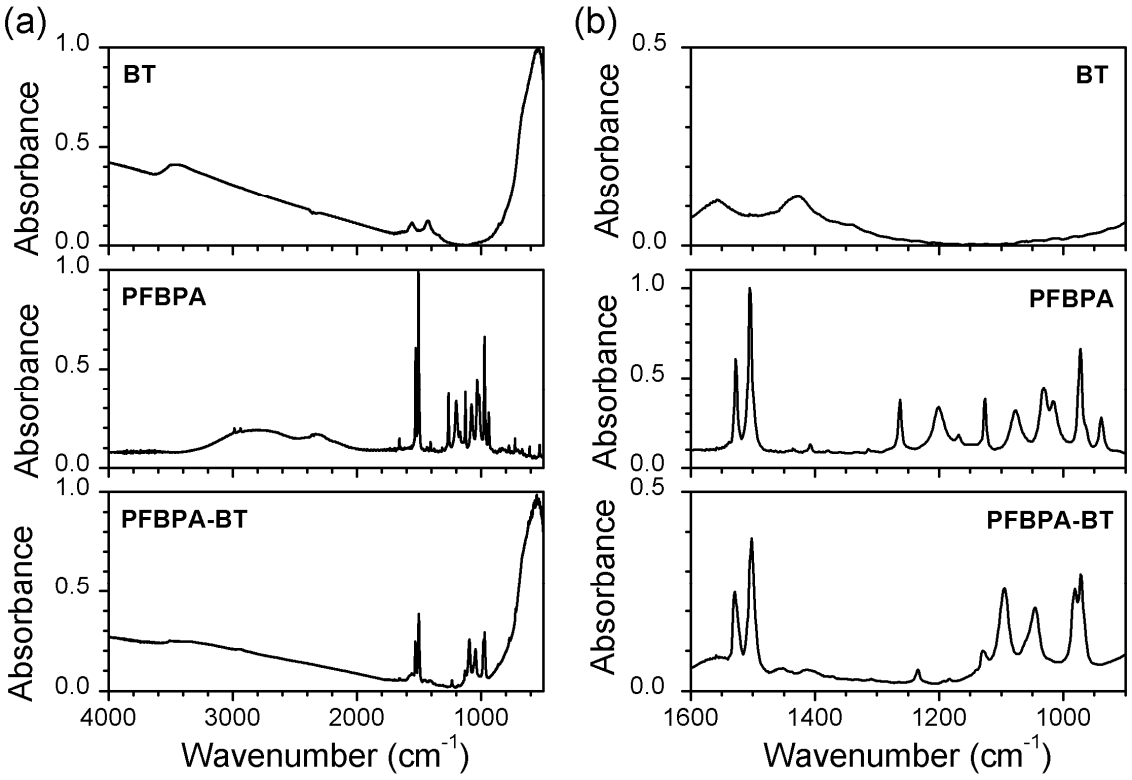

Figure 5.2 FT-IR absorption spectra of unmodified BT, PFBPA, and PFBPA-BT. Wide range spectra (a) and the details of P-O stretching region (b). The spectra for BT and PFBPA-BT were normalized using the lattice Ti-O absorption peak centered at ~540 cm^{-1}. The spectrum of PFBPA was normalized using the maximum absorption peak.

^{31}P solid-state NMR (SS-NMR) revealed further details of the binding modes of PFBPA on BT surface. (Figure 5.3) Large chemical shifts were observed between unbound PFBPA (δ = 27.9 ppm) and bound PFBPA (δ = 11 – 23 ppm) on BT. The majority of bound PFBPA was detected as peaks centered at δ = 14.5, δ = 17.0, and δ = 20.6 ppm. The largest change in chemical shift from free PFBPA to bound PFBPA on the BT nanoparticle surface was 13.4 ppm. This change is close to the value for octylphosphonic acid binding to BT surface ($\Delta\delta$ = 14.3 ppm), which was assigned as tridentate and bidentate configurations.(Kim, Jones et al, 2007) The other peak is interpreted as slightly less associated monodentate and unbound PFBPAs linked to surface-bound PFBPA *via* P-O-P bond. There was no evidence of metal phosphonate gel that might have been formed by a self-condensation reaction, which would appear as a sharp peak around -4.0 – -7.0 ppm.(Bars, Tinet et al. 1991) Long-chain alkyl phosphonic acids binding to the BT nanoparticle surface are known to form densely packed crystalline-like layers, upon which the C-H stretching peaks shift to smaller wavenumbers in FT-IR spectrum. The alkyl phosphonic acids loosely bound to the BT nanoparticle surface do not seem to form crystalline-like layers, since they are detected only in the direct-polarization ^{31}P SS-NMR, and are not enhanced in the cross-polarization method. In contrast, PFBPAs binding to the BT nanoparticle surface appear to form crystalline-like layers, irrespective of the binding mode, as all of the ^{31}P atoms are detected in the cross-polarization experiment. This is attributed to the strong $\pi - \pi$ interaction between adjacent PFBPA molecules.

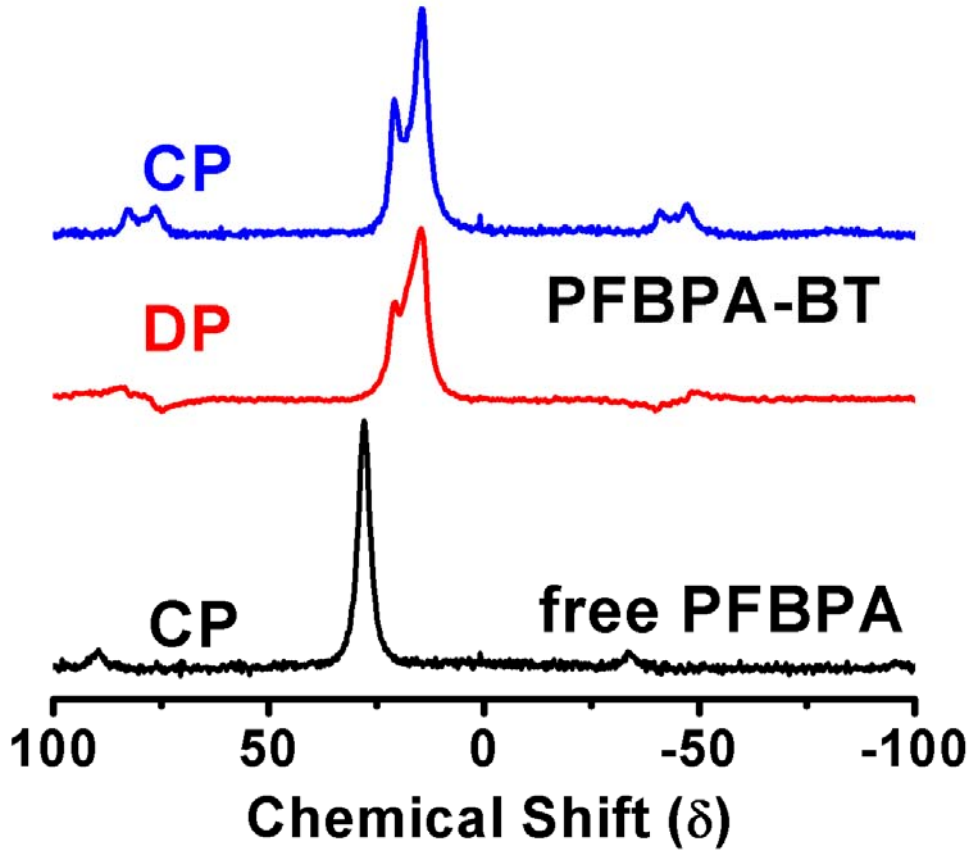

Figure 5.3 ^{31}P MAS SS-NMR spectra of free PFBPA (black, CP) and PFBPA-BT (blue, CP and red, DP).

To determine the surface coverage of PFBPA on BT nanoparticles, measurements of the BET specific surface area of dried and unmodified BT nanoparticles (25.8 m^2/g) and thermogravimetric analysis of both BT and PFBPA-BT nanoparticles were performed. The net weight loss from the surface bound PFBPA was found to be 3.49 %, which corresponds to 76 % of a theoretical monolayer, assuming that the footprint of each phosphonic acid is 24 $Å^2$. (Figure 5.4)

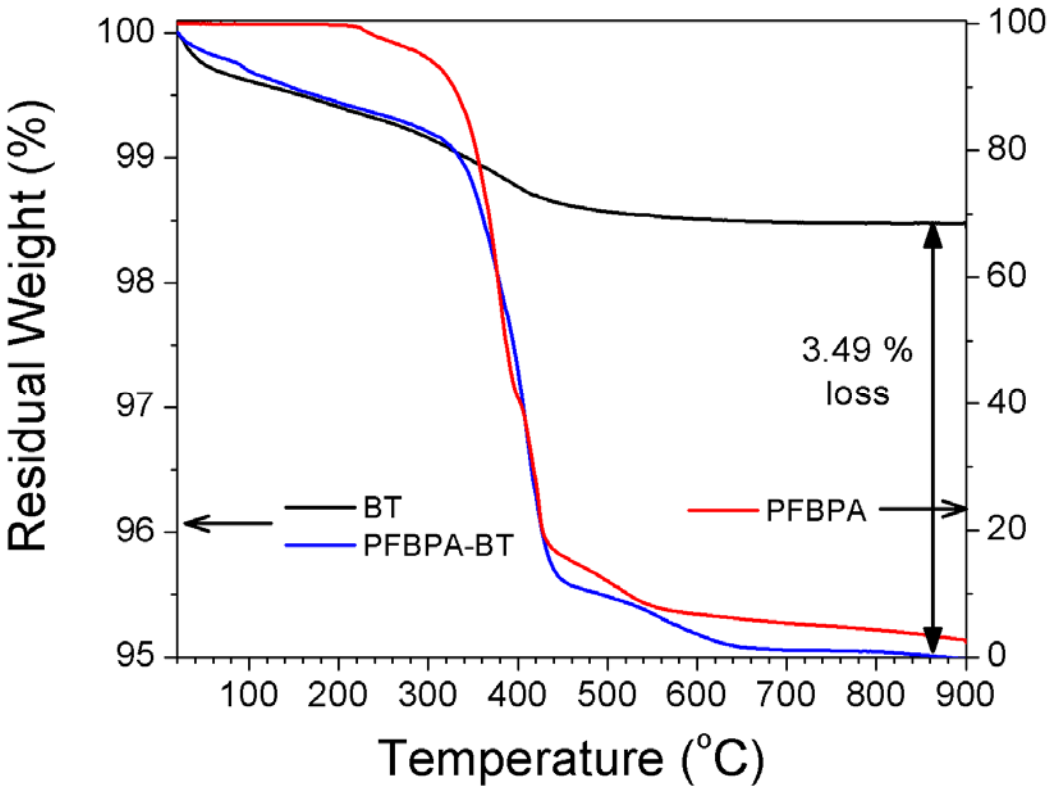

Figure 5.4 TGA of dried and unmodified BT (black), PFBPA-BT (blue), and PFBPA (red). Note that the scales of weight loss for BT and PFBPA-BT are the left Y-axis and for PFBPA is the right Y-axis.

The surface-modified BT formed a homogeneous dispersion in P(VDF-HFP)/DMF solution after ball-milling the mixture. In this study no external dispersant was used in the processing of the nanocomposites of surface-modified BT nanoparticles. Surface modification had a dramatic effect on the stability of the nanocomposite dispersions and improved the quality of nanocomposite films produced by spin coating.

The microscopic homogeneity of the nanocomposite films were investigated by imaging the top surface and the freeze-fractured cross-sections of nanocomposite films using a scanning electron microscope (SEM). Figure 5.5 and Figure 5.6 show the SEM images of the top surfaces and the freeze-fractured cross-sections of PFBPA-BT:P(VDF-

HFP) nanocomposite films. The surface-modified BT nanoparticles with PFBPA formed uniform, and high quality nanocomposite thin films in the P(VDF-HFP) host.

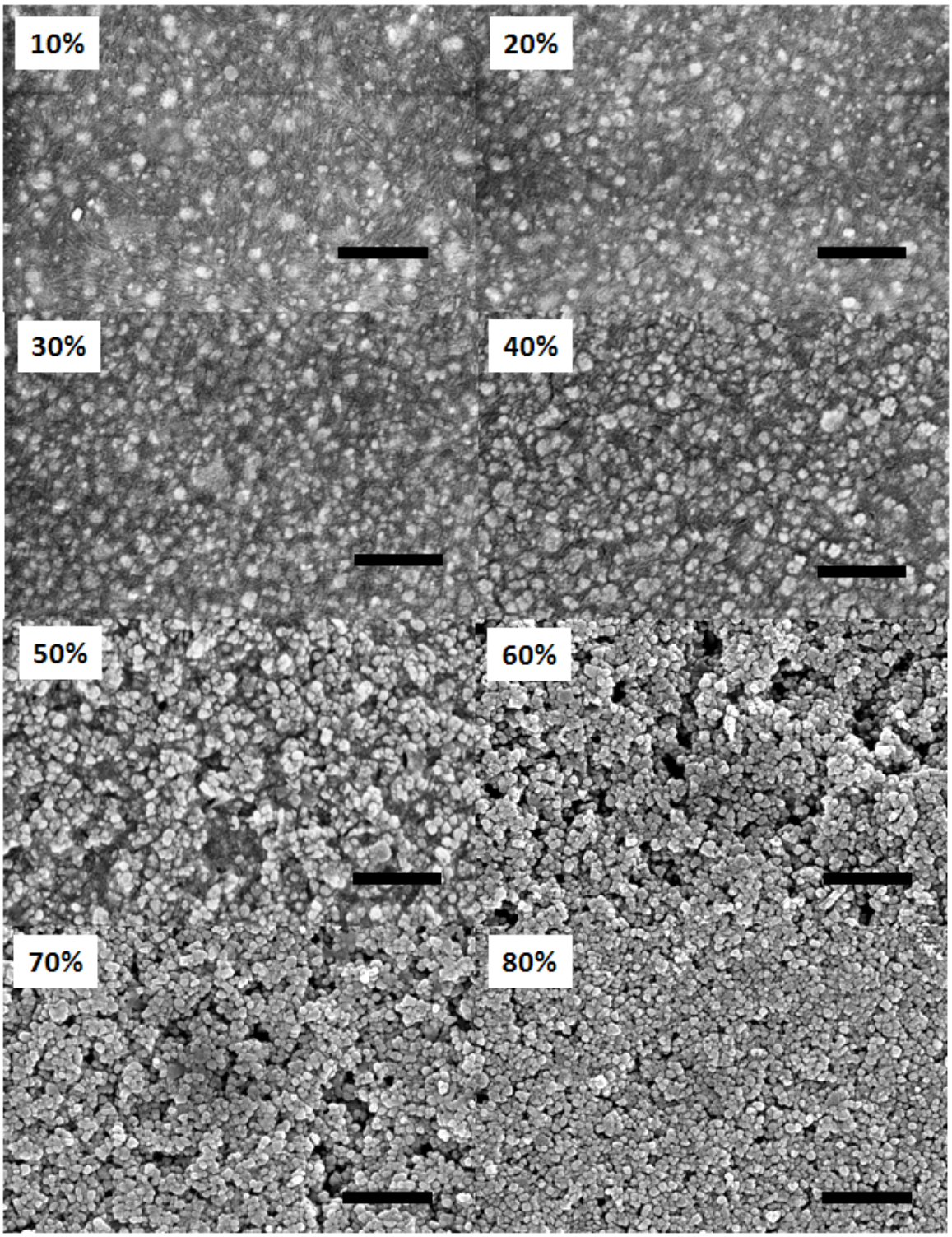

Figure 5.5 SEM images of the top surfaces of PFBPA-BT:P(VDF-HFP) nanocomposite films with different nanoparticle volume fractions. Scale bars are 300 nm.

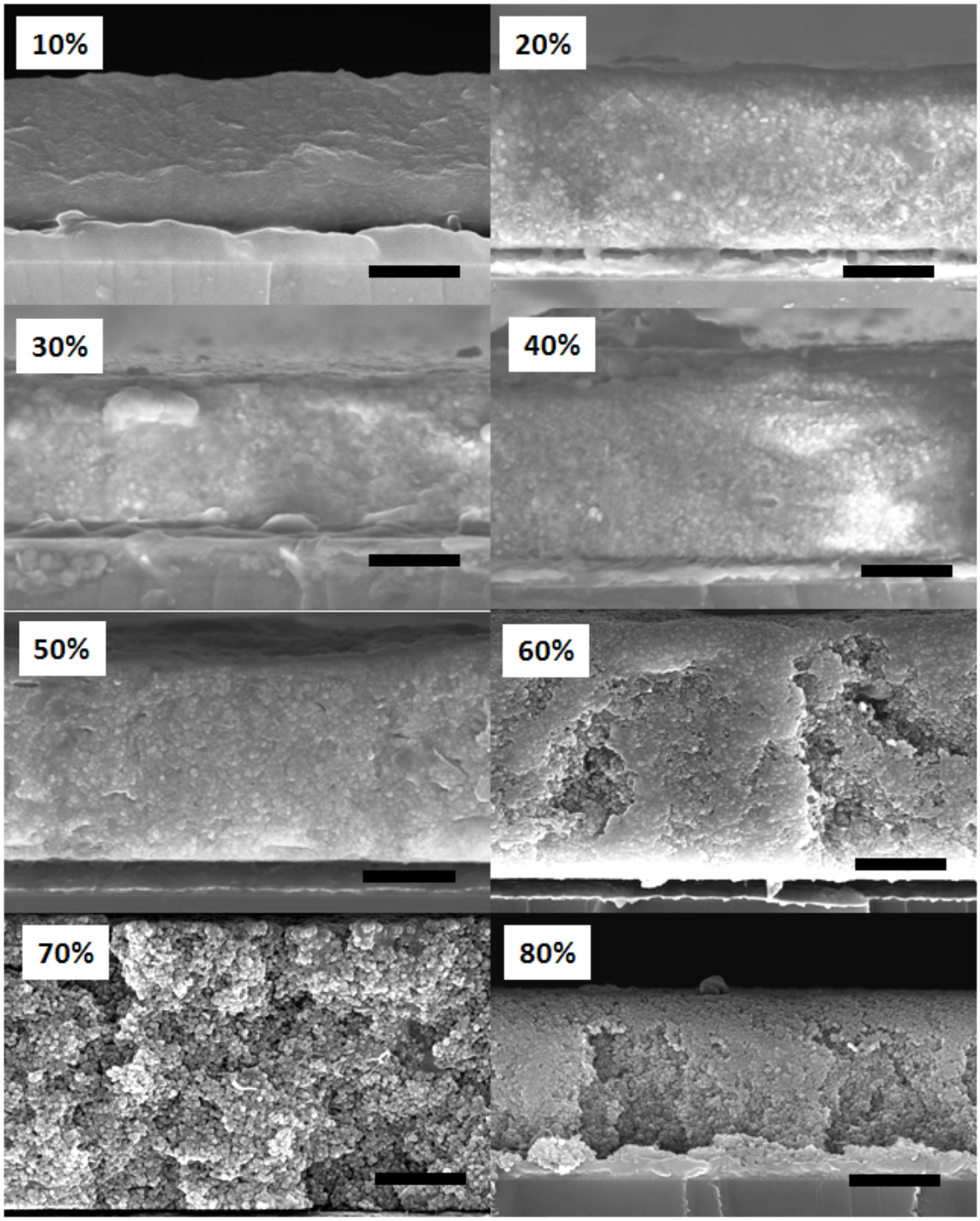

Figure 5.6 SEM images of the freeze-fractured cross-sections of PFBPA-BT:P(VDF-HFP) nanocomposite films with different nanoparticle volume fractions. Scale bars are 1 μm.

5.3.2 Dielectric Characterization of PFBPA-BT:P(VDF-HFP) Nanocomposites

The effective permittivities of the PFBPA-BT:P(VDF-HFP) nanocomposites were determined using dielectric spectroscopy for films with varying volume fractions of nanoparticles. The average permittivities at each nanoparticle volume fraction are shown in Figure 5.7. The experimental permittivity values gradually increased with increasing nanoparticle volume fraction followed by a maximum in the permittivity at around 50 – 60%, after which the permittivity decreased rapidly with further increase of the nanoparticle volume fraction.

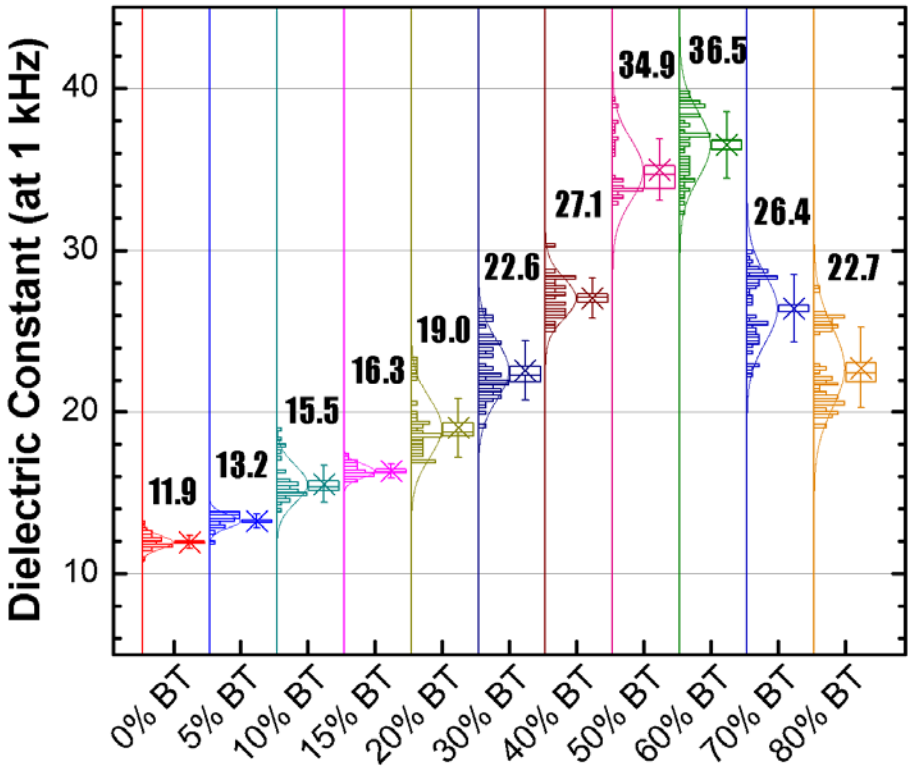

Figure 5.7 Effective permittivities of nanocomposites at different nanoparticle volume fractions. Host polymer: P(VDF-HFP), nanoparticle: PFBPA-BT, the boxes represent standard error and the whiskers represent standard deviation.

Figure 5.8 shows the dielectric spectroscopy of the nanocomposites with varying volume fractions of BT from 20 Hz to 1 MHz. The dielectric loss is expressed as the loss tangent (tan δ) which is defined as the ratio of the imaginary part to the real part of the permittivity ($\varepsilon''/\varepsilon'$). This value is also known as the dissipation factor (DF). The dielectric spectroscopy for the PFBPA-BT:P(VDF-HFP) with each nanoparticle volume fraction revealed that the dielectric loss is mainly due to the host material, and there is no significant contribution from either the BT nanoparticle filler or the phosphonic acid surface modifier.

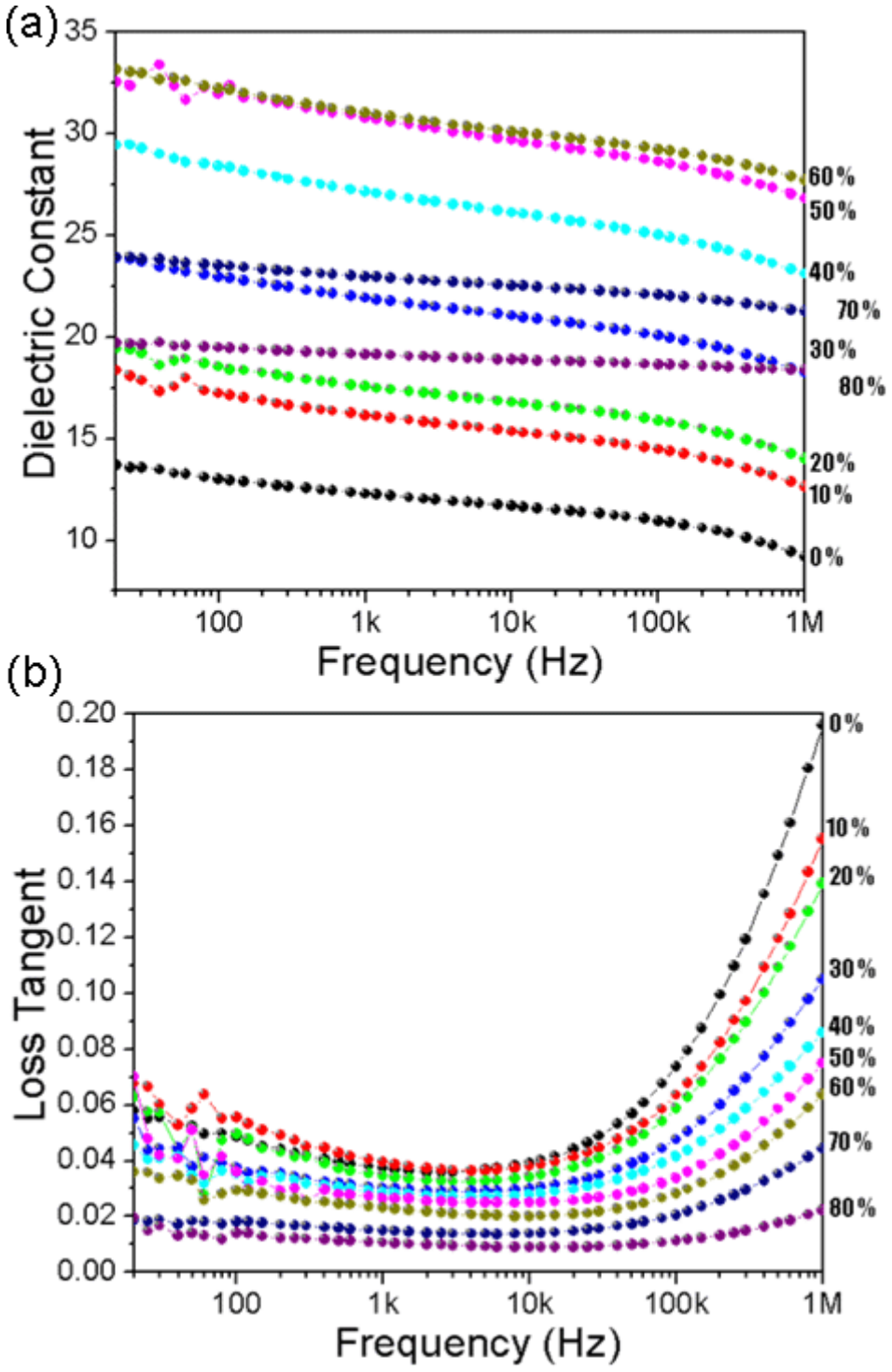

Figure 5.8 Dielectric spectroscopy of each PFBPA-BT:P(VDF-HFP) nanocomposite from 20 Hz to 1 MHz. Dielectric constant (a) and the loss tangent (b). The dielectric loss gradually increases with increasing frequency and it is mainly due to the polymer host.

The dielectric breakdown strength was also measured for the nanocomposites with BT volume fractions from 0 to 50 % and analyzed using Weibull statistics, as shown in Figure 5.9 and Figure 5.10. The breakdown strengths for the nanocomposites above 50 % volume fraction varied too much from sample to sample, possibly because of the randomly distributed porosity in the nanocomposites and thus no consistent values were obtained from the analysis. A separate batch of samples with different nanoparticle volume fractions was prepared and the effective permittivities and the breakdown fields were characterized by Natalie M. Doss (NMD) and John P. Tillotson (JPT). The results were reproducible within the error range.

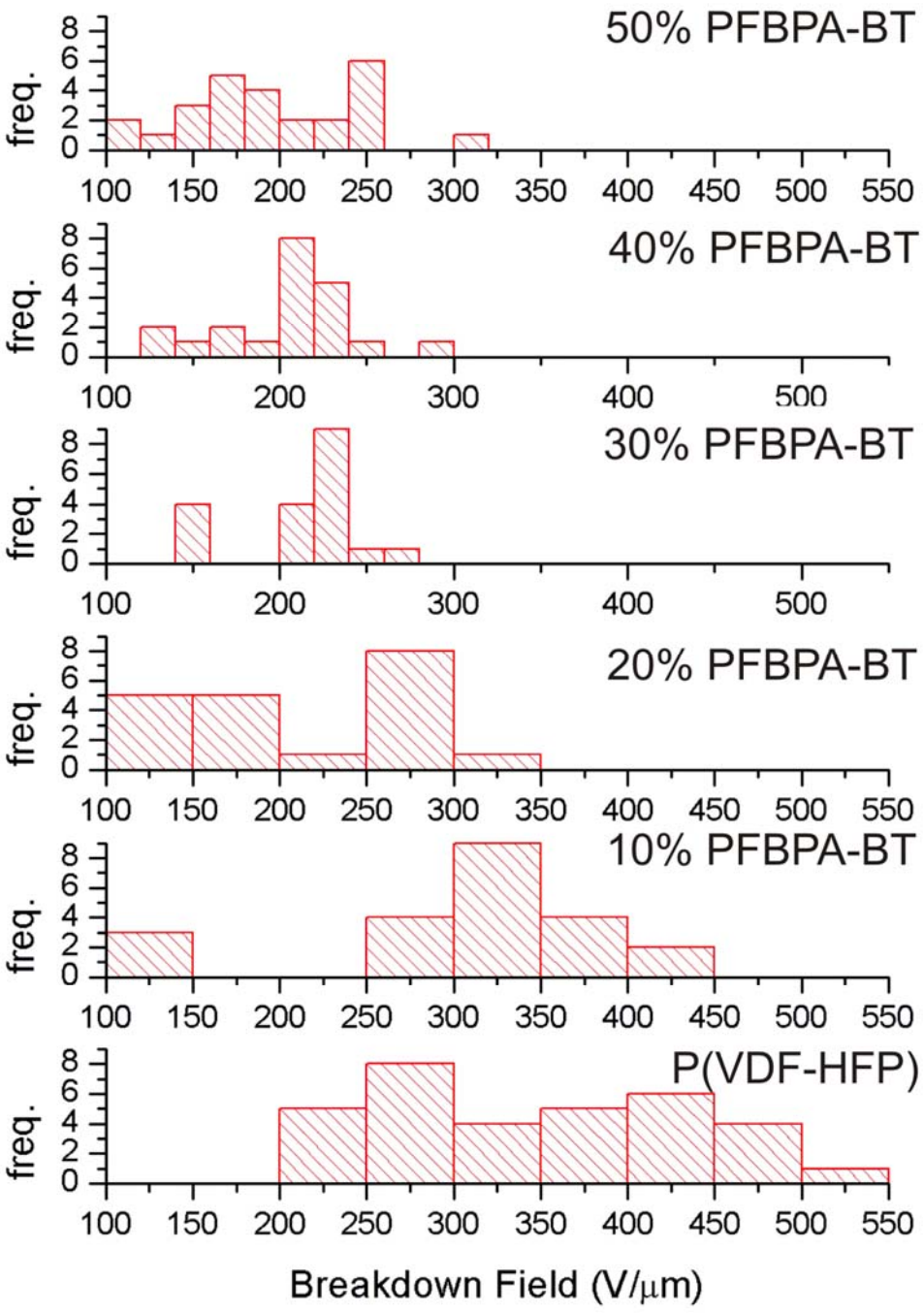

Figure 5.9 The histogram of measured breakdown field (raw data) at each volume fraction.

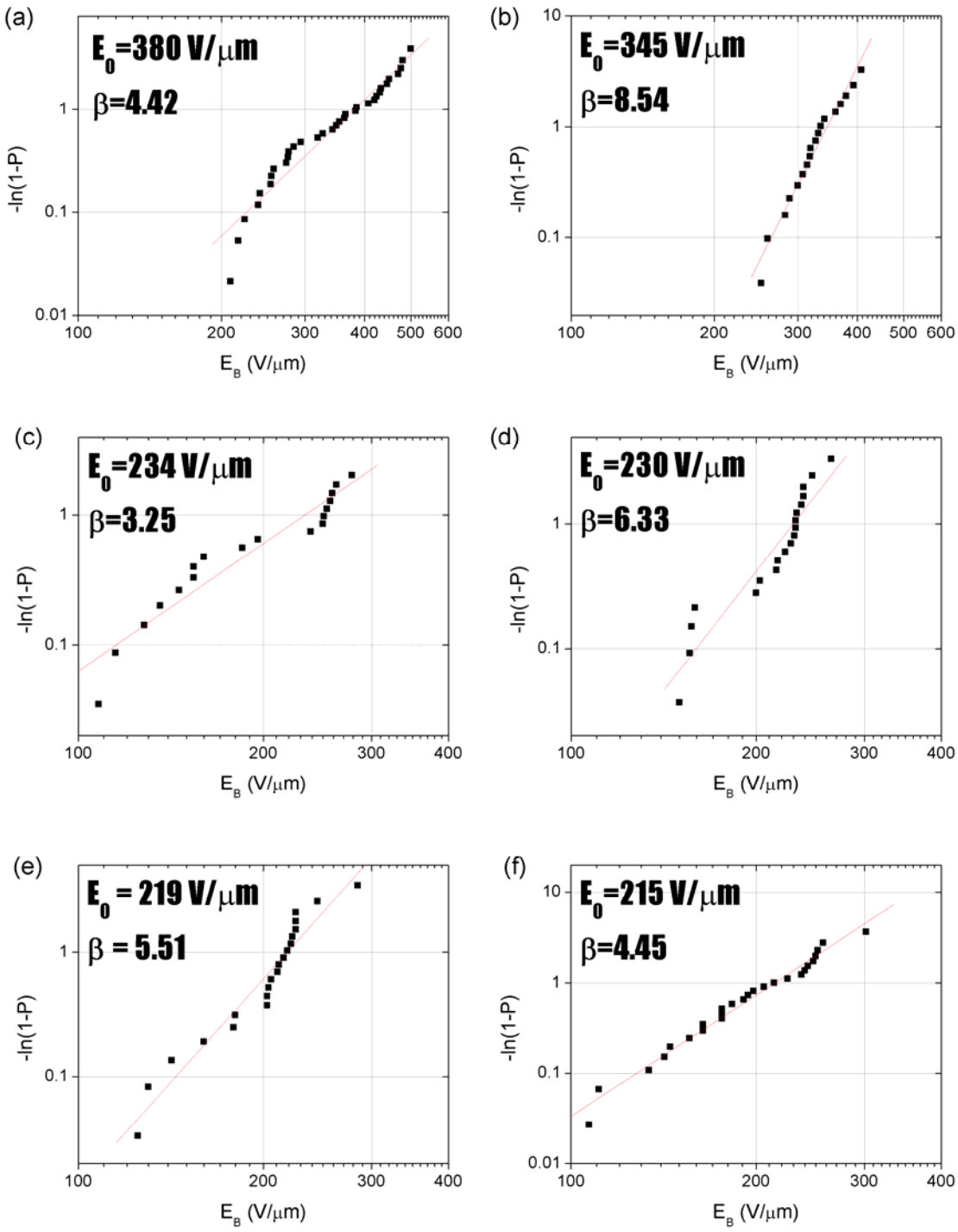

Figure 5.10 The Weibull analysis plot of the raw breakdown field data to extract the breakdown field (equal to the scale parameter α) and the dispersion (shape parameter β). (a – f): 0, 10, 20, 30, 40, and 50 vol. % PFBPA-BT in P(VDF-HFP). See section 2.7.4 for the details about Weibull analysis.

The analyzed results were replotted to give the percent cumulative distribution functions (% probability of failure) for each nanocomposite as a function of the applied electric field (Figure 5.11). Samples with volume fractions of 5 % and 15 % were also prepared and measured to better resolve the dielectric behavior of the nanocomposite around 10 % volume fraction.

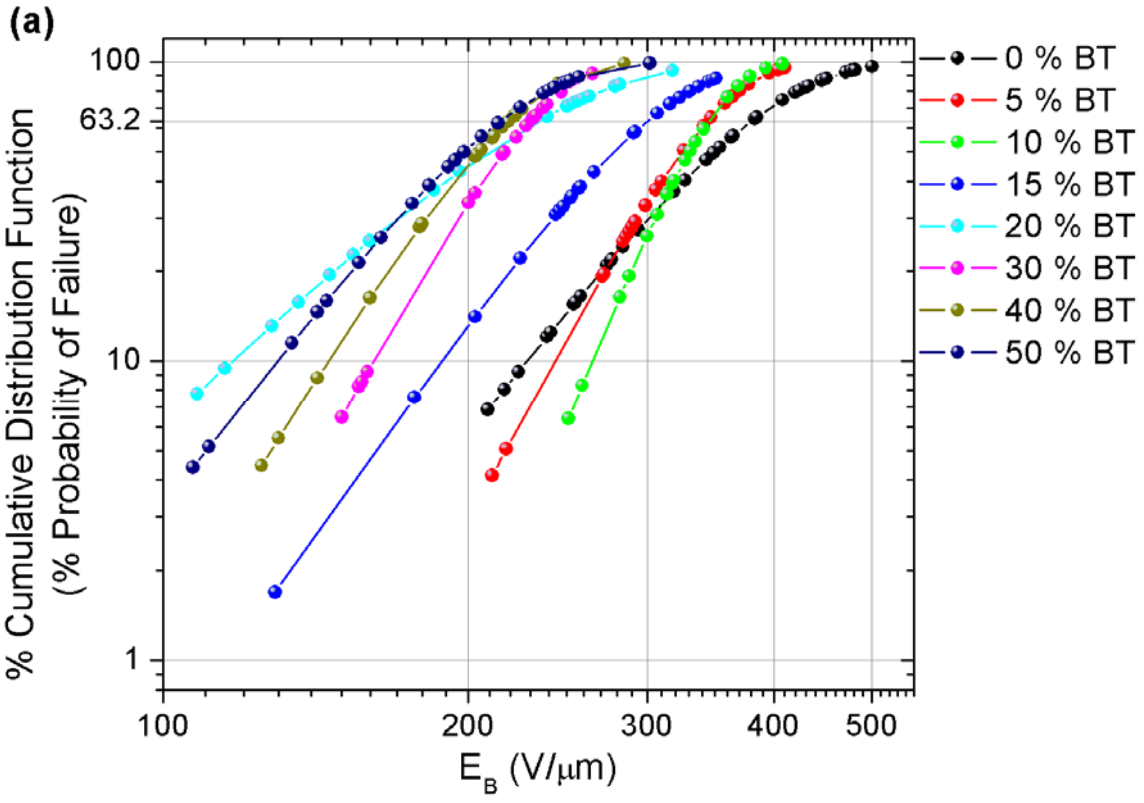

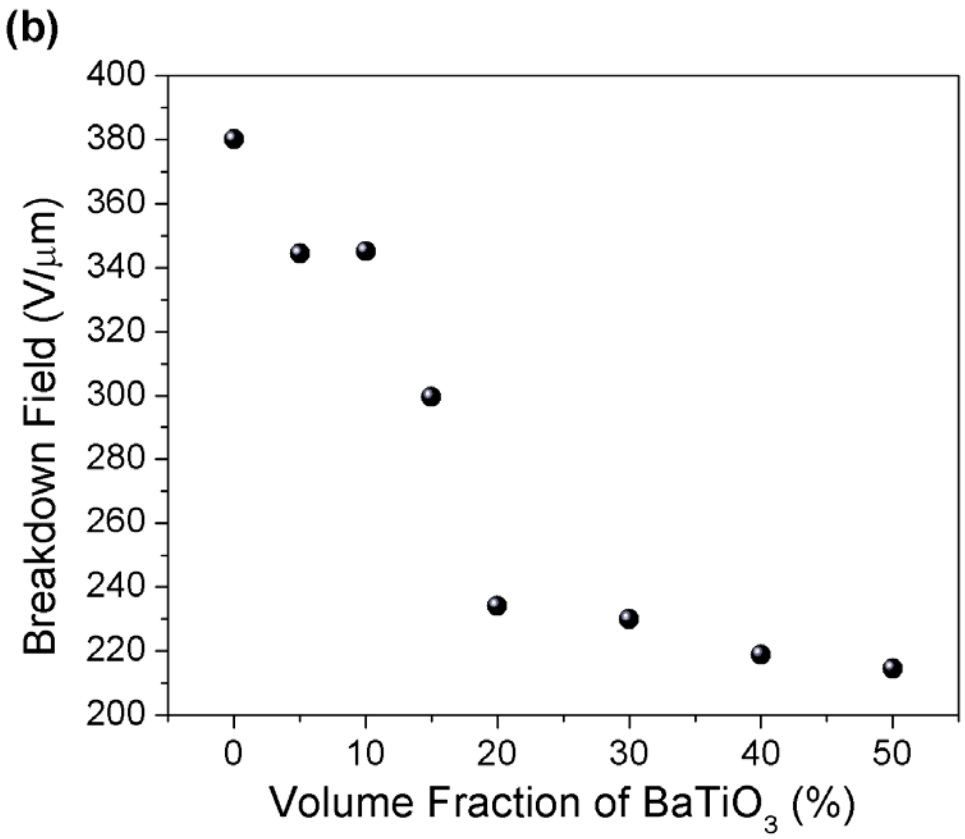

Figure 5.11 Percent cumulative distribution function (% probability of device failure) of each nanocomposite as a function of applied electric field (a), and the breakdown strengths at each volume fraction calculated from Weibull analysis (b). The raw breakdown measurement data were analyzed using Weibull method to find the slope (β, shape parameter, dispersion of $\mathbf{E}_B$), which in turn gave the breakdown value. The applied field corresponding to a failure probability of 1-1/*e* (63.2 %) is taken as the breakdown field of each composite.

The results show that the breakdown strength clearly decreases with the addition of fillers to the host material, as expected. It should be noted that there is a sudden decrease in the dielectric strength when the volume fraction changes from 0.1 to 0.2. Similar trends were also observed in previous works (Huang and Zhang 2004; Gilbert,

Schuman et al. 2005), though the authors did not explicitly discuss this trend. (Figure 5.12)

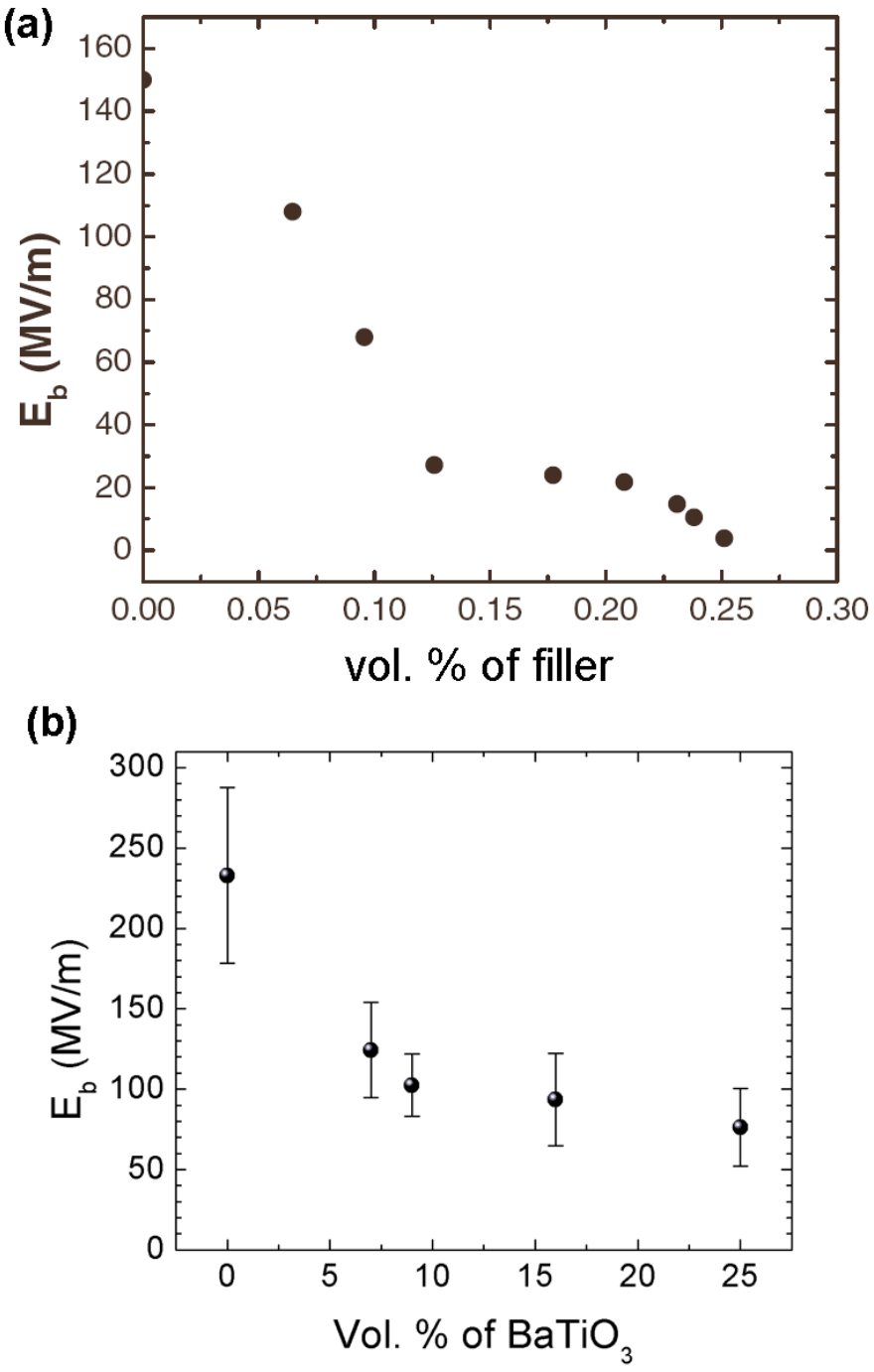

Figure 5.12 Dielectric breakdown strength as a function of increasing filler volume fraction. (a) from an all-polymer percolative composite based on polyaniline in P(VDF-TrFE-CTFE). (from Advanced Functional Materials) and from a $BaTiO_3$ ceramic particles filled in epoxy/polyamide (replotted from the data by Gilbert et al.).

We propose an explanation to this observation: as previously described by Calame, the percolation of particles in the composite is viewed as two different regimes: the 'soft' percolation and the 'hard' percolation. In the soft percolation regime, where the particles begin to gradually touch each other, a percolative pathway consisting of touching particles across the nanocomposite thin film can be formed. If this happens, then the breakdown strength will be abruptly reduced since the charges can easily travel across the film along the percolative channels formed. This effect can be effectively suppressed with the use of surface-modified nanoparticles owing to the organic passivation layer. As a result, the magnitude of the drop in the breakdown strength in this regime can be mitigated as compared to the nanocomposites with unmodified nanoparticles. In our study, the onset of such percolation pathway seems to be between 0.1 and 0.2. With further increase of the nanoparticle volume fraction, the 'hard' percolation takes place, in which the local packing density of the particles reaches a maximum. At this event, most of the particles are touching each other and the addition of particles does not increase the particle density. The composites may undergo a relaxation process to find a denser packing configuration to reduce the local concentration of air voids, but this process is typically kinetically limited. Increasing the ratio of particle/polymer to increase the volume fraction of the particles only results in the creation of localized air voids in the composite, due to insufficient amount of the polymer phase. Therefore, the dielectric breakdown strength will be decreased and strongly be dependent on the local distribution of the air voids. Since the particles are typically randomly packed, the air void distribution is also random and thus the breakdown behavior becomes unpredictable and shows a large statistical variation.

Another interesting observation is that the failure probability of pure P(VDF-HFP) film at moderate fields is higher than those of nanocomposites with 5 % and 10 % PFBPA-BT. (Figure 5.11a) This implies that doping of the polymer host with high permittivity filler under the 'soft' percolation threshold can reduce the failure probability

under moderate fields at which the capacitors are going to be operated. Even under a relatively low applied electric field, there are still chances for carrier generation inside the nanocomposite films that may lead to breakdown. The high permittivity nanoparticles can act as traps for these charges and also effectively scatter charges in the nanocomposite film, which results in the reduction of the failure probability. This result is somewhat similar to a previous observation by Tuncer et al., where they reported that doping poly(vinyl alcohol) with 10 – 30 wt. % TiO_2 nanoparticles makes the dielectric breakdown behavior more predictable (*i.e.* reproducible) and improves the breakdown characteristics.(Tuncer, Sauers et al. 2007)

With further increase of the nanoparticle volume fraction, the 'hard' percolation takes place, where some particles begin to physically touch each other. At this event, if there is a percolative pathway across the nanocomposite thin film, then the breakdown strength will be significantly reduced due to the fact that the charges can travel through the film in the channels formed. However, in the case of surface-modified nanoparticles, this effect can be suppressed owing to the organic passivation layer. As a result, the drop in the breakdown strength can be also suppressed as compared to the nanocomposites with unmodified nanoparticles.

5.3.3 Comparison with Theoretical Models

The comparisons of the experimentally obtained effective permittivity with the predictions from simple models described in section 5.1.2 are shown in Figure 5.13. A large discrepancy was observed at volume fractions above 60 %, due to the decrease in the experimentally observed permittivities.

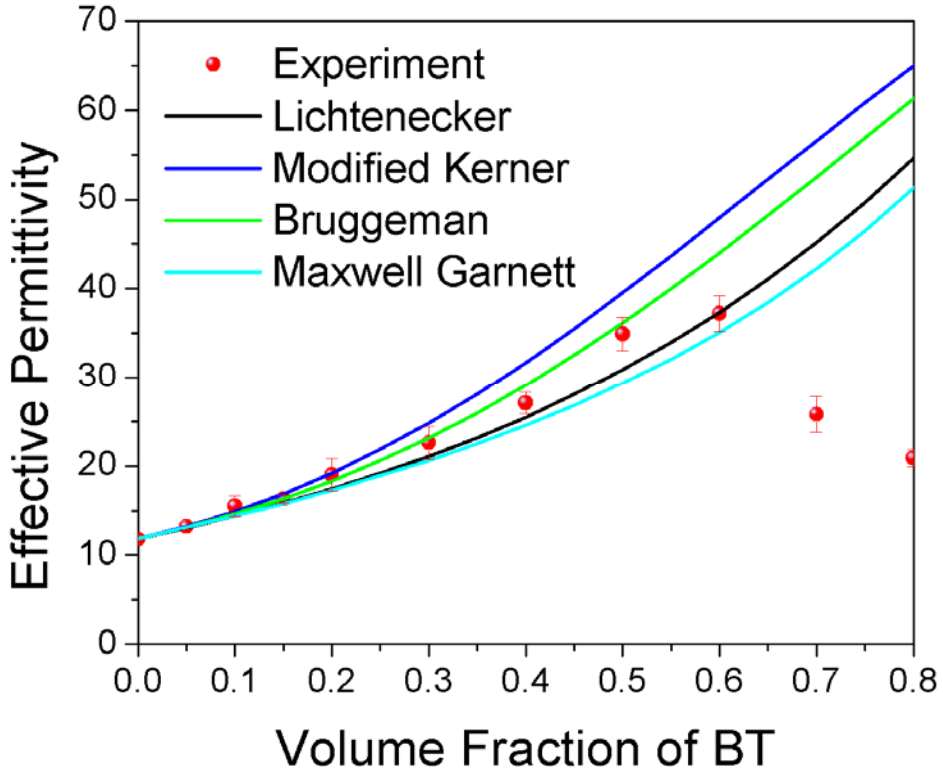

Figure 5.13 Comparison of measured permittivity (at 1 kHz) with simple theoretical models described in section 5.1.2. The permittivities for the nanoparticle filler and the host were 100 and 11, respectively.

Figure 5.14 compares the experimental values and the predicted dielectric properties using self-consistent effective medium approximation without considering the air voids in the nanocomposite. Similarly to other simple models, this model agrees very well with the experimental results at low volume fractions. However, the predicted effective permittivity values were overestimated at high nanoparticle volume fractions. Breakdown strengths predicted without considering the field fluctuation overestimated than the experimental results. When the field fluctuations are taken into account, calculation results are close to the experimental values but still did not show the sudden decrease at around 10 vol. %.

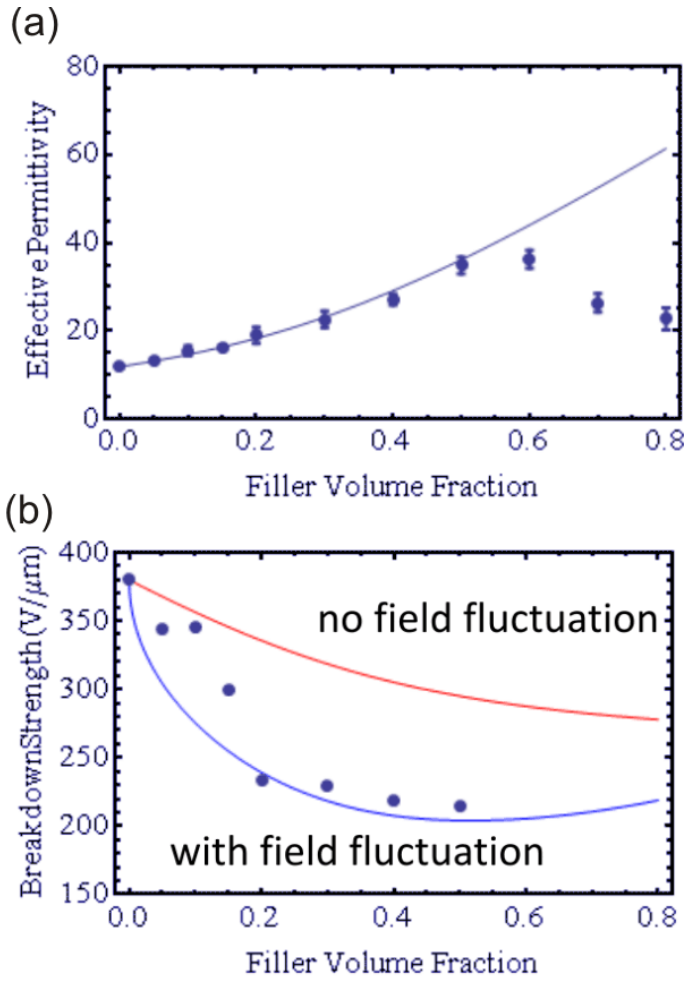

Figure 5.14 Comparison of permittivities (a) and breakdown strengths (b) predicted by using self-consistent effective medium approximation (lines) with experimental values (dots). The breakdown calculation results without field fluctuation and with field fluctuation are shown in red and blue, respectively.

A possible explanation for the decrease in the permittivity is the effect of the formation of air voids in the nanocomposite. It is well known that when composite materials are formed under kinetically controlled conditions, that the packing of particles is statistical in nature and the interstitial volume can significantly exceed that of a densely packed array of particles.(Schulze, Zaman et al. 2003; Calame 2006) The formation of air voids can be understood as follows: if the high permittivity nanoparticle fillers are

assumed to be hard spheres, then there is a certain volume fraction at which the total volume of ceramic fillers in a given space is at its maximum and can no longer increase due to tight packing and the incompressibility of the particles. Therefore, to fill up the given space, all the interstices between adjacent spherical fillers must be filled with a continuous phase, *i.e.* the host polymer. However, when we intend to put more nanoparticle fillers by increasing the volume ratio of filler to polymer, the net effect is a decrease in the polymer phase volume which inevitably creates voids inside the composite. This was predicted by JPC in his previous finite difference simulation, as shown in Figure 5.15.

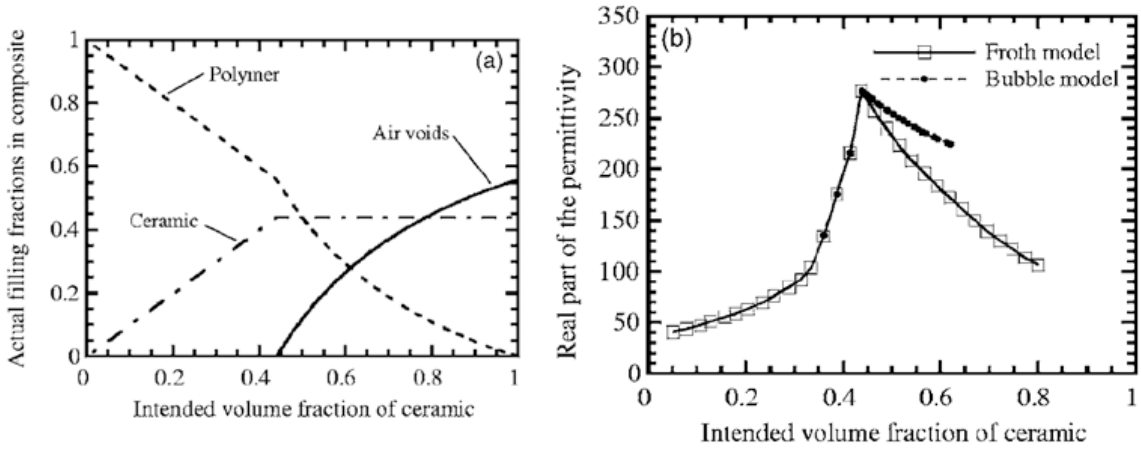

Figure 5.15 (a) Relationship between the actual filling fractions of filler, polymer, and air voids as a function of the intended volume fraction of the filler. (b) Corresponding simulation results for a randomly packed sphere composite considering the formation of air voids at high intended volume fractions (from Journal of Applied Physics)(Calame 2006).

Therefore, the porosity effect at high filling ratios should be taken into account to better explain the changes in the effective permittivity.

In the finite difference simulation for this particular system performed by JPC, the maximally filled model space contained 283 particles including partially placed particles, corresponding to a particle volume fraction of 0.397. Representative packings of particles in this model space at selected volume fractions are shown in Figure 5.16.

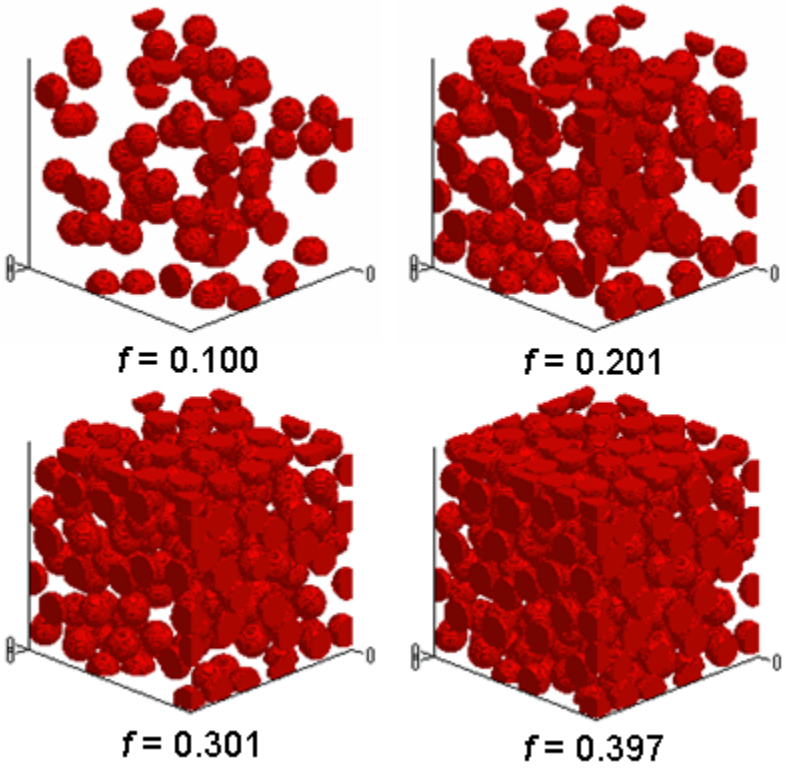

Figure 5.16 Examples of particle packing in finite difference simulations at different volume fractions. Note that at $f = 0.397$, a maximal number of spherical particles has been placed in a given model space and no additional particle can be added to this model space. The intended increase of particle volume fraction over $f = 0.397$ can only be made by decreasing the volume of host polymer, which inevitably creates air voids. (data from JPC)

This threshold volume fraction was used as the onset volume fraction of porosity in the nanocomposite. The total volume fraction of air voids were obtained by fitting the

previous air void volume calculation result described in Figure 5.15 (a) using a polynomial function with a threshold volume fraction (f_T) for the onset of the air void formation given below:

$$V(f) = a(f - f_T)^p \qquad \text{Equation 5.16}$$

where f is the volume fraction, f_T is the threshold volume fraction below which no void is formed (f_T = 0.397 from finite difference simulation), and a and p are fitting parameters. The fitting parameters were found to be a = 0.032 and p = 0.74331. Substituting these parameters in Equation 5.16 generated a void volume function. Using this void volume function, the actual volume fractions of each constituent (nanoparticle, host, and the air void) as a function of intended nanoparticle volume fraction can be calculated as shown in Figure 5.17.

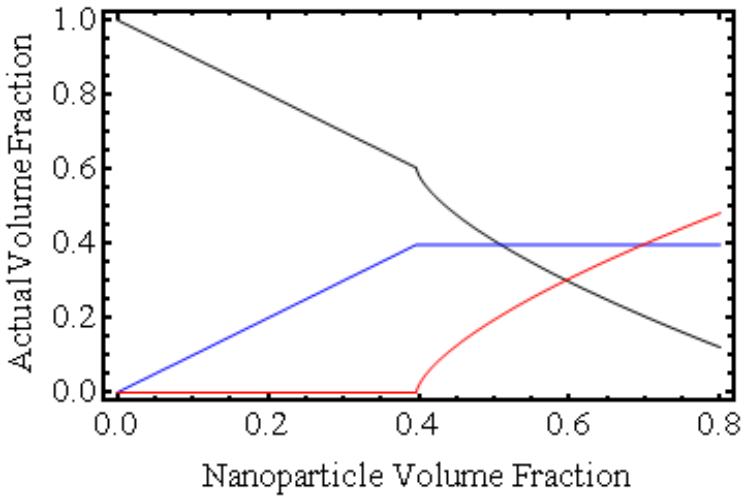

Figure 5.17 The volume fractions of nanoparticle (blue), polymer (black), and the air voids (red) as functions of intended nanoparticle volume fraction.

With these actual volume fractions, SC-EMT calculation was performed and the results are shown in Figure 5.18.

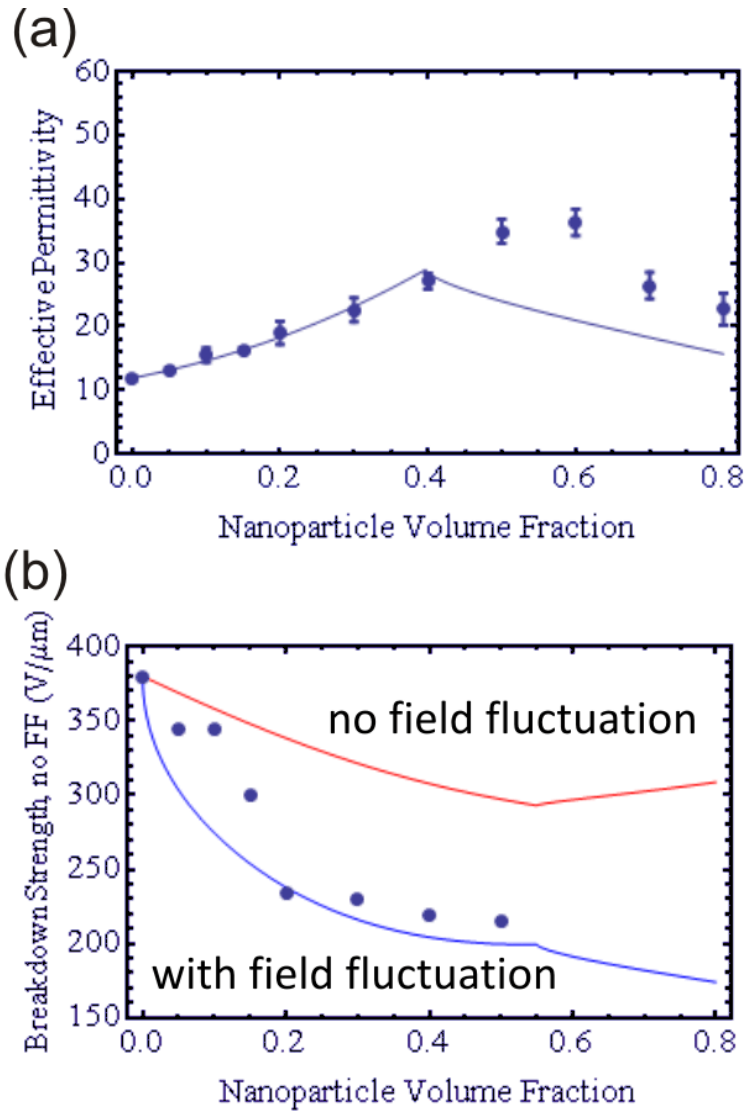

Figure 5.18 Comparison of permittivities (a) and breakdown strengths (b) predicted by combined self-consistent effective medium approximation and finite difference simulation (lines) with experimental values (dots). The breakdown calculation results without field fluctuation and with field fluctuation are shown in red and blue, respectively.

The void volume fraction function based on the finite difference simulation overestimated the amount of air voids as indicated by the premature and rapid decrease of the effective permittivity in Figure 5.18. This is due to the difference in the experimental procedure and the simulation. The films were produced by spin coating, which is

kinetically controlled condition. However, the films were thermally treated to allow the relaxation of nanoparticles to minimize the porosity of the film. This can effectively shift the threshold volume fraction of the rapid increase of the air void volume to a higher value than that from the calculated void volume function. In addition, the total air void volume fraction at low nanoparticle volume fractions cannot be practically zero and there should be very small but a certain level of porosity. Finally, the shape of the voids in the nanocomposites can be random but the effective medium calculation assumed it to be spherical. The consideration of the shape and the orientation of the voids relative to the applied electric field can also improve the dielectric breakdown calculation. All of these aspects need to be considered to improve the models.

Experimental determination of the void volumes at each volume fraction would help understand the actual trend of the void volume. X-ray tomography on the nanocomposite films was performed using a Dage XiDAT XD7600 NT digital X-ray tomography. However, the absolute point resolution (250 nm) was too large to determine the porosity. Density measurement can be also a way of determining the porosity. However, thick specimens need to be prepared using different film fabrication method, which no longer reflects the kinetically controlled film formation condition. Other possible experimental methods are a microscopic image analysis of the fractured cross-sections of statistically large number of samples and the measurement of the volume of a nanocomposite sample and its surface area using a gas adsorption/desorption experiment. SEM images shown in Figures 5.5 and 5.6 show that the porosity is not so significant up to 50 % of nanoparticles and the porosity is obvious above 60 % of nanoparticles. Based on this observation, the threshold volume fraction (f_T) in Equation 5.16 was adjusted to a more realistic value between 0.5 and 0.6. Figure 5.19 shows the actual volume fractions of each constituent with an adjusted threshold volume fraction (0.55).

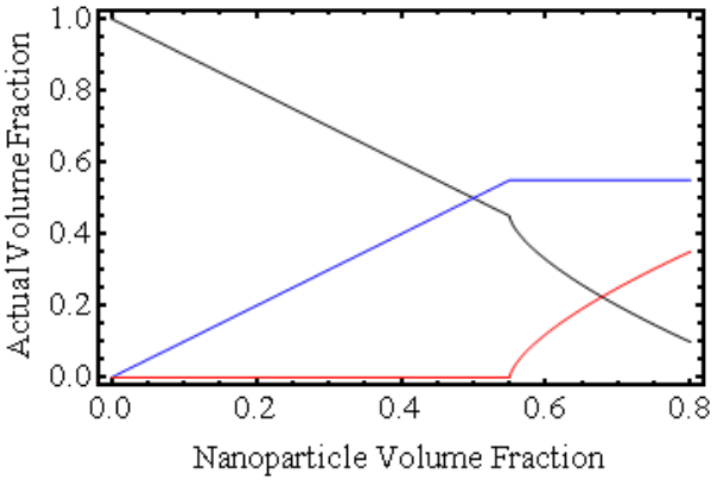

Figure 5.19 The actual volume fractions of nanoparticle (blue), polymer (black), and the air voids (red) as functions of intended nanoparticle volume fraction with adjusted threshold volume fraction of nanoparticles (0.55) for air void creation.

Using the adjusted volume fractions, the SC-EMT calculation resulted in a better agreement with the experimental values as shown in Figure 5.20.

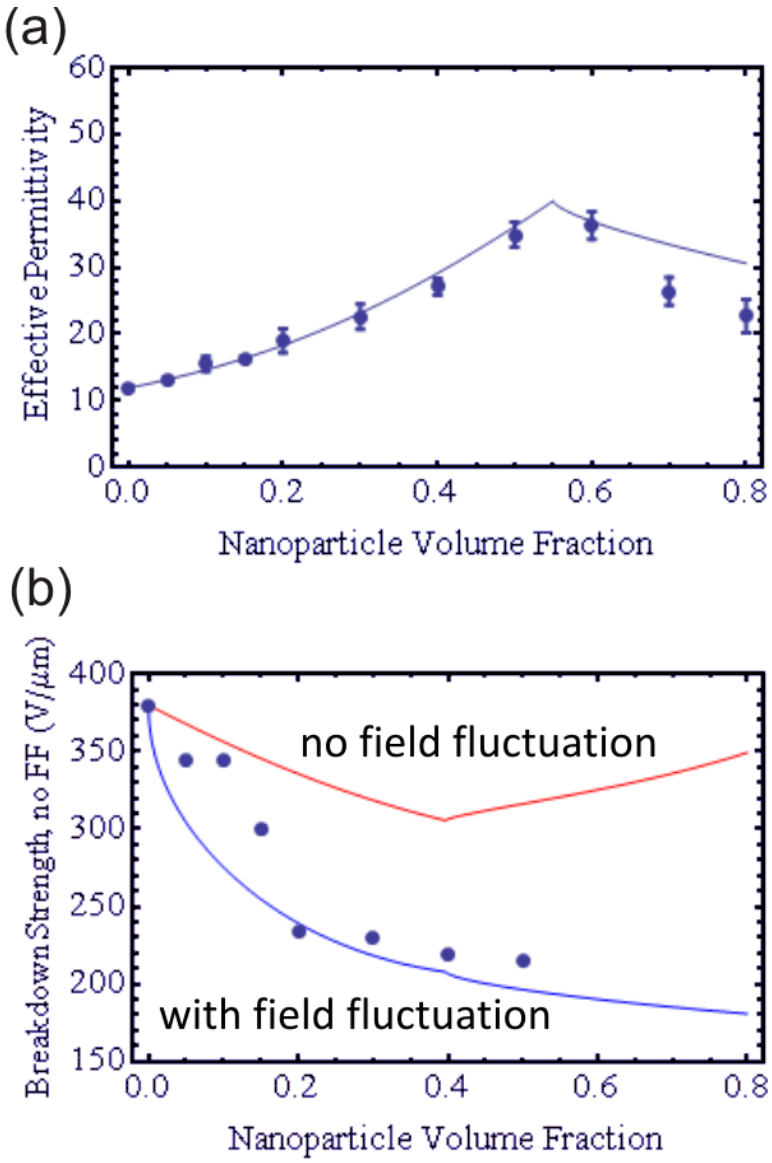

Figure 5.20 Comparison of permittivities (a) and breakdown strengths (b) predicted by combined self-consistent effective medium approximation and finite difference simulation (lines) with experimental values (dots) after adjusting the onset volume fraction based on SEM observation. The breakdown calculation results without field fluctuation and with field fluctuation are shown in red and blue, respectively.

Therefore, the combined self-consistent effective medium approximation and the finite difference simulation can be a good model to describe the dielectric properties of

nanocomposites especially with high nanoparticle volume fractions where air void has a significant role.

The breakdown behavior of high volume fraction (> 0.5) nanocomposites should be closely related to the relative volume fraction of air voids, which will significantly lower the breakdown strength of the nanocomposites due to the low breakdown strength of air (3 V/μm).(Davies, Dutton et al. 1965) It should be noted that the sudden drop of the breakdown strength at ~10 % volume fraction of nanoparticles was not very well predicted by the self-consistent effective medium theory. This seems to be closely related to the onset of the soft percolation. Breakdown requires a continuous percolating pathway of each local breakdown sites through the film.(O'Dwyer 1964) In a randomly packed nanocomposite, the average number of neighboring nanoparticles can be assumed to be approximately 10.(Rice 1998) Therefore, if there is at least one breakdown occurring out of ten neighboring sites, then the avalanche breakdown takes place. This can be modeled by using the finite difference simulation, in which the probability of the electric field enhancement relative to the applied electric field can be calculated. If we define the breakdown criteria as the local field exceeding the breakdown strength of pure host material, then the breakdown strength of the nanocomposites can be approximately calculated when the applied field induces about 10 % probability of the local field exceeding the breakdown strength of the host material.

5.3.4 Optimization of Volume Fraction for Maximum Energy Density

The expression for the maximum energy storage density of a capacitor is given by

$$U_{\max} = \frac{1}{2}\varepsilon_0 \varepsilon_{eff} \mathbf{E}_B^2 \qquad \text{Equation 5.17}$$

where ε_{eff} is the effective permittivity of the composite and $\mathbf{E}_B$ is the breakdown field. In order to have a maximum energy density, the nanoparticle volume fraction in a nanocomposite should be rationally chosen in such a way that the combination of the

effective permittivity and the breakdown strength give the maximum value of energy density. The maximum energy storage densities of the nanocomposite capacitors at each volume fraction of PFBPA-BT were calculated using Equation 5.17 and are plotted in Figure 5.21. The permittivity values measured at 1 MHz and the DC breakdown strength were used in the calculation.

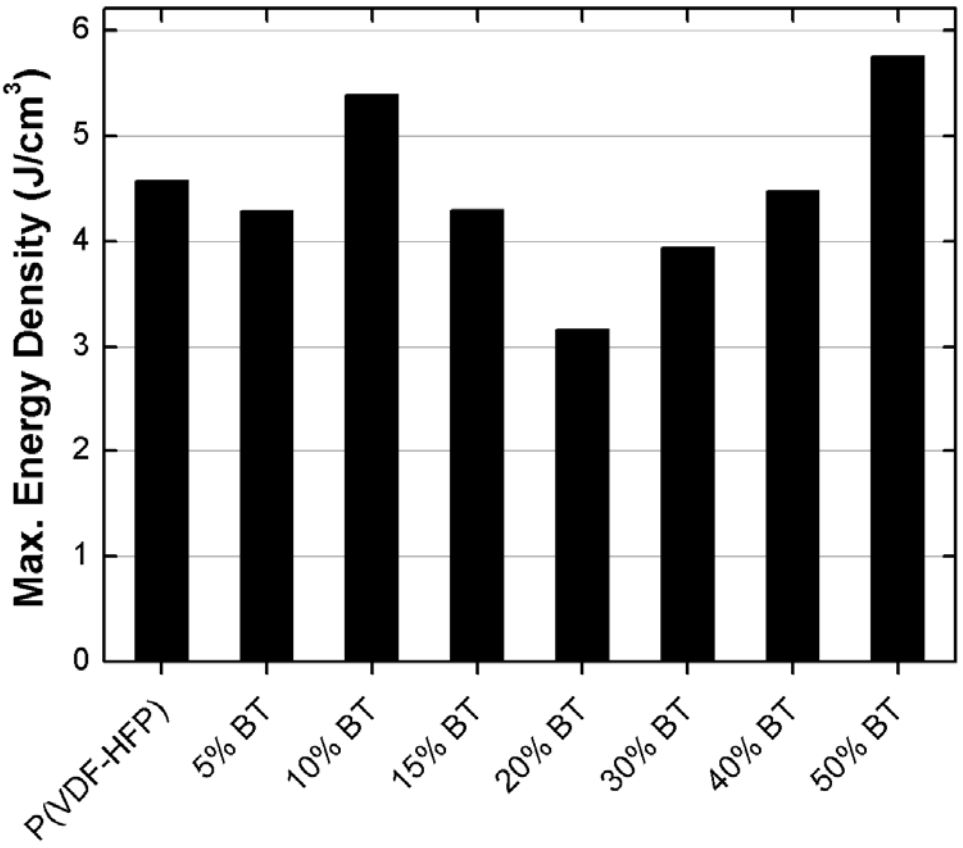

Figure 5.21 Maximum energy storage density of PFBPA-BT:P(VDF-HFP) nanocomposites with different nanoparticle volume fractions at 1 MHz.

The results indicate that a large energy storage density for PFBPA-BT:P(VDF-HFP) nanocomposites can be obtained with the nanoparticle volume fractions of 10 % and 50 %. Another important factor to consider in these types of nanocomposite is the dielectric loss. Typically, high-energy-density capacitors are used in peak pulse

applications requiring high frequency operation conditions. Dielectric materials with a large dielectric loss tend to dissipate its stored energy as a form of heat which can be detrimental to the device performance as premature thermal breakdown can occur. Therefore, 50 % nanocomposite may be desirable to have low loss characteristics. However, considering the energy storage per weight and the mechanical properties of the nanocomposite films, relatively low volume fraction is desirable. In this case, 10 % nanoparticle volume fraction seems to be the optimum volume fraction for PFBPA-BT:P(VDF-HFP) nanocomposites. The study of the effect of the nanoparticle volume fraction thus provides a guideline to find an optimum nanoparticle volume fraction depending on specific applications.

5.4 Conclusions

The volume fraction of nanoparticles in PFBAP-BT:P(VDF-HFP) nanocomposites has significant effect on both effective permittivity and the dielectric breakdown strength. The self-consistent effective medium theory model agreed well with the experimental findings when no significant porosity was present in the nanocomposites. However, at high nanoparticle volume fractions (>50 %), significant fractions of air voids were present in the nanocomposites, as observed by the decrease of the effective permittivity. Due to this porosity, high volume fraction nanocomposites are not desirable for higher energy storage density. The optimum volume fraction of BT nanoparticles for PFBPA-BT:P(VDF-HFP) nanocomposites was found to be about 10 % or 50 % for maximum extractable energy at 1 MHz, which requires further consideration of the dielectric loss and energy per weight depending on the target applications. This result provides a useful insight to designing and choosing the materials parameters in dielectric nanocomposites.

CHAPTER 6

NANOCOMPOSITE CAPACITORS BASED ON HIGH PERMITTIVITY POLYMER HOSTS

This chapter describes fabrication and characterization of nanocomposite capacitors based on surface-modified BT nanoparticles and high permittivity ferroelectric host materials.

6.1 Introduction

6.1.1 High Permittivity Polymers

The effective permittivity of a polymer/ceramic nanocomposite can be greatly enhanced by using high permittivity host polymers. Recently, ferroelectric polymers based on vinylidene fluoride (VDF) and the copolymers of poly(vinylidene fluoride) (PVDF) have gained interest as electro-active polymers and energy storage materials.(Zhang, Bharti et al. 1998; Bai, Cheng et al. 2000; Chu, Zhou et al. 2006; Faria, Welter et al. 2006; Ranjan, Yu et al. 2007) These materials exhibit very large permittivities (up to 50 at 1 kHz) due to their strong polarization originating from the microscopic domains with large dipole moment. In these semi-crystalline VDF-based polymers, the conformation of the backbone in crystalline phase can be in *all trans* configuration, in which the dipoles from the C-F bonds are aligned in one direction. This 'ferroelectric' conformation can exist over large macroscopic distances and form a ferroelectric domain.(He, Yao et al. 2005; Ranjan, Yu et al. 2007) When the backbone is in *gauch-trans* configuration, the orientations of the adjacent dipoles are anti-parallel to each other and the net dipole moment becomes zero. This gives rise to 'paraelectric'

conformation which can also exist over large distances and form a paraelectric domain, as shown in Figure 6.1.

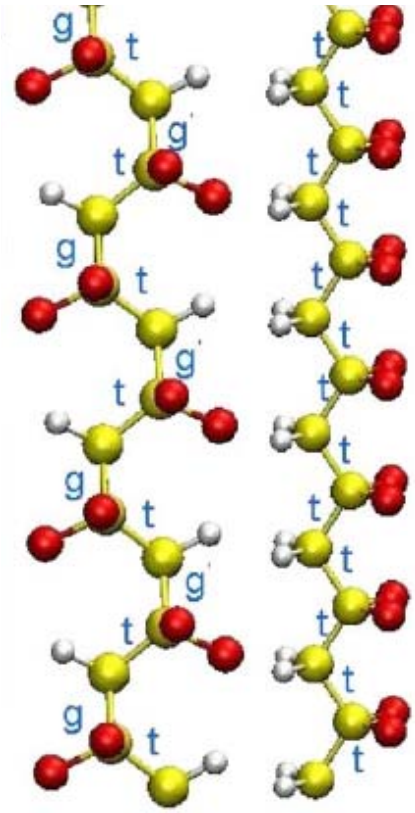

Figure 6.1. The two major crystalline structures of PVDF. The carbon, fluorine, and hydrogen atoms are yellow, red, and white, respectively. Left: paraelectric α phase with *gauchy-trans* conformation, in which all dipoles are summed to zero (anti-parallel). Right: ferroelectric β phase with *all-trans* conformation, in which the net dipole moment is non-zero.(Ranjan, Yu et al. 2007)

Similarly, polymers with repeating units containing a large dipole moment such as –CN bonds can exhibit large permittivity due to the anisotropic orientation of the dipoles. For example, cyanoethylated O-(2,3-dihydroxypropyl)-cellulose (cyanoethylpullulan (CEP)) has many cyanoalkyl side groups attached to pullulan, a polysaccharide polymer, that can

be aligned in one direction inducing a macroscopic non-zero polarization. Its permittivity at room temperature is close to 20 (at 1 kHz). (Figure 6.2)(Chiang and Popielarz 2002)

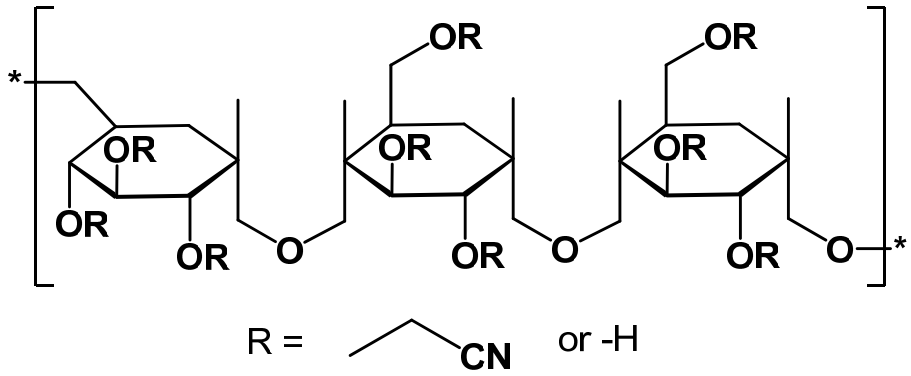

Figure 6.2 The structure of cyanoethylpullulan, CEP.

The phase transition temperature between ferroelectric (polar) and paraelectric (non-polar) crystalline domains in ferroelectric materials is called the Curie temperature, and around this temperature, a dielectric anomaly is typically observed.(Kittel 1996) Therefore, many research efforts have been devoted to control the Curie temperature close to the application temperatures to obtain a very high dielectric response. The incorporation of trifluoroethylene (TrFE) into PVDF brings the transition temperature below the melting point of the polymer. Introduction of a small amount of slightly bulky, chlorinated monomer, such as chlorotrifluoroethylene (CTFE), into P(VDF-TrFE) copolymers further decreases the Curie temperature close to room temperature by reducing the crystalline domain size and the energy barrier to phase transition. The thermal and electrical properties of this terpolymer, P(VDF-TrFE-CTFE), are very sensitive to the chemical composition. However, due to the quite different reactivity of TrFE compared to VDF and CTFE, the resulting terpolymers usually show a broad distribution of compositions and inhomogeneous crystalline domains leading to a broad distribution of phase transition temperatures. Since the ratio cannot be simply controlled by changing the monomer feed ratio, the preparation of these polymers with well-

controlled chemical compositions has been a big challenge. Q. Wang et. al introduced a modular approach, allowing a systematic and straightforward control of the chemical structures of P(VDF-TrFE-CTFE) terpolymers and thus their dielectric properties, as described in Figure 2.6.(Lu, Claude et al. 2006)

6.2 Materials and Methods

In this study, a terpolymer, P(VDF-CTFE-TrFE), with 78.8 mol% VDF, 7.2 mol% TrFE, and 14.0 mol% CTFE, prepared in Q. Wang's group at Penn State, was used. This terpolymer exhibits room-temperature dielectric constant of 50 and a low dielectric loss (tan δ<0.05 at 1 kHz) below 10 kHz. Initially, two different barium titanate nanoparticles, BT (30~50 nm, Aldrich) and BT8 (120 nm, Cabot Corp.), were used to prepare nanocomposite thin films. Nanocomposite solutions were prepared by first ball milling various amounts of pentafluorobenzyl phosphonic acid-modified $BaTiO_3$ in *N,N*-dimethylformamide (DMF) for one day, then the P(VDF-CTFE-TrFE) terpolymer was added to the dispersion. This was followed by further ball-milling (3-5 days). Thin films were then fabricated by spin coating the nanocomposite solution onto aluminum-coated glass substrates that were surface treated with cold plasma to ensure cleanliness and wettability of the surface. The films were then soft baked at 100°C for one minute on a hot plate and then hard baked at 120°C overnight in a vacuum oven. The films thicknesses were measured using a Tencor KLA P15 contact profilometer. Capacitors were fabricated using a Kurt J. Lesker PVD75 Filament Evaporator in order to deposit a top electrode (Al, 500nm) of known area through a shadow mask onto the thin film. An Agilent 4284A LCR meter was used to measure the capacitance and dielectric loss of the devices as a function of frequency from 20Hz to 1MHz. An Agilent E5272A two-channel source meter unit was used to measure leakage current. All electronic characterizations were performed in a nitrogen-filled dry box. The morphology of the samples was viewed using a Scanning Electron Microscope (SEM).

6.3 Results and Discussion

6.3.1 Dielectric Properties of High Permittivity Hosts

The dielectric spectroscopy results of selected high permittivity host polymers are shown in Figure 6.3 and in Table 6.1. In general, high permittivity polymers showed large dielectric losses above 10 kHz making these materials not desirable for peak pulse applications that typically require low dielectric loss, ideally less than 3%, at 1 MHz. However, the dielectric losses below 10 kHz are less than 5 %, which still makes these materials potentially useful for high-energy-density capacitors. Moreover, the dielectric loss can be further reduced and the permittivity can be further increased at these frequencies by doping these materials with barium titanate nanoparticles.

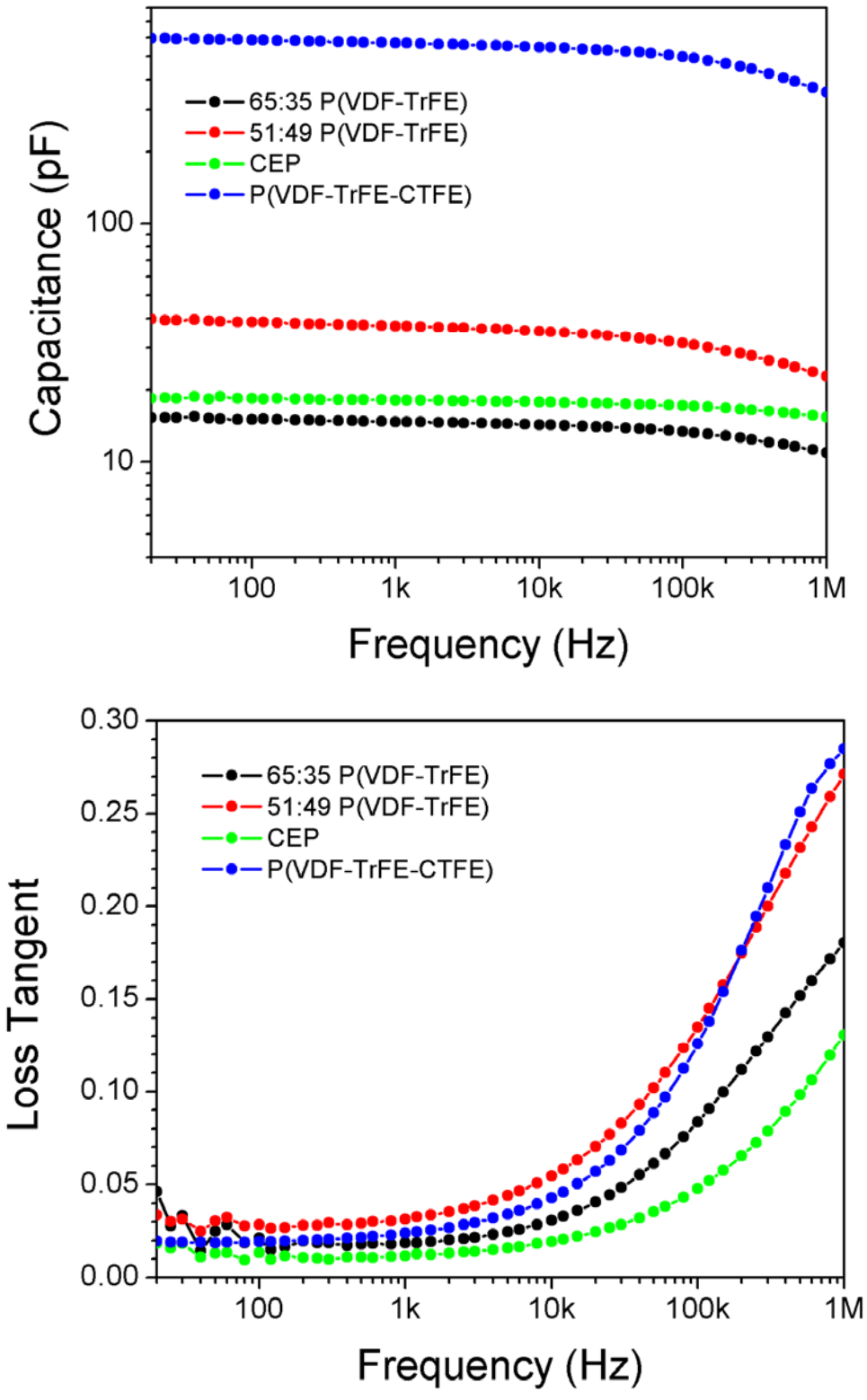

Figure 6.3 Dielectric spectroscopy of selected high permittivity polymer host materials.

Table 6.1 Properties of selected host polymers.

Host Polymer	permittivity (at 1 kHz)	solvent
polycarbonate	3	pyridine
P(VDF-HFP)	11.9	DMF
65:35 P(VDF-TrFE)	~14	DMF
51:49 P(VDF-TrFE)	~14	DMF
CEP	18.5	pyridine
P(VDF-TrFE-CTFE)	32.3[†]	DMF

[†]highly sensitive to the measurement temperature.

The film forming properties of VDF-based co-polymers were not so great mainly due to the semi-crystalline nature of these materials. Due to the hydrophilic nature of CEP, it formed excellent quality thin films by spin coating. The permittivity was fairly high with relatively lower dielectric loss at high frequency than other high permittivity host polymers. However, CEP showed large leakage current primarily due to the presence of cyano groups that can be easily ionized. Both 65:35 and 51:49 P(VDF-TrFE) exhibited slightly higher permittivities than P(VDF-HFP) but their spin-coated films did not result in good quality films. Though the dielectric response of P(VDF-TrFE-CTFE) was very sensitive to the temperature, it showed very large permittivity and low leakage current and the film forming property using spin-coating was better than P(VDF-TrFE). For these reasons, P(VDF-TrFE-CTFE) was chosen for further investigation to make high permittivity barium titanate nanocomposites.

6.3.2 Characterization of PFBPA-BT in P(VDF-TrFE-CTFE) Nanocomposites

The nanocomposites of P(VDF-TrFE-CTFE) showed strong dependence on the measurement temperature as shown in Figure 6.4. The permittivity results marked at RT (room temperature) were obtained at ambient condition without active control of

temperature. The actual temperature may have been different from sample to sample due to the heating effect from the illumination lamp during the measurement. The results with active temperature control showed similar behavior to the PFBPA-BT in P(VDF-HFP) nanocomposites. The compatibility of PFBPA-BT in P(VDF-TrFE-CTFE) was not as good as in P(VDF-HFP) and so was the quality of the resultant nanocomposite thin films.

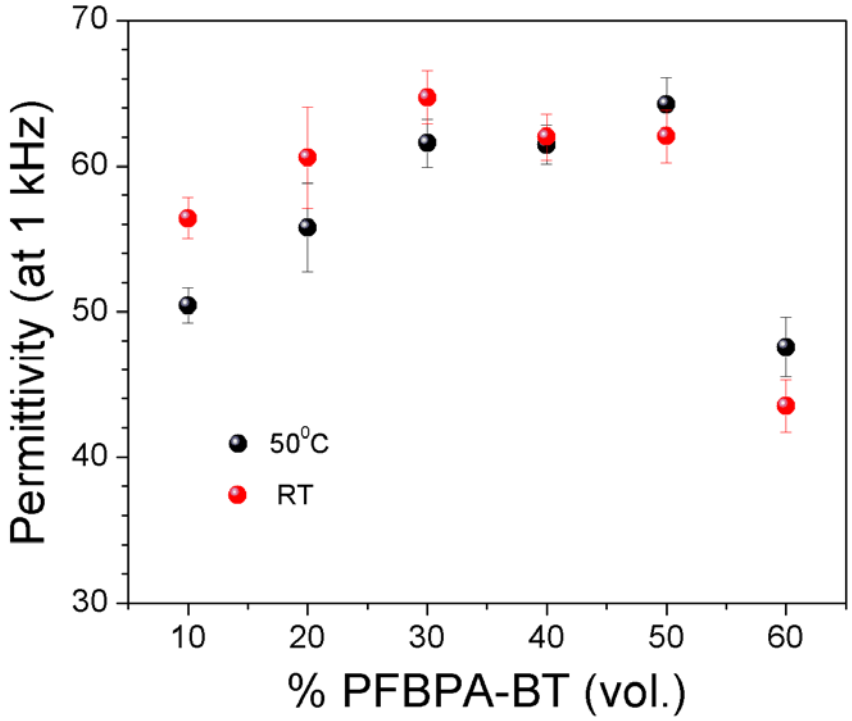

Figure 6.4 The effective permittivity of PFBPA-BT:P(VDF-TrFE-CTFE) nanocomposites characterized at different temperature. Average values were taken from multiple measurements.

The dielectric loss is typically expressed using the loss tangent which is defined as the ratio of the imaginary part to the real part of permittivity. The frequency-dependent dielectric loss is mainly related to the polarization mechanisms.(Zaky and Hawley 1970) The switching of ferroelectric domains in vinylidene fluoride-based

polymers that gives rise to high permittivity is too slow to catch up with the high frequency AC over 10 kHz (Debye relaxation). Materials with a high dielectric loss are not suitable for high frequency applications, since these materials usually generate a lot of heat due to the large dielectric loss. Figure 6.5 shows the dielectric spectroscopy (20 Hz – 1 MHz) of 10 – 60 vol. % PFBPA-BT:P(VDF-TrFE-CTFE) nanocomposites showing the strong temperature-dependence of the host polymer's dielectric response. The dielectric loss was mainly originated from the host polymer as the dielectric loss gradually decreased with decreasing the amount of the polymer in the nanocomposite.

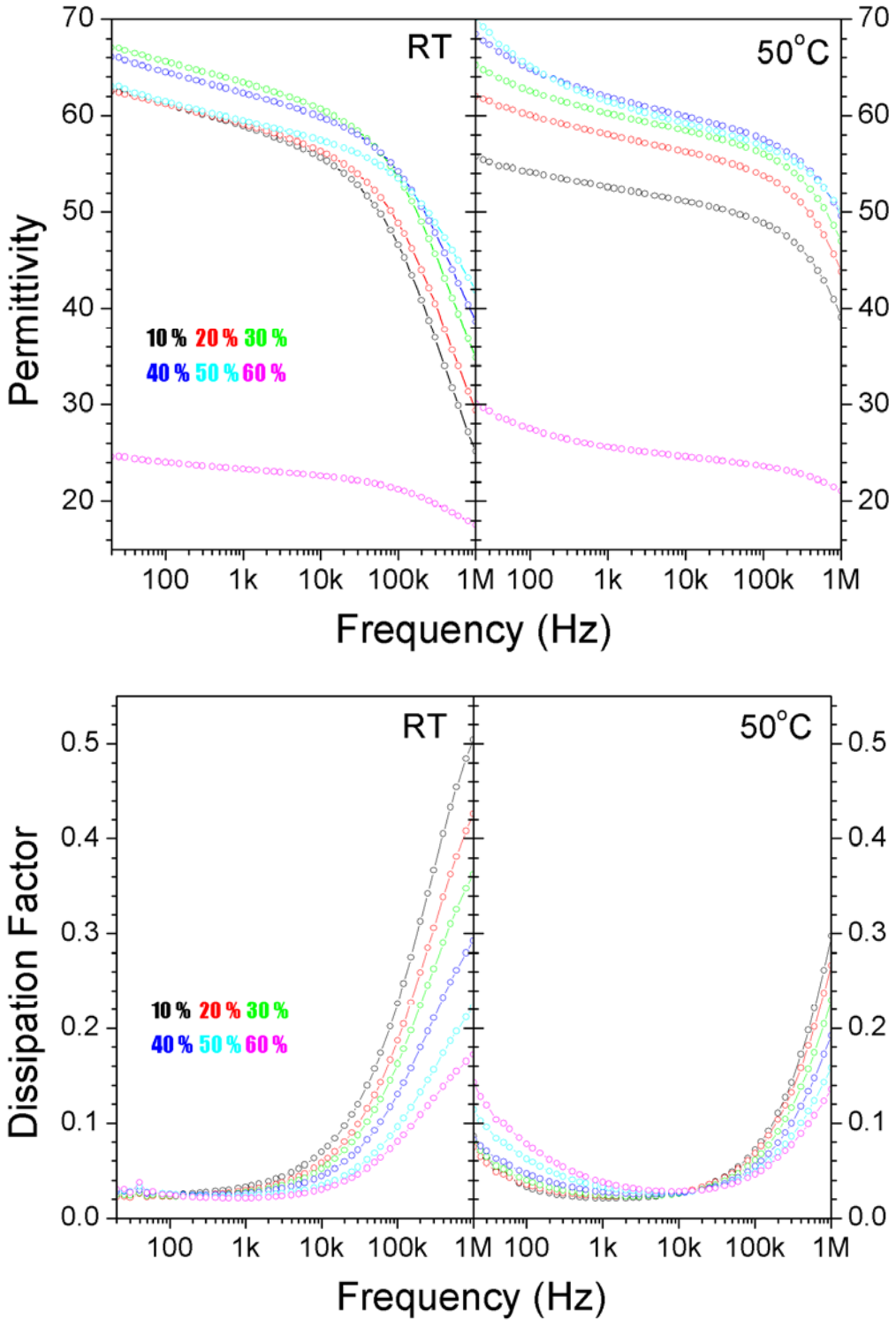

Figure 6.5 Dielectric spectroscopy of 10 – 60 vol. % PFBPA-BT:P(VDF-TrFE-CTFE) nanocomposites at room temperature and at 50°C. Dissipation factor is an alternative term for the loss tangent and has the same physical meaning.

Temperature dependent-dielectric spectroscopy (25 – 150°C) for a 50 % PFBPA-BT:P(VDF-TrFE-CTFE) nanocomposite capacitor revealed the details of dielectric loss characteristics. Although, the frequency window used for this study (20 Hz – 1 MHz) was too narrow to see the actual peak of the dielectric loss, it is obvious that there are two dielectric resonance peaks gradually shifting toward high frequency with increasing the temperature. (Figure 6.6) Increasing the temperature of the material reduces the viscosity of the materials, which in turn makes the response of reorienting dipoles of the ferroelectric terpolymer faster. This effectively shifts the peak of the dielectric loss toward higher frequency with increasing the temperature.(Ang and Yu 2004) There should be no significant effect on this temperature-dependent behavior from the BT nanoparticles as they are in cubic phase and paraelectric.

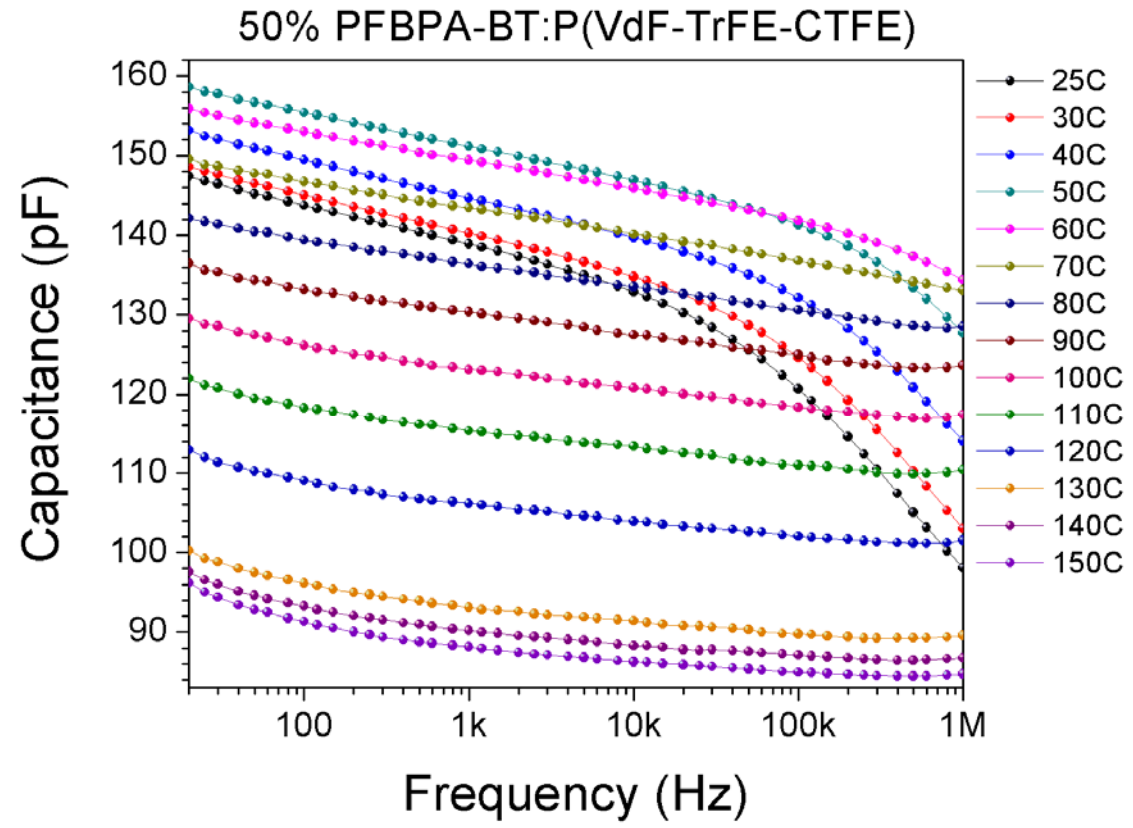
50% PFBPA-BT:P(VdF-TrFE-CTFE)
Capacitance (pF)
160
150
140
130
120
110
100
90
100
1k
10k
100k
1M
Frequency (Hz)
25C
30C
40C
50C
60C
70C
80C
90C
100C
110C
120C
130C
140C
150C

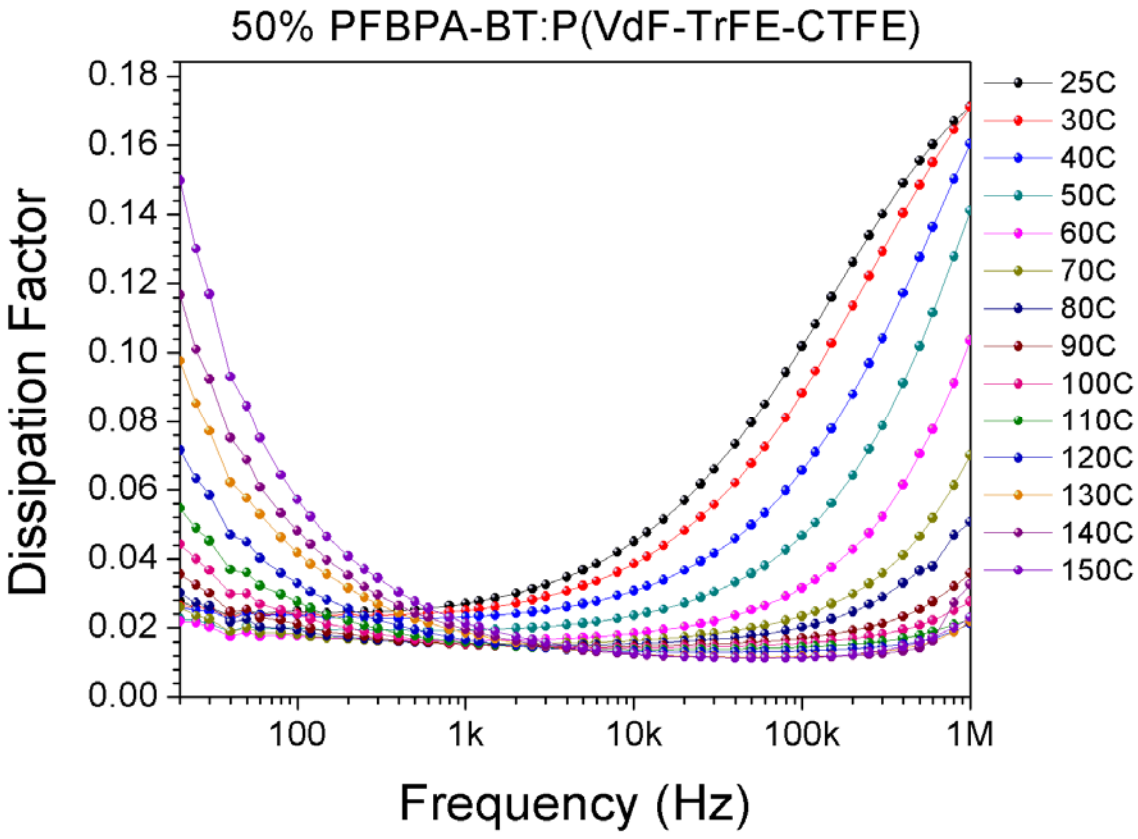
50% PFBPA-BT:P(VdF-TrFE-CTFE)
Dissipation Factor
0.18
0.16
0.14
0.12
0.10
0.08
0.06
0.04
0.02
0.00
100
1k
10k
100k
1M
Frequency (Hz)
25C
30C
40C
50C
60C
70C
80C
90C
100C
110C
120C
130C
140C
150C

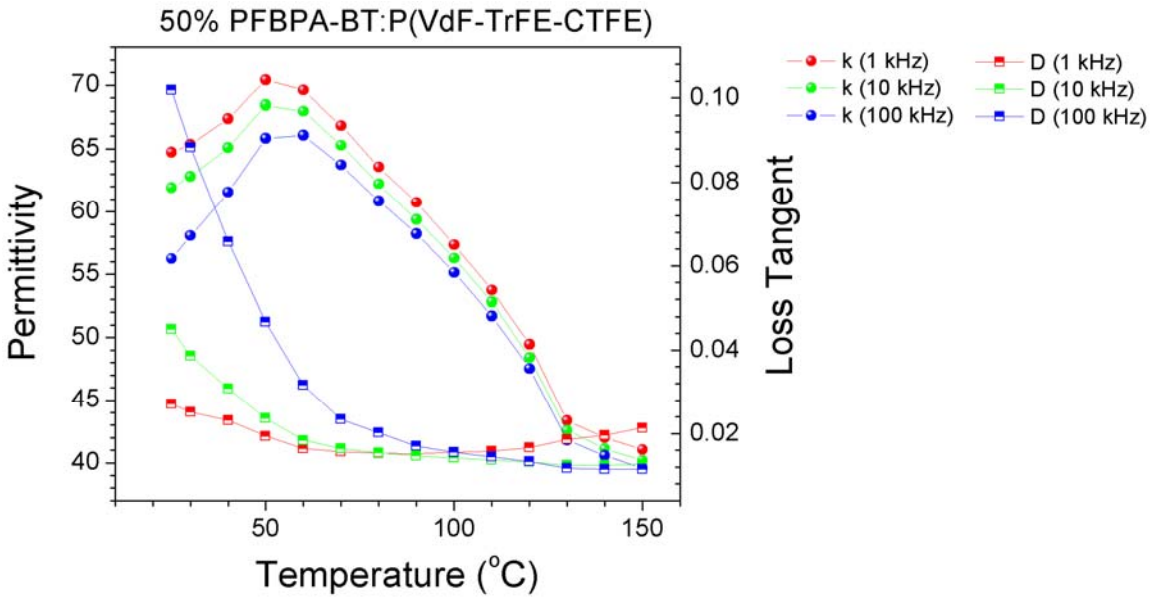

Figure 6.6 Temperature-dependent dielectric characteristics of 50 % PFBPA-BT:P(VDF-TrFE-CTFE) nanocomposite (k: permittivity, D: dissipation factor or loss tangent).

6.3.3 The Effect of Particle Size

The nanocomposites with high volume fractions (50, 60, and 70 vol. %) of PFBPA-BT (30 – 50 nm) and PFBPA-modified BT-8 (120 – 150 nm) were prepared to compare the effect of high permittivity fillers on the effective permittivity of nanocomposites in P(VDF-TrFE-CTFE) host. (Figure 6.7) An average dielectric constant of 111.0 was achieved for 50% volume loading of PFBPA-BT-8 in this high permittivity polymer, which is the highest permittivity reported so far based on nano-sized $BaTiO_3$ particles dispersed in a polymer host. The measured permittivity values are approximately twice of the effective permittivity values obtained using PFBPA-BT-8 in P(VDF-HFP) as host polymer (permittivity = 11.9), showing the importance of increasing the host permittivity. The effect of increasing the permittivity of the filler by a factor of approximately 10 is also reflected by nearly doubled effective permittivities at each volume fraction. However, this effect was less significant than that of increasing the host permittivity (factor of 4 increase gave doubling of the effective permittivity). Larger

permittivities based on barium titanate/polymer nanocomposites, based on micron-sized $BaTiO_3$ particles and high permittivity host polymer, have been reported so far: 130 with 51 vol. % of ~2 μm $BaTiO_3$ in CEP)(Chiang and Popielarz 2002) and ~120 with 60 vol. % of bimodal (micron-sized and nano-sized) $BaTiO_3$ particles in PVDF.(Dang, Xie et al. 2007) Qing Wang et. al recently reported the fabrication and properties of nanocomposites using nano-sized $BaTiO_3$ (50 – 70 nm, permittivity = 180 at 1 kHz), modified with ethylene diamine, dispersed in the same terpolymer host material discussed in this chapter. The highest permittivity they achieved was only about 55 from a 30 vol. % nanocomposite.(Li, Claude et al. 2008)

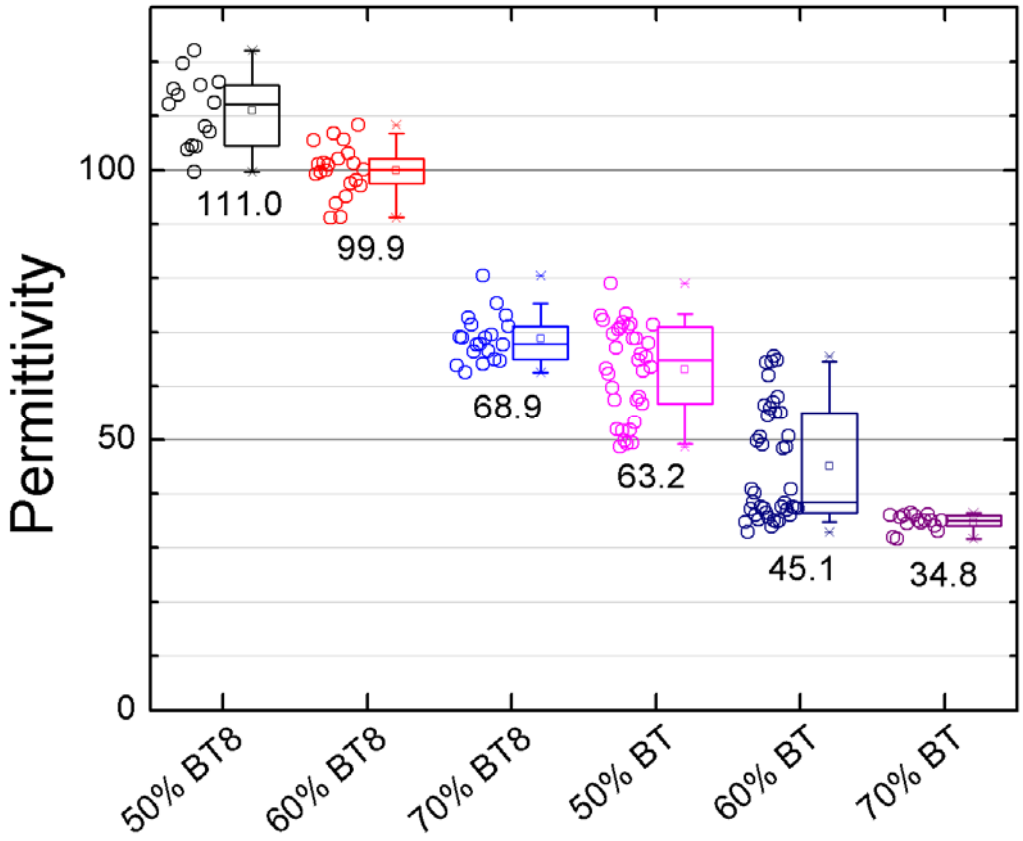

Figure 6.7 Dielectric constants (at 1 kHz) of P(VDF-TrFE-CTFE) and the nanocomposites containing 50, 60, and 70 % of PFBPA-modified BT and BT8 nanoparticles by volume.

The effective permittivity of the nanocomposites examined in this volume fraction range decreased as the percent loading of nanoparticles increased, due to the creation of voids. SEM images of nanocomposite films revealed that the microscopic film quality was greatly dependent on the volume loading of the nanoparticles as shown in Figure 6.8. With increasing volume fractions, the nanocomposite films exhibited many defective areas with cracks and voids, especially at 60% and 70% volume loading, supporting the decreasing trend in the effective permittivity with increasing nanoparticle volume fraction.

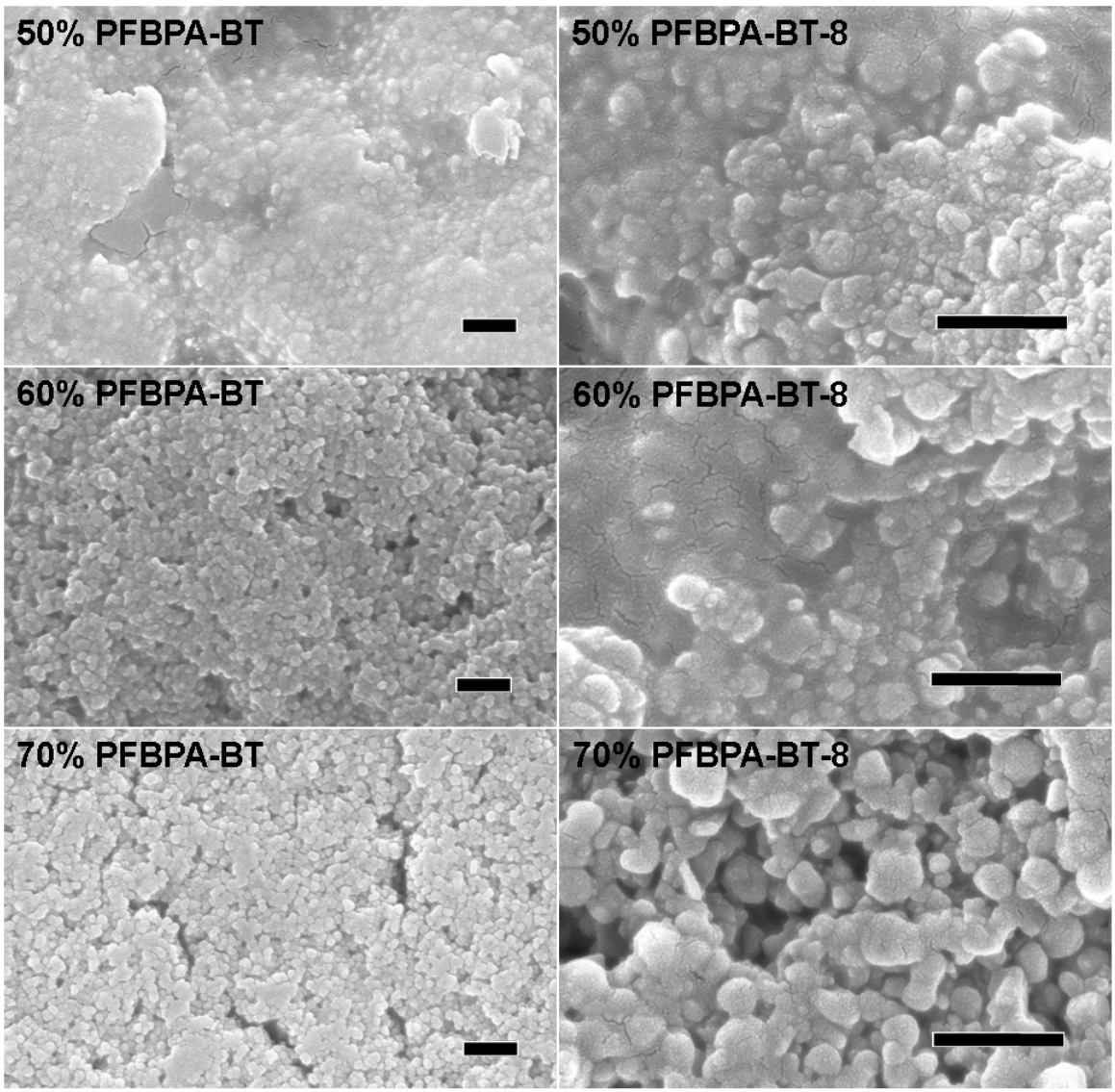

Figure 6.8 SEM images of P(VDF-TrFE-CTFE) nanocomposites with PFBPA-BT and PFBPA-BT-8. Scale bars: 300 nm.

Frequency-dependent dielectric response data on these nanocomposites again confirmed that the dielectric loss is mainly from the host polymer. (Figure 6.9) As the volume percent loading of BT and BT-8 nanoparticles increases, the dielectric loss decreased in both cases.

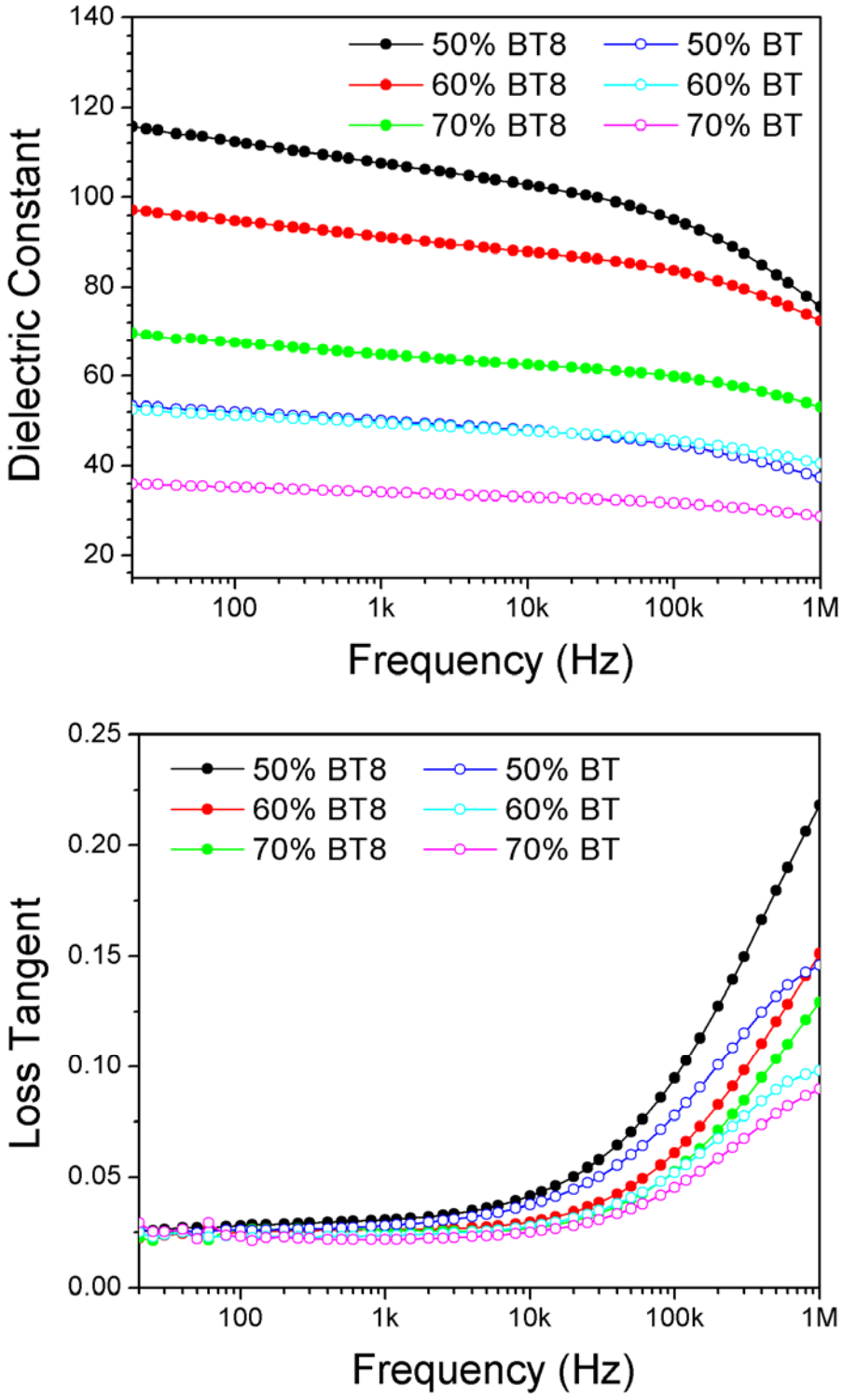

Figure 6.9 Dielectric spectroscopy of high volume fraction P(VDF-TrFE-CTFE) nanocomposites containing PFBPA-BT and PFBPA-BT.

The breakdown measurements shown in Figure 6.10 on the nanocomposites showed thickness-dependent strength. When the film was relatively thin (~ 1 μm), the thermal stress induced by the applied field is not effectively dissipated and led to premature thermal breakdown. In contrast, when the film was thick, the breakdown strength was much higher even for a high volume fraction nanocomposite. Therefore, to obtain meaningful dielectric breakdown strength data, at least 2~3 μm thick nanocomposite films are desirable.

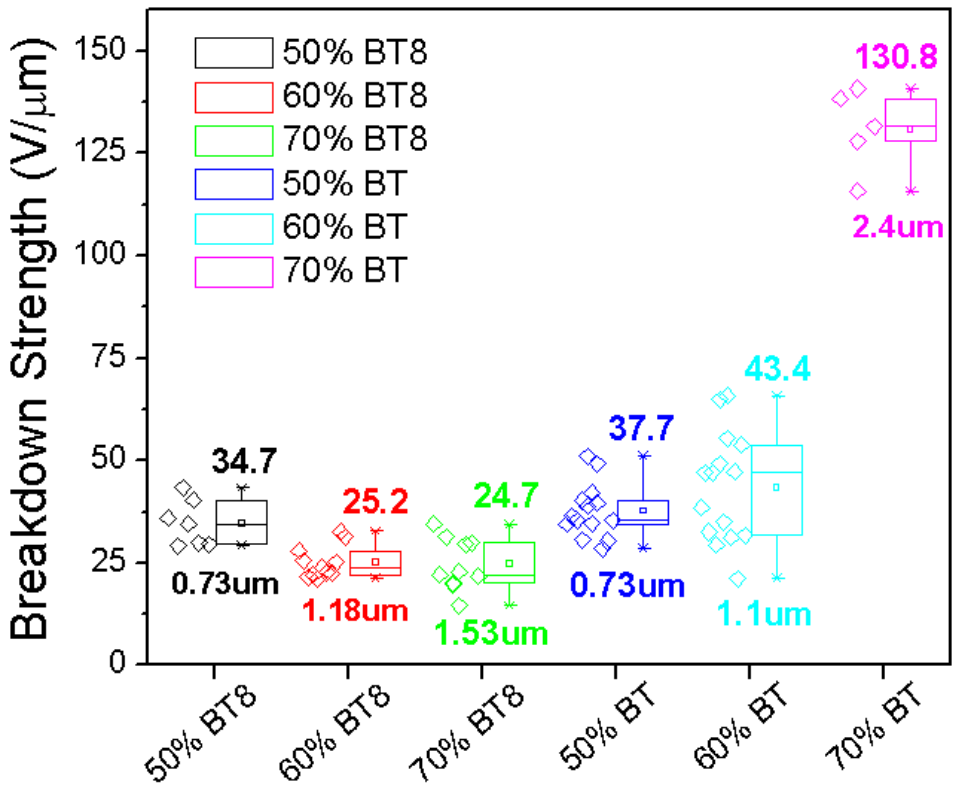

Figure 6.10 Dielectric breakdown strengths of surface modified barium titanate nanocomposites in P(VDF-TrFE-CTFE).

When large volume fractions of nanoparticles are used, there are large interstitial volumes between nanoparticles. By combining large size and small size nanoparticles (bimodal packing), the interstitial volume between large nanoparticles can be filled with

small nanoparticles. Bimodal packing of PFBPA-BT-8 (120 – 150 nm) and PFBPA-BT (30 – 50 nm) with 5:1 volume ratio was used to improve the packing density of nanoparticles in P(VDF-TrFE-CTFE) host as shown in Figure 6.11. However, the packing was not so greatly improved possibly due to the small size difference between the two nanoparticles.

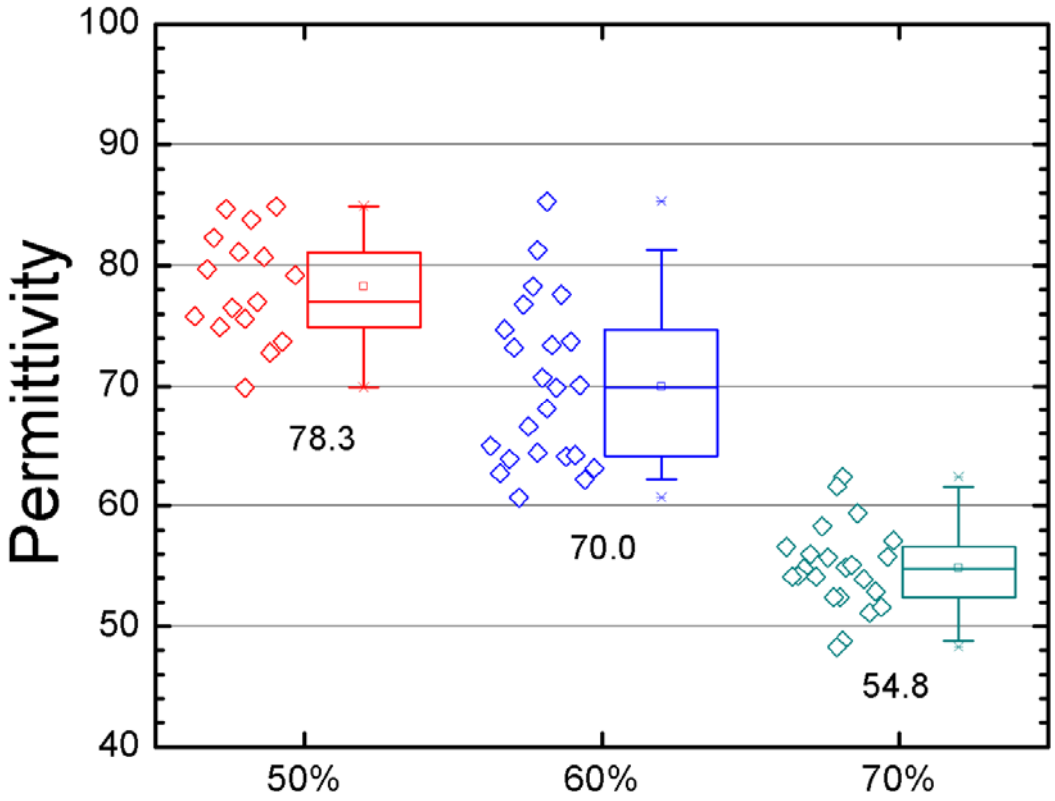

Figure 6.11 Effective permittivity (at 1 kHz) of bimodally filled PFBPA-BT:P(VDF-TrFE-CTFE) as a function of total nanoparticle volume fraction. The volume ratio of large BT nanoparticle (PFBPA-BT-8) to small BT nanoparticle (PFBPA-BT) in each nanocomposite was kept to be 5:1.

6.4 Conclusions

Ferroelectric terpolymer, P(VDF-TrFE-CTFE), exhibits a large permittivity, low leakage current, and fairly good solution processability. When combined with surface modified barium titanate (BT-8, 120 – 15 nm), a very large effective permittivity (111.0 at 1 kHz) was measured based on barium titanate/polymer nanocomposite. This value is the highest permittivity reported so far based on nano-sized $BaTiO_3$ particles dispersed in a polymer host. P(VDF-TrFE-CTFE), however, showed a large dielectric loss above 10 kHz and the dielectric response was very sensitive to the temperature. PFBPA may not be the best structure of the surface modifier in this host polymer as observed in the processability of the nanocomposite and the microstructure analysis by SEM. For this reason, reasonably good quality of 2 – 3 μm thick films were very challenging to fabricate and the dielectric breakdown study was not completed. Bimodal packing of large and small sized barium titanate nanoparticles resulted in the permittivity values in between the cases of using only large and only small barium titanate nanoparticles. This may be also due to the mediocre compatibilizing capability of PFBPA surface modification in this matrix.

CHAPTER 7

PRINTABLE HIGH PERMITTIVITY NANOCOMPOSITE GATE INSULATORS FOR ORGANIC FIELD-EFFECT TRANSISTORS

This chapter describes the application of nanocomposites based on surface-modified $BaTiO_3$ and a cross-linkable polymer to solution-processable thin film gate dielectrics in organic field-effect transistors (OFETs).

7.1 Introduction

7.1.1 Organic Field-Effect Transistors

Organic field-effect transistors (OFETs) are rapidly gaining interest as building blocks for printable and flexible electronics, which have many advantages over conventional silicon based technology, such as low cost, light weight, large area, and flexible form factors. OFETs are excellent candidates for radio-frequency identification (RFID) tags, driving circuits for electronic paper (e-Paper), flat panel displays, and flexible analog circuits for power management.(Bao and Locklin 2007)

The three fundamental components in an OFET are the contacts (source, drain, and gate), the organic semiconductor, and the gate dielectric layers. The typical geometries of these components are shown in Figure 7.1.(Facchetti, Yoon et al. 2005)

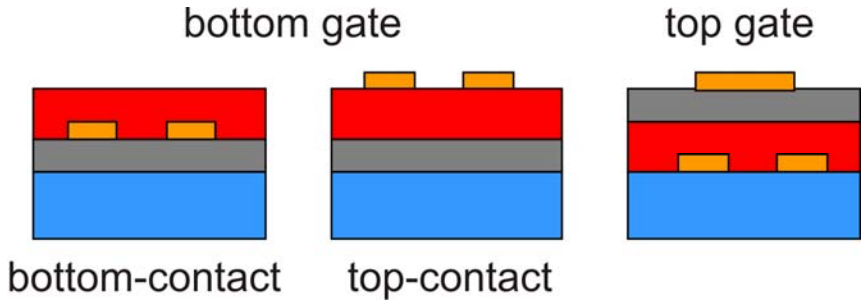

Figure 7.1 Typical device geometry of OFETs.

In this study, bottom-gate and bottom-contact geometry that can be readily applied to a large area substrate is employed. The source electrode is usually defined as a ground electrode, and the current between source and drain is called drain current (I_{DS}) which is defined as below.(Wilk, Wallace et al. 2001)

$$I_{DS,linear} = \frac{W}{L}\mu C\left((V_{GS} - V_T)V_{DS} - \frac{V_{DS}^{\ 2}}{2}\right) \qquad \text{Equation. 7.1}$$

where W is the channel width, L is the channel length, μ is the carrier mobility (electron mobility for *n*-type and hole mobility for *p*-type semiconductor) of the organic semiconductor (assumed to be constant), C is the capacitance density of the gate insulator layer, V_{GS} is the gate-source voltage, V_T is the threshold voltage, and V_{DS} is the drain-source voltage. Initially, I_{DS} increases linearly with V_{DS} until it saturates when $V_{DS,sat} = V_G - V_T$ ('pinch-off') to yield a saturated drain current $I_{DS,sat}$.(Wilk, Wallace et al. 2001)

$$I_{DS,sat} = \frac{W}{L}\mu C\frac{(V_{GS} - V_T)^2}{2} \qquad \text{Equation 7.2}$$

The range of the term (V_G - V_T) is limited by the reliability of the operation. Excessive gate voltage induces a high electric field across the dielectric layer that can cause high gate leakage current and eventually the breakdown of the insulator. V_T cannot be infinitely reduced, due to the statistical fluctuations in thermal energy (k_{BT}). Therefore, I_{DS} can be increased by increasing W/L ratio, increasing the carrier mobility, μ, and increasing the capacitance of the gate dielectric, C.

Ignoring quantum mechanical and depletion effects, the maximum possible electric displacement that the gate insulator can sustain is given as

$$D_{\max} = \varepsilon_0\varepsilon_r\mathbf{E}_B \qquad \text{Equation 7.3}$$

where ε_r is the dielectric constant, $\mathbf{E}_B$ is the dielectric breakdown field of the gate insulator. Considering the parallel-plate capacitor-like geometry of the gate insulators in an OFET, the capacitance is expressed as

$$C = \varepsilon_0 \varepsilon_r \frac{A}{t} \qquad \text{Equation 7.4}$$

Thus, not only the dielectric constant, but also the thickness of the gate dielectric layer, and its dielectric breakdown strength govern the magnitude of the capacitance of the gate insulator. Conventionally widely used SiO_2 gate insulators have a dielectric constant of only 3.9. The carrier mobilities of organic semiconductors are now competitive with that of amorphous Si (~1 $cm^2/V \cdot sec$). Therefore, on such low-ε_r gate insulators, typically a large source-drain or source-gate voltages are required to obtain a useful magnitude of I_{DS}. This is not desirable, due to excessive power consumption. Therefore, a viable approach to increase I_{DS} while maintaining a low bias voltage is to increase the capacitance density of the gate dielectric.

The carrier mobility and threshold voltage can be derived from a linear fitting of $(I_{DS})^{1/2}$ *vs.* V_{GS} using equation 7.2. The ratio of ON-state to OFF-state current of OFET is called the on/off current ratio, I_{on}/I_{off}, which is another very important characteristic of an OFET device which is given as

$$I_{on} \Big/ I_{off} = \frac{\mu C V_G}{2\mu_r q N_A t} \qquad \text{Equation 7.5}$$

where μ, μ_r, N_A, t, and q are the field-effect mobility, carrier mobility of semiconductor layer, off-state carrier concentration, the film thickness, and the electron charge, respectively.(Facchetti, Yoon et al. 2005) Since the conductivity, σ, is given as $\mu_r q N_A$, the on/off current ratio is proportional to the ratio μ/σ, meaning that a higher on/off ratio needs large carrier mobility and low off-conductivity.

7.1.2 Gate Insulators in Organic Field-Effect Transistors

While most research efforts have been centered in the development of new organic semiconductors with high mobility, intrinsically low carrier mobilities of organic semiconductors require the development of suitable gate dielectric materials to reduce the operating voltages and to achieve high output currents. Thus, the study of gate insulators

and the interfaces with organic semiconductors recently became very important research topics in organic electronics.(Bao and Locklin 2007; Koch 2007) Silicon dioxide (SiO_2) has been the benchmark of gate dielectrics as it has served the basis of complementary metal oxide semiconductor (CMOS) technology. Typically silicon dioxide is thermally grown to form an amorphous film (thermal silicon dioxide) and has excellent insulating properties due to the large band gap (8.9 eV). Optimized thermal silicon dioxide exhibits very low dielectric charge density, low interface state densities, and very high dielectric strength (15 MV/cm).(Bao and Locklin 2007) However, silicon dioxide is not easy to print or solution process and thus not easy to adapt to organic electronics which often require processing on flexible substrates. One exception to this limited processability of silicon dioxide material is the 'spin-on glass' which uses a liquid form precursor such as $Si(CH_2COOH)_4$) that can be spin on a substrate. The spin-on glass technique has been engineered to an art but is still rather problematic. Their porous structure rather yields a low permittivity (< 2.2) and the layers have cracking and adhesion problems.(Cook and Liniger 1999) Therefore, for organic electronics, it is desirable to develop gate insulator materials that exhibit low-temperature processability into thin films of large area suitable for solution processing techniques, such as ink-jet printing and spin-coating, without compromising dielectric properties such as high dielectric constants, low leakage currents, and high dielectric strengths.

High permittivity gate insulator materials based on inorganic metal oxides other than SiO_2 are attractive, since their dielectric constants range from 10 – 300, which makes them ideal candidates for low voltage operating transistors.(Wilk, Wallace et al. 2001) These materials are typically processed by vacuum deposition techniques such as e-beam deposition, RF sputtering, pulsed laser deposition (PLD), and plasma enhanced chemical vapor deposition (PECVD). These techniques require both high temperature and/or high vacuum conditions, which complicates the application of these materials to flexible organic substrates. Anodization of TiO_2 and Al_2O_3 can be used to deposit

inorganic materials on flexible organic substrates, but the high etch-resistivity of these oxides renders the patterning of such materials a difficult task.(Majewski, Schroeder et al. 2005) Alternative deposition techniques, such as atomic layer deposition (ALD), have been recently demonstrated to prepare gate dielectrics with improved performance on substrates even with high roughness.(Zhang, Domercq et al. 2007) ALD is a low temperature deposition technique that allows defect-free and conformal dielectric layers such as Al_2O_3 with excellent barrier properties and high resistivity, but typically requires a long processing time to grow thick layers.

On the other hand, gate dielectrics based on thin film organic polymers, cross-linked small molecules, and self-assembled monolayers (SAMs) of small molecules have been reported.(Veres, Ogier et al. 2004) (Kobayashi, Nishikawa et al. 2004) (Yoon, Facchetti et al. 2005) (Klauk, Zschieschang et al. 2007) These materials can be solution processed on a large area and are readily applicable to flexible substrates. However, the permittivities of typical organic materials are only about 2 – 6. Therefore, the capacitance densities of the dielectric layers are not very high. Ultrathin, cross-linked organic materials have sufficiently large capacitance densities due to their thicknesses.(Yoon, Facchetti et al. 2005) However, the reliability of such thin films is questionable, as there can be thermal effects induced by high field-effect during the operation, which can potentially lead to degradation of organic materials and breakdown. In addition, the processing of defect-free large area thin films at such thickness can be quite challenging. Ion gels have also been used as ultra-high capacitance gate dielectrics but are only applicable to top-gate geometry.(Cho, Lee et al. 2008)

Nanocomposites gate dielectrics in which the high permittivity of inorganic metal oxides is combined with the processability of organic polymers, have been reported as another alternative approach, providing high-capacitance gate insulators that are processed by easy, cheap, and large area-applicable solution processing techniques.(Chen, Chuang et al. 2006) (Chen, Chu et al. 2004; Maliakal, Katz et al. 2005; Schroeder,

Majewski et al. 2005; Chen, Chuang et al. 2006; Jung, Maliakal et al. 2007) However, OFETs using these nanocomposite gate insulators typically exhibit low on/off current ratios ($I_{on/off}$ $10^3 \sim 10^4$) due mainly to large leakage currents.(Chen, Chu et al. 2004; Schroeder, Majewski et al. 2005; Bao and Locklin 2007) Previously reported methods using a nanocomposite approach used nanoparticles of less than 5% by volume.(Chen, Chu et al. 2004; Chen, Chuang et al. 2006) To obtain higher capacitance, larger volume fractions (> 30%) of nanoparticles are needed but this usually leads to poor film quality due to nanoparticle aggregation. As a result, large leakage currents and low breakdown strength are obtained from these films. To avoid these problems, especially at high volume fractions of nanoparticles, better control over the particle-particle interaction and particle-polymer interfaces is required.

7.2 Materials and Methods

7.2.1 Surface Modification of BT and Nanocomposite Thin Film Processing

BT nanoparticles (30~50 nm, ε_r ~100, Aldrich) were modified with {2-[2-(2-Methoxyethoxy)ethoxy]ethyl}phosphonic acid (PEGPA, see Figure 2.12 and 2.13) as described in chapter 2, then dispersed in 1-butanol with poly(4-vinylphenol) (PVP, M_W ~20,000, Aldrich), hexamethoxymethylmelamine (HMMM, Cyamel 300, Mitsui Cyanamide) as a cross-linker, and a catalytic amount of p-toluenesulfonic acid (TsOH, Aldrich) (PVP:HMMM:TsOH = 15:5:1 by weight). The ratio of PEGPA-modified BT (PEGPA-BT) to PVP was varied from 16 to 37% by volume. The nanocomposite dispersion was homogenized by ball-milling. The suspensions were filtered through 1 μm syringe filters prior to spin coating to remove dust and large aggregates of nanoparticles.

The dispersion was spin coated on the polished surface of heavily *n*-doped Si wafers, which were treated with a cold air plasma(Han, Lee et al. 2006) and had a Ti/Au (10 nm/100 nm) backside contact. The films were soft baked at 100°C for 1 minute and

thermally cured under vacuum at 160 °C for 72 hours to ensure full crosslinking of the PVP matrix. The film thickness was controlled in the 200 - 500 nm range by changing the viscosity and spin speed. Control samples were prepared in the same way without surface modification of the BT nanoparticles.

7.2.2 Device Fabrication and Characterization

After the optimization of the nanocomposite gate insulator, the fabrication and characterization of the pentacene-based OFET devices were performed by Ms. Xiao-Hong Zhang (XZ) and Dr. Benoit Domercq (BD) in Kippelen group. Bottom gate and top contact p-type OFETs of various channel widths and lengths were fabricated on top of the nanocomposite thin films by physical vapor deposition of 50 nm thick pentacene films at room temperature (by BD), followed by deposition of Au electrodes (40 nm) capped with Al (100 nm) (by XZ), (Figure 7.2). A series of capacitor devices was also fabricated using the nanocomposite thin films for dielectric characterization. Film thicknesses were measured using a contact profilometer (Dektak 6M, Veeco) and the capacitance was measured using an LCR meter (4284A, Agilent). OFETs were characterized using a source/monitor unit (E5272A, Agilent) (by XZ). The carrier mobility and threshold voltage were derived from a linear fitting of $(I_{DS})^{1/2}$ *vs.* V_{GS} using equation 7.2 (by XZ). All of the electrical characterizations were performed in a glove box filled with nitrogen. Scanning electron microscopy (SEM) and atomic force microscopy (AFM) images were recorded using a LEO 1530 SEM and a Dimension 3100 SPM operating in TappingMode^{TM} under ambient conditions, respectively.

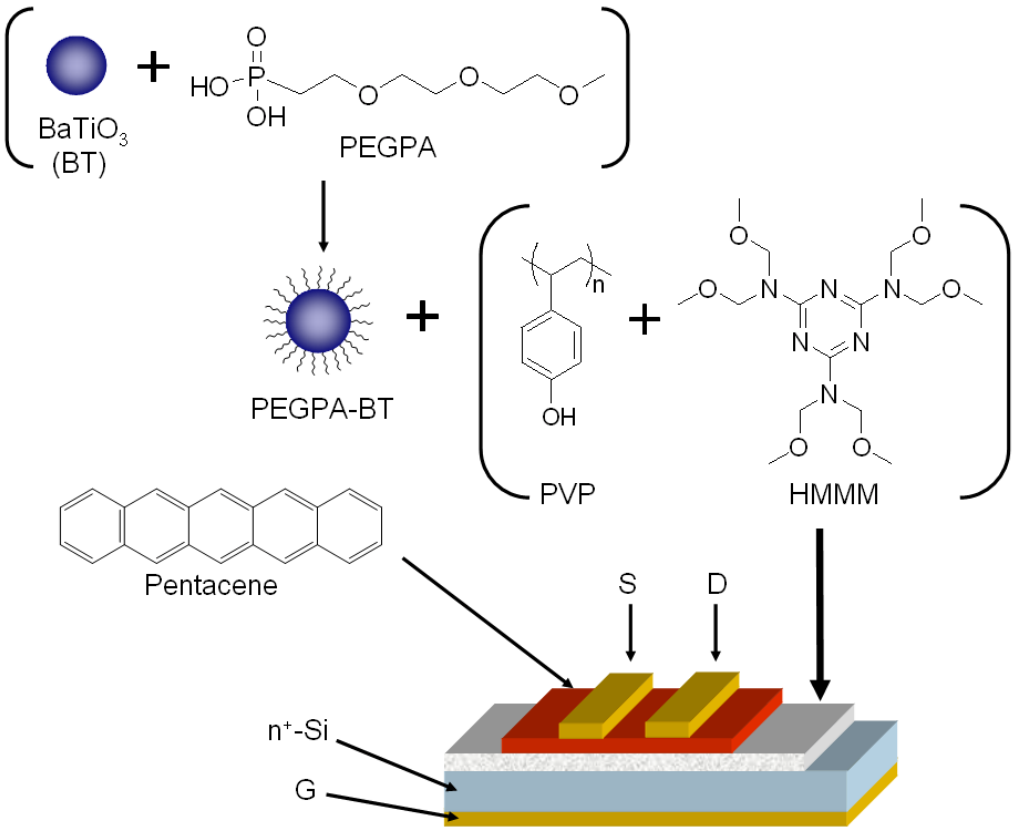

Figure 7.2 Schematics of PEGPA-BT:PVP nanocomposite preparation and fabrication of pentacene-based OFETs.

7.3 Results and Discussion

7.3.1 Properties of Nanocomposites

Poly(4-vinyl phenol) was chosen as a polymer matrix since it has been shown as one of best polymeric gate insulators for OFETs with excellent processability and good dielectric properties.(Halik, Klauk et al. 2002) (Halik, Klauk et al. 2002) The dielectric constant of cross-linked PVP was separately measured by fabricating and characterizing parallel-plate capacitors and found to be 3.9 at 1 kHz. Nano crystalline barium titanate has a high dielectric constant ranged from hundreds to thousands varying from its size. In order to achieve a large permittivity, the volume fraction of BT nanoparticle in PVP matrix needs to be at least 30 % as shown in Figure 7.3 which shows the predicted

permittivity of BT:PVP nanocomposites at different volume loading. Dispersion of unmodified BT nanoparticles directly into the polymer matrix is difficult due to the nanoparticle aggregation, which yields low permittivity and large leakage current.

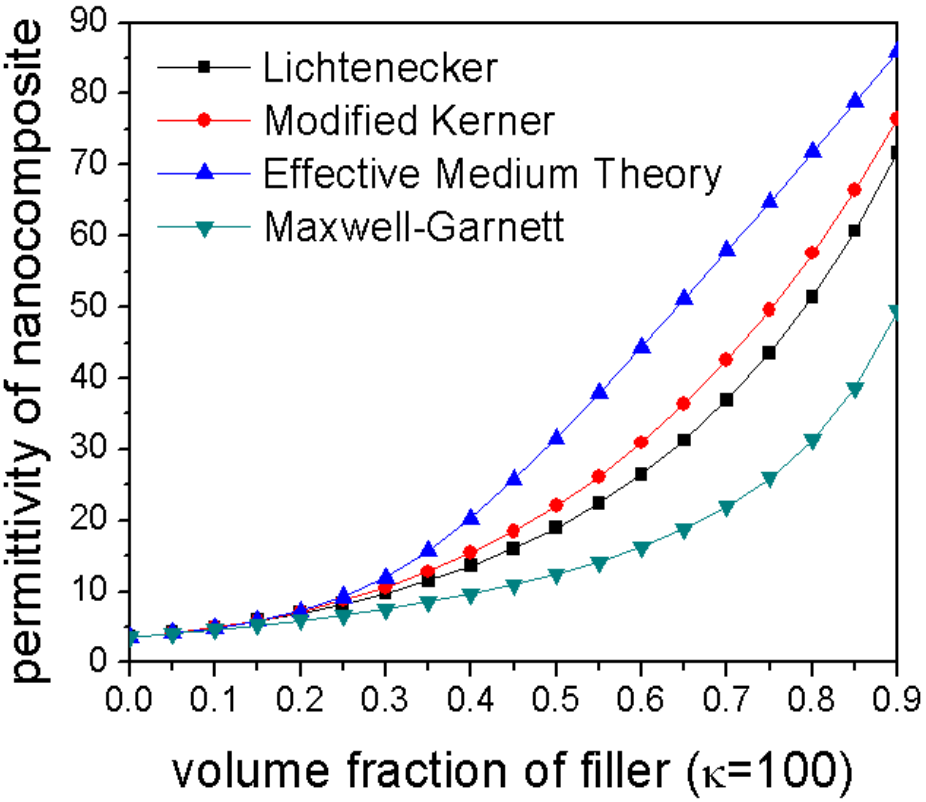

Figure 7.3 Predicted permittivity of BT:PVP nanocomposite as a function of nanoparticle volume fraction using simple models.

Figure 7.4 shows the SEM images of the nanocomposites prepared on Si substrates after finishing all the fabrication steps (crosslinking, deposition of electrodes, and deposition of organic semiconductor). The films were uniform and homogeneous in sufficiently large areas for the fabrication of multiple OEFT devices. In contrast, the nanocomposite films using unmodified BT nanoparticles showed defects. The thicknesses of the films ranged from 250 nm to ~500 nm. This can be easily controlled by varying the viscosity of the dispersion and the speed and time of spin coating process.

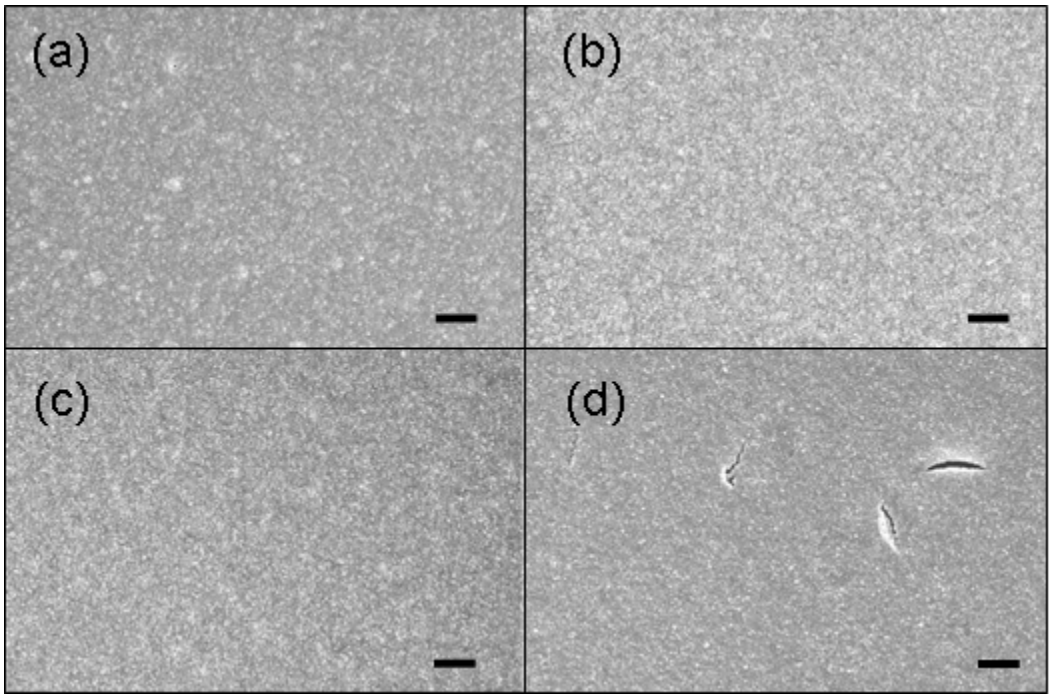

Figure 7.4 SEM images of PEGPA-BT:PVP nanocomposite thin films with nanoparticle volume fractions of 16 vol. % (a), 28 vol. % (b), and 37 vol. % (c), respectively. 37 vol. % film of unmodified BT (d) is shown for comparison. Scale bars represent 1 μm.

The nanocomposite gate insulators prepared using surface-modified BT showed significantly reduced leakage current density than those using unmodified BT as shown in Figure 7.5.

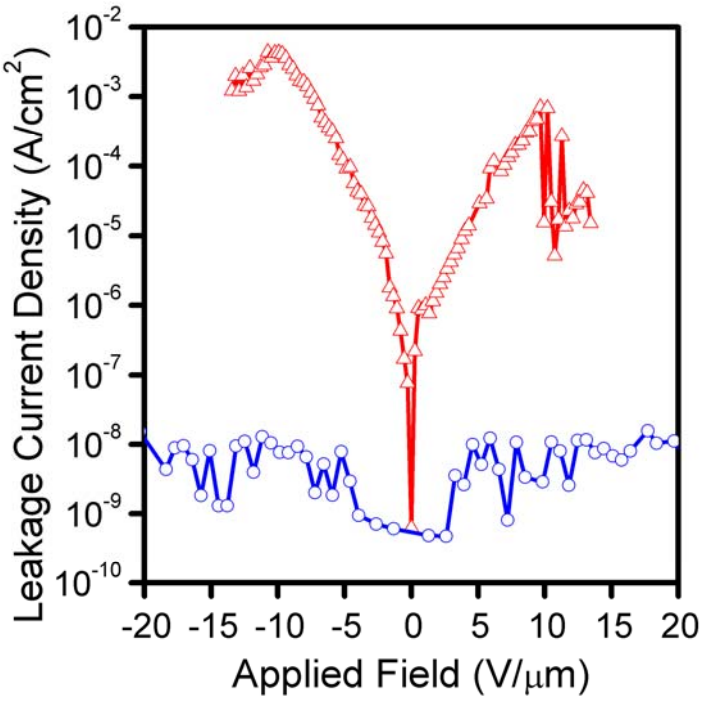

Figure 7.5 Leakage current densities of nanocomposites with 37 vol. % BT nanoparticles in PVP.

The reduction in the leakage current can be attributed to the reduction of direct particle-particle contacts and improved dispersion of the BT nanoparticles in the PVP matrix as represented in Figure 7.6. The surface passivation of ionizable hydroxyl groups by the phosphonic acid is also thought to reduce the leakage current by eliminating possible charge conduction pathways in the film.

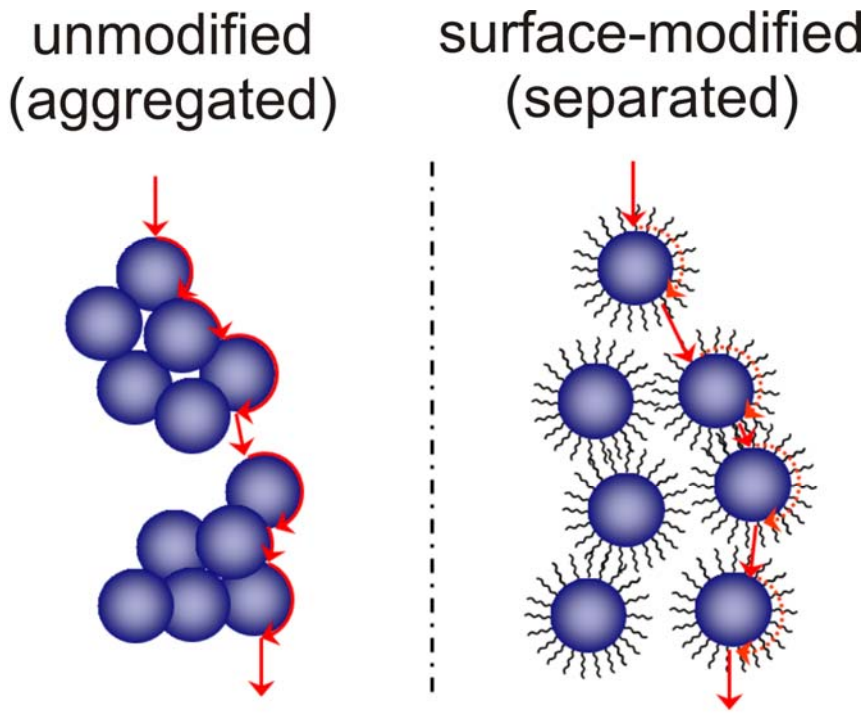

Figure 7.6 Schematics illustration comparing the migration of charges in nanocomposites with aggregated nanoparticles and surface-modified/well-dispersed nanoparticles.

The properties of the nanocomposites with varying amounts of BT are summarized in Table 7.1. With the increase of the volume fractions of BT nanoparticles (from 4 with no BT to 14 with 37 vol. % BT) the permittivity increased up to 14 which is more than three times larger than that of cross-linked PVP ($\varepsilon_r = 3.9$). The spin coated films using the same spinning conditions resulted in thicker films with increasing nanoparticle loading due to the increase in the viscosity of the dispersion. By changing the viscosity of the nanocomposite dispersion and the spin speed, thinner films were obtained and the capacitance density could be increased to ~50 nF/cm^2.

Table 7.1. Properties of PEGPA-BT:PVP nanocomposite thin films.

vol. % $BaTiO_3$	t (nm)	ε_r at 1 kHz	C (nF/cm^2)	J_L (A/cm^2)	RMS roughness (nm)	μ ($cm^2/V \cdot s$)
16	250	6.0	22	$\sim 1 \times 10^{-8}$	6.2	0.34
28	386	9.6	22	$\sim 1 \times 10^{-8}$	7.8	0.11
37	406	14.0	31	$\sim 1 \times 10^{-8}$	8.8	0.04

Due to the variations in film thickness (t), the capacitance density (C) was not necessarily proportional to the dielectric constant (ε_r) of the layer. Leakage current density (J_L) is the average measured over the range of ±20 V/μm. RMS roughness was obtained from a 5 μm × 5 μm scan area. The RMS roughness of a pure PVP film over a 5 μm × 5 μm area was 0.26 nm. The surface roughness showed a strong effect on the charge mobility (μ). (mobility data from XZ)

7.3.2 OFET Performance

The output current and the transfer characteristics of pentacene-based OFETs using PEGPA-BT:PVP nanocomposite gate insulators are shown in Figure 7.7.

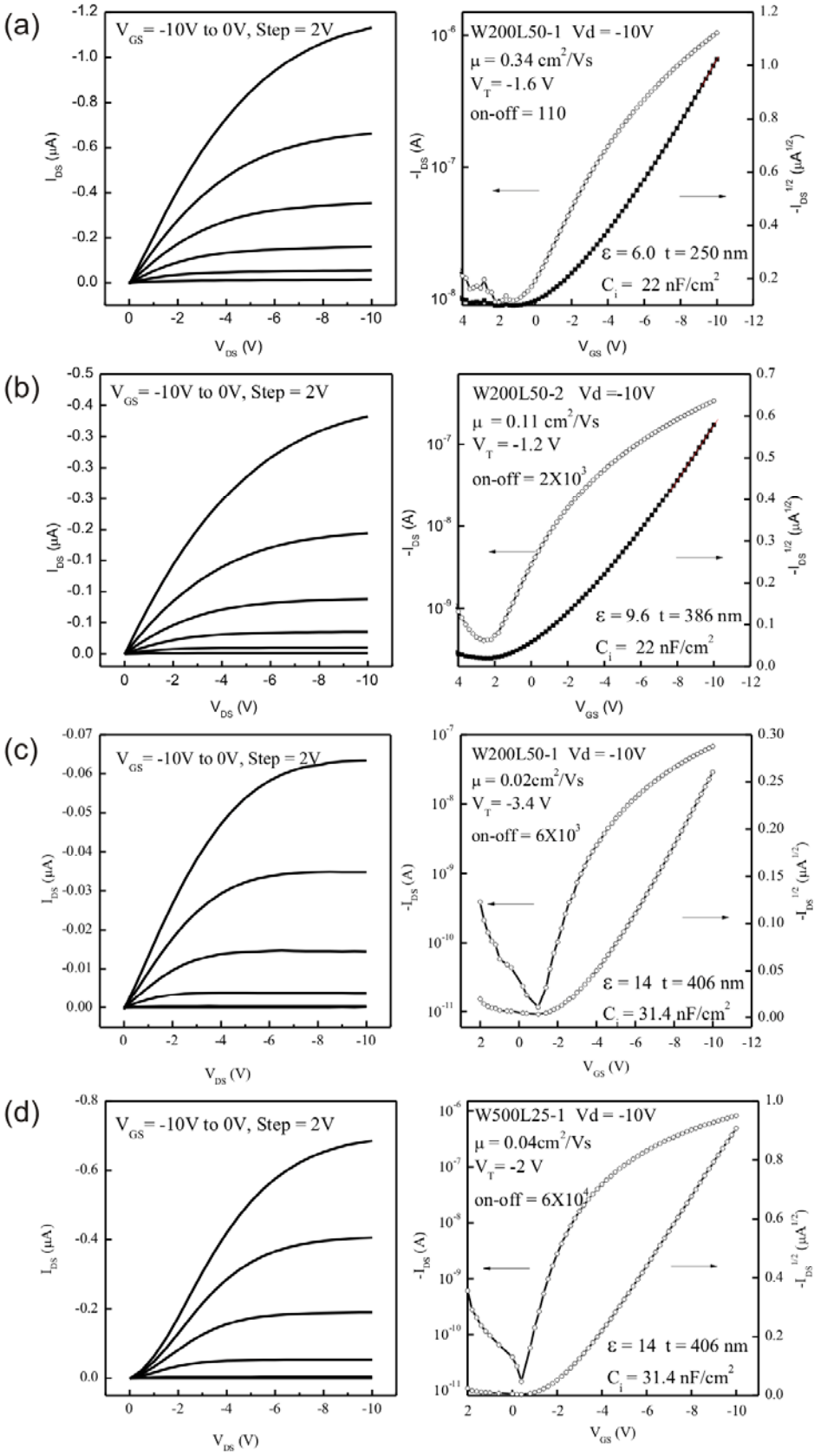
(a)
V_GS = -10V to 0V, Step = 2V
I_DS (μA)
V_DS (V)
W200L50-1 Vd = -10V
μ = 0.34 cm²/Vs
V_T = -1.6 V
on-off = 110
ε = 6.0 t = 250 nm
C_i = 22 nF/cm²
-I_DS (A)
-I_DS^1/2 (μA^1/2)
V_GS (V)
(b)
V_GS = -10V to 0V, Step = 2V
I_DS (μA)
V_DS (V)
W200L50-2 Vd =-10V
μ = 0.11 cm²/Vs
V_T = -1.2 V
on-off = 2X10³
ε = 9.6 t = 386 nm
C_i = 22 nF/cm²
-I_DS (A)
-I_DS^1/2 (μA^1/2)
V_GS (V)
(c)
V_GS = -10V to 0V, Step = 2V
I_DS (μA)
V_DS (V)
W200L50-1 Vd = -10V
μ = 0.02cm²/Vs
V_T = -3.4 V
on-off = 6X10³
ε = 14 t = 406 nm
C_i = 31.4 nF/cm²
-I_DS (A)
-I_DS^1/2 (μA^1/2)
V_GS (V)
(d)
V_GS = -10V to 0V, Step = 2V
I_DS (μA)
V_DS (V)
W500L25-1 Vd = -10V
μ = 0.04cm²/Vs
V_T = -2 V
on-off = 6X10⁴
ε = 14 t = 406 nm
C_i = 31.4 nF/cm²
-I_DS (A)
-I_DS^1/2 (μA^1/2)
V_GS (V)

Figure 7.7 OFET characteristics of pentacene-based OFETs on PEGPA-BT:PVP nanocomposite gate insulators. The volume fractions PEGPA-BT nanoparticles were 16% (a), 28% (b), and 37% (c) and (d). (data from XZ)

The surface roughness of the dielectric layer has great influence on the performance of OFETs. (Fritz, Kelley et al. 2005; Maliakal, Katz et al. 2005; Stadlober, Zirkl et al. 2005; Koch 2007) The dielectric roughness is believed to induce disorder in the accumulation layer, increase grain boundaries in rough semiconductor films, and produce irregular channel geometries. As a result, reduction of the carrier mobility of organic semiconductor is observed. Streudel et al. observed 98 % reduction of the mobility of pentacene-based TFTs by changing the RMS surface roughness of SiO_2 gate dielectrics from 1.7 nm to 92 nm.(Steudel, Vusser et al. 2004)

It should be noted that the RMS roughness of the BT:PVP nanocomposite surface increased with increasing volume fraction of BT nanoparticles and the carrier mobility decreased with increasing the volume fraction of BT (Table 7.1). The surface roughness of the nanocomposites at high nanoparticle-filling conditions was quite large compared with that of pure PVP films. Consequently, the morphology of pentacene semiconductor films deposited on top of the nanocomposite gate showed a small grain size and a morphology that mimicked the underlying nanocomposite, as shown in Figure 7.8.

Application of a thin polymer layer has been shown to planarize the rough surface of nanocomposite layers and can improve the interfacial properties by reducing the trap density and by changing the relative surface energies between the layers.(Stadlober, Zirkl et al. 2005; Chen, Chuang et al. 2006; Jung, Maliakal et al. 2007) Spin-coating of a thin (*ca.* 20 nm) PVP films from a 5% by weight solution of PVP in 1-butanol on top of the nanocomposite layer, the surface roughness was significantly reduced and the morphology of pentacene film was changed restoring large grains, as shown in Figure 7.8.

The large grain size of pentacene semiconductor film is crucial for high carrier mobility.(Steudel, Vusser et al. 2004; Fritz, Kelley et al. 2005)

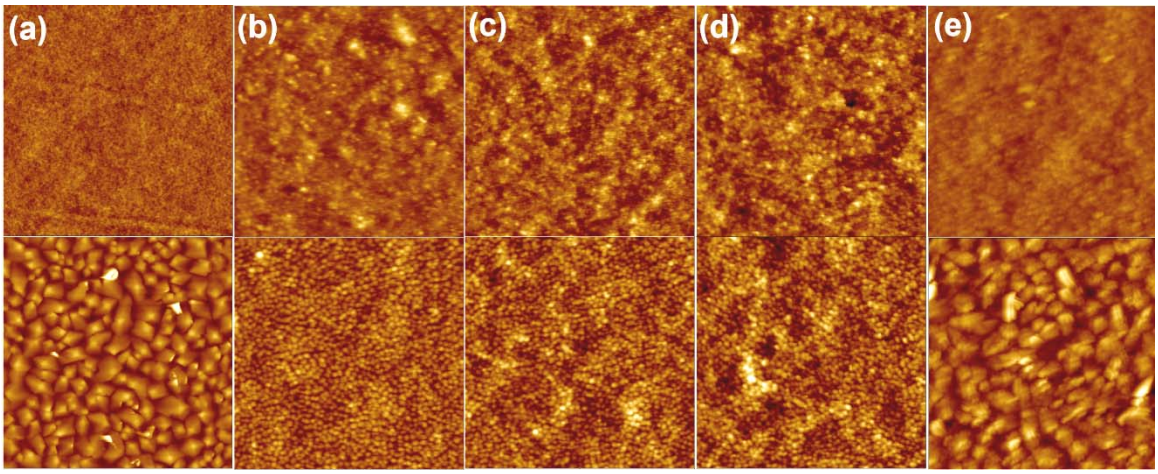

Figure 7.8 AFM height images of gate insulator surfaces (top row) and pentacene layer deposited on each surface (bottom row). (a): pure PVP, (b – d): PEGPA-BT:PVP nanocomposites with 16, 28, and 37 vol. % BT, respectively, (e) 37 vol. % PEGPA-BT:PVP nanocomposite with a planarization layer of pure PVP. Image size = 5 μm × 5 μm, height = 100 nm, except for pure PVP (height = 5 nm).

Though there was a slight reduction in the effective permittivity of the insulator due to this additional layer, the final permittivity ($\varepsilon_r = 12$) was still three times larger than that of pure crosslinked PVP ($\varepsilon_r = 4$). Additionally, the leakage current was further reduced by a factor of ~2-5 after the application of the planarization layer. Figure 7.9 shows the changes in leakage current density, dielectric constant, and the capacitance density of the gate layers with the addition of a PVP planarization layer. The decrease in the effective dielectric constant in these 'bi-layered' nanocomposite gates is compensated by a decrease in the leakage current and reduced surface roughness.

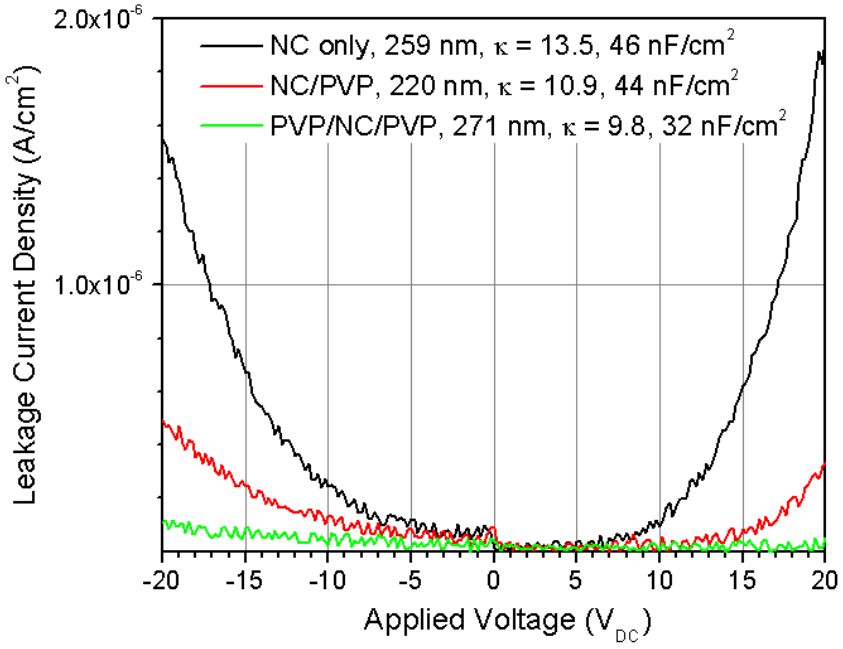

Figure 7.9. Plot of the leakage current densities of 3:1 PEGPA-BT:PVP nanocomposite thin films as a function of applied voltage. The total thickness of each multilayered nanocomposite gate insulator is given in nanometers. Note that the improved leakage characteristic comes at the cost of a decrease in the dielectric constant, and thus the capacitance density is compromised as well. The dielectric breakdown strengths were found to be greater than 1 MV/cm for all films tested.

The surface planarization by a thin polymer layer reduced the surface roughness by more than a factor of 2. The morphology of pentacene semiconductor films deposited on top of the nanocomposite gate almost had no distinct grains and followed the shape of the underlying BT nanoparticles dispersed in PVP. After depositing a thin PVP planarization layer, the pentacene films on the layer exhibited large grains that are crucial for high carrier mobility. Initial results using this bi-layer nanocomposite gate insulator are shown in Figure 7.10 where the carrier mobility was calculated as 0.16 $cm^2/V \cdot sec$.

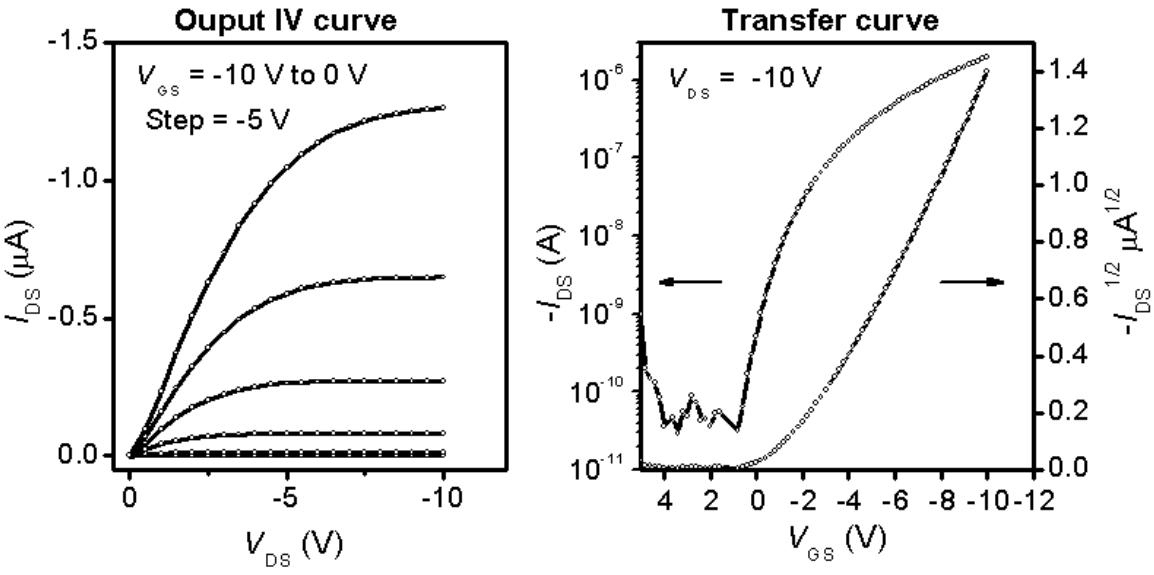

Figure 7.10. OFET characteristics obtained from a device with a channel width of 500 μm and a channel length of 50 μm prepared on a 3:1 PEGPA-BT:PVP nanocomposite gate dielectric layer with a thin PVP planarization layer. (data from XZ)

In order to quantitatively compare the effect of the planarization layer, devices with the same ratio of channel width and length (W/L = 20) were analyzed and their characteristics are summarized in Figure 7.11 and Table7. 2. The dependence of the saturation mobility of an organic semiconductor on the permittivity of the gate insulator has recently been studied.(Jung, Maliakal et al. 2007); (Jang, Kim et al. 2005) In these high permittivity nanocomposites with high volume fractions of nanoparticle fillers, the mobility was influenced to a greater extent by the morphology of the semiconductor than the permittivity of the gate insulator. As a result, the combined high permittivity nanocomposite gate insulator with a thin planarization layer yielded increased carrier mobility up to 0.17 $cm^2/V{\cdot}s$. OFET devices based on this bi-layer nanocomposite gate exhibited a low threshold voltage (-1.1 V), a small sub-threshold swing (0.3 V/decade), and a large on/off current ratio (2.3×10^5).(Kim, Zhang et al. 2008)

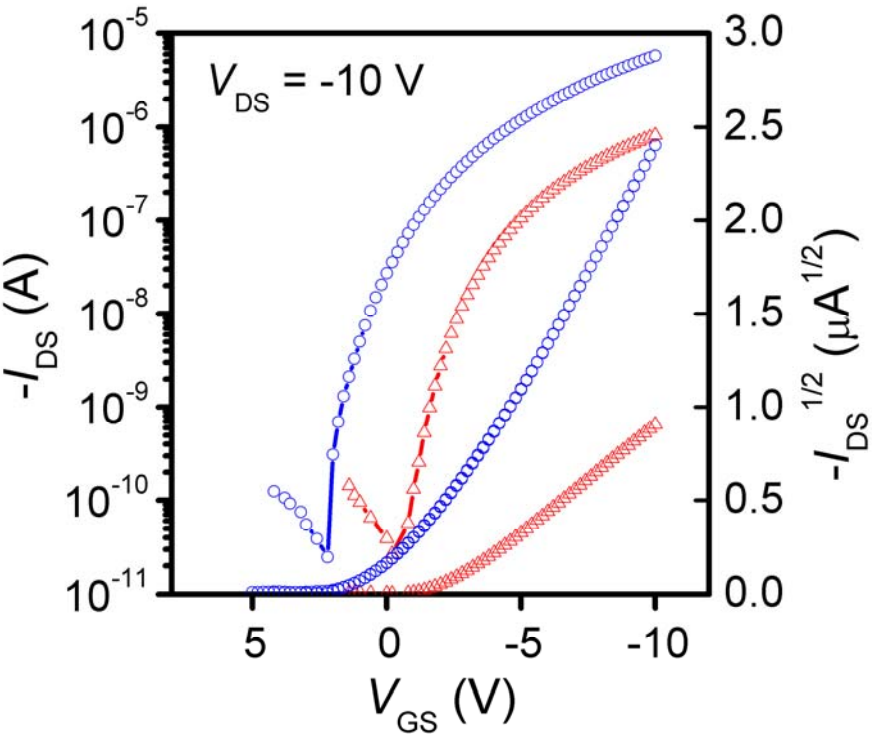

Figure 7.11 OFET transfer characteristics obtained from the devices (W/L = 20, 500 μm/25 μm for NC only and 2000 μm/1000 μm for NC/PVP) fabricated on 37 vol. % PEGPA-BT in PVP nanocomposite gate insulators without a planarizing layer (triangle) and with a planarizing layer (circle). (data from XZ)

Table 7.2 Comparison of the OFET device characteristics with and without planarization.

	t (nm)	C (κ) (nF/cm^2)	RMS roughness (nm)	μ (cm^2/V·s)	V_T (V)	S (V/decade)	$I_{on/off}$
NC only	406	31 (14)	8.8	0.04	-2.0	0.7	6.0×10^4
NC/PVP	251	42 (12)	3.8	0.17	-1.1	0.3	2.3×10^5

RMS roughness was obtained from a 5 μm × 5 μm scan area.

(OFET characterization data from XZ)

Experiments with other planarization materials with low polarity, such as benzocyclobutene (BCB), may be a suitable approach for *n*-type OFETs, since PVP may not be applicable to *n*-type semiconductors due to the residual hydroxyl groups. BCB is known to provide a hydrophobic interface for the deposition of hydrophobic semiconductors and is also known to have a very low density of charge traps that can affect the carrier mobility of the semiconductor.(Chua, Zaumseil et al. 2005)

In order to further reduce the leakage current from the metal-semiconductor contact, the semiconductors of unnecessary areas were scratched out and a higher on/off ratio (1.2×10^{6}) was observed using same PEGPA-BT:PVP nanocomposite gate insulators. (Figure 7.12) This was mainly due to an order of magnitude decrease of the off-state current (I_{off}) from 2.5×10^{-9} A to 2.4×10^{-10} A, while other properties remained unchanged.

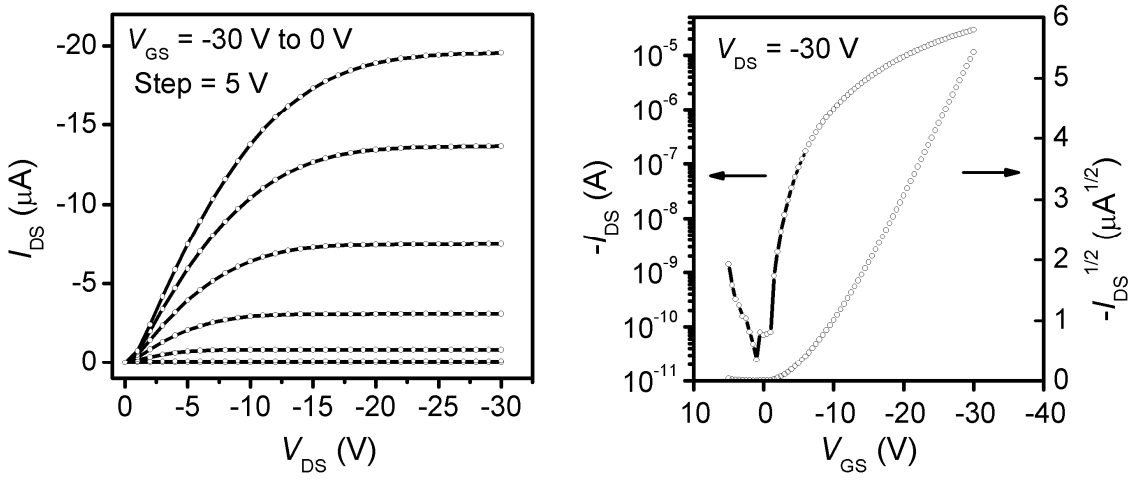

Figure 7.12 OFET characteristics of a device with reduced metal-semiconductor contact on 37 vol. % PEGPA-BT:PVP nanocomposite gate insulator planarized with a thin PVP layer. (data from XZ)

7.4 Conclusions

In conclusion, the use of surface-modified BT nanoparticles allows solution processable, high quality, high permittivity, and low leakage current nanocomposite thin films suitable for gate insulators in OFETs. Surface modification of the nanoparticles results in improved on/off current ratio, due to the effective reduction of leakage current. The problem of the high surface roughness of the nanocomposite layer at high filler fraction can be solved by using a thin planarizing layer. A further increase in the capacitance density may be possible by optimization of surface-modified nanoparticle/polymer composite approach by increasing the filler volume fractions and/or using a higher permittivity polymer host and nanoparticles. Further investigation of the materials choice for the planarization layer can potentially allow the use of high permittivity nanocomposite gate insulators for both *p*-type and *n*-type organic semiconductors.

CHAPTER 8

CONCLUSIONS AND SUGGESTED FUTURE WORK

8.1 Conclusions

A novel approach to modify the surface of BaTiO3 nanoparticles was developed in this thesis. This novel technique was applied to the processing of new polymer/ceramic nanocomposite dielectric materials that exhibited a remarkable combination of a high permittivity, low leakage, and high dielectric breakdown strength. Further optimization of such nanocomposite materials and the development of new applications in organic field-effect transistors were carried out and promising results were obtained. Inspired by this thesis work, various types of functional phosphonic acid ligands have been used to modify wide range of metal oxide surfaces to control interface-related properties such as compatibility, contact angle, wetting, adhesion, friction, passivation, encapsulation, surface energy, etc. in many applications.

Phosphonic acids were found to give more robust surface modification on $BaTiO_3$ and related perovskite nanoparticles than analogous silanes, carboxylic acids, or sulfonic acids. Phosphonic acids were found to bind to the surface of $BaTiO_3$ mainly in tridentate and some bidentate form, which provided a stable passivation layer on the surface of $BaTiO_3$ nanoparticles. The binding kinetics of phosphonic acids on $BaTiO_3$ was found to be very fast reaching equilibrium within 1 hour at 80 °C. The coverage of *n*-octylphosphonic acid on $BaTiO_3$ nanoparticles was found to be on the order of a monolayer with a footprint of 18.7 Å and with a binding energy of 82 kJ/mol. The surface-bound phosphonic acids were stable against solvolysis by a wide range of organic solvents and a strong acid. Phosphonic acids were also found to strongly bind to the surface of various metal oxides suggesting that they can be used as a universal surface modifier for metal oxides.

The surface modification using properly designed functional phosphonic acid-based ligands on $BaTiO_3$ nanoparticles dramatically improved the compatibility and dispersability of $BaTiO_3$ nanoparticles in polymer hosts as evidenced by dispersion test and dynamic light scattering experiments. The use of high permittivity hosts as well as directed surface modification enabled processable high quality dielectric materials with high energy storage capability. The capacitors fabricated using PFBPA-BT:P(VDF-HFP) nanocomposite materials developed in this study exhibited maximum energy storage density as high as 6.1 J/cm^3, which is twice of that of the state-of-the-art commercially available high-energy-density capacitors based on wound metalized BOPP films.

The effective permittivity of nanocomposites was found to match very well with simple theoretical models but showed a large discrepancy at high volume loading. There was a turning over behavior in the effective permittivity of nanocomposites at high volume fractions of nanoparticles, which turned out to be due to the porosity in the nanocomposite films. The porosity was not so significant at low volume fractions (up to ~50 %), but was found to be obvious over 60 % volume of nanoparticles by microscopic observation. This was partially supported by a finite difference simulation. However, the finite difference simulation did not accurately predict the onset of the porosity in the nanocomposites due to lack of the relaxation process of the nanocomposite system. A combined approach considering the porosity of nanocomposites provided a good model that can describe the dielectric behavior of a nanocomposite system from low volume fractions (0 %) to high volume fractions (~80 %) of nanoparticles, in which a self-consistent effective medium approximation, finite difference simulation, and empirical electron microscopy data were used.

Breakdown strengths of nanocomposites were found to decrease with increasing volume fraction of nanoparticles, as expected. The behavior of the breakdown field strength change as a function of the nanoparticle volume fraction could be explained by ‘soft’ and ‘hard’ percolation model.

There is an optimum volume fraction of high permittivity nanoparticles for maximum extractable energy. Therefore, the volume fraction of the nanoparticles should be rationally chosen based on the dielectric characteristics of the nanocomposite system for maximum extractable energy at certain operation frequency.

Surface modified $BaTiO_3$ nanoparticles using a polar phosphonic acid-based ligand in cross-linked poly(4-vinyl phenol) host allowed solution processable high permittivity thin films of good quality. The surface modification in this example was found to greatly reduce leakage current density of nanocomposite thin films making them suitable as the gate insulators in organic field-effect transistors (OFETs). The use of this novel dielectric material in pentacene-based OFETs significantly reduced the device operating voltage. However, low carrier mobilities due to the rough surface morphology of a high volume fraction nanocomposite were observed. This problem was solved by using a bilayer approach. The OFETs with high permittivity bilayer nanocomposites developed in this study resulted in low threshold voltage (<-2 V) and a high on/off current ratio (~10^6). The capacitance of the solution-processable nanocomposite gate insulator can be further increased by loading more nanoparticles, using high-permittivity nanoparticles, and decreasing the film thickness (< 200 nm).

8.2 Suggested Future Work

8.2.1 Surface-Modified BT:Polymer Nanocomposites

This thesis provided a basic concept of the surface modification of barium titanate nanoparticles with functional phosphonic acid ligand and its utility in solution processable high quality nanocomposites with high permittivity, low leakage current, and high breakdown strength. Though some studies have been covered in chapters 5 and 6, there are still many interesting remaining studies. Suggested further studies on the properties of dielectric nanocomposites derived from this initial study are illustrated in Figure 8.1.

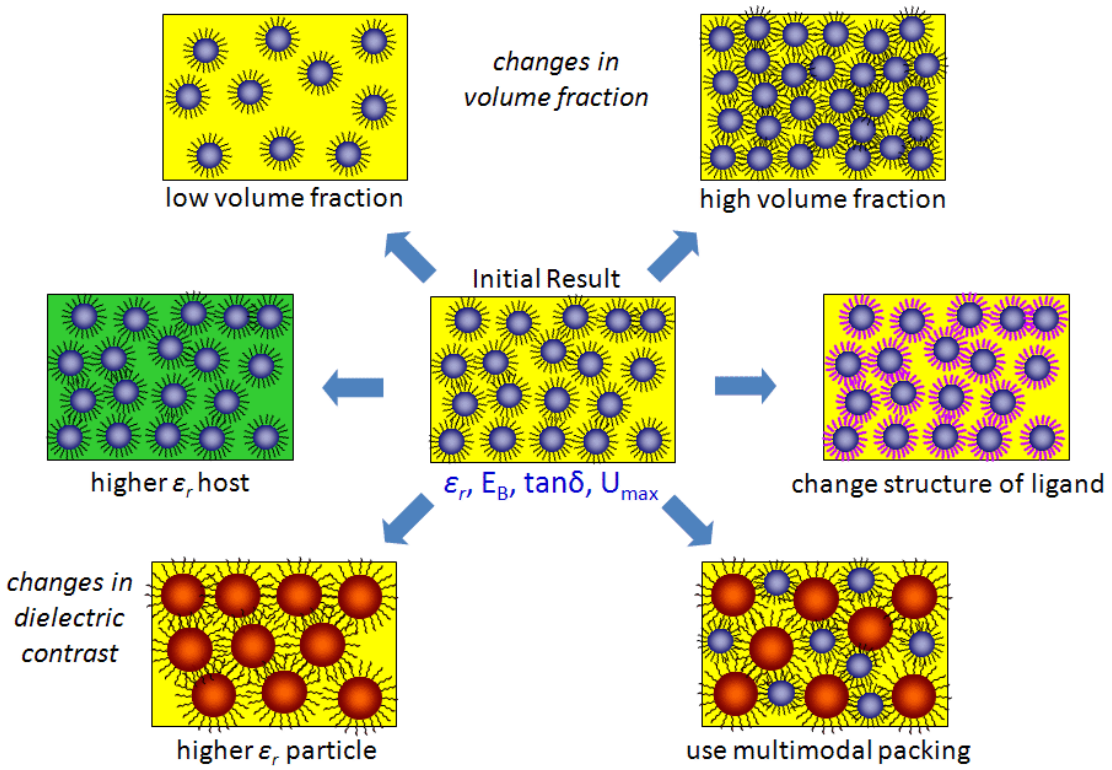

Figure 8.1 Schematic illustration of suggested future work.

Typical dielectric nanocomposites employ a high dielectric contrast (the ratio of the dielectric constant of the filler to that of host material). Reducing the dielectric contrast, thus closer matching of the dielectric constants of the filler and host, can effectively reduce the local electric field in the host material. This can potentially lead to a high dielectric strength. So far many people have studied different nanocomposites where the dielectric contrast is typically on the order of at least 300.(Ramesh, Shutzberg et al. 2003; Rao and Wong 2004) In the study presented here uses BT nanoparticles with permittivity of only ~100 due to the size effect and the crystalline phase (cubic phase).(Yashima, Hoshina et al. 2005) The permittivity of the typical polymer host is less than 6 but the permittivity is greater than 11 for some of the high permittivity polymers discussed in this thesis. Therefore, the dielectric contrasts of the materials studied were less than 10. This maybe a reason for such high dielectric strengths

observed in this study. Therefore, the study of the effect of dielectric contrast on the dielectric strength of nanocomposites based on surface-modified barium titanate/polymer is suggested. In modeling these systems, consideration of the surface coating layer in the calculation would also improve the results.

Dielectric contrast seems to affect the behavior of the effective permittivity of nanocomposites with increasing volume fractions of the high permittivity fillers. Figure 8.2 shows the effective permittivities of nanocomposites with a low dielectric contrast and a high dielectric contrast as a function of the nanoparticle volume fraction, which were modeled by self-consistent effective medium theory. The effective permittivity does not increase significantly until a certain threshold volume fraction in both cases. However, this effect is more pronounced for high dielectric contrast nanocomposite. It would be also interesting to experimentally confirm these different behaviors.

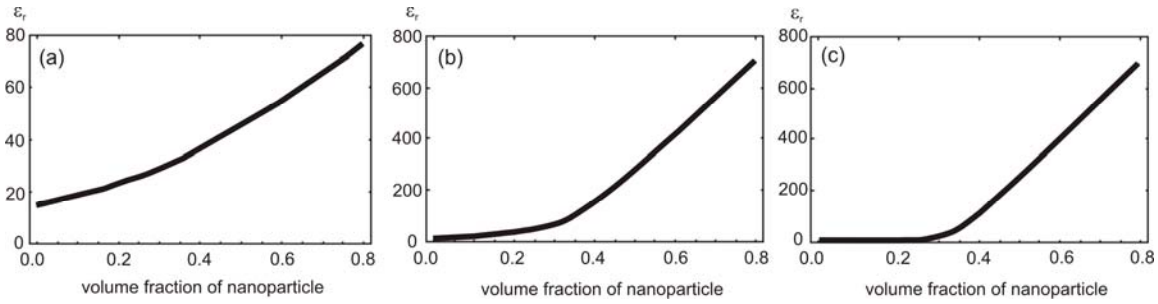

Figure 8.2 Effective permittivities of nanocomposites of different dielectric contrast as a function of nanoparticle volume fraction. The dielectric contrast of model systems are: (a) 6.7, (b) 66.7, and (c) 300. The values were derived from self-consistent effective medium theory.

Multi-modal packing of different size particles in a polymer matrix has been demonstrated.(Rao and Wong 2004) Combining multi-modal packing with the volume fraction optimization study in a high permittivity polymer host can further increase the energy density.(Dang, Xie et al. 2007) However, there are not sufficient theoretical

studies on these types of micro-nanocomposites. In this case, the effective medium theory may not be able to accurately model the system because the large and small nanoparticles are randomly packed in polymer host. This may be modeled by using simulations such as finite difference calculation. The study on the dielectric strengths of these micro-nanocomposites with various volume fractions is also suggested.

8.2.1 Applications of Ceramic:Polymer Nanocomposites

The study of the dielectric properties of nanocomposites at microwave frequency is important for the development of candidate materials for antenna substrates, flexible substrates for RF ID tags, and microwave photonic band gap materials. (Popielarz, Chiang et al. 2001; Biswas, Bayer et al. 2007; Cheng, Lin et al. 2007; Lott, Xia et al. 2008). High permittivity is desirable for tunable microwave devices, such as tunable filters, tunable phase shifters, and steerable antennas, as the tunability generally increases with increasing permittivity.(Kim, Kazmirenko et al. 2002) The application of phosphonic acid surface modification on barium titanate or related perovskite nanoparticles can potentially allow processable high permittivity and low dielectric loss materials at this frequency. Therefore, the study of microwave dielectric properties of nanocomposites utilizing phosphonic acid surface modification is suggested. For this study, the characterization of pure polymers to find a good candidate has to be performed. With this host material, the phosphonic acid ligand should be designed and synthesized. The incorporation of metallic nanoparticles (*e.g.* copper, silver) and/or magnetic nanoparticles (*e.g.* $CoFe_2O_4$, $NiFe_2O_4$) can be also considered to improve the dielectric properties and the magnetic permeability of the nanocomposites.(Mooney, Nelson et al. 2004; Lu, Salabas et al. 2007) Dielectric properties (permittivity and loss tangent) can be calculated by measurement of S-parameters with a network analyzer over a wide range of frequency, and analyzing the data.(Kim, Kazmirenko et al. 2002)

Electrowetting has been widely used as a tool for manipulating tiny volumes of liquid droplets on surfaces that can be applied to ‘lab-on-a-chip’, tunable microlenses,

and electronic displays.(Yang, Krupenkin et al. 2003; Heikenfeld and Steckl 2005; Mugele and Baret 2005) Conventional substrates for electrowetting typically consist of an electrode and a hydrophobic surface layer (*e.g.* fluoropolymer) on the electrode. The liquid droplet contains electrolytes and an external electric field can be applied by immersing an electrode into the droplet. The contact angle of the droplet changes by application of a voltage, which can be macroscopically observed as shown in Figure 8.3.

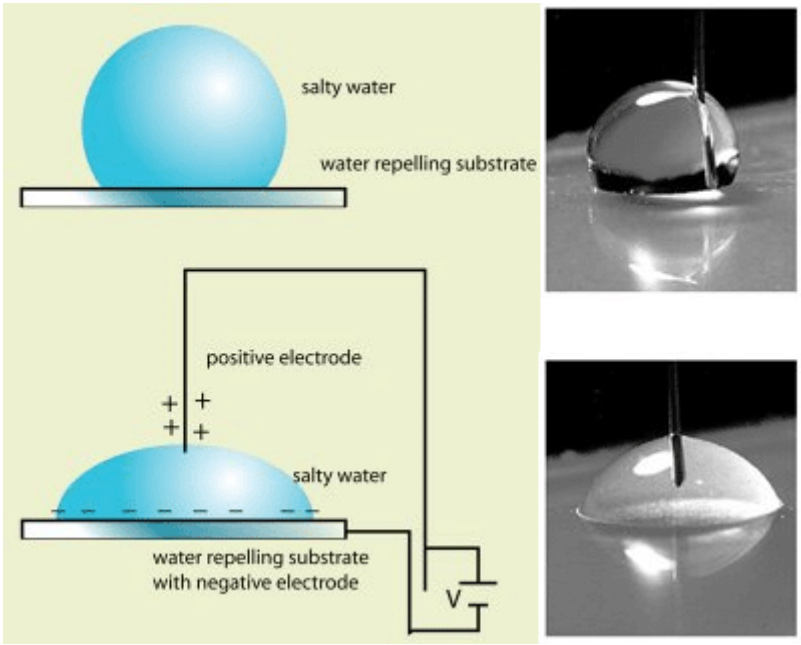

Figure 8.3 Schematic illustration of the operation principle of electrowetting.

The wetting is reversible and can be dynamically tuned (~ms response for >mL droplets) by the magnitude of the applied voltage. The electrowetting behavior is described as the following electrowetting equation.(Kilaru, Heikenfeld et al. 2007)

$$\cos(\theta_V) = \cos(\theta_Y) + \frac{\varepsilon_r V^2}{2\gamma z} \qquad \text{Equation 8.1}$$

where θ_V is the electrowetted contact angle at an electrical potential of V, θ_Y is Young's contact angle determined by interfacial surface tensions at zero applied voltage, ε_r is the

permittivity of the dielectric layer underneath the droplet, γ is the liquid/air interfacial surface tension, z is the thickness of the dielectric layer, and V is the applied voltage. Thus, the tunability of the contact angle can be improved by increasing the permittivity of the dielectric and/or decreasing the thickness of the dielectric layer. Improved dielectrics can reduce the voltage required to actuate the water droplets. The surface roughness and the hydrophobicity of the interfacial layer of the dielectrics are very important parameters as they affect the 'off' state contact angle of the droplet (*i.e.* no applied voltage). Recently, nanocomposites of $BaTiO_3$ ($\varepsilon_r \approx 200$) dispersed in a hydrophobic fluoropolymer, poly(tetrafluoroethylene) ($\varepsilon_r \approx 2$), prepared in a fluorosolvent have been used in electrowetting devices.(Kilaru, Heikenfeld et al. 2007) The films were prepared using spin coating and the thicknesses of the nanocomposite layer ranged from 800 nm to 1200 nm. However, the effective permittivity of the nanocomposite dielectric was only about 10 even with the incorporation of over 75 % $BaTiO_3$ by volume due to the low permittivity of the polymer host used. As a result, over -60V of applied voltage was required to change the contact angle of the droplet. In addition, the authors observed strong charge trapping and hysteresis with increasing the volume fraction of $BaTiO_3$. This can be attributed to the presence of strong charge trapping sites on the surface of $BaTiO_3$ nanoparticles since the authors did not use any surface modification. Therefore, it would be very interesting to apply phosphonic acid surface modified $BaTiO_3$ nanoparticles to fabricate dielectric substrates for electrowetting devices. The surface passivation layer is expected to prevent the charge trapping and to reduce the hysteresis. In addition, the combination of some high permittivity fluoropolymers with surface-modified $BaTiO_3$ will result in increased effective permittivity and further reduce the operation voltage of electrowetting devices. However, as mentioned above, the interfacial layer of the dielectrics with the liquid droplet must exhibit strong hydrophobicity. Therefore it is suggested that a bilyer high permittivity nanocomposite should be used to control the interfacial hydrophobicity, to improve the surface roughness

in the case of high volume fraction nanocomposite, and to minimize the charge trapping at the interface.

The use of phosphonic acid self-assembled monolayer on the substrate electrode is also suggested. For this, the structure of the phosphonic acids should be carefully designed: 1) it should possess a long-chain alkyl group next to the phosphonic acid binding group for dense packing, 2) a high polarizability moiety next to the alkyl chain for high permittivity, and 3) a perfluorinated terminal group for achieving hydrophobic interface with the droplet.

8.2.3 Synthesis of Non-Stoichiometric Barium Strontium Titanate Nanoparticles

Throughout the study presented in this thesis, one big challenge was to obtain a small sized (~100 nm or less), spherical high permittivity (>1000) nanoparticles with high concentration of surface hydroxyl groups for phosphonic acid modification. Tetragonal phase barium titanate nanoparticles are usually prepared by high-temperature methods which eliminate the surface hydroxyl groups required for the surface modification. Large size barium titanate (>200 nm) nanoparticles with high permittivities were also commercially available but dispersing large nanoparticles involved many problems due to the low surface to bulk ratio. In addition, large size nanoparticles cannot be used to fabricate thin nanocomposite films (~ 1 μm or less) for high capacitance applications (*e.g.* gate dielectrics). Recently, new synthetic methods based on sol-gel, hydrothermal, solvothermal, microwave-assisted hydrothermal, and biologically assisted synthesis have been investigated to prepare tetragonal phase and ferroelectric high permittivity nanoparticles with many surface hydroxyl groups.(Kim and Lim 2003; Xu and Gao 2003; Kwon, Choi et al. 2006; Kwon, Park et al. 2006; Lee, Wang et al. 2006; Lee, Park et al. 2006; Nuraje, Su et al. 2006; Sun, Li et al. 2006; Yoon, Baik et al. 2006; Mandal 2007; Yoon, Baik et al. 2007; Ahmad, Dickerson et al. 2008) Among these methods, Choi's method allows fine tuning of the size, shape, and the tetragonality of barium titanate nanoparticles. This method uses solvothermal treatment of the mixtures

of titanium oxide nanoparticles and barium hydroxide. Non-stoichiometric perovskite nanoparticles such as $Ba_xSr_{1-x}TiO_3$ are known to exhibit ferroelectric relaxor behavior.(Ravez and Simon 2000) By fine tuning of their size and the ratio of Ba/Sr (usually close to 7:3), colossal permittivities ($>10^5$) can be obtained.(Su, Nuraje et al. 2007) The synthesis of non-stoichiometric barium strontium titanate (BST) combining Choi's solvothermal method is thus suggested as a new method for producing high permittivity nanoparticle fillers, which can significantly improve the dielectric properties of the nanocomposites described throughout this thesis.

8.2.4 Barrier Layer Capacitor Ceramics

Recently giant dielectric constants ($>10^4 - 10^6$) have been observed in $CaCu_3Ti_4O_{12}$ (calcium copper titanate, CCTO), CuO, and ultrafine grain size $BaTiO_{3-x}$ and non-stoichiometric mixtures of them.(Adams, Sinclair et al. 2002; Zang, Zhang et al. 2005; Maensiri, Thongbai et al. 2007; Guillemet-Fritsch, Valdez-Nava et al. 2008; Sarkar, Jana et al. 2008) Unlike ferroelectric relaxor materials, these materials exhibit only little variation in dielectric properties over a wide range of temperature and frequency, which is desirable for technological point of view. The reason for such colossal permittivity is unclear but many observations support the Maxwell-Wagner interfacial polarization effect, in which two different materials share a same interface.(Hughes 2003) There are two or more different phases of ultrafine grain sizes co-existing in these materials that are sharing interfaces each other. When the different phases have different conductance (i.e. a semiconductor and a insulator), the materials transfer charge in different ways (i.e. by conduction or polarization). Therefore there is a discontinuity at the interfaces and charges are accumulated at these interfaces just like charge accumulation in a capacitor. This net effect is called internal barrier layer capacitor effect. Current research is mainly focused on the measurement of permittivity over wide ranges of frequency and temperature with the variation of the compositions by doping exotic element.(Maensiri, Thongbai et al. 2007; Guillemet-Fritsch, Valdez-Nava et al. 2008) However, the studies

on the dielectric breakdown strength, processing, and the approaches using composites in polymers for these materials still need attention.

APPENDIX A

CONJUGATED POLYMER DOPED WITH GOLD NANOPARTICLES WITH CHROMOPHORIC SHELL AS HIGH MOBILITY AND HIGH EFFICIENCY PHOTO-GENERATION MATERIALS

A.1 Introduction

Conducting polymers such as poly(3-hexylthiophene) (P3HT) and poly(3-octylthiophene) (P3OT) show better hole transporting properties than electron.(Coakley and McGehee 2004; Mihailetchi, Xie et al. 2006) These materials blended with electron accepting materials such as C_{60} derivatives (*e.g.* PCBM), CdSe, and PbS have been demonstrated as promising photovoltaic systems.(Erb, Raleva et al. 2004; Huang, Li et al. 2005; McDonald, Konstantatos et al. 2005; Kim, Lee et al. 2007) Nanoparticles of noble metals such as gold and silver show enhanced local electric field in the vicinity of their surface due to the excitation of plasmons. This leads to a strong electronic coupling with the ligands attached on the surface. As a result, enhanced charge transfer, energy transfer, and improved light absorption can be expected.(Wong, Wang et al. 2007) By combining electron accepting chromophore-coated metal nanoparticles (chromophore-shell nanoparticles) with low band gap and hole conducting polymers, one can potentially develop photovoltaic materials with efficient light absorption and enhanced charge carrier generation.(Kim and Carroll 2005) Furthermore, fine tuning of organization of nanoparticles can be possible by using the interactions of surface bound ligands. These metal nanoparticle fractal clusters show broad absorption band and improved conducting properties and can be used as broadband light harvester and/or nano-sized conductor elements to develop efficient photovoltaic materials systems.(Cole and Halas 2006) The chromophoric shell around metal nanoparticles can be quantitatively introduced *via* place exchange reactions of amine-terminated capping agents with thiolated chromophores.

The variation in the degree of place exchange reaction will allow the investigation of the effect of controlled interfacial organization in such host materials.

There are a number of different ways (space-charge limited current (SCLC), time-of-flight (ToF), and field-effect transistor (FET) methods) to measure the carrier mobility of a solid film. SCLC is observed under low mobility conditions and/or under strong illumination conditions where the injected charge density is comparable to the charge density on the electrodes.(Mihailetchi, Duren et al. 2003) SCLC can be expressed by the Child's equation (also known as square law, Mott-Gurney law) for trap-free semiconductors:

$$J = \frac{9}{8}\mu\varepsilon_0\varepsilon_r\frac{V^2}{L^3} \quad \text{or} \quad \log J = 2\log V + C \qquad \text{Equation A.1}$$

where J is current density, μ is charge mobility, ε_r is the dielectric constant of the material, V is the applied voltage, and L is the thickness of the film.

By using the disorder formalism, the mobility can be expressed in terms of zero-field mobility (μ_0) and applied filed (**E**):

$$\mu = \mu_0 \exp(\gamma\sqrt{\mathbf{E}}) \qquad \text{Equation A.2}$$

then, the SCLC can be approximated to(Kaafarani, Kondo et al. 2005):

$$J \cong \frac{9}{8}\varepsilon_0\varepsilon_r\mu_0 \exp\left(0.891\gamma\sqrt{\frac{V}{L}}\right)\frac{V^2}{L^3} \qquad \text{Equation A.3}$$

Therefore, plotting $\log(J/V^2)$ *vs.* $V^{1/2}$ and the linear fitting (Y = a + bX) the plot will give the following:

$$\gamma = bL^{0.5}/0.891$$
$$\mu_0 = \frac{8}{9\varepsilon_r\varepsilon_0}L^3\exp(a) \qquad \text{Equation A.4}$$

A.2 Materials and Methods

Regioregular P3OT was purchased from Aldrich and used without further purification. VA18 is an electron accepting dye as shown in Figure A.1.

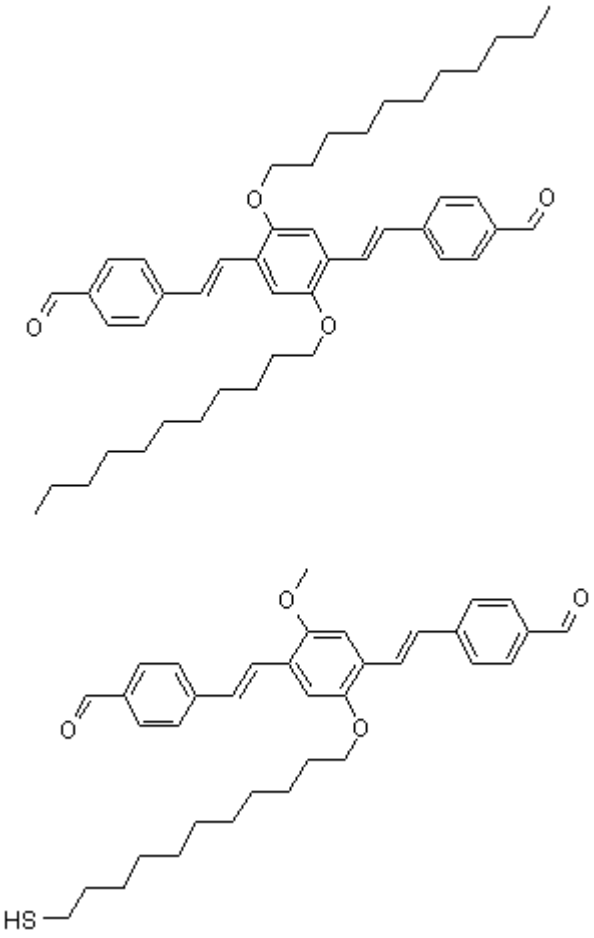

Figure A.1 Chemical structures of VA18 (top) and its thiolated derivative used for place exchange reaction (bottom).

A series of gold metal nanoparticles capped with alkylthiols and oleylamines was synthesized using one-phase method and characterized by Wojtek Haske (WH) (Figure A.2).(Hiramatsu and Osterloh 2004) The average particle size of the gold nanoparticle was about 11.5 nm. Gold nanoparticles were initially capped with oleylamine (OLA). Place exchange was performed with ~20 % ratio. 15.5 wt.% of 20% place exchanged

Au-OLA corresponds to 0.1 vol.% of chromophore and 67.0 wt.% of 20% place exchanged Au-OLA corresponds to 1.0 vol.% of chromophore, respectively.

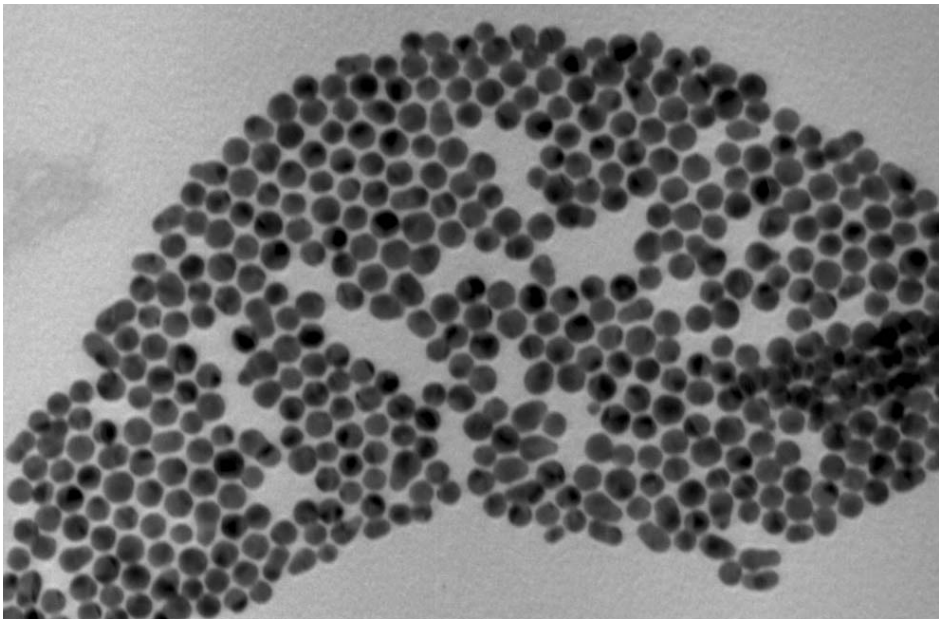

Figure A.2 TEM image of gold nanoparticles with narrow size distribution (11.6 ± 1.7 nm).

P3OT-based composite materials were prepared by dissolving appropriate amount of chromophore-shell metal nanoparticles and P3OT in dry toluene or chloroform. Thin films of these composites were prepared by spin coating as summarized in Table A.1.

Table A.1 Chemical composition and thickness of nanocomposite thin films prepared.

Composition (wt. %)	Sample Name	Solvent	Thickness (nm)
100% P3OT	PK4130B	CHCl3	285
0.1% VA18 in P3OT	PK4130C	CHCl3	298
15.0% VA18 in P3OT	PK4130D	CHCl3	258
15.5% Au-OLA in P3OT	PK4130G	Toluene	151
15.5% Au-PE in P3OT	PK4130H	CHCl3	215
67.0% Au-OLA in P3OT	PK4130K	Toluene	126
67.0% Au-PE in P3OT	PK4130L	CHCl3	185

PEDOT-PSS (Baytron F 4083, Bayer) was spin-coated at 5,000 rpm for 60 sec. on cold plasma-treated and etched ITO-glass (4 SCFH, air, 3 min.) through 0.45 μm PVDF syringe filter. The films were then soft baked at 140°C on a hot plate under ambient air for 10 minute to evaporate residual water. The layer was about 20 nm thick and acted as both a hole injection layer and a protective layer for ITO. The composite films in Table A.1 were then prepared on PEDOT-PSS/ITO/glass substrate. Soft baking condition for non-Au containing films was 100°C, 4 min. and for Au-containing films was 40°C, 4 min.

UV-VIS absorption spectra of the films were recorded on Agilent 8453A spectrometer before depositing the top electrodes.

Top finger electrodes with bottom ITO contact (Al, ~200 nm) were deposited by an e-beam evaporator. The device structure for standard I-V characterization is shown in Figure A.3. Space charge limited current (SCLC) method was used to study the electric properties of the nanocomposite thin films. Digital photograph of final devices are shown in Figure A.4 with description for each device.

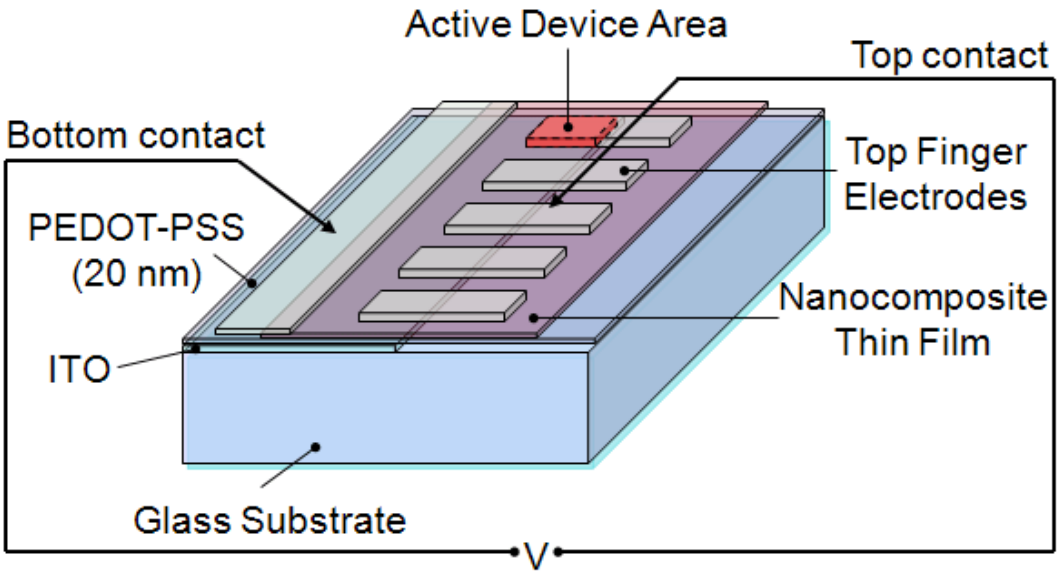

Figure A.3 The device structure for standard I-V characterization.

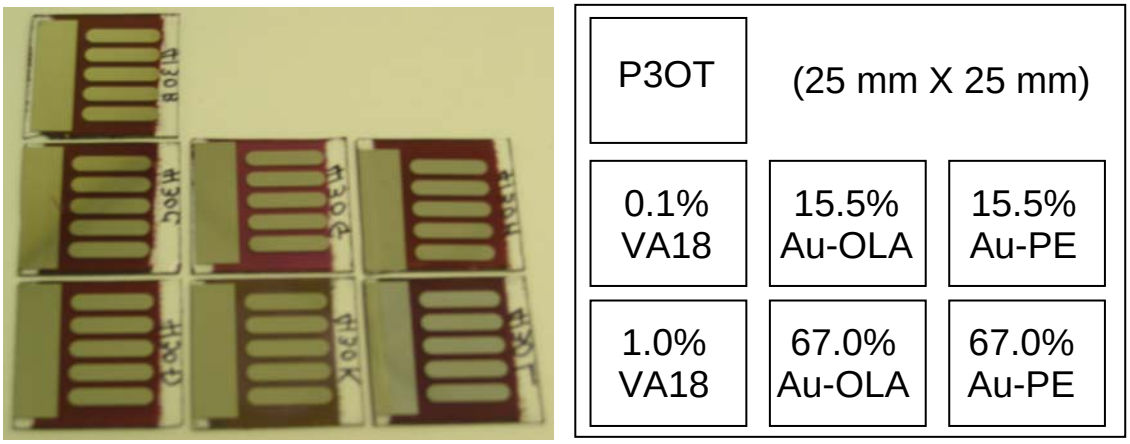

Figure A.4 Digital photography of the final devices for SCLC measurement.

A.3 Results and Discussion

Figure A.5 shows normalized absorption spectra of the nanocomposite thin films acquired at transmission geometry. The background spectrum was taken by using bare ITO/glass. The absorption spectrum of pure P3OT peaks at around 516 nm. The green spectrum is the absorption spectrum of pure Au-OLA aggregate films on a glass slide

which shows characteristic plasmon absorption band of the gold. The nanocomposite films doped with sufficient amount of Au-OLA showed superposed absorption spectra of pure P3OT and pure Au-OLA. The loading amount of place exchanged Au nanoparticles (Au-PE) seemed to be lower than expected due to the loss of the nanoparticles during the filtration to remove dust and aggregates. The broadened peak at shorter wavelength from the films containing 67.0 % Au is due to the contribution from the inter-band transitions of Au nanoparticles. The shoulders at longer wavelength seem to be the interference fringes from thin films and should be ruled out as films with varying thickness are prepared.

Time-of-flight (ToF) method is a straightforward method to determine the carrier mobility. However, this method may not be a good option for the samples prepared since the optical thickness of the films at 337 nm, which is used for excitation, is not thick enough to absorb all of the incident photons and the preparation of optical quality thick film was quite challenging due to the poor film forming property and limited availability of the materials. However, if the wavelength of the excitation can be tuned close to optically thick area, the use of ToF seems feasible. (NB: when this experiment was in progress, only 337 nm was available) The optical density of P3OT films at the thickness range (150~300 nm) was already at around 0.5~1.5 depending on the mass fraction of P3OT. Therefore, increasing the thickness of the films by a factor of 2 – 5 would offer good chances to test the materials using ToF method. Investigation of thermal properties of each composite (TGA and DSC) will provide good guidelines to processing the materials into relatively thick films for time-of-flight (ToF) measurement. The choice of excitation wavelength for ToF measurement should also be considered along with the absorption spectra of the composite materials to find the wavelengths at which the films are optically thick enough to obtain non-dispersive ToF results.

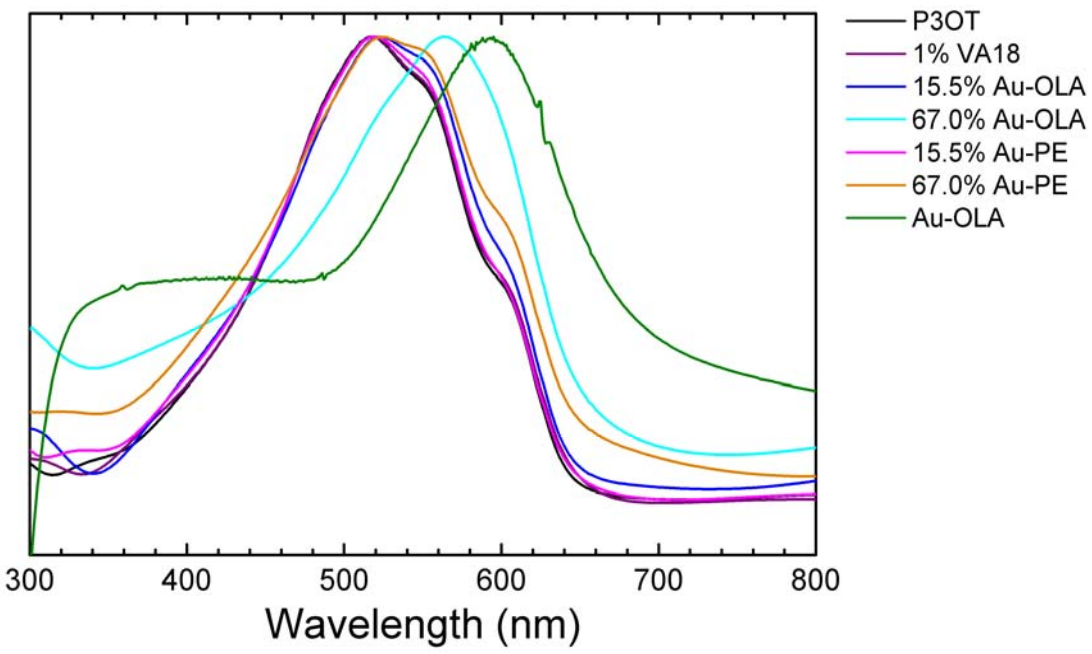

Figure A.5 Normalized UV-VIS absorption spectra of nanocomposite thin films after soft bake.

The dark current of each device was measured by applying DC bias and plotted in Figure A.6. The dark current under zero bias was zero from all the devices tested. P3OT films showed rectification behavior since it has higher hole mobility. However, it was not clear whether the dominant charge carrier is hole or electron in the SCLC measurement. Au-OLA doped P3OT films showed increased current which may be due to the increase of both hole and electron mobility as it showed Ohmic current under negative bias. In contrast, the VA18 did not give significant effect on the mobility. The chromophore-shell capped gold nanoparticle appeared to block the charge carriers. Under higher biases, all of the devices showed negative resistivity-like behavior. This can be explained by too many carriers generated in the film which effectively blocks the carriers from moving along the applied field. Under high applied field, >8 V or >12 V depending on the compositions, swelling of the material under the top electrode was observed. This was observed only in the perimeter of the device bordering the composite

film. It may be due to the burning of pinholes or due to the thermal effect under such high applied field. The data reported here preliminary results and thus it is not sufficient to make a conclusion. However, the results are promising because P3OT and its metal nanoparticle composites can be easily processed into thin films with decent optical quality.

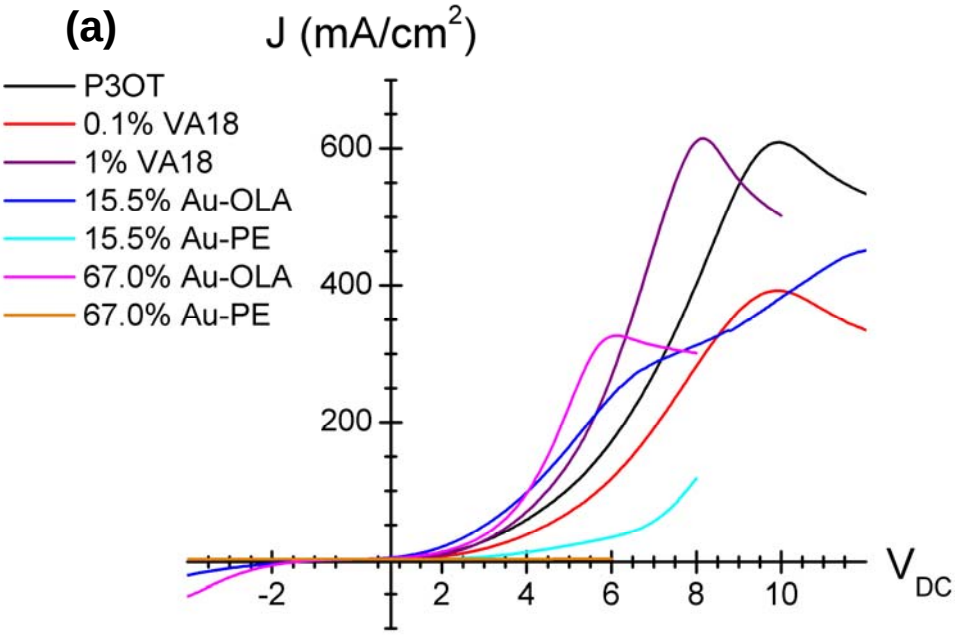
(a)
J (mA/cm^2)
P3OT
0.1% VA18
1% VA18
15.5% Au-OLA
15.5% Au-PE
67.0% Au-OLA
67.0% Au-PE
600
400
200
-2
2
4
6
8
10
V_{DC}

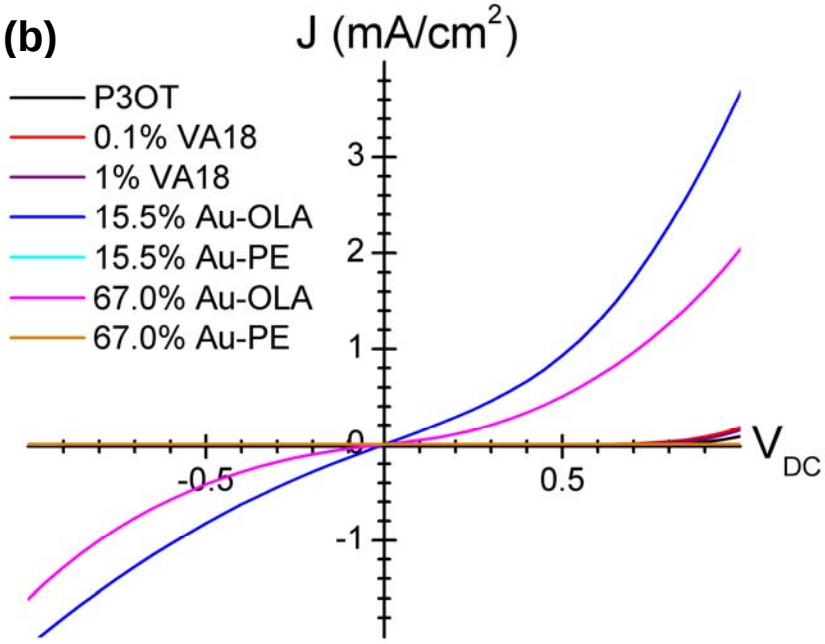
(b)
J (mA/cm^2)
P3OT
0.1% VA18
1% VA18
15.5% Au-OLA
15.5% Au-PE
67.0% Au-OLA
67.0% Au-PE
3
2
1
0
-1
-0.5
0.5
V_{DC}

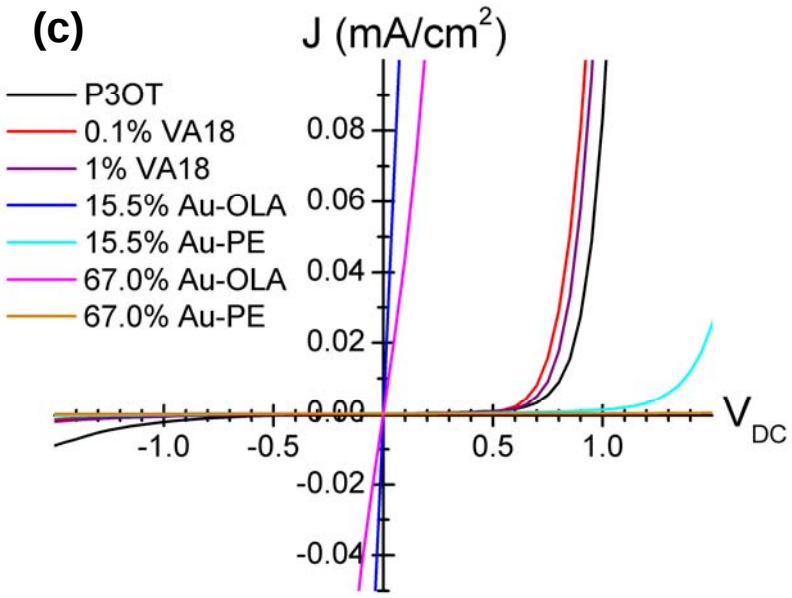

Figure A.6 Characteristic I-V curve of the devices tested under dark condition. (a) from -4 V_{DC} up to the point where each device begins to show abnormal behavior. (b) and (c) are the plots zoomed close to zero applied field.

Figure A.7 shows the plots of logJ *vs.* logV for each device. The regions with slope of 1 corresponds to Ohmic regime, slope > 2 corresponds to trap-limited SCLC (TL-SCLC) regime, and slope = 2 corresponds to trap-free SCLC regime. The Ohmic regions in each device were clearly distinguished and appeared at low applied voltage. However, it was difficult to find SCLC (slope=2) region which usually appears after TL-SCLC region. The slope was actually slightly greater than 2 and so it is not safe to say that this region is SCLC regime. For this reason, the carrier mobility cannot be calculated. The increased slope may be due to the increased conductivity of the film and/or due to the leakage current. Repeating experiments should be performed whether this is intrinsic materials response or errors in measurements.

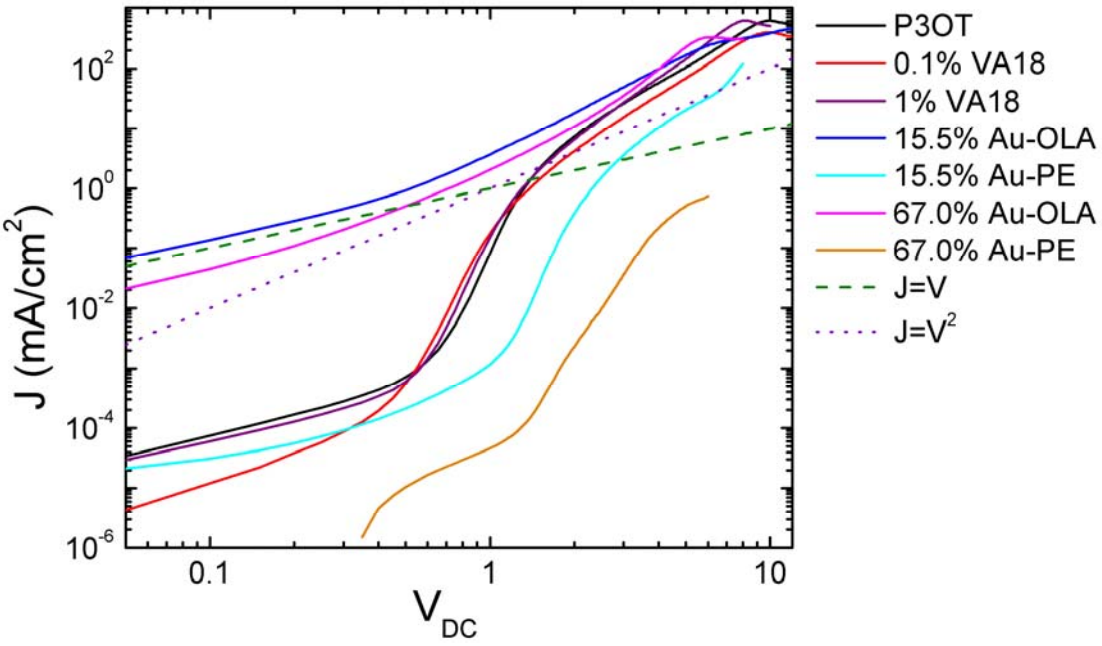

Figure A.7 Log-Log plot of J *vs.* V to monitor the change in the slope. Each region can be assigned as Ohmic (slope=1), TL-SCLC (slope>2), and SCLC (slope=2) region.

A.4 Conclusions and Future Work

Chromophore-shell metal nanoparticles dispersed in conducting polymer host, P3OT was prepared in thin film forms with optical quality suitable for SCLC measurement. The UV-VIS absorption spectra of nanoparticle-doped P3OT exhibited broadened absorption band. P3OT doped with Au-OLA showed increased current and showed smooth transition from Ohmic to TL-SCLC then to SCLC regime. However, it was not enough to conclude that the observed current is SCLC since the slope was greater than 2.

Suggested future work include the characterization of capacitance and conductance of the nanocomposites, thick film fabrication and employing ToF method to measure the carrier mobility, and the I-V characterizations under varying illumination conditions. Thermal annealing of P3HT films is known to affect the ordering and micro-crystallinity of the films after preparation due to the crystalline nature of P3HT. Similarly, thin films of P3OT are expected to show changes after thermal treatment.

Therefore, it would be interesting to study the effect of thermal annealing of nanocomposite films on the absorption spectra and other electrical properties.

APPENDIX B

DIRECT LASER WRITING HIGH REFRACTIVE INDEX NANOCOMPOSITES

B.1 Introduction

Photonic crystals are periodic dielectric structures with nanometer scale periodicity which alters the propagation of electromagnetic waves (photons) in a similar way that the motion of electrons is affected by the periodicity of semiconductor crystals.(Joannopoulos, Meade et al. 1995; Busch, Freymann et al. 2007) Woodpile structure is one of the best photonic crystal structures because it has a large gap size (~25% of the central frequency) and a low critical refractive index (n = 1.9) for achieving a three-dimensional (3D) complete band gap inside the structure.(Ho, Chan et al. 1994) However, typical processable materials do not have high enough refractive indices for achieving 3D complete band gaps.

Two-photon microfabrication (TPM) is a maskless, straightforward direct laser writing lithography that can build three-dimensional micro-structures of arbitrary shapes with high resolutions.(Cumpston, Ananthavel et al. 1999) In recent years, it became a widely used tool to build 3D microstructures or nanostructures, for example, photonic crystal or photonic band gap (PBG) structures, optical limiting devices, microfluidic devices, micro electro-mechanical systems, etc. To date, the majority of the micro-structures prepared by TPM have been simple organic polymers that can be photo-polymerized using two-photon active dyes.(Marder, Brédas et al. 2007) These structures have been used as templates to make secondary structures by back-filling of other materials and removing the parent template.(Tetreault, Freymann et al. 2006) However, these inversion processes are not straightforward and involve many delicate and complicated fabrication steps.

Materials based on titanium dioxide have gained interest in photonics as the two common crystalline phases have high refractive indices (2.5 for anatase and 3.0 for rutile

phase). Organic-inorganic hybrid titania materials combining sol-gel process of titania precursors and photo-sensitive organic groups have been used for photo-patterning.(Segawa, Tateishi et al. 2004) Nanocomposites of titanium oxide in a polymer matrix have been demonstrated as transparent UV filters.(Nussbaumer, Caseri et al. 2003) Combining high refractive index titanium oxide nanoparticles with photo-crosslinkable polymers thus can allow a high refractive index nanocomposite capable of patterning with direct laser writing technique. Recent development of high refractive index, direct laser writing materials based on chalcogenide glass materials and quantum dot-doped polymers(Wong, Deubel et al. 2006; Ventura, Bullen et al. 2007) have proved that titania-based nanocomposites can be also a possible approach to realize such materials.

This appendix describes the concepts and ideas on the high refractive index, direct laser writing materials based on titanium oxide-organic nanocomposites with some preliminary experimental results and suggested future work.

B.2 Materials and Methods

B.2.1 Surface Modification of TiO_2 Nanoparticles

1.40 g of Degussa P25 TiO_2 nanoparticles (AEROXIDE, 21 nm, BET sp. surface area = 45 ± 5 m^2/g, d = 3.9, mixed phase of 70 % anatase + 30 % rutile)(Guerrero, Mutin et al. 2001) were dispersed in 100 mL of 200 proof absolute ethanol and ultrasonicated for 3 hours in a ice-bath cooled container by using a 750 W ultrasonic processor running at 35 % power. The dispersion was then stirred overnight at room temperature. 1.22 mmol (375 mg) of ACPA (acryloyloxyundecylphosphonic acid, synthesized and characterized by Peter J. Hotchkiss, pure by NMR, Figure B.1), which corresponds to *ca.* 2.52 excess of monolayer, and 1.875 g of BHT as a stabilizer (5,000 ppm of monomer) were mixed and dissolved in absolute ethanol. The monomer solution was added to the P25 dispersion. The mixture was stirred for 21 hours at room temperature, then 1 hour at 80°C. The final reaction product was cooled to room temperature and washed by

centrifuge using 2 × 200 mL of absolute ethanol. The particles were dried under vacuum at 80°C before analysis.

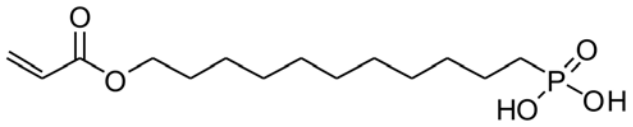

Figure B1. The structure of ACPA (acryloyloxyundecylphosphonic acid).

A high refractive index phosphonic acid ligand, pentabromobenzylphosphonic acid (PBBPA) was also synthesized and characterized by Peter J. Hotchkiss. The structure is shown below.

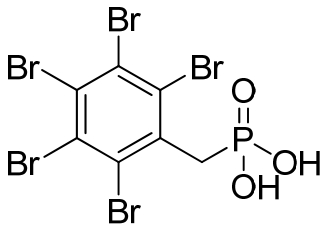

Figure B2. The structure of PBBPA (pentabromobenzylphosphonic acid).

B.2.2 Preparation of TiO_2 Dispersion in Acrylate Monomer

Both unmodified P25 and ACPA-modified P25 (ACPA-P25) were used to form dispersions in MAEAA (2-(Methacryloyloxy)ethyl acetoacetate, 98 %, stabilized with 200 ppm MEHQ, Aldrich, n20/D = 1.456). Titanium dioxide nanoparticles were initially dispersed in a large quantity of methanol (99.9 % ACS reagent grade, Aldrich) by ball milling. Ball milling did not cause any susceptible polymerization of acrylate, which was confirmed by taking FT-IR spectra before and after ball-milling the mixture. The grinding media were removed and the resultant dispersions were mixed with MAEAA to form 5 vol. % titania dispersions. The inhibitor in the MAEAA was not removed and

used as received. Most excess methanol was removed by rotary evaporation to yield white viscous sol.

B.2.3 High Refractive Index Host Materials

EXP04054 (high index coating material: propyleneglycol methyl ether (PGME) 10~25 %, methyl acetoacetate 1~10 %, n-butanol 0~30 %, proprietary polymer solids (titanium alkoxide oligomer + polystyrene based polymer) 35~65, $n_D \approx 1.59$) was obtained from Brewer Science, Inc. (Rolla, MO). The refractive index of EXP04054 after gelation is 1.96 at 700 nm. The density of EXP04054 was found to be ~1.05 g/mL at room temperature. EXP04054 can be crosslinked at 254 nm (10~20 J/cm^2) for very thin films (<400 nm). EXP04054 can be developed by PGME, Acetone, NMP, PGMEA, and Ethyl lactate. To make a thick film, the raw material was concentrated to 50~60% of its original volume by rotary evaporator at 50~60°C to give a highly viscous yellow liquid.

EXP04215-90 (proprietary composition, $n_D \approx 1.63$) was also obtained from Brewer Science, Inc. Crosslinked EXP04215-90 has refractive index of 1.59 at 700 nm and can be cross-linked by exposure to a broadband UV source (3.5 J/cm^2) and has excellent adhesion property to glass, quartz, and silicon substrates. EXP04215-90 can be developed by PGMEA.

Pentabromophenyl methacrylate (PBPM, $n_D = 1.17$) was purchased from Aldrich and used without further purification. PBPM is soluble in toluene but the polymerized product is insoluble in toluene. The polymerized PBPM is soluble in chloroform.

B.2.4 Preparation of Nanocomposite Films

The viscosity of the dispersions containing 5 vol. % of unmodified P25 and ACPA-P25 each in MAEAA matrix was adjusted by propyleneglycol methyl ether acetate (PGMEA), though it turned out to be a poor solvent for the particles later. Thick films from the dispersions of ACPA-P25:MAEAA were prepared by using 50 μm thick 1" diameter circular Teflon spacer sandwiched between two regular glass slides clamped

by four small binder clips. Glass slides were cut into 1" x 1" pieces and cleaned in ethanol by ultrasonication. The bottom glass slide was pre-heated on a hot plate at 100°C for 2 minutes. Too long pre-heating time was not desirable as the film showed too many trapped air bubbles. Optimized condition would be found by decreasing the pre-heating temperature and time. The films were then dried overnight at ambient condition followed by drying *in vacuo* at 100°C for 1 day. Drop cast films were also prepared by similar method.

B.2.5 Characterization of Nanocomposite Films

UV-VIS absorption spectra were recorded using a HP8453A diode array. One photon UV exposure experiments were performed using a mask aligner (MJB-3, Karl Suss) to illuminate UV light of specific wavelengths through a photomask. The dose was controlled by exposure time after measuring the power of UV source each time. No filter was used for the test experiments. 60% concentrated EXP04054 (*vide infra*) films with and without Irganox-907 photo-initiator were prepared. 0.1 mL of I-907 stock solution (100 mg/mL in PGME) was added to 1 mL of concentrated EXP04054. Glass slides and Si wafers were used as substrates depending on the subsequent characterizations (glass slide for UV-VIS absorption and Si wafers for FT-IR measurements). The adhesion of the substrates was promoted by repeating three times of spin coating of 5% MeOH solution of methacryloylpropyl trimethoxysilane followed by soft baking the substrate at 90°C for 1 minute. Spin coating of the prepared materials at 1,000~1,500 rpm gave uniform and thin films. The films were soft baked at 100°C hot plate for 1 minute and aged at room temperature under dark for 2 days before the UV exposure experiment. The films remained wet and were not hard enough for the thickness measurement using a contact profilometer. The lamp power measured at 240 nm and 320 nm was 5.7 mW/cm^2 and 14.5 mW/cm^2, respectively. Exposure times were set to give the dose of 20 and 40 mJ/cm^2 calculated from the power at 240 nm (without I-907) and 320 nm (with I-907). Acetone was used as development solvent but nothing remained on the substrate,

implying that either the developing condition was too aggressive or the dose was too low. After the first trial, post-exposure bake step (100°C, 1 minute) was added and the dose was increased to 200 and 400 mJ/cm^2.

B.3 Results and Discussion

B.3.1 Characterization of Surface Modified TiO_2 Nanoparticles

Phosphonic acid and phosphonate esters are known to bind strongly on the surface of metal oxides such as titania, alumina, and zirconia under mild conditions.(Gao, Dickinson et al. 1996; Mutin, Guerrero et al. 2005) The kinetics of binding is much faster for phosphonic acid than phosphonate. The FT-IR spectra of ACPA and ACPA-modified P25 (ACPA-P25) are shown in Figure B.3. There is still some C=C bond left on the surface (1634 cm^{-1}) and the broadened C=O stretching peak indicates the presence of C=O modes in different environments. The shoulder at 1725 cm^{-1} corresponds to unreacted acrylate and the peak at 1731 cm^{-1} is attributed to the C=O stretching mode of reacted acrylate where the increased double bond character comes from the absence of adjacent conjugated C=C double bond that used to take part in the resonance stabilization. In order to prevent the acrylate group from reacting during the surface modification, a large quantity of stronger inhibitors, such as MEHQ, may be used during the surface modification since the inhibitor can be easily removed in the washing step after modification.

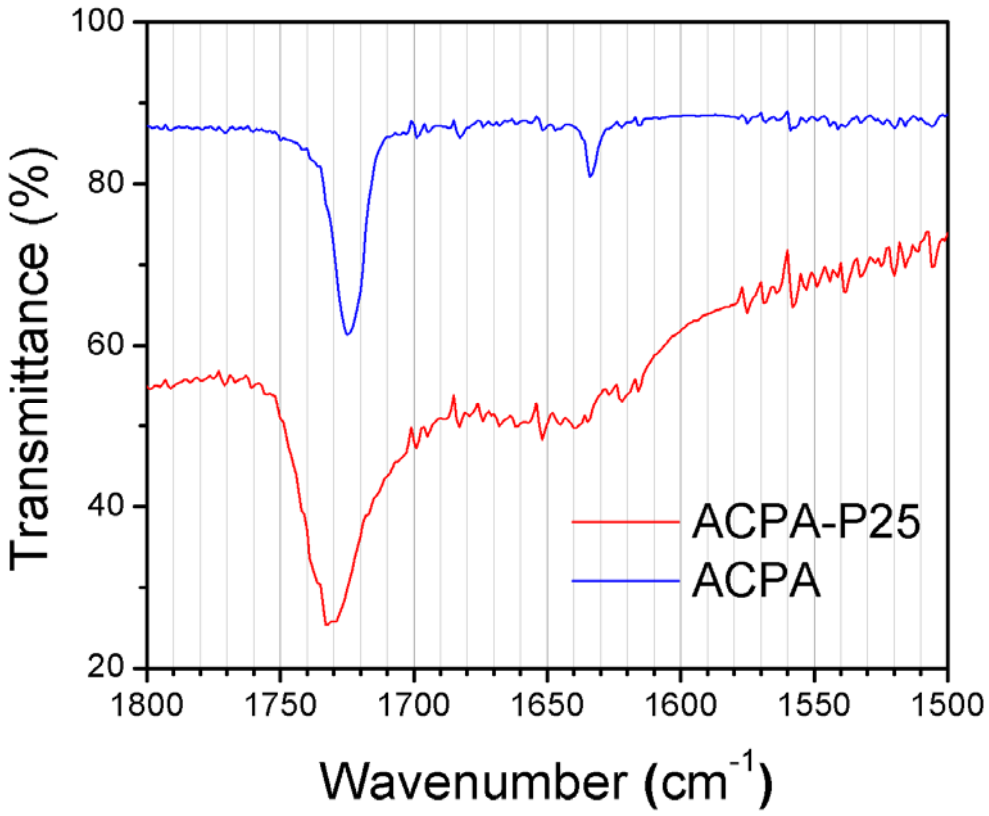

Figure B.3 FT-IR spectra of pure ACPA (blue) and ACPA-modified P25 (red).

B.3.2 Effective Refractive Index of Nanocomposites

Titanium dioxide nanoparticles, P25, has mixed phase of 70 % anatase and 30 % rutile and thus has refractive index ($n_{D,20}$) of 2.595 as calculated by Equation B.1.(Zhao, Wang et al. 2005) When this value is plugged into Equation B.1, the effective refractive index of a nanocomposite (n_C) at normal incidence with varying volume fractions of P25 (v_f) in a host material of refractive index (n_h) ranging from 1.2 to 1.7 can be obtained as depicted in Figure B.4.

$$n_c = \left[n_f^2 v_f + n_h^2 \left(1 - v_f\right)\right]^{1/2} \qquad \text{Equation B.1}$$

In order to achieve a 3D photonic band gap by using a woodpile structure, the refractive index of the material used in the fabrication should be greater than 1.9~2.0.(Ho,

Chan et al. 1994) In addition, sufficient transmittance is required at the wavelength of writing from about 50 micron thick films for the direct laser writing.

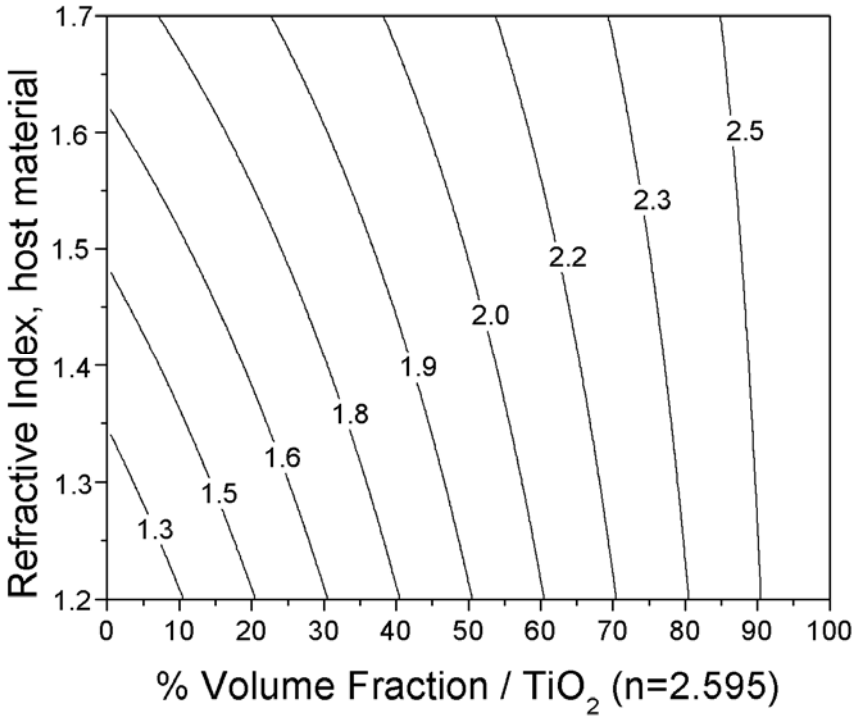

Figure B.4 Contour plot showing the refractive index of a nanocomposite made of P25 titania in a host matrix with varying volume fractions and varying refractive index. Note that the composite refractive index of 2.0 or greater can be achieved when at least ~60 vol. % of P25 is incorporated into a common organic host.

B.3.3 Stability of ACPA-P25 Dispersion

The dispersions of ACPA-P25 (acryloyloxyundecylphosphonic acid-modified 21 nm titania) in methyl isobutyl ketone (MIBK), $CHCl_3$, DMF, Toluene, and CCl_4 were prepared (10 mg / 10 mL) and their stability was observed over a week. ACPA-P25 was very unstable in non-polar solvents (toluene and CCl_4) and showed rapid sedimentation within a few hours. After 24 hr, toluene and CCl_4 dispersions showed complete sedimentation, while $CHCl_3$ dispersion exhibited slight sedimentation of nanoparticles.

Only the dispersions of MIBK and DMF were stable with no noticeable sedimentation after a week.

The dispersions of unmodified and surface modified $BaTiO_3$ and TiO_2 nanoparticles in PGME were tested for a month period at room temperature and are shown in Figure B.5.

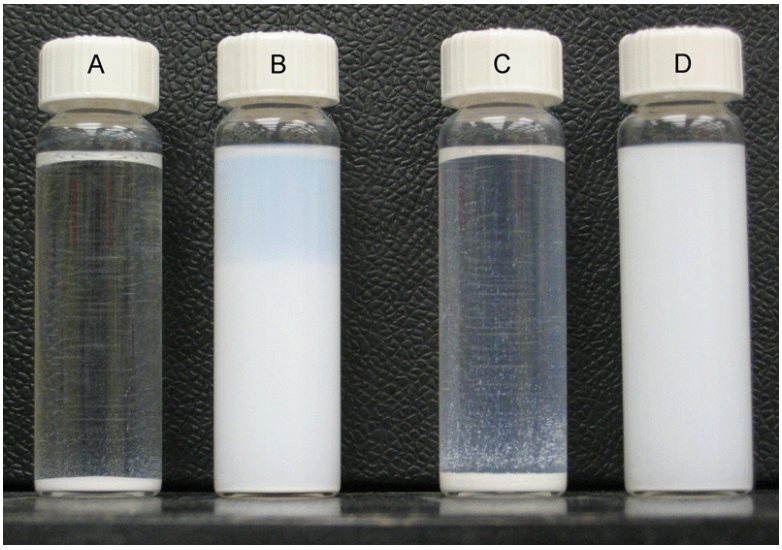

Figure B.5 Dispersions of nanoparticles in PGME (1 mg/mL) stored at room temperature for one month. A: unmodified Aldrich $BaTiO_3$ (30~50 nm), B: PEGPA-$BaTiO_3$, C: unmodified TiO_2 (P25, 21 nm), D: ACPA-P25 (acryloyloxyundecyl phosphonic acid modified TiO_2).

Since the ACPA-P25 was very stable in PGME, ACPA-P25 was mixed in concentrated EXP04054 forming light yellow opaque viscous liquid. The amount of ACPA-P25 was 10 mg per mL of concentrated EXP04054. The primary intention of adding TiO_2 nanoparticles is to increase the effective refractive index of composite. The TiO_2 nanoparticles may also act as filler material to enhance the mechanical strength of the polymer host and as nucleation sites in the mixture for the growth of crystalline phase titania network from the titania precursors in EXP04054.

B.3.4 Titania Composite Film Fabrication and Optical Characterization

The unmodified P25-filled films after drying showed many cracks in both spacer method and drop casting method. Drop cast film of ACPA-P25 did not develop cracks but the film was very opaque. ACPA-25 filled films prepared by pre-heating the substrate for long time showed many trapped air bubbles due to the fast evaporation of solvents. However, the film prepared by short pre-heating yielded uniform and homogeneous film with no crack inside though it had some cracks along the edges of the circular area. Figure B.6 shows the UV-VIS absorption spectra taken from a good area of unmodified P25-filled film and ACPA-P25-filled film.

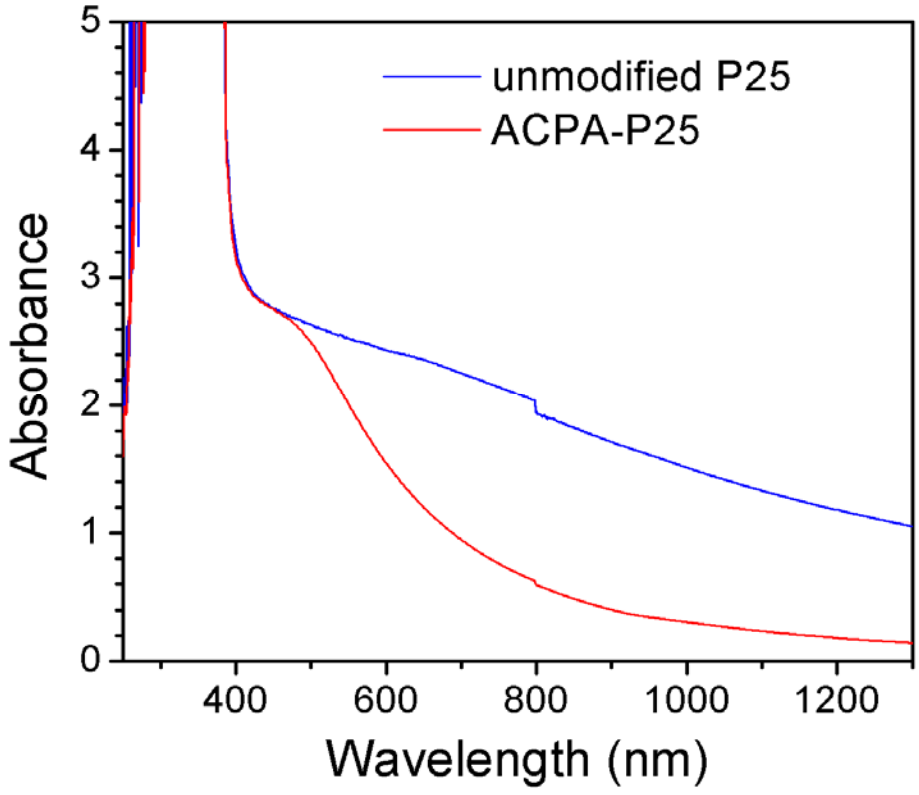

Figure B.6 UV-VIS absorption spectra of 50 μm thick nanocomposite films containing 5 vol. % of P25 (blue) and ACPA-P25 (red).

Though the quality of the film was good at this volume loading, the refractive index contrast between the nanoparticle and the host was still too high to form a transparent film which is desirable for direct laser writing. The scattering can be further reduced by using better dispersion solvent (not PGMEA) and using higher index monomers such as highly brominated aryl (phenyls, naphthalenes, bis-phenols, etc.) with polymerizable groups. Similar phosphonic acids should also be prepared as compatibilizers for titania nanoparticles.

B.3.5 Titania Nanocomposites in High Refractive Index Host Materials

In general, materials containing titanium oxide precursors and/or highly polarizable groups show high refractive index. Some of the proposed structures for high index host and high index surface modifiers are given below:

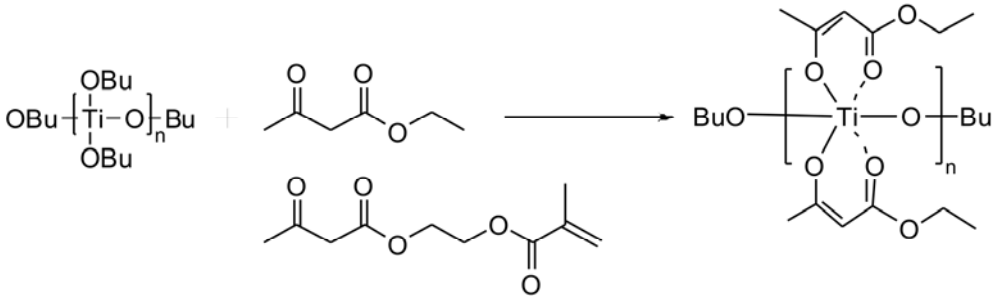

Figure B.7 The proposed structure of high refractive index titania precursors.

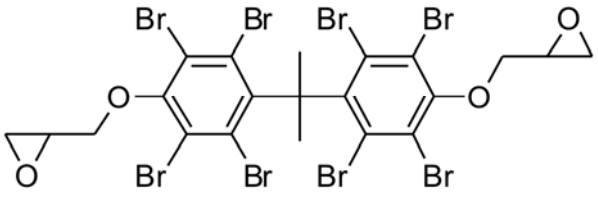

Figure B.8 Proposed structure of a high refractive index brominated epoxy. This material is not commercially available and no record was found in SciFinder search.

Surface-modified titanium dioxide nanoparticles (P25) containing photo-polymerizable group (acrylate) were incorporated in commercially available high index materials with sufficiently high volume loading. Theoretically, those composites will show effective refractive index greater than 2.0.

The initial compositions studied are: 50:50 vol. ACPA-P25:EXP04054, 50:50 vol. ACPA-P25:EXP04215-90, 1:1 wt. PBBZPA-P25:PBPM, 50:50 vol. PBBZPA-P25:EXP04215-90. (PBBZPA: pentabromobenzyl phosphonic acid, PBPM: pentabromophenyl methacrylate). One photon UV exposure experiments on the spin coated films of ACPA-P25 composite in Brewer EXP04054 concentrated to its 60 % of original volume (10 mg/mL) as well as those of concentrated EXP04054 without P25 were performed. Under the exposure conditions described in section B2.5, the one-photon UV patterning was successful only in the composites containing EXP04215-90 after developing the exposed films in acetone. However, the films were subject to severe crack problems. Same method was used for ACPA-P25 added concentrated EXP04054 (10 mg/mL) but the crack problem was even worse. Changing conditions such as the use of less aggressive solvents (PGME, PGMEA, ethyl lactate, DMF, etc.) for development, using plasticizers such as propylene carbonate to lower T_g, and using an elastic sub-layer (fluoropolymers or PDMS) may be considered as options to minimize the crack problems.

The composites of EXP04054 (titania precursor) initially showed cracks but did not show cracks when the films were prepared after aging the composite solution for one week at room temperature. PBPM is a solid monomer and is soluble in toluene but not very soluble in solvents good for dispersing ACPA-modified P25 such as PGME or PGMEA. Mixed solvent was also attempted but the photo-patternability was not obtained. Addition of initiators and control of UV dosage will probably give photo-patternability of this composite system. However, the transmittance of the film was not very good. The use of PBBZPA-modified P25 nanoparticles is expected to improve this

problem. Figure B.9 shows the UV-VIS absorption spectra for different composite thin films prepared.

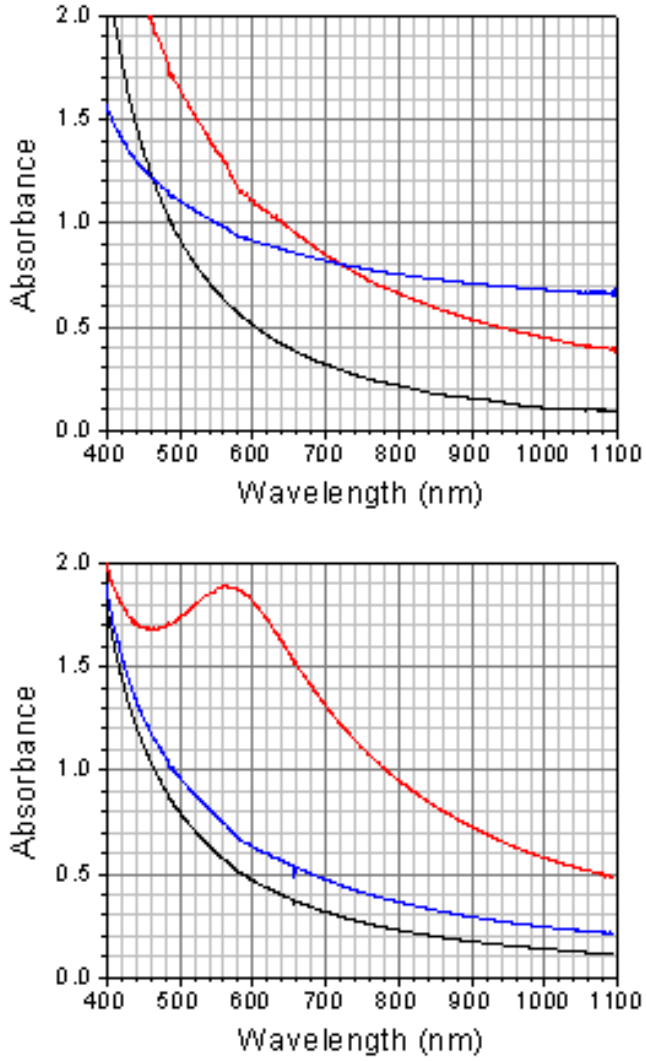

Figure B.9 UV-Vis absorption spectra of the P25-nanocomposite films prepared on glass slide. The transmittances observed were much lower than those calculated from theoretical scattering coefficient. Top: ~1.75μm thick spin-coated films of 50:50 AC-P25:EXP04054 (black), 50:50 AC-P25:EXP04215-90 (red), and 1:1 wt. AC-P25:PBPM (blue). Bottom: 50:50 AC-P25:EXP04215-90, 3.41 μm (black), 1:1 wt. AC-P25:PBPM, 0.92 μm (red), and 50:50 AC-P25:EXP04215-90, 1.60 μm (blue).

After performing a set of initial experiments with P25 nanoparticles (21 nm), it turned out that the size of the nanoparticle is the most critical parameter that must be considered to enhance the transmittance of the thick nanocomposite films.

B.3.6 Problems of Nanocomposites Based on Commercial Titania Nanoparticles

As mentioned above, one big problem of the approaches described in this appendix is the Rayleigh light scattering. The scattering coefficient (light scattered fraction per unit length) of nanocomposite films can be expressed as:

$$\alpha_{SC} = 32\pi n_p^4 \frac{r^3}{\lambda^4} \eta \left(\frac{s^2 - 1}{s^2 + 2} \right)^2 \qquad \text{Equation B.2}$$

where r is the radius of the nanoparticle, n_p is the refractive index of the nanoparticle, η is the volume fraction of the nanoparticle, and s is the refractive index contrast (n_p/n_h, n_h is the refractive index of the host material).(Bohren and Huffman 1983) From this equation derived from Rayleigh light scattering by a particle, the scattering coefficient can be plotted as a function of the nanoparticle diameter and the refractive index of the host material, as shown in Figure B.10.

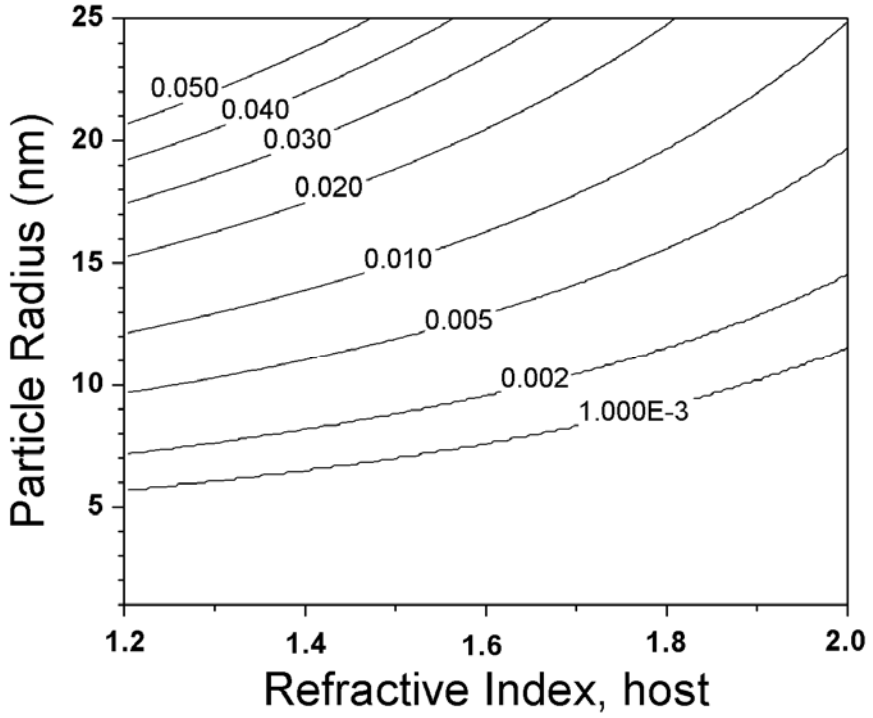

Figure B.10 Contours of the scattering coefficient (fraction of the scattered light per each μm travel of light) of nanocomposite films filled with 50% vol. nanoparticle, whose refractive index is 2.595 at Sodium-D line (589 nm).

According to this model, particle diameter of 11 nm with host refractive index of 1.6 should give 0.3 % loss of incident light per micron due to Rayleigh light scattering. However, the transmittance of the films was only at most ~50 % implying the presence of large aggregates. Therefore, it is critical to decrease the size of the nanoparticles and the nanoparticle aggregation in order to reduce the light scattering at the wavelength of direct laser writing (typically at 730 nm).

In conclusion, the main issues of the approach described in this appendix are: i) film formation property, especially for thick enough film to employ two-photon 3D microfabrication without defects such as cracks, ii) Rayleigh light scattering due to the agglomeration of the nanoparticles as well as the refractive index contrast, iii) maintaining the photo-pattering properties at high volume loading, iv) optimization of

thermal treatment and development conditions for the best results. The first issue can be overcome by using surface modification methodology which effectively reduces the interfacial interactions between the nanoparticles and increases the compatibility of the particles with host matrix. In order to reduce the crack problem of thick films, elastomeric substrate (PDMS, rubberlike materials) or internal/external plasticizers can be considered. Bi-functional co-monomers with low shrinkage property that bares at least one ring-opening mechanism such as glycidoxy methacrylate can also be considered. In order to minimize the light scattering problem, the size of the titania nanoparticles should be carefully considered.

B.3.7 Optimizing the Nanoparticle Size

Figure B.11 shows the effective refractive index contours of nanocomposites based on rutile phase titania nanoparticles of different sizes. The refractive index of each titania nanoparticle was calculated based on the volume fraction of the titania nanoparticle core and that of the ligand shell. The results indicate that 5 nm diameter titania should be used more than 50 vol. % in the nanocomposites using typical high refractive index host in order to achieve the effective refractive index of 1.9. This is well above the percolation limit of the nanoparticles. In the case of 15 nm titania, the required volume fraction is lower than that of 5 nm titania. However, the refractive index contrast can be still problematic with this size. Therefore, the optimum size of the rutile titania is close to 10 nm. Based on this model, the synthesis of 10 nm rutile phase titania nanoparticles were investigated.

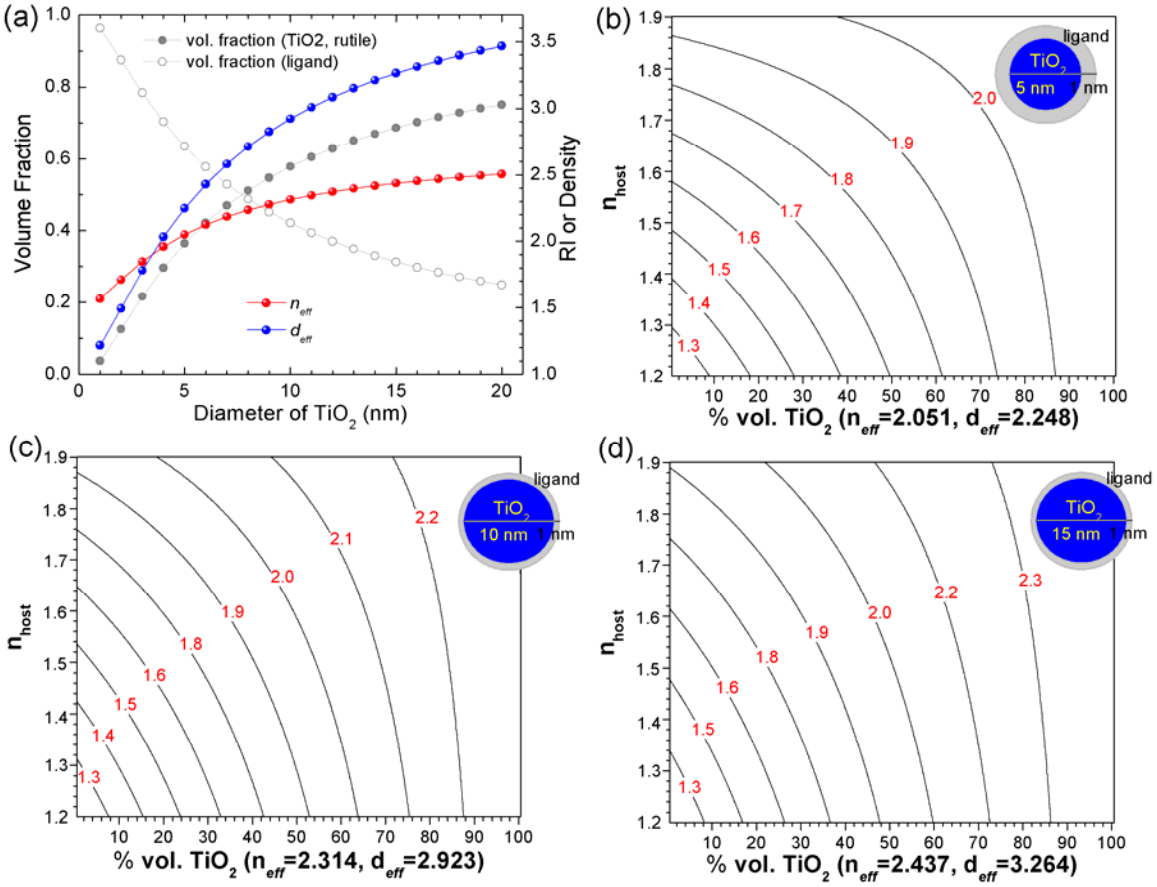

Figure B.11 The contours of the effective refractive indices of nanocomposites based on ligand-coated rutile titania nanoparticles of different sizes. The refractive index of ligand-coated rutile titania was calculated based on the volume fractions of titania core and the ligand shell, as shown in the graph (a).

B.3.8 Synthesis of 10 nm Rutile Phase Titanium Dioxide Nanoparticles

Among the various known methods to prepare titania nanoparticles, the use of $TiCl_4$ precursor seems to be a desirable approach to prepare rutile phase titania nanoparticles because $TiCl_4$ favors the formation of rutile phase at relatively low temperatures.(Cheng, Ma et al. 1995; Borse, Kankate et al. 2002; Li, Fan et al. 2002; Zhang and Gao 2003; Wang, Gu et al. 2004) Other conditions that favor the formation of rutile phase titania from $TiCl_4$ are low pH, high precursor concentration, and high

temperature.(Cheng, Ma et al. 1995; Cozzoli, Kornowski et al. 2003; Wang, Gu et al. 2004) The titania from $TiCl_4$ is formed in the following hydrolysis steps:(Trentler, Denler et al. 1999)

$$TiCl_4 + H_2O \rightarrow TiOCl_2 + 2HCl$$

$$TiOCl_2 + H_2O \rightarrow TiO_2 + 2HCl$$

The high reactivity of $TiCl_4$ with water often leads to largely aggregated rutile crystals. Therefore, the control of the hydrolysis reaction of $TiCl_4$ is the key point to control the size and shape of the rutile titania formed. One approach to control the hydrolysis reaction is to confine the growth of titania crystals within a micelle.(Zhang, Qi et al. 2002) The hydrolysis of $TiCl_4$ generates HCl as a side product, which makes the reaction media highly acidic. Therefore, anionic surfactants are not suitable as they are protonated and precipitated in aqueous system. In this regard, a cationic surfactant, benzyl dodecyl dimethyl ammonium chloride (BDDAC) was chosen as the surfactant. (Figure B.12)

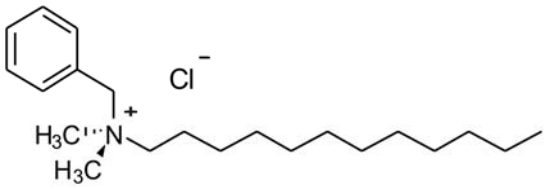

Figure B.12 The structure of benzyl dodecyl dimethyl ammonium chloride, BDDAC.

The aggregation number of BDDAC is 27 and the critical micelle concentration (CMC) is 8.8 mM at 25°C.(Castillo, Czapkiewicz et al. 1999) The mixture of BDDAC above its CMC with $TiCl_4$ in aqueous medium will form a micelle, in which the intermediate product, $TiOCl_2$ is confined. This mixture can be aged at various temperatures to allow the growth of titania nanoparticles, then the growth of titania can

be quenched by the addition of a phosphonic acid ligand with a nonpolar group, such as octadecyl phosphonic acid, which will bind to the surface of titania nanoparticles formed and precipitate the titania in the aqueous medium. An aqueous solution of 0.729 M $TiCl_4$ with 20 mM BDDAC was prepared and the solution was separated into four different containers. The solution was transparent and no precipitation was observed for more than 19 days at room temperature. Each part of the solution was thermally aged for 1 hour at room temperature, 40°C, 50°C, and 60°C, respectively. The rate of the hydrolysis increases with increasing the aging temperature. After the aging, octadecyl phosphonic acid (ODPA) was added to the mixture to quench the growth of the titania nanoparticles and precipitate them out of the aqueous solvent. White precipitation was observed from all of the mixtures as the ODPA binds to the titania nanoparticles. The product was then washed multiple times by centrifugation using ethanol. Figure B.13 shows the transmission electron microscope (TEM) images of the titania nanoparticles prepared.

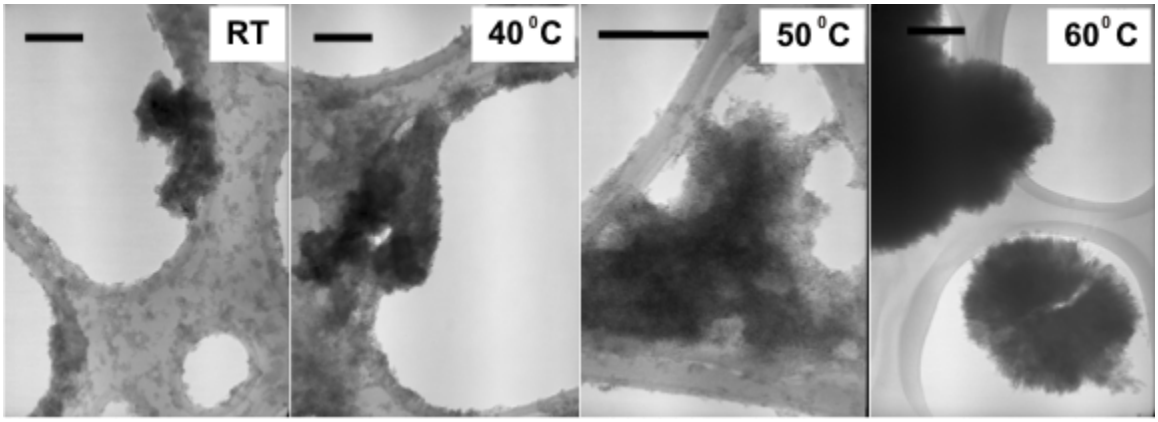

Figure B.13 TEM images of titania nanoparticles prepared from a solution of 0.729 M $TiCl_4$ and 20 mM BDDAC after aging at various temperatures. Scale bars are 100 nm.

There was a dramatic change in the morphology of the titania nanoparticles formed between 50°C and 60°C. The nanoparticles were spherical and very small (<10 nm) when aged below 60°C. Aging the mixture at 60°C resulted in largely aggregated

spherulites (>100 nm) of small needle-like titania. The powder X-ray diffraction of the nanoparticles revealed the crystallinity and their crystalline phase, as shown in Figure B.14.

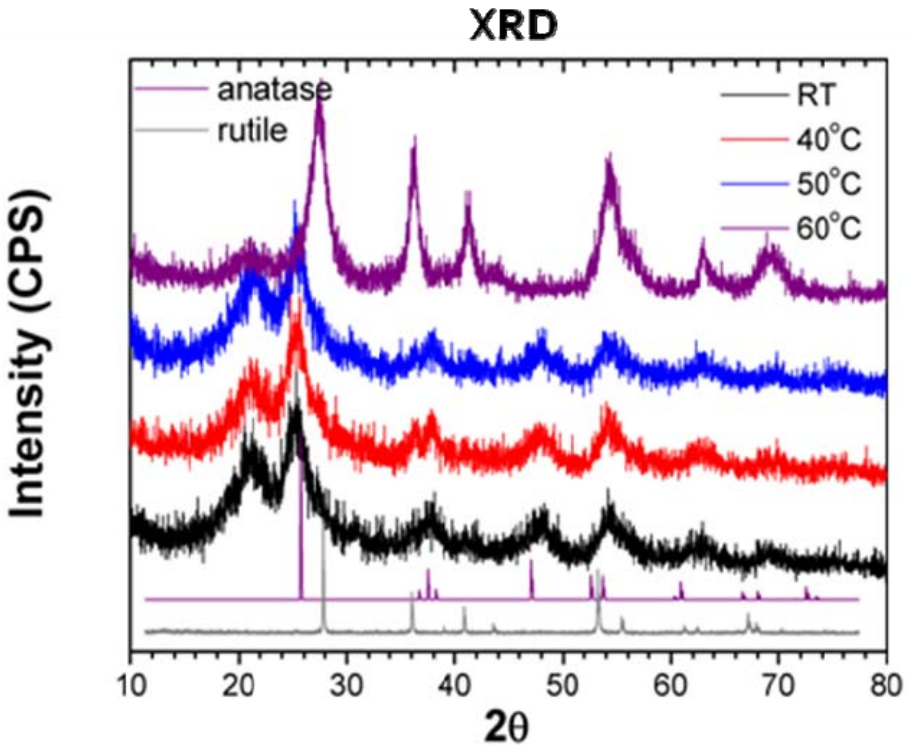

Figure B.14 XRD patterns of the nanoparticles described in Figure B.12. The diffractogram of bulk anatase and rutile titania are also displayed as references.

There was a major change in the crystalline phase of the titania from anatase to rutile phase between 50°C aging and 60°C aging. There were also a large portion of amorphous phase titania below 60°C aging appearing as a broad peak below 25° in 2θ scale.

Further studies on the effect of the preparation conditions, such as the concentration of $TiCl_4$, adjustment of pH, addition of Cl^- salt, and temperature need to be performed to prepare rutile phase titania of desired size.(Zhang and Gao 2003)

B.4 Conclusions

Preliminary studies on the high refractive index TiO_2:polymer nanocomposites indicated that very small (~10 nm) rutile phase TiO_2 nanoparticles are desirable to achieve nanocomposites with low scattering loss for direct laser writing. Synthesis of small rutile titania nanoparticles by using micelles to control the growth of the titania, then by using phosphonic acid surface modifier to quench and isolate the titania nanoparticles is suggested. Combining the 10 nm rutile titania with photo-patternable high refractive index host material would enable the preparation of high refractive index (>1.9), direct laser writing nanocomposite materials useful for the fabrication of 3D photonic band gap structures.

REFERENCES

Adams, T. B., D. C. Sinclair, et al. (2002). "Giant Barrier Layer Capacitance Effects in $CaCu_3Ti_4O_{12}$ Ceramics." Advanced Materials **14**(18): 1321-1323.

Ahmad, G., M. B. Dickerson, et al. (2008). "Rapid Bioenabled Formation of Ferroelectric $BaTiO_3$ at Room Temperature from an Aqueous Salt Solution at Near Neutral pH." Journal of the American Chemical Society **130**(1): 4-5.

Aizenberg, J. (2000). "Patterned crystallization on self-assembled monolayers with integrated regions of disorder." Journal of the Chemical Society, Dalton Transactions: 3963-3968.

Ang, C. and Z. Yu (2004). "Ferroelectric, Electroactive, and Dielectric-Relaxation Behavior of Fluoropolymers." Advanced Materials **16**(12): 979-982.

Arit, G., D. Hennings, et al. (1985). "Dielectric Properties of Fine-Grained Barium Titanate Ceramics." Journal of Applied Physics **58**(4): 1619-1625.

Aspnes, D. E. (1982). "Local-field effects and effective-medium theory: A microscopic perspective." American Journal of Physics **50**(8): 704-709.

Bai, Y., Z.-Y. Cheng, et al. (2000). "High-Dielectric-Constant Ceramic-Powder Polymer Composites." Applied Physics Letters **76**(25): 3804-3806.

Balazs, A. C., T. Emrick, et al. (2006). "Nanoparticle Polymer Composites: Where Two Small Worlds Meet." Science **314**(1107-1110).

Bao, Z. and J. Locklin, Eds. (2007). Optical Science and Engineering. Organic Field-Effect Transistors. Boca Raton, CRC Press.

Bars, N. L., D. Tinet, et al. (1991). "Adsorption mechanism of ester phosphate on baryum titanate in organic medium. Preliminary results on the structure of the adsorbed layer." Journal de Physique III **1**(5): 707-718.

Bhattacharya, A. K. and G. Thyagarajan (1981). "The Michaelis-Arbuzov Rearrangement." Chemical Review **81**(4): 415-430.

Biswas, A., I. S. Bayer, et al. (2007). "Nanostructured barium titanate composites for embedded radio frequency applications." Applied Physics Letters **91**: 212902.

Bohren, C. F. and D. Huffman (1983). Absorption and scattering of light by small particles. New York, John Wiley.

Borse, P. H., L. S. Kankate, et al. (2002). "Synthesis and investigations of rutile phase nanoparticles of TiO_2." Journal of Materials Science: Materials in Electronics **13**: 553-559.

Bottcher, C. J. F., O. C. v. Belle, et al. (1973). Theory of Electric Polarization. New York, American Elsevier Publishing Co.

Brodard-Severac, F., G. Guerrero, et al. (2008). "High-Field ^{17}O MAS NMR Investigateion of Phosphonic Acid Monolayers on Titania." Chemistry of Materials **20**: 5191-5196.

Brodard-Severac, F., G. Guerrero, et al. (2008). "High-Field ^{17}O MAS NMR Investigation of Phosphonic Acid Monolayers on Titania." Chemistry of Materials **20**: 5191-5196.

Busch, K., G. v. Freymann, et al. (2007). "Periodic nanostructures for photonics." Physics Reports **444**: 101-202.

Caballero, A. C., J. F. Fernandez, et al. (1997). "Effect of Residual Phosphorus Left by Phosphate Ester on $BaTiO_3$ Ceramics." Materials Research Bulletin **32**(2): 221-229.

Calame, J. P. (2006). "Finite difference simulations of permittivity and electric field statistics in ceramic-polymer composites for capacitor applications." Journal of Applied Physics **99**: 084101.

Castillo, J. L. d., J. Czapkiewicz, et al. (1999). "Micellar properties of alkyldimethylphenylammonium bromides in water." Colloid and Polymer Science **277**: 422-427.

Chen, F.-C., C.-W. Chu, et al. (2004). "Organic thin-film transistors with nanocomposite dielectric gate insulator." Applied Physics Letters **85**(15): 3295-3297.

Chen, F.-C., C.-S. Chuang, et al. (2006). "Low-voltage organic thin-film transistors with polymeric nanocomposite dielectrics." Organic Electronics **7**: 435-439.

Cheng, H., J. Ma, et al. (1995). "Hydrothermal Preparation of Uniform Nanosize Rutile and Anatase Particles." Chemistry of Materials **7**: 663-671.

Cheng, K.-C., C.-M. Lin, et al. (2007). "Dielectric properties of epoxy resin-barium titanate composites at high frequency." Materials Letters **61**: 757-760.

Chiang, C.-W. and J.-H. Jean (2003). "Effects of barium dissolution on dispersing aqueous barium titanate suspensions." Materials Chemistry and Physics **80**: 647-655.

Chiang, C. K. and R. Popielarz (2002). "Polymer Composites with High Dielectric Constant." Ferroelectrics **275**: 1-9.

Cho, J. H., J. Lee, et al. (2008). "High-Capacitance Ion Gel Gate Dielectrics with Faster Polarization Response Times for Organic Thin Film Transistors." Advanced Materials **20**: 686-690.

Cho, S.-D. and K.-W. Paik (2001). "Relationships Between Suspension Formulations and the Properties of $BaTiO_3$/Epoxy Composite Films for Integral Capacitors." Proceedings of 51st IEEE Electronic Components and Technology Conference: 1418-1422.

Chu, B., X. Zhou, et al. (2006). "A Dielectric Polymer with High Electric Energy Density and Fast Discharge Speed." Science **313**: 334-336.

Chua, L.-L., J. Zaumseil, et al. (2005). "General observation of n-type field-effect behavior in organic semiconductors." Nature **434**: 194-199.

Coakley, k. M. and M. D. McGehee (2004). "Conjugated Polymer Photovoltaic Cells." Chemistry of Materials **16**: 4533-4542.

Coates, G. W., A. R. Dunn, et al. (1997). "Phenyl-Perfluorophenyl Stacking Interactions: A New Strategy for Supermolecule Construction." Angewandte Chemie International Edition **36**(3): 248-251.

Cole, J. R. and N. J. Halas (2006). "Optimized plasmonic nanoparticle distributions for solar spectrum harvesting." Applied Physics Letters **89**: 153120.

Cook, R. F. and E. G. Liniger (1999). "Stress-Corrosion Cracking of Low-Dielectric-Constant Spin-On-Glass Thin Films." Journal of The Electrochemical Society **146**(12): 4439-4448.

Cozzoli, P. D., A. Kornowski, et al. (2003). "Low-Temperature Synthesis of Soluble and Processable Organic-Capped Anatase TiO_2 Nanorods." Journal of the American Chemical Society **125**: 14539-14548.

Cumpston, B. H., S. P. Ananthavel, et al. (1999). "Two-photon polymerization initiators for three-dimensional optical data storage and microfabrication." Nature **398**: 51-54.

Dang, Z.-M., Y.-H. Lin, et al. (2003). "Novel Ferroelectric Polymer Composites with High Dielectric Constants." Advanced Materials **15**(19): 1625-1629.

Dang, Z.-M., D. Xie, et al. (2007). "Theoretical prediction and experimental study of dielectric properties in poly(vinylidene fluoride) matrix composites with micronanosize $BaTiO_3$ filler." Applied Physics Letters **91**: 222902.

Dang, Z. M., Y. Shen, et al. (2002). "Dielectric behavior of three-phase percolative Ni-BaTiO3-polyvinylidene
fluoride composites." Applied Physics Letters **81**(25): 4814-4816.

Davies, W. E. V. J., J. Dutton, et al. (1965). "Electrical Breakdown of Air at High Voltages." Nature **205**: 1092-1093.

Electrocube (2008). "Surge Suppressors and Capacitors: PF, DF and QF." from http://www.electrocube.com/support/bullet5.asp.

Erb, T., S. Raleva, et al. (2004). "Structural and optical properties of both pure poly(3-octylthiophene) (P3OT) and P3OTyfullerene films." Thin Solid Films **450**: 97-100.

Facchetti, A., M.-H. Yoon, et al. (2005). "Gate Dielectrics for Organic Field-Effect Transistors: New Opportunities for Organic Electronics." Advanced Materials **17**: 1705-1725.

Faria, L. O., C. Welter, et al. (2006). "Relaxor ferroelectric behavior of poly(vinylidene fluoride-trifluoroethylene) copolymer modified by low energy irradiation." Applied Physics Letters **88**: 192903.

Ferreira, J. M., S. Marcinko, et al. (2005). "Calorimetric study of the reactions of n-alkylphosphonic acids with metal oxide surfaces." Journal of Colloid and Interface Science **286**: 258-262.

Folkers, J. P., C. B. Gorman, et al. (1995). "Self-Assembled Monolayers of Long-Chain Hydroxamic Acids on the Native Oxides of Metals." Langmuir **11**: 813-824.

Fritz, S. E., T. W. Kelley, et al. (2005). "Effect of Dielectric Roughness on Performance of Pentacene TFTs and Restoration of Performance with a Polymeric Smoothing Layer." Journal of Physical Chemistry B **109**: 10574-10577.

Fujishima, S. (2000). "The History of Ceramic Filters." IEEE Transactions on Ultrasonics, Ferroelectrics, and Frequency Control **47**(1): 1-7.

Gao, W., L. Dickinson, et al. (1996). "Self-Assembled Monolayers of Alkylphosphonic Acids on Metal Oxides." Langmuir **12**: 6429-6435.

Garnett, J. C. M. (1904). "Colours in Metal Glasses and in Metallic Films." Philosophical Transaction of the Royal Society of London **203**: 385-420.

Gilbert, L. J., T. P. Schuman, et al. (2005). Dielectric Powder/Polymer Composites for High Energy Density Capacitors. Advances in Electronic and Electrochemical Ceramics: Proceedings of the 107th Annual Meeting of The American Ceramic Society, Baltimore, Maryland, USA, Wiley.

Guerrero, G., P. H. Mutin, et al. (2001). "Anchoring of Phosphonate and Phosphinate Coupling Molecules on Titania Particles." Chemistry of Materials **13**(4367-4373).

Guerrero, G., P. H. Mutin, et al. (2001). "Anchoring of Phosphonate and Phosphinate Coupling Molecules on Titania Particles." Chemsitry of Materials **13**(4367-4373).

Guillemet-Fritsch, S., Z. Valdez-Nava, et al. (2008). "Colossal Permittivity in Ultrafine Grain Size $BaTiO_{3-x}$ and $Ba_{0.95}La_{0.05}TiO_{3-x}$ Materials." Advanced Materials **20**: 551-555.

Halik, M., H. Klauk, et al. (2002). "Fully patterned all-organic thin film transistors." Applied Physics Letters **81**(2): 289-291.

Halik, M., H. Klauk, et al. (2002). "Polymer gate dielectrics and conducting polymer contacts for high-performance organic thin-film transistors." Advanced Materials **14**(23): 1717-1722.

Han, K.-k., S. W. Lee, et al. (2006). "Oxygen plasma treatment of gate metal in organic thin-film transistors." Applied Physics Letters **88**: 233509.

Hanson, E. L., J. Schwartz, et al. (2003). "Bonding Self-Assembled, Compact Organophosphonate Monolayers to the Native Oxide Surface of Silicon." Journal of the American Chemical Society **125**: 16074-16080.

He, X., K. Yao, et al. (2005). "Phase transition and properties of a ferroelectric poly(vinylidene fluoride-hexafluoropropylene) copolymer." Journal of Applied Physics **97**: 084101.

Heikenfeld, J. and A. J. Steckl (2005). "High-transmission electrowetting light valves." Applied Physics Letters **86**: 151121.

Hess, D. W. and K. F. Jensen (1989). Microelectronics Processing: Chemical Engineering Aspects. Washington DC, American Chemical Society Publication.

Hiramatsu, H. and F. E. Osterloh (2004). "A Simple Large-Scale Synthesis of Nearly Monodisperse Gold and Silver Nanoparticles with Adjustable Sizes and with Exchangeable Surfactants." Chemistry of Materials **16**(13): 2509-2511.

Ho, K. M., C. T. Chan, et al. (1994). "Photonic Band Gaps in Three Dimensions: new Layer-By-Layer Periodic Structures." Solid State Communications **89**(5): 413-416.

Houston, J. E. and H. I. Kim (2002). "Adhesion, Friction, and Mechanical Properties of Functionalized Alkanethiol Self-Assembled Monolayers." Accounts of Chemical Research **35**(7): 547-553.

Huang, C. and Q. Zhang (2004). "Enhanced Dielectric and Electromechanical Responses in High Dielectric Constant All-Polymer Percolative Composites." Advanced Functional Materials **14**(5): 501-506.

Huang, J., G. Li, et al. (2005). "Influence of composition and heat-treatment on the charge transport properties of poly(3-hexylthiophene) and [6,6]-phenyl C61-butyric acid methyl ester blends." Applied Physics Letters **87**: 112105.

Hughes, M. P. (2003). Nanoelectromechanics in Engineering Biology. Boca Raton, FL, CRC Press.

Ihlefeld, J., B. Laughlin, et al. (2005). "Copper Compatible Barium Titanate Thin Films for Embedded Passives." Journal of Electroceramics **14**: 95-102.

Jang, Y., D. H. Kim, et al. (2005). "Influence of the dielectric constant of a polyvinyl phenol insulator of the field-effect mobility of a pentacene-based thin-film transistor." Applied Physics Letters **87**: 152105.

Jayannavar, A. M. and N. Kumar (1991). "Generalization of Bruggeman's unsymmetrical effective-medium theory to a three-component composite." Physical Review B **44**(21): 12014-12015.

Jayasundere, N. and B. V. Smith (1993). "Dielectric Constant for Binary Piezoelectric 0-3 Composites." Journal of Applied Physics **73**(5): 2462-2466.

Jennings, G. K., T.-H. Yong, et al. (2003). "Structural Effects on the Barrier Properties of Self-Assembled Monolayers Formed from Long-Chain ω-Alkoxy-n-alkanethiols on Copper." Journal of the American Chemical Society **125**(10): 2950-2957.

Joannopoulos, J. D., R. D. Meade, et al. (1995). Photonic Crystal: Molding the Flow of Light. Princeton, NJ, Princeton University Press.

Johnson, G. L. (2001). Solid State Tesla Coil. Manhattan, KS.

Jung, C., A. Maliakal, et al. (2007). "Pentacene-based thin film transistors with titanium oxide-polystyrene/polystyrene insulator blends: High mobility on high k dielectric films." Applied Physics Letters **90**: 062111.

Kaafarani, B. R., T. Kondo, et al. (2005). "High Charge-Carrier Mobility in an Amorphous Hexaazatrinaphthylene Derivative." Journal of the American Chemical Society **127**: 16358-16359.

Kaboudin, B. and R. Nazari (2001). "A Convenient and Mild Procedure for the Preparation of agr-Keto Phosphonates of 1-Hydroxyphosphonates under Solvent-Free Conditions Using Microwave." Synthetic Communications **31**(15): 2245-2250.

Kerner, E. H. (1956). "The Electrical Conductivity of Composite Media." Proc. Phys. Soc. London Sec. B **69**: 802-807.

Kilaru, M. K., J. Heikenfeld, et al. (2007). "Strong charge trapping and bistable electrowetting on nanocomposite fluoropolymer:$BaTiO_3$ dielectrics." Applied Physics Letters **90**: 212906.

Kim, B.-K. and D.-Y. Lim (2003). "A New Glycothermal Process for Barium Titanate Nanoparticle Synthesis." Journal of the American Ceramic Society **86**(10): 1793-1796.

Kim, B., V. Kazmirenko, et al. (2002). Microwave Dielectric Spectroscopy of Ferroelectric Thin Films. Materials Research Society Symposium, Materials Research Society.

Kim, J. Y., K. Lee, et al. (2007). "Efficient Tandem Polymer Solar Cells Fabricated by All-Solution Processing." Science **317**: 222-225.

Kim, K. and D. L. Carroll (2005). "Roles of Au and Ag nanoparticles in efficiency enhancement of poly(3-octylthiophene)/C60 bulk heterojunction photovoltaic devices." Applied Physics Letters **87**: 203113.

Kim, P., S. C. Jones, et al. (2007). "Phosphonic Acid-Modified Barium Titanate Polymer Nanocomposites with High Permittivity and Dielectric Strength." Advanced Materials **19**: 1001-1005.

Kim, P., X.-H. Zhang, et al. (2008). "Solution-processible high-permittivity nanocomposite gate insulators for organic field-effect transistors." Applied Physics Letters **93**: 013302.

Kirkpatrick, S. (1973). "Percolation and Conduction." Reviews of Modern Physics **45**(4): 574-588.

Kitaigorodskii, A. I. (1961). Organic Chemical Crystallography. New York, Consultants Bureau.

Kittel, C. (1996). Introduction to Solid State Physics. New York, NY, John Wiley and Sons, Inc.

Klauk, H., U. Zschieschang, et al. (2007). "Ultralow-power organic complementary circuits." Nature **445**: 745-748.

Kobayashi, S., T. Nishikawa, et al. (2004). "Control of carrier density by self-assembled monolayers in organic field-effect transistors." Nature Materials **3**: 317-322.

Koch, N. (2007). "Organic Electronic Devices and Their Functional Interfaces." European Journal of Chemical Physics and Physical Chemistry **8**: 1438-1455.

Kwon, S.-G., K. Choi, et al. (2006). "Solvothermal synthesis of nano-sized tetragonal barium titanate powders." Materials Letters **60**: 979-982.

Kwon, S.-G., B.-H. Park, et al. (2006). "Solvothermally synthesized tetragonal barium titanate powders using H_2O/EtOH solvent." Journal of the European Ceramics Society **26**: 1401-1404.

Landauer, R. (1952). "The Electrical Resistance of Binary Metallic Mixtures." Journal of Applied Physics **23**(7): 779-784.

Lee, B. I., X. Wang, et al. (2006). "Synthesis of high tetragonality nanoparticle $BaTiO_3$." Microelectronic Engineering **83**: 463-70.

Lee, C. H., S. H. Hur, et al. (2005). "Charge-trapping device structure of dielectric for high-density flash memory." Applied Physics Letters **86**(15): 152908-152908.

Lee, J. J., K. J. Park, et al. (2006). "Synthesis of Ultrafine and Spherical Barium Titanate Powders Using a Titania Nano-Sol." Journal of the American Ceramic Society **89**(10): 3299-3301.

Li, J., J. Claude, et al. (2008). "Electrical Energy Storage in Ferroelectric Polymer Nanocomposites Containing Surface-Functionalized $BaTiO_3$ Nanoparticles." Chemistry of Materials **ASAP**.

Li, J. Y., C. Huang, et al. (2004). "Enhanced electromechanical properties in all-polymer percolative composites." Applied Physics Letters **84**(16): 3124-3126.

Li, J. Y., L. Zhang, et al. (2007). "Electric energy density of dielectric nanocomposites." Applied Physics Letters **90**: 132901.

Li, Y., Y. Fan, et al. (2002). "A novel method for preparation of nanocrystalline rutile TiO_2 powders by liquid hydrolysis of $TiCl_4$." Journal of Materials Chemistry **12**: 1387-1390.

Lichtenecker, K. (1926). "Dielectric Constant of Natural and Synthetic Mixtures." Phys. Zeitung **27**: 115-158.

Lopez, M. d. C. B., G. Fourlaris, et al. (1999). "Characterization of Barium Titanate Powders: Barium Carbonate Identification." Journal of the American Ceramic Society **82**(7): 1777-1786.

Lorentz, H. A. (1916). Theory of Electrons and Its Applications to the Phenomena of Light and Radiant Heat. Leipzig, B. G. Teubner.

Lott, J., C. Xia, et al. (2008). "Terahertz Photonic Crystals Based on Barium Titanate/Polymer Nanocomposites." Advanced Materials **20**: 3649-3653.

Love, J. C., L. A. Estroff, et al. (2005). "Self-Assembled Monolayers of Thiolates on Metals as a Form of Nanotechnology." Chemical Review **105**: 1103-1169.

Lu, A.-H., E. L. Salabas, et al. (2007). "Magnetic Nanoparticles: Synthesis, Protection, Functionalization, and Application." Angewandte Chemie International Edition **46**: 1222-1244.

Lu, J. and C. P. Wong (2007). Tailored dielectric properties of high-k polymer composites via nanoparticles surface modification for embedded passives applications IEEE Electronic Components and Technology Conference, Atlanta, GA, Institute of Electrical and Electronics Engineers.

Lu, Y., J. Claude, et al. (2006). "A Modular Approach to Ferroelectric Polymers with Chemically Tunable Curie Temperatures and Dielectric Constants." Journal of the American Chemical Society **128**: 8120-8121.

Maensiri, S., P. Thongbai, et al. (2007). "Giant dielectric permittivity observed in $CaCu_3Ti_4O_{12}$/(Li,Ti)-doped NiO composites." Applied Physics Letters **90**: 202908.

Majewski, L. A., R. Schroeder, et al. (2005). "One Volt Organic Transistor." Advanced Materials **17**: 192-196.

Maliakal, A., H. Katz, et al. (2005). "Inorganic oxide core, polymer shell nanocomposite as a high k gate dielectric for flexible electronics applications." Journal of the American Chemical Society **127**(14655-14662).

Mandal, T. K. (2007). "Characterization of tetragonal $BaTiO_3$ nanopowders prepared with a new soft chemistry route." Materials Letters **61**: 850-854.

Marder, S. R., J.-L. Brédas, et al. (2007). "Materials for Multiphoton 3D Microfabrication." MRS Bulletin **32**: 561-565.

Markovic, S., M. Mitric, et al. (2008). "Ultrasonic de-agglomeration of barium titanate powder." Ultrasonics Sonochemistry **15**: 16-20.

McDonald, S. A., G. Konstantatos, et al. (2005). "Solution-processed PbS quantum dot infrared photodetectors and photovoltaics." Nature Materials **4**: 138-142.

McDonald, S. E. K. K. D., D. H. Holt, et al. (2006). "Phenylphosphonic Acid Functionalization of Indium Tin Oxide: Surface Chemistry and Work Functions." Langmuir **22**: 6249-6255.

Mihailetchi, V. D., J. K. J. v. Duren, et al. (2003). "Electron Transport in a Methanofullerene." Advanced Functional Materials **13**: 43-46.

Mihailetchi, V. D., H. Xie, et al. (2006). "Charge Transport and Photocurrent Generation in Poly(3-hexylthiophene):Methanofullerene Bulk-Heterojunction Solar Cells." Advanced Functional Materials **16**: 699-708.

Mikeska, K. R. and W. R. Cannon (1988). "Non-Aqueous Dispersion Properties of Pure Barium Titanate for Tape Casting." Colloids and Surfaces **29**: 305-321.

Mingalyov, P. G. and G. V. Lisichkin (2006). "Chemical modification of oxide surfaces with organophosphorous(V) acids and their esters." Russian Chemical Reviews **75**(6): 541-557.

Mooney, K. E., J. A. Nelson, et al. (2004). "Superparamagnetic Cobalt Ferrite Nanocrystals Synthesized by Alkalide Reduction." Chemistry of Materials **16**: 3155-3161.

Moore, G. E. (1965). "Cramming more components onto integrated circuits." Electronics **38**(8): 114-117.

Mugele, F. and J.-C. Baret (2005). "Electrowetting: from basics to applications." Journal of Physics: Condensed Matter **17**: R705-R774.

Mutin, P. H., G. Guerrero, et al. (2005). "Hybrid Materials from Organophosphorous Coupling Molecules." Journal of Materials Chemistry **15**: 3761-3768.

Neouze, M.-A. and U. Schubert (2008). "Surface Modification and Functionalization of Metal and Metal Oxide Nanoparticles by Organic Ligands." Monatshefte fur Chemie **139**: 183-195.

Newnham, R. E., D. P. Skinner, et al. (1978). "Connectivity and Piezoelectric-Pyroelectric Composites." Materials Research Bulletin **13**(5): 525-536.

Nilsing, M., S. Lunell, et al. (2005). "Phosphonic acid adsorption at the TiO_2 anatase (101) surface investigated by periodic hybrid HF-DFT computations." Surface Science **582**: 4-60.

Nuraje, N., K. Su, et al. (2006). "Room Temperature Synthesis of Ferroelectric Barium Titanate Nanoparticles Using Peptide Nanorings as Templates." Advanced Materials **18**: 807-811.

Nussbaumer, R. J., W. R. Caseri, et al. (2003). "Polymer-TiO_2 Nanocomposites: A Route Towards Visually Transparent Broadband UV Filters and High Refractive Index Materials." Macromolecular Materials Engineering **288**(1): 44-49.

O'Dwyer, J. J. (1964). The Theory of Dielectric Breakdown of Solids. London, Oxford University Press.

Ogitani, S., S. A. Bidstrup-Allen, et al. (2000). "Factors Influencing the Permittivity of Polymer/Ceramic Composites for Embedded Capacitors." IEEE Trans. Adv. Packag. **23**(2): 313-322.

Paniagua, S. A., P. J. Hotchkiss, et al. (2008). "Phosphonic Acid Modification of Indium-Tin Oxide Electrodes: Combined XPS/UPS/Contact Angle Studies." Journal of Physical Chemistry C **112**: 7809-7817.

Pecharroman, C., F. Esteban-Betegon, et al. (2001). "New Percolative $BaTiO_3$-Ni Composites with a High and Frequency-Independent Dielectric Constant ($e_r \sim 80,000$)." Advanced Materials **13**: 1531.

Perry, R. H. (1997). Perry's Chemical Engineers' Handbook. New York, McGraw-Hill.

Polini, W. and L. Sorrentino (2003). "Improving the wettability of 2024 aluminum alloy by means of cold plasma treatment." Applied Surface Science **214**: 232-242.

Popielarz, R., C. K. Chiang, et al. (2001). "Dielectric Properties of Polymer/Ferroelectric Ceramic Composites from 100 Hz to 10 GHz." Macromolecules **34**: 5910-5915.

Prendergast, J., E. O'Driscoll, et al. (2005). "Investigation into the correct statistical distribution for oxide breakdown over oxide thickness range." Microelectronics Reliability **45**: 973-977.

Qi, L., B. I. Lee, et al. (2005). "High-Dielectric-Constant Silver-Epoxy Composites as Embedded Dielectrics." Advanced Materials **17**: 1777-1781.

Rabuffi, M. and G. Picci (2002). "Status Quo and Future Prospects for Metallized Propylene Energy Storage Capacitors." IEEE Transactions on Plasma Science **30**(5): 1939-1942.

Raju, G., A. Katebian, et al. (2003). "Breakdown Voltages of Polymers in the Temperature Range 23^{o}-250^{o}C." IEEE Transactions on Dielectrics and Electrical Insulation **10**(1): 117-127.

Ramesh, S., B. A. Shutzberg, et al. (2003). "Dielectric Nanocomposites for Integral Thin Film Capacitors: Materials Design, Fabrication and Integration Issues." IEEE Transactions on Advanced Packaging **26**(1): 17-24.

Randon, J. and R. Paterson (1997). "Preliminary studies on the potential for gas separation by mesoporous ceramic oxide membranes surface modified by alkyl phosphonic acids." Journal of Membrane Science **134**: 219-223.

Ranjan, V., L. Yu, et al. (2007). "Phase Equilibria in High Energy Density PVDF-Based Polymers." Physical Review Letters **99**: 047801.

Rao, Y., J. Qu, et al. (2000). "A Precise Numerical Prediction of Effective Dielectric Constant for Polymer-Ceramic Composite Based on Effective-Medium Theory." IEEE Transactions on Advanced Packaging Technologies **23**(4): 680-683.

Rao, Y. and C. P. Wong (2004). "Material Characterization of a High-Dielectric-Constant Polymer-Ceramic Composite for Embedded Capacitor for RF Applications." Journal of Applied Polymer Science **92**: 2228-2231.

Ravez, J. and A. Simon (2000). "Non-Stoichiometric Perovskites Derived from $BaTiO_3$ with a Ferroelectric Relaxor Behavior." Physica Status Solidi (a) **178**: 793-797.

Rice, R. W. (1998). Porosity of Ceramics. New York, Marcel Dekker, Inc.

Sarkar, S., P. K. Jana, et al. (2008). "Colossal internal barrier layer capacitance effect in polycrystalline copper(II) oxide." Applied Physics Letters **92**: 022905.

Schroeder, R., L. A. Majewski, et al. (2005). "High-Performance Organic Transistors Using Solution-Processed Nanoparticle-Filled High-k Polymer Gate Insulators." Advanced Materials **17**: 1535-1539.

Schulze, K. A., A. A. Zaman, et al. (2003). "Effect of filler fraction on strength, viscosity and porosity of experimental compomer materials." Journal of Dentistry **31**: 373-382.

Segawa, H., K. Tateishi, et al. (2004). "Patterning of hybrid titania film using photopolymerization." Thin Solid Films **466**: 48-53.

Slenes, K. M. and L. E. Bragg (2005). "Compact Capacitor Technology for Future Electromagnetic Launch Applications." IEEE Transactions on Magnetics **41**(1): 326-329.

Socrates, G. (1994). Infrared and Raman Characteristic Group Frequencies - Tables and Charts. New York, John Wiley and Sons, Ltd.

Stadlober, B., M. Zirkl, et al. (2005). "High-mobility pentacene organic field-effect transistors with a high-dielectric-constant fluorinated polymer film gate dielectric." Applied Physics Letters **86**: 242902.

Steudel, S., S. D. Vusser, et al. (2004). "Influence of the dielectric roughness on the performance of pentacene transistors." Applied Physics Letters **85**(19): 4400-4402.

Su, K., N. Nuraje, et al. (2007). "Open-Bench Method for the Preparation of $BaTiO_3$, $SrTiO_3$, and $Ba_xSr_{1-x}TiO_3$ Nanocrystals at 80^0C " Langmuir **23**(23): 11369-11372.

Sun, W., J. Li, et al. (2006). "Preparation of Fine Tetragonal Barium Titanate Powder by a Microwave-Hydrothermal Process." Journal of the American Ceramic Society **89**(1): 118-123.

Tetreault, N., G. v. Freymann, et al. (2006). "New Route to Three-Dimensional Photonic Band Gap Materials: Silicon Double Inversion of Polymer Templates." Advanced Materials **18**: 457-460.

Thomas, L. C. (1974). Interpretation of the Infrared Spectra of Organophosphorous Compounds. London, Heyden & Son, Ltd.

Trentler, T. J., T. E. Denler, et al. (1999). "Synthesis of TiO_2 Nanocrystals by Nonhydrolytic Solution-Based Reactions." Journal of the American Chemical Society **121**: 1613-1614.

Tummala, R. R., E. J. Rymaszewski, et al., Eds. (1999). Microelectronics Packaging Handbook, Kluwer Academic Publishers.

Tuncer, E., D. R. James, et al. (2006). "On Dielectric Breakdown Statistics." Journal of Physics D: Applied Physics **39**: 4257-4268.

Tuncer, E., I. Sauers, et al. (2007). "Electrical properties of epoxy resin based nano-composites." Nanotechnology **18**: 025703.

Tuncer, E., I. Sauers, et al. (2007). "Enhancement of dielectric strength in nanocomposites." Nanotechnology **18**: 325704.

Ul-Haq, S. and G. R. G. Raju (2002). Weibull Statistical Analysis of Area Effect on the Breakdown Strength in Polymer Films. 2002 Annual Report Conference on Electrical Insulation and Dielectric Phenomena**:** 518-521.

Ventura, M. J., C. Bullen, et al. (2007). "Direct laser writing of three-dimensional photonic crystal lattices within a PbS quantum-dot-doped polymer material." Optics Express **15**(4): 1817-1822.

Veres, J., S. Ogier, et al. (2004). "Gate Insulators in Organic Field-Effect Transistors." Chemistry of Materials **16**: 4543-4555.

Viornery, C., Y. Chevolot, et al. (2002). "Surface Modification of Titanium with Phosphonic Acid to Improve Bone Bonding: Characterization by XPS and ToF-SIMS." Langmuir **18**(7): 2582-2589.

Wang, W., B. Gu, et al. (2004). "Synthesis of Rutile (α-TiO_2) Nanocrystals with Controlled Size and Shape by Low-Temperature Hydrolysis: Effects of Solvent Composition." Journal of Physical Chemistry B **108**(39): 14789-14792.

Wenzl, I., C. M. Yam, et al. (2003). "Structure and Wettability of Methoxy-Terminated Self-Assembled Monolayers on Gold." Langmuir **19**(24): 10217-10224.

Werne, T. v. and T. E. Patten (2001). "Atom Transfer Radical Polymerization from Nanoparticles: A Tool for the Preparation of Well-Defined Hybrid Nanostructures and for Understanding the Chemistry of Controlled/"Living" Radical Polymerizations from Surfaces." Journal of the American Chemical Society **123**: 7497-7505.

White, M. A., J. A. Johnson, et al. (2006). "Toward the Syntheses of Universal Ligands for Metal Oxide Surfaces: Controlling Surface Functionality through Click Chemistry." Journal of the American Chemical Society **128**(35): 11356-11357.

Whitesides, G. M. and P. E. Laibinis (1990). "Wet chemical approaches to the characterization of organic surfaces: self-assembled monolayers, wetting, and the physical-organic chemistry of the solid-liquid interface." Langmuir **6**.

Wilk, G. D., R. M. Wallace, et al. (2001). "High-k gate dielectrics: Current status and materials properties considerations." Journal of Applied Physics **89**(10): 5243-5275.

Wong, S., M. Deubel, et al. (2006). "Direct Laser Writing of Three-Dimensional Photonic Crystals with a Complete Photonic Bandgap in Chalcogenide Glasses." Advanced Materials **18**: 265-269.

Wong, W.-Y., X.-Z. Wang, et al. (2007). "Metallated conjugated polymers as a new avenue towards high-efficiency polymer solar cells." Nature Materials **6**: 521-527.

Wu, X., L. Zou, et al. (2001). "Structural Characterizations of Organo-Capped Barium Titanate Nanoparticles Prepared by the Wet Chemical Route." Journal of Colloid and Interface Science **239**: 369-373.

Xu, H. and L. Gao (2003). "Tetragonal Nanocrystalline Barium Titanate Powder: Preparation, Characterization, and Dielectric Properties." Journal of the American Ceramic Society **86**(1): 203-205.

Xu, J. and C. P. Wong (2005). High-K nanocomposites with core-shell structured nanoparticles for decoupling applications IEEE Electronic Components and Technology Conference, Institute of Electrical and Electronics Engineers.

Yang, S., T. N. Krupenkin, et al. (2003). "Tunable and Latchable Liquid Microlens with Photopolymerizable Components." Advanced Materials **15**: 940-943.

Yashima, M., T. Hoshina, et al. (2005). "Size effect on the crystal structure of barium titanate nanoparticles." Journal of Applied Physics **98**: 014313.

Yoon, D.-H., B. I. Lee, et al. (2003). "Barium ion leaching from barium titanate powder in water." Journal of Materials Science: Materials in Electronics **14**: 165-169.

Yoon, M.-H., A. Facchetti, et al. (2005). "Sigma-phi molecular dielectric multilayers for low-voltage organic thin-film transistors." Proceedings of National Academy of Sciences **102**: 4678-4682.

Yoon, S., S. Baik, et al. (2006). "Formation Mechanisms of Tetragonal Barium Titanate Nanoparticles in Alkoxide-Hydroxide Sol-Precipitation Synthesis." Journal of the American Ceramic Society **89**(6): 1816-1821.

Yoon, S., S. Baik, et al. (2007). "Synthesis of Tetragonal Barium Titanate Nanoparticles Via Alkoxide-Hydroxide Sol-Precipitation: Effect of Water Addition." Journal of the American Ceramic Society **90**(1): 311-314.

Zaky, A. A. and R. Hawley (1970). Dielectric Solids. New York, Dover Publications Inc.

Zallen, R. (2004). The Physics of Amorphous Solids. New York, John Wiley & Sons, Inc.

Zang, G., J. Zhang, et al. (2005). "Grain boundary effect on the dielectric properties of $CaCu_3Ti_4O_{12}$." Journal of Physics D: Applied Physics **38**: 1824-1827.

Zhang, D., L. Qi, et al. (2002). "Formation of crystalline nanosized titania in reverse micelles at room temperature." Journal of Materials Chemistry **12**: 3677-3680.

Zhang, Q. and L. Gao (2003). "Preparation of Oxide Nanocrystals with Tunable Morphologies by the Moderate Hydrothermal Method: Insights from Rutile TiO_2." Langmuir **19**: 967-971.

Zhang, Q. M., V. Bharti, et al. (1998). "Giant Electrostriction and Relaxor Ferroelectric Behavior in Electron-Irradiated Poly(vinylidene fluoride-trifluoroethylene) Copolymer." Science **280**: 2101-2104.

Zhang, X.-H., B. Domercq, et al. (2007). "High-performance pentacene field-effect transistors using Al_2O_3 gate dielectrics prepared by atomic layer deposition (ALD)." Organic Electronics **8**: 718-726.

Zhao, Y., J. Wang, et al. (2005). "Colloidal Subwavelength Nanostructures for Antireflection Optical Coating." Optics Letters **30**(14).

VITA

PHILSEOK KIM

Philseok Kim was born in Bosung, South Korea. He attended Seoul National University, Seoul, South Korea, received a B.S. in Chemistry Education in 1995, and received a M.S. in Chemistry in 1997 under the supervision of Professor Du-Jeon Jang. He conducted a spectroscopic study and time-domain and frequency-domain kinetic studies on the cation binding sites of Y-Zeolite utilizing Eu(III) as a luminescent probe.

He joined R&D division of Daelim Industrial Company and conducted chemical analyses on various petrochemical products from 1997 to 1999. He moved to the R&D Park of LG Chemical company in 1999, where he investigated the chemical analysis of polymers and additives, detection methods of nucleic acid hybridization using surface plasmon resonance, development of sol-gel encapsulated protein chip materials, and the characterization of electronic materials using electron microscopy, scanning probe microscopy, and photoelectron spectroscopy before coming to Georgia Tech to pursue a doctorate in Physical Chemistry.

Outside his academic pursuits, Mr. Kim enjoys racquet sports such as tennis, table tennis, and racquet ball.